Summer 5-2020

Calculation of Exposed Length of Anchor Bolts in Shear I: Monotonic Loading

Da Luo
Guangxi University, dada923@qq.com

Jian Zhao
University of Wisconsin - Milwaukee, jzhao@uwm.edu

Calculation of Exposed Length of Anchor Bolts in Shear I: Monotonic Loading

Final Report

Prepared by:

Da Luo
BS, Central South University, 2013
MS, Guangxi University, 2015
PhD, Guangxi University, 2020
Visiting Scholar, UW-Milwaukee, 2019

Jian Zhao

Department of Civil & Environmental Engineering
University of Wisconsin-Milwaukee

May 2020

This page is blank

Technical Report Documentation Page

1. Report No. SERZ-2019-1	2. Government Accession No.	3. Recipient's Catalog No.	
4. Title and Subtitle Calculation of Exposed Length of Anchor Bolts in Shear I: Monotonic Loading		5. Report Date **May 2020** 6. Performing Organization Code	
7. Author(s) **Da Luo and Jian Zhao**		8. Performing Organization Report No.	
9. Performing Organization Name and Address Department of Civil & Environmental Engineering University of Wisconsin at Milwaukee 3200 N. Cramer Street Milwaukee, WI 53211		10. Work Unit No. 11. Contract or Grant No.	
12. Sponsoring Agency Name and Address		13. Type of Report and Period Covered Final Report (10/01/2018-10/30/2019) 14. Sponsoring Agency Code	
15. Supplementary Notes			
16. Abstract This report describes a study of stand-off anchors in shear with various exposed lengths. Anchor bolts embedded in concrete are commonly used in construction, and often leveling nuts are used to adjust the position of attached steel components. In this case, a portion of anchor bolts may be exposed as in a typical column footing connection without grouting. Such anchor bolts in shear are subjected to combined bending, shear and tension depending upon the stand-off heights, concrete compressive strength, and anchor diameter. The shear capacity of exposed anchors is critically related to the total exposed length, including the stand-off height and the depth of crushed concrete, because the bending moment applied to anchor shaft is directly related to the applied shear by the the exposed length. This is the focus of this study. A group of shear tests of anchors made of ASTM F1554 Grade 55 threaded rods were conducted to simulate the behavior of exposed anchors in shear. Finite element analyses using TNO DIANA® were conducted to explore key parameters, including the concrete and anchor materials, the anchor diameters, and the stand-off heights. The study indicated that the exposed length reduces with an increase in concrete compressive strength and the stand-off heights while increases with an increase in anchor diameter and strength. Equations were proposed for estimation of total exposed length based on the experimental and numerical results. Design equations were proposed for the shear capacity of stand-off/exposed anchors and the equations are verified by 90 tests collected from four sources in the literature.			
17. Key Words exposed length; concrete anchor; shear; stand-off; finite element analysis; nonlinear analysis		18. Distribution Statement No restrictions.	
19. Security Classification (of this report) Unclassified	20. Security Classification (of this page) Unclassified	21. No. of pages 120	22. Price

Disclaimers

Authors' disclaimer: The contents of this report reflect the views of the authors, who are responsible for the facts and the accuracy of the data presented herein. This report does not constitute a standard, specification, or regulation.

Patent disclaimer: There was no invention or discovery conceived or first actually reduced to practice in the course of or under this contract, including any art, method, process, machine manufacture, design or composition of matter, or any new useful improvement thereof, or any variety of plant, which is or may be patentable under the patent laws of the United States of America or any foreign country.

Acknowledgments

The authors would like to acknowledge the support from the Department of Civil and Environmental Engineering (CEE) at the University of Wisconsin, Milwaukee (UWM). Mr. Da Luo is grateful to the CEE department at UWM for hosting Mr. Da Luo during October 2018 through October 2019. The authors also thank the colleagues in American Concrete Institute (ACI) Committee 355 for their valuable inputs.

We are grateful to China Scholarship Council. The provided funding made it possible for Mr. Da Luo to visit UWM in 2018-19 and work with Dr. Zhao on this topic.

The laboratory tests were conducted by Dr. Zhibin Lin in 2011 at UWM with specimens made by Petersen as part of his MS study.

We thank Dr. Keaton E. McBride for providing details of his research and making unpublished images and data available to the research team.

We are grateful to Mr. Hua Liu, PhD student at the UWM CEE department for his help throughout the entire period.

Executive Summary

This report describes a study of anchors in shear commonly used in stand-off connections, where the connected based plate is elevated from the concrete surface, and often leveling nuts are used to adjust the position of attached steel components. In this case, a portion of anchor bolts may be exposed as in a column footing connection without grouting. Exposed anchor bolts in shear are subjected to combined bending, shear and tension. The shear capacity of exposed anchors is critically related to the total exposed length, including the stand-off height and the depth of crushed concrete, because the bending moment developed in the anchor shaft is directly related to the applied shear by the exposed length as a lever arm. Equations have been proposed in the literature to calculate shear capacities of exposed anchors, mostly based on stand-off heights; however, concrete can be crushed in front of an anchor shaft in shear, especially in ungrouted stand-off connections. The crushed concrete causes an increase in the total length of the exposed anchor shaft, laterally unsupported, from which the applied shear leads to a bending moment both ends of the exposed anchor shaft. This crushed concrete depth in front of anchors in shear is the focus of this study.

A total of 12 tests of anchors made of ASTM F1554 Grade 55 threaded rods were conducted to simulate the behavior of exposed anchors in shear. Knowing that the crushed concrete depth can be affected by concrete strength (Grosser, 2012) and the anchor diameter (Gomez *et al*. 2009), this group of tests explored the impact of stand-off height (l_s). Three stand-off heights, $0.08d_a$, $0.5d_a$ and $1.0d_a$, were chosen that were allowed by the geometry of the available specimens. No leveling nut was used beneath the loading plate. Four types of loading were used: 1) monotonic loading in displacement control; 2) cyclic loading in displacement control with three cycles per displacement level; 3) cyclic loading in force control with three cycles per peak load level; and 4) cyclic loading in force control with indefinite number of cycles at roughly 75 percent of the measured monotonic loading capacity. The experimental tests indicated that the exposed length in general decreases with an increase in concrete compressive strength and the stand-off heights while the exposed length increases with an increase in anchor diameter and strength. In addition, the limited testes indicate that the crushed concrete depths did not increase much under displacement-controlled cyclic loading, hence the ultimate shear capacities were close to those achieved by the anchors under monotonic loading. When the cyclic load is controlled by peak loads (Type CL1 cyclic loading), the crushed concrete depths increased after each loading cycle. Correspondingly, the ultimate shear capacities were lower than those achieved by the anchors under monotonic loading.

A parametric study with a total of 101 finite element (FE) analyses was then conducted to investigate the key factors for the crushed concrete depth: the concrete/steel materials, anchor diameters, and stand-off heights (assuming no leveling nuts). The parametric study was based on the models created for the specimens used in the experimental tests. A concrete model considering concrete behavior under passive confinement was selected and the model parameters were calibrated using experimental tests of concrete under both active and passive confinement in the literature. Furthermore, mesh sensitivity studies were conducted to determine optimized mesh sizes, especially in the direction of anchor embedment. Finally, we assumed that concrete is crushed below the concrete surface when the lateral compressive strain of concrete reached a value of 0.1 mm/mm. The parametric study indicated that crushed concrete depths are rather different under various parameter combinations. Within the parameter investigate range, the crushed concrete depth reaches the maximum value when the stand-off height is $0.5d_a$. With a further increase in stand-off height, the failure mode of the anchor turns from shear fracture into bending

failure, and its shear capacity decrease with the increase of effective exposed length, which means that the lateral compressive stress in concrete was decreased under peak load, which eventually lead to the reduction of crushed concrete depth. In addition, when the stand-off height is greater than $0.5d_a$, the crushed concrete depth shows a significant increase with an increase in anchor diameters and steel ultimate strengths. Furthermore, with an increase in concrete strengths, the crushed concrete depth can be significantly reduced.

Equations were proposed for the estimation of total exposed length based on the experimental tests and finite element analysis results. The proposed equations fit well the total exposed lengths determined from the FE analyses; however, the predicted total exposed lengths are higher than the measured values though the number of measured crushed concrete depths is very limited. A reduction factor of 0.6 was applied to the proposed equation for practical uses. With the equivalent exposed lengths, which include the apparent exposed length measured from the bottom of leveling nuts (or base plate if no leveling nut is used) and the crushed concrete depth, design equations were proposed for the shear capacity of stand-off/exposed anchors. The equation is modified from that proposed by Lin et al. (2011), and considers combined shear, bending and tension applied to an anchor shaft from applied shear forces. The equations are verified by 90 tests, including 79 collected from three sources in the literature and 11 tests reported in this study. The proposed equation fits well the available tests.

It is envisioned that the proposed shear capacity equation can improve the safety of stand-off anchor connections. Meanwhile, further study must be conducted for such connections with grout pads and subjected to seismic loading.

Table of Content

List of Figures

List of Tables

Nomenclature

A = total area of element

A_s = area of single anchor corresponding to the nominal diameter

$A_{se,V}$ = effective cross-sectional area of single anchor in shear

E_c = Young's modulus of concrete

G_f^I = tension fracture energy

M_{group} = applied overturning moment is a group

M_u = ultimate bending moment of anchor under combined load of shear and moment

M_u^0 = ultimate bending moment at fixed end of anchor shaft

N_{group} = applied axial force is a group

P_u = factored shear force on the bolt

S = section modulus of the anchor calculated from the net tensile area

S_{group} = section modulus of bolt positioned for maximum global moment-induced tension

T = applied tensile force

T_{group} = applied torsion within a group

$T_{u,test}$ = ultimate applied normal load on a per-bolt basis

T_u = ultimate tension strength of anchor bolt

T_{usa} = tensile load corresponding to the maximum shear load

V = volume of element

V_{sa} = shear strength of anchor bolt

$V_{u,test}$ = ultimate applied shear load (on a per-bolt basis)

V_s = characteristic shear resistance of anchor bolt

W_{el} = elastic section factor of anchor

Z_{bolt} = plastic section modulus of the bolt

b = a factor related by concrete strength

c_{a1} = edge distance

d_a = anchor diameter

d_{ae} = anchor effective diameter

f_c' = concrete strength

f_{cc} = cube compressive strength

f_{ct} = tensile strength of concrete

f_p = peak compressive stress

f_t = factored tensile stress from both axial bolt tension and bolt bending

$f_{t,1}$ = the individual bolt tensile stress from global equilibrium

$f_{t,2}$ = individual bolt tensile stress produced by bolt bending over the exposed length

f_{uta} = ultimate tensile strength of anchor steel

f_{uva} = ultimate shear strength of anchor steel

f_{va} = factored shear stress

f_y = yield strength of anchor steel

h = assumed stressed concrete height

h_{ele} = crack bandwidth of an element (or the equivalent length of the element)

h_{ef} = embedment depth

k = factor of concrete strength caused by confinement

l_b = bending depth

l_{ea} = apparent exposed length

l_{ec} = additional exposed length due to concrete crushing

l_{ee} = effective exposed length

l_p = length of plastic hinge

l_s = stand-off height

m_2 = bolt-level moment

n = number of bolts

r_{group} = radius of bolt group

β = rotation of exposed anchor with respect to the initial undeformed shape

α = compressive stress

α_M = factor of V_{sa} based on boundary condition

α_b = factor of V_{sa} related to steel yield strength

α_{sm} = factor of V_{sa}

α_m = factor of V_{sa} related to steel class

α_p = strain corresponding to peak compressive stress

δ_u = ultimate displacements

$\delta_{u..test}$ = tested ultimate displacements

φ = maximum curvature

θ = initial end rotation allowed by the oversized holes and/or concrete deformation

$\varepsilon^{cr}{}_{nn,ult}$ = ultimate crack strain of concrete

ε^{cr}_{nn} = tensile stress

ψ_s = factor related to the stand-off height to reduce the maximum shear

Chapter 1. Introduction

1.1 Introduction

Steel components and reinforced concrete member are usually connected by anchor bolts. Flush-mounted, ungrouted stand-off or grouted stand-off base plates are used in the case of luminaires, signal structures. The failure of anchor connections is mostly controlled by anchor fracture and concrete breakout failure. Specifically, an anchor bolt in an anchor connection can be subjected to both axial and shear forces, which depend on the anchor location and the applied axial load, bending moment, shear force and torsion from the connected steel element caused by wind loads or seismic loads. Current design codes and guides (AASHTO, 2013; AISC, 2010; and ACI 318, 2019) adopt formulas considering both axial and shear stresses to design the capacity of a bolt, which has been proved to be correct in both steel-to-steel (Chesson *et al*., 1965) and flush-mounted base plate connections to concrete (Cook and Klingner, 1992).

During the past decades, extensive works have been conducted by various researchers to investigate on single bolts (Adihardjo and Soltis, 1979 and Nakashima, 1999)) and multiple-bolt groups (Fichtner, 2011; Gresnigt et al., 2008; Gomez et al., 2011; and McBride, 2014) under shear loading or combined shear-tension loadings, where much attention was paid to the ultimate capacity, ductility, stiffness and failure modes of such connections. The double shear tests by Lin et al. (2011) on threaded rods with a variety of exposed lengths indicate that losing concrete around an anchor can cause significant reduction on ultimate shear strength of anchors. In addition, both experimental (Mcbride, 2014) and numerical (Liu, 2014) studies show that stand-off anchors will be subjected to large bending stresses, which will seriously reduce the bearing capacity and bending moment of components, even when the exposed length is less than one bolt diameter. Furthermore, multiple test results show that the concrete at the front of an anchor bolt can be significantly crushed when the bolt was encountered large deformation or lateral load, especially when the concrete strength is low, and the bolt strength is high (Klingner et al., 1982; Hoehler, 2006; Petersen, 2010; Pallares and Hajjar, 2010; and Cook et al., 2013). This phenomenon will obviously increase the bending length of anchor shafts, leading to an additional local bending stress, which will serious influent the ultimate strength and stiffness of the bolt. In addition, Foley et al. (2004) pointed out that excessive bending stress in bolts may affect their fatigue strength.

1.2 Definition of Problem

For anchors with grouted or ungrouted base plate, the stress variation law in bolt under shear load is different from that of flush-mounted anchors. As shown in Figure 1.1, the stand-off height, l_s, is usually defined as the distance between the concrete surface and the bottom of base plate. The apparent exposed length for the anchor, l_{ea}, is the same as the stand-off height for anchors without a leveling nut below the base plate (Figure 1.1a); otherwise it is defined in this research the distance between the concrete surface and the bottom of the leveling nut (Figure 1.1b). Most design recommendations use l_s or l_{ea}; however, compared with the top end, where the anchor shaft bears against a steel element, the bottom end of the anchor can crush the surrounding concrete, lowering the lateral supporting point further down. Therefore, an additional exposed length, l_{ec}, is necessary. Note that l_{ec} is not measured from the point, where anchor shaft is subjected to the highest normal stress, thus may fracture. This is because down from the surface where concrete completely crushes, deformed concrete can sustain some lateral pressure from the anchor shaft and can in turn provide

lateral support to the anchor shaft. The level of lateral strength in concrete is difficult to quantify because in addition to the lateral pressure from the anchor shaft, concrete is subjected to confinement from the undeformed concrete.

We attempted to determine the crushed concrete depths in this study using finite element (FE) analyses. The FE models were verified against a group of experimental tests, followed by a parametric study of four key parameters: the compressive strength of concrete, the ultimate strength of anchor steel, the diameter of anchors, and the stand-off height/apparent exposed length. The proposed effective exposed length was used in a proposed equation to predict the shear capacity of 90 single anchors subjected to shear.

1.3 Organization of Report

In this study, an effective exposed length (l_{ee}) is defined as the apparent exposed length (l_{ea}) plus the additional exposed length due to concrete crushing (l_{ec}). Note that CEB-*fib* use $0.5d_a$ as the additional exposed length while in this study, l_{ec} was determined using finite element (FE) analyses. The FE model, including element and material definitions (Chapter 3), was verified against the results of eleven laboratory tests (Chapter 4) before a series of analyses (Chapter 5) were conducted. The proposed effective exposed length (l_{ee}) was later used in the existing capacity models in the literature and the results were compared with experimental data, based on which a design recommendation is presented in Chapter 6. The report is summarized in Chapter 7, which also includes a list of suggested future research topics.

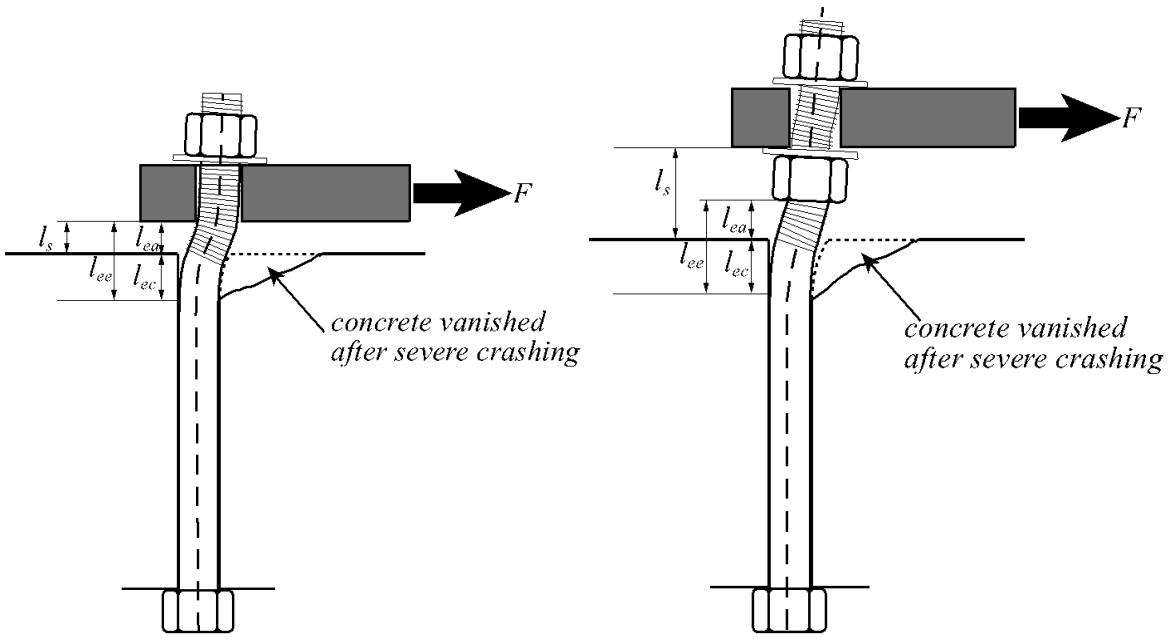

Figure 1.1: Schematics of anchors with exposed lengths, defined as (a) the stand-off height or (b) the stand-off height minus the leveling nut plus the crushed concrete depth

Chapter 2. Literature Review

2.1 Research by Nakashima (1998)

Nakashima (1998) studied the behavior of column base-connections with concrete anchors under combined tension and shear loading. Four groups of shear tests were conducted with exposed length of 0, 10, 20 and 40 mm [0, 0.4, 0.8, and 1.6 in.]. One or two M12 anchors (d_a=12 mm [0.472 in.]) were installed in a short reinforced concrete column as shown in Figure 2.1. The anchor steel had a measured yield strength of 341 MPa [49.5 ksi] and ultimate strength 482.5 MPa [70 ksi]. In addition, the concrete compressive strength was 31.4 MPa [4550 psi], and the tensile strength was 2.8 MPa [412 psi].

The stand-off height below the 20-mm [0.8-in.] thick loading plate varied from 0 to 3.3d_a. The location of the shear failure plane relative to the threads is not clear from the report; hence, it is assumed that the threads were included in the shear planes in the database. The report did not indicate the specimen type; hence, the geometric parameters of these anchors, such as the edge distances in the database were taken from specimen type B in Figure 2.1. In addition, the author did not report the depth of crushed concrete in front of the anchor shaft; however, as shown in Figure 2.2, the displacement at failure increases with an increase in the exposed length, indicating that the anchors were more vulnerable to bending or tensile failure than to shear failure.

2.2 Research by Gomez *et al.* (2009)

Gomez *et al*. (2009) carried out experimental tests of two groups of anchor bolts in exposed column base plates under combined loading of axial tension and cyclic lateral displacements. Figure 2.3 shows a schematic of the rebar details of the concrete pedestals used for the column base connection tests. As indicated in the figure, the concrete pedestals include specifically designed rebar details to ensure failure of the anchor rod itself, rather than failure within the concrete. Both test specimens consist of four anchor rods with a space of approximately 609.6 mm [24 in.] square. A stiff grout mix with the thickness of 31.8 mm [1.25 in.] and 25.4 mm [1 in.] was placed on concrete for the 19 mm [0.75 in.] anchor rod specimen and 31.8 mm [1.25 in.] anchor rod specimen, respectively. The holes in the 50.8 mm [2 in.] thick base plate was 52.4 mm [2.1 in.] in diameter, the recommended size for 31.8 mm [1.25 in.] diameter anchor rods stated in the AISC *Steel Design Guide 1* (Fisher and Kloiber, 2006). Note that since the same base plate was reused for both rod sizes, the rod hole size was larger than the recommended hole diameter of 33.3 mm [1.31 in.] for the 19-mm [0.75-in.] diameter anchor rods. As recommended by the AISC *Steel Design Guide 1*, plate washers, provided for the anchor rods, were fillet welded to the base plate to reduce the amount of slip before the shear loading was transferred to all rods. Machined square plate washers, measuring 63.5×63.5×35.6 mm [2.5×2.5×1.4 in.] with an internal diameter of 20.3 mm [0.8 in.] (≈ rod diameter plus 1.6 mm [1/16 in.]), were used for the 19 mm [0.75in.] anchor rods and plate washers, measuring 88.9×88.9×12.7 mm [3.5×3.5×0.5 in.], with holes approximately 33 mm [1.3 in.] in diameter (≈ rod diameter plus 3.2 mm [1/8 in.]), were fabricated from thermally cut plate stock for the 31.8 mm [1.25 in.] diameter rods. The sizes and hole diameters of these plate washers reflect recommendations from the AISC *Steel Design Guide 1*. Additional washers were placed (un-welded) over the rods on top of the plate washers to prevent dishing of the welded plate washers due to the large tension forces in the rods. Nuts were hand tightened snug with an additional 1/8 turn.

The measured mean ultimate strength B is 428.8 kN [96.4 ksi] for the 19-mm [0.75-in.] diameter rod and 333.6 kN [75.0 ksi] for the 31.8 mm [1.25 in.] diameter rod. The average yield strength B (as determined by the 0.2% offset method) is 297.1 kN [66.8 ksi] for the 19-mm [0.75-in.] diameter rod and 242 kN [54.4 ksi] for the 31.8 mm [1.25 in.] diameter rod.

Pedestals representing the concrete foundation for the base plate tests, measuring 1219×2134 mm [4×7 ft] in plan area and 826 mm [32.5 in.] in height, were cast using commercial ready-mixed concrete with a 32.8 MPa [4760 psi] 28-day compressive strength which was calculated by 12 concrete compressive cylinder specimens. However, prior to testing, all concrete pedestal specimens were air cured well beyond 28 days (i.e. between 3-5 months), which may cause the concrete compressive strength in pedestals higher than that of measured.

General construction, mineral-aggregate non-shrink grout was installed between the steel base plate and concrete pedestal for both tests. The average compressive strength of the grout ranged between 40 and 50 MPa [5780 and 7210 psi].

Figure 2.4a schematically illustrates the test setup and a photograph is provided in Figure 2.4b. Referring to Figure 2.4a, a large steel beam-column loading frame provided a rigid load path for both compressive and tensile axial loading. The loading frame was braced laterally onto a concrete reaction wall. Horizontal loads were applied via two steel assemblies bolted directly onto the base plate (see Figure 2.5), thus applying direct shear loading with negligible moment at the base connection.

The axial tensile load of two specimens was approximately 31% and 39% of the sum of the ultimate load of the four rods respectively. After this applied, an instantly broke of the bond between the steel base plate and the grouted pad were observed. Then the gap between the base plate and grouted pad increased as continuing lateral deformations were applied.

As shown in Figure 2.6, the anchor rod with a diameter of 19 mm [0.75 in.] fractured within the grout pad and at about 6.4 mm [0.25 in.] from the top of the concrete surface, while the anchor rod with a diameter of 31.8 mm [1.25 in.] fractured within the concrete pedestal and about 25.4 mm [1 in.] below the surface of the undamaged concrete. Furthermore, as shown in Figure 2.7, at two anchor rods locations, the grout cracked and completely separated from the concrete pedestal. For the later test, exhibited significant residual deformations up to about 25 mm [1.0 in.] below the surface of the damaged concrete was observed. Cracking of the grout pad was observed during the 5.1 mm [0.2 in.] amplitude displacement cycle for both anchor rod tests. This observation is important because the tests by Cook *et al*. (2013) using non-seismic loading indicated that grout pads do not usually crack. Cracked grout pads have also been observed in the study by Fichtner (2011) and Gresnigt et al. (2008). In addition, the different anchor fracture locations shown in Figure 2.6 indicates that the depth of crushed concrete, which is related to l_{ec} as defined in Section 1.2, can be affected by anchor diameters.

2.3 Research by Petersen (2010)

Petersen (2010) studied the behavior of reinforced anchors under monotonic and cyclic shear. The loading plate was flush mounted to the concrete block, and a small gap (up to 1.5 mm [1/16 in.]) was kept between the loading plate and the concrete during the shear tests. Concrete cover spalling was observed in some specimens, which led partial anchor shaft unsupported. Therefore, a total of nine such tests are included in the database, as discussed by Lin *et al*. (2011). The tests were

conducted for anchors made from 19.0 mm [0.75 in.] diameter ASTM F1554 threaded rods with a measured ultimate tensile stress of 524.7 MPa [76 ksi] and 25.4 mm [1.0 in.] diameter ASTM Grade B7 threaded rods with a measured ultimate tensile stress of 896.3 MPa [130 ksi]. The dimensions of the test blocks are shown in Figure 2.8 portrayed in terms of embedment depth (h_{ef}) and edge distance (c_{a1}). The concrete compressive strength was 24.3 MPa [3520 psi] for the specimens with 19 mm [0.75 in.] diameter anchors and was 26.2 MPa [3800 psi]. for the specimens with 25.4 mm [1.0 in.] diameter anchors, which were obtained from 100 × 200 mm [4 × 8 in.] cylinder samples with similar curing conditions as the corresponding specimens. Concrete cover of 38.1 mm [1.5 in.] was used for all the specimens. Anchor reinforcements were laid out as shown in Figure 2.9, designed to ideally resist tension, shear, and combined tension-shear loading. Nine tests specimens can be divided into four categories. Specifically, (1) tests with 19 mm [0.75 in.] diameter anchors have an embedment of 152.4 mm [6 in.] and a front edge distance of 101.6 mm [4 in.], and two No. 4 stirrups (d_a = 12.7 mm [0.5 in.]) with yield strength of 413.7 MPa [60 ksi] touch the sides of the anchor rod; (2) Four No. 4 stirrups were used to reinforce 25.4 mm [1 in.] diameter ASTM Grade B7 threaded anchor rods in the same way as above, which has 152.4 mm [6 in.] embedment depth and 152.4 mm [6 in.] front edge distance; (3) The 25.4 mm [1 in.] diameter ASTM Grade B7 threaded anchor rods were also used here and has similar dimensions detail as the second one except the side edge distances. As shown in the Figure 2.3, both sides edge distances of the anchor are 152.4 mm [9 in.]. Two No. 4 bars and four No. 3 bars were selected here for reinforcing the anchor, and No. 4 bars were located closed to the anchor; (4) An additional test block with 25.4 mm [1 in.] diameter anchor has the same dimensions and anchor location as the second one. Five No. 3 reinforcing bars were used on each side of the anchor with 50.8 mm [2 in.] center-on-center spacing extending to 222.25 mm [8.75 in.] from the center of the anchor.

Test blocks were cast with anchors protruding from the bottom of the formwork. This inverted orientation produced a perfect surface finish on the top of the test blocks where the loading plate was placed. The smooth surface around the anchor bolts helped the loading plate rest evenly on the test block.

Both the specimens and the actuator were attached to the laboratory strong floor instead of using a self-balanced loading frame. A constant small tension force of 0.89 kN [200 pounds] was applied by vertical actuator to eliminate any friction between the load plate and the test block during shear tests, then monotonic shear loading was applied by horizontal actuator pistons. the nut was hand tightened onto the load plate firstly then loosened 1/8 of a turn (it is about 0.32 mm [0.0126 in.] between load plate and concrete surface) to allow slight vertical movement of the loading plate when the tension force was applied at the beginning of the test.

None of the above-mentioned specimens was designed purposefully with an exposure length or stand-off distance; however, as shown in Figures 2.10 and 2.11, after the front concrete spalling above the anchor reinforcement, the anchors in shear had a slight capacity loss and continued to deform and the measured load increased gradually till fracture of the anchor shafts. Specifically, for the 19 mm [0.75 in.] diameter reinforced anchor tests, the concrete cover around the reinforcement spalled at lateral load of roughly 44.5 kN [10 kips]. After that, the cover concrete was not able to resist load and the location of the shear restraining reaction on the anchor shaft was moved to a point just below the center of the anchor reinforcement causing a slight decrease in capacity and an exposed length to form between the applied load and the point of restraint provided by the reinforcement. The resistance of anchor was retained until the displacement up to 17.8 mm [0.7 in.], after that, the resistance was increasing until failure at displacement of around 33.0 mm

[1.3 in.]. The front concrete spalling above the reinforcing bar was also been found in the tests with 25.4 mm [1 in.] diameter anchors when the load increased to approximate 98 kN [22 kips]. However, after that, unlike the load versus displacement behavior of the 19 mm [0.75 in.] diameter anchor plot, the 25.4 mm [1.0 inch] diameter reinforced anchor tests did not show any decrease or plateau. Instead the load versus displacement plot made a smooth transition from the anchor bearing against the surface concrete to being restrained at the level of the reinforcement after concrete spalling takes place. Altogether, as shown in Figure 2.11, an exposed length which equal to the concrete cover 38.1 mm [1.5in.] plus 0.5 times the diameter of the shear reinforcement below the surface of concrete was occurring to this type of specimens after concrete spalling. In addition, as shown in Figure 2.11, a small area in front of the anchor measuring half the anchor diameter in depth experienced local concrete crushing as is typical for anchors loaded in shear. Therefore, those specimens with an assumed exposed length which was equal to concrete cover plus half of anchor reinforcement diameter are compared with other dataset in the following discuss.

2.4 Research by Grosser (2012)

Shear tests of single bolt were carried out by Grosser (2012). As shown in Figure 2.12, a large bending displacement of the section of the anchor rod on the surface of the concrete pedestal caused by the destruction of the concrete at the front end of the anchor rod was observed. Further, anchors located far away from concrete edges fail in steel provided the embedment depth is sufficiently large to avoid concrete breakout failure. The result of test of the influence of the embedment depth for various compressive strength of the concrete on capacity by Grosser (2012) indicates that anchors failed in steel with prior concrete spalling in front of the anchor. Specifically, as shown in Figure 2.13, in the concrete slab with a compressive strength of 22.7 MPa [3290 psi], the concrete spalling is more pronounced for the shorter embedment depth whereas no difference for tests with shorter embedment depth can be observed in the concrete slab with 34.6 MPa [5020 psi] strength. However, concrete spalling is more pronounced for larger anchor diameter. In Figure 2.13, the measured ultimate loads are plotted as a function of the embedment depth for the various concrete compressive strengths. For the tests performed in the concrete slab with 22.7 MPa [3290 psi], the capacity decreases with decreasing embedment depth, even though all anchors failed in steel. This agrees with the failure pattern discussed in Figure 2.14. For the tests performed in concrete with 34.6 MPa [5020 psi], no reduction with decreasing embedment depth for the anchors failed in steel can be observed. The average ultimate loads are related to the averaged ultimate loads for anchors with embedment depth h_{ef} = 130 mm [5.1 in.]. A 20% load reduction was observed for short embedment depth. Therefore, in concrete with lower compressive strength, a reduction of steel capacity seems to be necessary to take into account that the concrete spalling is more pronounced. This leads to a reduction of the capacity since the anchor experiences additional bending stresses. Considering that the shear capacity of anchors reduces with an increased in the exposed length (Lin *et al*. 2011), this observation indicates that depth of crushed concrete, which is related to l_{ec} as defined in Section 1.2, can be affected by concrete strength.

2.5 Research by Cook *et al*. (2013)

Cook *et al*. (2013) conducted extensive experiments to investigate the steel shear strength of anchors with a stand-off height. The tests were designed to simulate those usually at the base of highway signage structures. The tests of anchors under direct shear in Phase 1 focused on the

impact of anchor diameters (d_a) and stand-off heights (l_s). Annular stand-off base plate connections, both grouted and un-grouted, were tested in Phase 2 to investigate the impact of anchor diameters and grouts. The tests in Phase 3 contained four full-scale circular groups of six 1.25 in. diameter bolts loaded predominantly in torsion.

In all tests, the anchors were made with ASTM F1554 Grade 55 threaded rods with an ASTM A563 heavy hex nuts. The embedment depths used were 8.6, 7.0, and 16d_a for 15.9 mm [5/8 in.], 25.4 mm [1.0 in.], and 31.8 mm [1.25 in.] diameter anchors, respectively. The embedment depth was assumed to have no impact on the results of direct shear tests of single anchors and torsion tests of anchor connections. All concrete used in the study was the FDOT Class IV Drilled Shaft mix with a specified 28-day compressive strength of 27.6 MPa [4000 psi]. Reinforcement within the blocks was provided only to prohibit failure modes other than anchor bolt steel fracture. The grout chosen was non-shrink with specified 28-day strength of 62.0 MPa [9000 psi].

2.5.1 Phase 1 study

A total of 14 unique direct shear test series were included in Phase 1 study with a variety of bolt diameter, stand-off distance, number and type of anchor bolts. Two of test series abnegated by authors for they were not run to completion are discarded by authors, they are still summarized here. Therefore, the main design parameters of 14 test series are tabulated in Table 2.2. All the top nuts of anchors were used finger-tightened technique. A layer of Teflon was below the flush-mounted base plate to reduce the friction, and no pretensioned technique were used here for reducing an additional contribution to strength from friction. The specimens with stand-off distance were using ungrouted base plate.

The tests anchors were installed in a 1181×1181×305 mm [46.5×46.5×12 in.] concrete block as shown in Figure 2.15. The blocks were designed such that the test anchors had a sufficient edge distance and embedment depth to prohibit concrete breakout per ACI 318-11 without reinforcement. Meanwhile, No. 3 reinforcing bars were place at mid-height to prevent cracking from self-weight of the blocks. The shear force was applied to the anchors through a 25.4 mm [1 in.] thick loading plate, which was connected to a hydraulic jack through a 22 mm [7/8 in.] diameter ASTM A193 B7 threaded rod supplied load. The dimensions of rectangular base plate are 102×368×30 mm [4×14.5×1.18 in.]. In flush-mounted tests and double-bolt stand-off base plate tests the loading rod was threaded directly into the base plate. Single-bolt stand-off base plate tests, however, included a roller to restrain base plate rotation as shown in Figure 2.16. The hydraulic jack was positioned on the back side of a steel frame made of two steel C channel sections with a 50.8 mm [2.0 in.] gap. The steel frame was fixed to the strong wall and strong floor of the laboratory. A square steel tube was used between the concrete block and the frame to provide direct reaction to the applied shear. Meanwhile the concrete block was clamped down on the far size to restrain against overturning moments during the shear tests. Note that the square tube that provided reaction force may have provided additional confinement to the concrete in front of the anchor shaft, which in turn may have impacted the test results, critical to this study. A nut was placed before tests and tightened to a “snug tight” condition at a torque of approximately 114.2 mm-N [20 in.-lb].

Blocks were cast with anchor bolts installed upside-down in the formwork to accommodate the high number of bolt specimens and to achieve a formed flat concrete top surface, similar to that in Pertesen (2010). Holes were drilled through both the bottom sheet of plywood and a second reference piece of plywood as shown in Figure 2.17 to set the position and plumbness of anchor

bolts. Embedment depth of the anchors was set by placing a nut above and a nut below the reference sheet of plywood. Four coil loops were embedded at mid-depth of the slab to tie into for handling. A perimeter of No. 3 rebar was placed at mid-depth for handling precautions. ASTM A563 heavy hex nuts were placed on the embedded ends of the anchors and locked against rotation during concrete placement with a bead of adhesive. Two additional blank blocks were cast without anchors to allow for adhesive anchor installation. Blocks were wet-cured for seven days after pouring using a drip hose covered by painter's tarp and 4-mil plastic sheeting. After 28 days, formwork was removed. Two sets of cylinders were made, one cured alongside the test blocks in the lab and the other cured in a lime bath.

Figure 2.18 indicates the locations of instrumentation used for direct shear testing. Load was measured by a through-hole 444.8 kN [100 kips] moment-compensating load cell located at the back end of the loading actuator with steel plates on either end of the load cell. Displacement was measured at the back end of the rectangular base plate with a linear potentiometer. The potentiometer, which contained a spring-retracting plunger, was connected to the back of the base plate through a stiff steel cord that fastened magnetically to the center of the top surface. A 133.4 kN [30 kips] tension load cell was placed at the top of the anchor bolts in most tests.

Displacement-controlled loading procedure was used for all the test specimens. Table 2.3 provides a summary of Phase 1 results. Datasets DS7 and DS8 contained two bolts per test. Thus, the value reported $V_{u,test}$ represents the ultimate shear load divided by two. The 28-day concrete compressive strength for Phase 1 was 34.4 MPa [4990 psi]. All 15.9 mm [5/8 in.] and 25.4 mm [1.0 in.] bolts were from the same batch. Ultimate tension strength, T_u, of anchor bolt threaded rod specimens, were determined according to ASTM F606 methodology (ASTM, 2011). Ultimate displacements, δ_u, correspond to the value of $V_{u,test}$ for each test. A limited number of bending depths, l_b, defined as the distance from the concrete surface to the deepest point below the surface of the concrete where the anchor experienced any bending deformations, were taken from cored anchor bolt specimens from datasets DS1 through DS8.

The influence of tension load cell, as illustrated in Figure 2.18, on the shear load curve of bolts has been proved negligible, whether in flush-mounted or $2d_a$ stand-off single bolt or double bolt experiments. Most 15.9 mm [5/8 in.] bolt tests contained tension load cells, thus, the tensile load, T_{usa}, corresponding to the maximum shear load is recorded in the database, and the average tensile load has been recorded in Table 2.4.

Figure 2.19 displays typical load-displacement behavior for representative tests within the Phase I test program. Flush-mounted tests performed nearly identically between 15.9 mm [5/8 in.] cast-in-place (CIP), adhesive (AD) single-bolt, 15.9 mm [5/8 in.] double-bolt, and 25.4 mm [1.0 in.] bolt tests. At $2d_a$ and $4d_a$ base plate stand-off, however, differences emerged. For 15.9 mm [5/8 in.] bolt specimens, double-bolt stand-off tests (DS8) demonstrated earlier stiffness degradation than single-bolt tests. In double-bolt stand-off tests, the base plate was free to displace vertically over its entire length. The roller in single-bolt tests, however, restrained base plate vertical movement and rotation, preventing anchor bolt "flagpole" action. As the stand-off bolt deformed horizontally the restraint of downward base plate movement caused a tension force to develop in the single anchor resulting in increased stiffness and strength. Representative curves for the 1 in. diameter stand-off tests are shown below in gray. In the 25-mm [1-in.] diameter tests the roller prevented downward movement at its location but permitted plate rotation at the location of the anchor. As a result, the anchor bolt experienced "flagpole" rotation while still adding tension force to the anchor to balance the compressive reaction from vertical restraint at the roller. Because the roller

restrained downward movement of the base plate at one location yet allowed the anchor to experience "flagpole" action, the anchor essentially turned into a truss tension element with the roller acting as the truss compression strut. Thus, large tension forces developed in the anchors resulting in significantly increased capacity.

2.5.2 Phase 2 study

The torsion test matrix is provided below in Table 2.5. Six test groups with 15.9 mm [5/8 in.] diameter anchor bolts included flush-mounted base plates, ungrouted base plates, grouted base plates, a single test with an FRP-retrofitted grout pad, and three test groups containing 25.4 mm [1.0 in.] diameter anchor bolts. The anchor with FRP is not contained in the following database, because it didn't really reflect the shear behavior of anchor with grouted base plate.

As illustrated in Figure 2.20, anchor bolt groups were installed in 1181 mm×1181 mm×305 mm [46.5×46.5×12 in.] deep reinforced concrete blocks. Two independent, opposite actuators provided torque to the system by connecting the so called "loading wings" on the top of base plate. Self-reacting system was used here by using tension ties running through the bottom portion of the block were designed to transfer loads from the rolling frames to a compression reaction on the other side of block. The 50.8 mm [2 in.] diameter PVC pipes for tension reaction ties were installed 76.2 mm [3 in.] from the bottom face of the block to the center of the PVC. Flush-mounted tests, which included a Teflon layer below the base plate as in Phase 1, were not pretensioned to reduce additional contributions to strength from friction.

Base plate assembly dimensions and details are provided in Figure 2.21. The 305×190×12.7 mm [12×7.5×0.5 in.] HSS pipe section was made of 379 MPa [55 ksi] Carbon Steel DOM Mechanical Tube. The circular base plate and steel for the loading wing were made of Grade 36 steel. All connections between assembly components were made with 9.5 mm [3/8 in.] fillet welds. For 2-bolt diameter spacing to the 127 mm [5 in.] bolt line radius, 95 mm [3.75 in.] and 159 mm [6.25 in.] radii to the outside of the pipe stub and the base plate, respectively, were chosen. To maintain the 1:1 base plate thickness to nominal anchor bolt diameter ratio for all tests, 9.5 mm [3/8 in.] thick plates were welded above holes for the 25.4 mm [1 in.] diameter bolts. According the ACI 318-11, top and bottom reinforcement were designed to restrain the breakout forces by the anchor bolts and the handing forces, respectively. No. 4 rebar was used for all reinforcement bent into U shapes with 1118 mm [44 in.] length and 203 mm [8 in.] legs. The bottom faces of all blocks contained five equally spaced bars in both horizontal directions to satisfy minimum temperature and shrinkage reinforcement. Blocks containing 15.9 mm [5/8 in.] diameter anchor specimens contained four bars in both horizontal directions on the top face, while those with 25.4 mm [1.0 in.] diameter anchors contained ten in each direction to restrain concrete breakout forces. All reinforcement contained a minimum cover of 38 mm [1.5 in.]

The cast-in-place anchor bolt installation technique from Phase 1 was again employed, with blocks cast upside-down and anchors passing underneath the formwork. Specimens with groups of six 15.9 mm [5/8 in.] diameter bolts were installed four to a block while specimens with three 25.4 mm [1 in.] diameter bolts were cast one per block. 15.9 mm [5/8 in.] anchors were embedded 152.4 mm [6 in.] to the bottom of the bolt head (h_{ef} = 136.5 mm [5.375 in.]), while 25.4 mm [1 in.] anchors were embedded 8 in (h_{ef} = 177.8 mm [7 in.]).

Figure 2.22a and Figure 2.23a display a view of a fully instrumented 15.9 mm [5/8 in.] diameter bolt test specimen. A plan view schematic of base plate instrumentation is provided in Figure 2.22b and Figure 2.23b.

Phase 2 results are summarized in Table 2.6. One test, T6-A, was not run to ultimate load. Values provided for T6, then, reflect only results from test T6-B. The 28-day concrete strength for Phase 2 blocks was 43.9 MPa [6360 psi]. Grout strengths were 37.0 MPa [5360 psi], 51.6 MPa [7480 psi], and 43.0 MPa [6230 psi] for T5, T6-B, and T7, respectively. All 15.9 mm [5/8 in.] bolts were from the same unique batch to Phase 2. 25.4 mm [1 in.] bolts were from the same batch as in Phase 1. Expressions of $V_{u,test}$ for Phase 2 reflect the average of the two load cell readings adjusted for loading rod geometry and distributed equally among the bolts in a given test. As in Phase 1 δ_u values correspond to $V_{u,test}$ for each test. Displacement values were calculated by adjusting the linear LVDT readings to the equivalent distance traveled along the bolt circle using geometry and adjusting the radius from the center of the base plate to the LVDT locations to the radius of the bolt circle.

Figure 2.24 displays load-displacement behavior of representative ungrouted Phase 2 tests. Flush-mounted tests demonstrated initial slip through the hole oversize followed by linear-elastic behavior. T1-B stiffness degraded at a lower displacement and failed at lower ultimate load ($0.51T_u$) than T1-A ($0.6T_u$) presumably from less favorable bolt position within the holes. Ungrouted stand-off base plate tests demonstrated linear-elastic behavior to approximately $0.15T_u$ and $0.8T_u$ or $2d_a$ and $4d_a$ tests, respectively, followed by a ductile inelastic Phase as the bolts deformed laterally over their exposed lengths. Strength and behavior between 15.9 mm [5/8 in.] and 1 in. bolts were nearly identical. Ultimate displacements of the $2d_a$ and $4d_a$ tests were on the order of one bolt diameter for both with the exception of the 25.4 mm [1 in.] diameter $4d_a$ torsion test (T10), which showed greater deformation with respect to d_a.

As shown in Figure 2.25, the concrete at the front end of the bolts with stand-off distance of $0.8d_a$ can be observed to be damaged, for both the bolts in pretensioned and non-pretensioned. Besides, it can be seen in Figure 2.25 that the bearing capacity of anchors with stand-off distance of $2d_a$ was lower than that with flush mount base plate.

Load-displacement behavior of grouted stand-off base plate tests is provided in Figure 2.26. Initial behavior of the grouted $4d_a$ stand-off torsion test with an FRP retrofit, T7, was similar to other grouted tests. With load less than approximately $0.3T_u$ there was rotation of the base plate relative to the FRP wrap. After initial grout cracking at approximately $0.3T_u$ radial grout material displacement was restrained by the FRP perimeter. Subsequent test rotation was shared equally between the base plate assembly and the retrofitted grout pad until an explosive failure, with all of the anchor bolts completely sheared away at the top surface of the grout pad at slightly greater than $0.7T_u$ The higher result than flush-mounted shear strength was attributed to the combination of the restraint of the grout pad from crack propagation, the leveling nuts immediately below the grout pad surface producing greater bearing area (no local spalls in front of anchor bolts were observed), and friction between the grout pad and the base plate. While only one FRP-retrofitted test was performed, this result shows promise for bringing anchor bolts in existing ungrouted and grouted stand-off base plates to flush-mounted strength or higher at low levels of ultimate displacement.

2.5.3 Phase 3 study

In total, four tests were conducted on groups of six 31.8 mm [1.25 in.] diameter anchor bolts under predominantly torsion loading as shown in Table 2.7. Tests FS1-FS3 contained a circular base plate while FS4 contained an annular base plate.

The loading assembly contained twelve 44.5 mm [1.75 in.] diameter holes at a 254 mm [10 in.] bolt circle radius with a base plate thickness of 25.4 mm [1 in.]. Each test specimen was composed of a 914×3048×76 mm [6×10×3 ft.] deep reinforced concrete block containing a single anchor bolt group in the center as shown in Figure 2.27. Blocks were tied to the strong floor using steel beams and 38 mm [1.5 in.] diameter threaded rods. Load was applied by a hydraulic actuator placed at a 2.743 m [9 ft.] torsion arm through a steel pin connection.

Details for reinforced concrete blocks are given in Figure 2.28. Anchor bolts were positioned such that the pipe loading assembly, which was offset 15 degrees from the nearest bolt circle radius through one of the base plate holes. An 8 by 15 grid of No. 4 top reinforcement in the concrete blocks was designed to accommodate anchor bolt breakout forces as described for Phase 2 block specimens. Bottom reinforcement duplicated the top reinforcement grid and was adequate for creep, shrinkage, and handling. A minimum cover of 76.2 mm [3 in.] was used for reinforcement. Additional No. 8 bars were placed at the top and bottom of the blocks to restrain block moment forces from the applied load and reactions.

Figure 2.29 displays a view of a fully instrumented test specimen and a plan view schematic of base plate instrumentation within the test setup.

Tests were displacement-controlled by through an electric hydraulic pump manned by an operator. Displacement rate was increased slightly through the much larger inelastic Phase of test behavior. At the loading arm, displacements nearing 762 mm [30 in.] were observed as the anchor bolts deformed, requiring in-test adjustment of the loading actuator. During adjustment periods, the loading arm was supported by an overhead crane while the actuator was retracted and reset. A shorter actuator was used at the beginning of the test and replaced by a taller actuator after one or two stroke cycles. Other than stopping for actuator adjustment, the consistent quasi-static displacement was continued until anchor bolt rupture.

Phase 3 results are summarized in Table 2.8. 28-day concrete strengths for the four blocks were 45.4 MPa [6590 psi], 49.4 MPa [7160 psi], 49.2 MPa [7140 psi], and 58.3 MPa [8460 psi] and grout strengths for FS2 through FS4 were 62.7 MPa [9100 psi], 62.1 MPa [9010 psi], and 56.3 MPa [8170 psi], respectively. All of the 31.8 mm [1.25 in.] bolts were from the same batch. Expressions of $V_{u,test}$, as in Phase 2, reflect geometrically adjusted values, in this case adjusted for the angle of loading with respect to the tangent of the pivoting loading arm. Contributions to bolt stresses by overturning moment from the short pipe section were negligible and are not reflected in the results. Again, ultimate displacements, δ_u, correspond to the value of $V_{u,test}$ for each test. Displacement values were calculated by adjusting the average of the two string potentiometer readings from their base plate radius location to the bolt circle radius.

Load-displacement behavior of all Phase 3 tests is provided in Figure 2.30. The ungrouted test, FS1, demonstrated similar behavior to ungrouted Phase 2 results. The magnitude of ultimate load for this $2.3d_a$ stand-off ($1d_a$ exposed length) test, $0.32T_u$, fell between the values for the $2d_a$ and $4d_a$ stand-off Phase 2 tests. Test FS4, which contained the modified base plate with the circle cut

out of the center, demonstrated behavior similar to Phase 2 and Phase 3 grouted tests with a circular base plate and a strength greater than its circular base plate counterpart FS3.

Figure 2.31 shows the displaced anchor bolts in ungrouted test FS1. It could be found that the front-end concrete of bolts was obviously crushed.

Figure 2.32 displays in-test grout pad cracking and post-test top views of the grout pads for tests FS2, FS3, and FS4. With the connection oriented 90 degrees to its in-service condition (i.e., anchor bolts parallel to the floor), fragments of grout material outside of the bolt circle fell away during post-test removal of the loading assembly. Remaining grout outside of the bolt circle was manually removed, explaining its absence in the top views.

2.6 Research by McBbride (2014)

Based on the research by Cook *et al.* (2013), McBride expanded the experimental data of Phase 2 study, as shown in Table 2.9. The results are summarized in Table 2.10. Note that some results have been included in Table 2.3, but it is difficult to distinguish which ones are repeated connected due to the test specimens are renumbered, all the test specimens are relisted here. Additionally, A new phase containing 32 eccentric shear tests were conducted. Test setup, test methods and test results are presented as follows.

The strength of anchor bolts experiencing combinations of axial and shear loading was investigated using an eccentric shear loading setup, where a horizontal load was applied at various eccentricities above bolt groups to produce various magnitudes of tension/compression to shear on bolts. Figure 2.33 shows the eccentric shear test setup.

Table 2.11 details the 32 tests that were conducted on 19 mm [0.625 in.] diameter anchor bolts under combined axial and shear loading. Bolt groups were arranged in three configurations: two-bolt groups under combined tension and shear, two-bolt groups under combined compression and shear, and four-bolt groups, all with and without grout pads installed in the void between the base plate and concrete.

A schematic of the eccentric shear loading setup is given in Figure 2.34. Loading was applied to the steel base plate loading assembly through a hydraulic hand pump to a 534 kN [120-kip] telescoping actuator, which was restrained by a double c-channel steel frame tied into the laboratory strong wall/floor. The base plate assembly transferred load to anchor bolts installed in a 1181×1181×305 mm [46.5×46.5×12 in.] deep concrete block, which was restrained by a steel beam assembly, also tied to the laboratory strong floor.

The base plate assembly consisted of a 51 mm [2 in.] thick by 406 mm [16 in.] long by 254 mm [10 in.] wide ASTM A572 Gr. 50 base plate, a 610 mm [24 in.] W8x28 A36 steel section, and a 25 mm [1 in.] by 76 mm [3 in.] by 610 mm [24 in.] steel loading “tab,” also made with A572 Gr. 50 steel. As with the torsion tests on 16 mm [5/8 in.] bolts, holes were oversized with a diameter of 0.81 in. To allow for the placement of tension load cells without inducing additional stretch length during the pretensioning process, anchor bolt holes were countersunk with 76 mm [3 in.] diameter holes to a thickness of 25 mm [1 in.] Load was applied laterally to the loading tab at approximate 152 mm [6 in.], 305 mm [12 in.], 457 mm [18 in.], and 610 mm [24 in.] eccentricities to the top of the concrete surface. Clusters of three overlapping 1 in. diameter holes were drilled at a center-to-center spacing of 16 mm [5/8 in.] into the loading tab to allow for anchor bolt

exposed lengths of one, two, and thee bolt diameters while maintaining a constant distance to the concrete surface for each loading eccentricity. Figure 2.35 and Figure 2.36 show profile and plan views of the base plate assembly, respectively.

Figures 2.37a and 2.38a display views of representative fully instrumented test specimens in two-bolt combined tension and shear tests and combined compression and shear tests, respectively. Plan view schematics of the placement of instrumentation are also provided. The placement of rollers for moment reaction restraint is also shown in Figure 2.37 and Figure 2.38; tension/shear tests contained a roller initially placed below the base plate 305 mm [12 in.] horizontally from the centerline of the two test specimens, while compression/shear tests contained a roller initially placed above the base plate 305 mm [12 in.] horizontally from the centerline of the two test specimens. In all tests, the following instrumentation was present: a load cell threaded into the loading actuator, a 76 mm [3 in.] diameter through-hole load cells installed on test specimens, two horizontally oriented LVDTs installed at base plate mid-height (H1 and H2), and two vertically oriented LVDTs (V1 and V2).

Four tests, two grouted and two ungrouted, were conducted with four-bolt arrangements, all containing anchor bolt exposed lengths of three diameters. One of each of the grouted and ungrouted specimens was subjected to a lower eccentricity and one of each to a higher eccentricity. Two of the four bolts in each test resisted the tension component and two resisted the compression component of overturning moment, requiring no additional reaction restraint to maintain equilibrium. As such, no roller was implemented in four-bolt tests.

In one grouted compression and shear test, double layers of Teflon were installed above and below the grout pad to demonstrate the effect of friction in resisting shear force in a grouted assembly. This test can be directly compared with ES29, which was identical less the presence of the Teflon sheets. The two double layers of Teflon are shown in Figure 2.39.

To prepare every eccentric shear test, the concrete block was set into place onto two steel beams using an overhead crane with adjustments made as necessary such that the top surface of the block was level with steel shims below the block. Horizontal block position adjustments were made until the centroid of the bolt group was in line with the loading rod. In two-bolt tension and shear and four-bolt tests the rectangular tube section restraining rotation of the block was set directly against the concrete surface, while in two-bolt compression and shear tests the tube section was placed directly above the back end of the base plate. The stand-off height of the test was established on both the front and the rear of the base plate. The loading rod and actuator were set collinearly with attachment point on the base plate to produce the desired loading eccentricity. All remaining instrumentation and test components (e.g. rollers, clevis hinge) were installed. Pretensioning as indicated in Table 2.11 for each test was then conducted, securing the position of the loading apparatus. Load was applied to the single telescoping actuator through a hand pump until failure with most tests being lasting between five and ten minutes. As with other test setups, loading was paused for observational and instrument resetting purposes.

The location of the free-body cut used to determine anchor bolt tensile forces was the point of anchor bolt contraflexure, assumed to be the midpoint of the exposed length, as indicated with a dashed line. Figure 2.40 shows the external and internal forces in the free body resulting from this cut for the three types of test conducted.

Eccentric shear test results are summarized in Table 2.12. Included in this table are the ultimate applied shear load, $V_{u,test}$, and normal load, $T_{u,test}$, on a per-bolt basis. Additionally, for the test

specimens in Phase 1 (Table 2.2), two split specimens**,** DS8-2 and DS6-5 were exhibited, as shown in Figure 2.3, one with an exposed length of $0.8d_a$, the other $2.8d_a$. In addition to l_b profiles of concrete spalling in front of and behind the displaced anchor bolt are outlined; it can be seen on both bolts that more concrete spalled away on the trailing end of the bolt and, significantly, that curvature of the bolt occurred below the depth of the shallower spall profile on the leading edges of the bolts, the bolts bearing against the concrete at an angle . As a result, the cross-section of the bolt at the concrete surface effectively rotates into a more favorable orientation to resist load, a plausible explanation for failure predominantly occurring at the top of the exposed length below the leveling nut.

At last, a formula for predicting the anchor bolt strength under the combined action of normal and shear force base on an assumption that the actual exposed length of the bolt is equal to the stand-off height plus $0.5d_a$ was proposed.

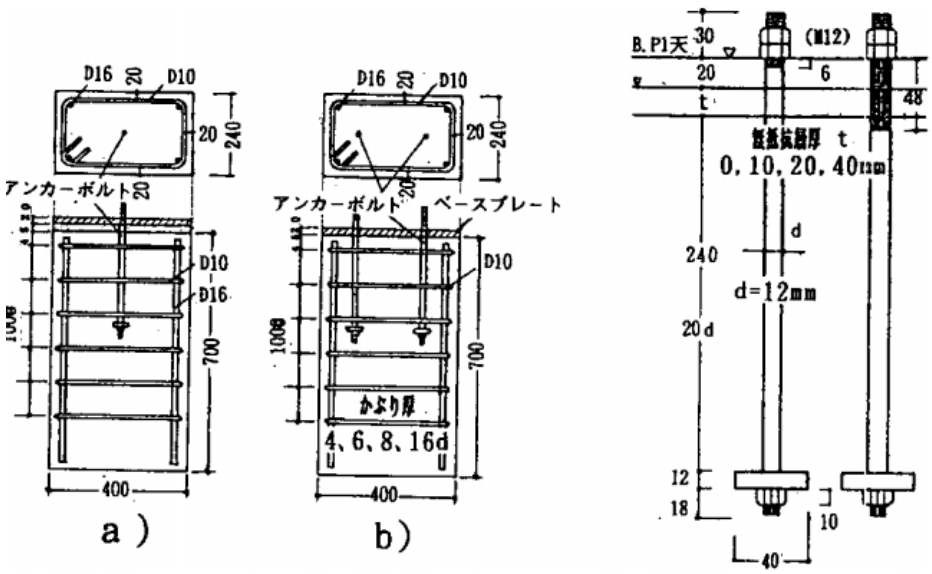

Figure 2.1 The reinforced detail and the dimension of specimens

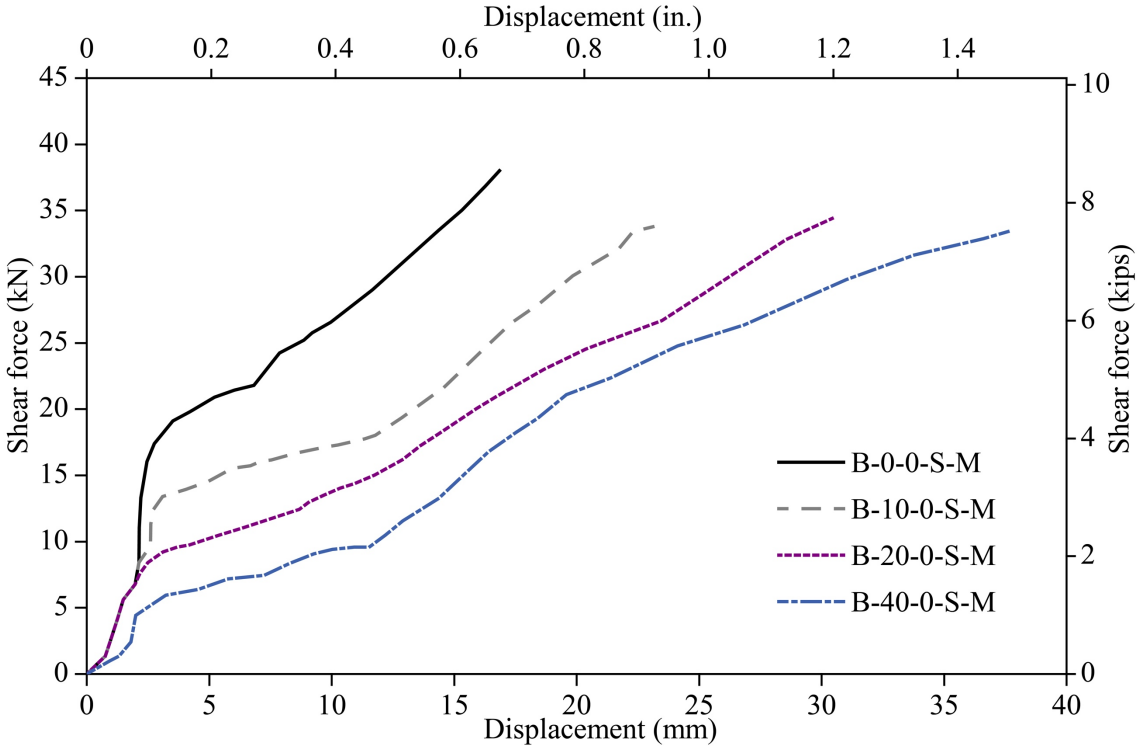

Figure 2.2 Measured load–Displacement relationships in the tests by Nakashima (1999)

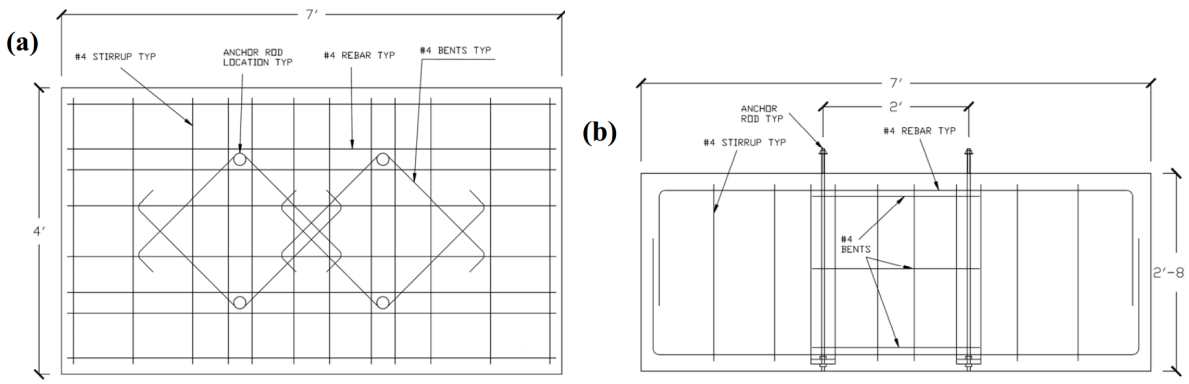

Figure 2.3 Schematic (a) plan view and (b) elevation view of reinforcing bar details used in the concrete pedestals for the anchor rod tests No. 4 and No. 5

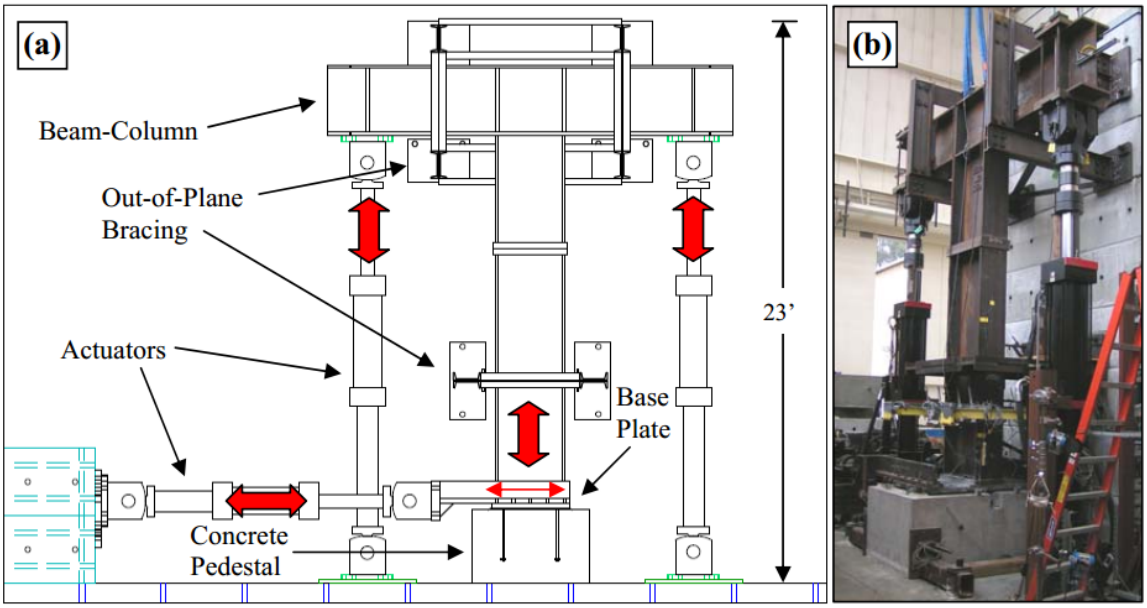

Figure 2.4 Base plate shear test setup (a) schematic and (b) photograph

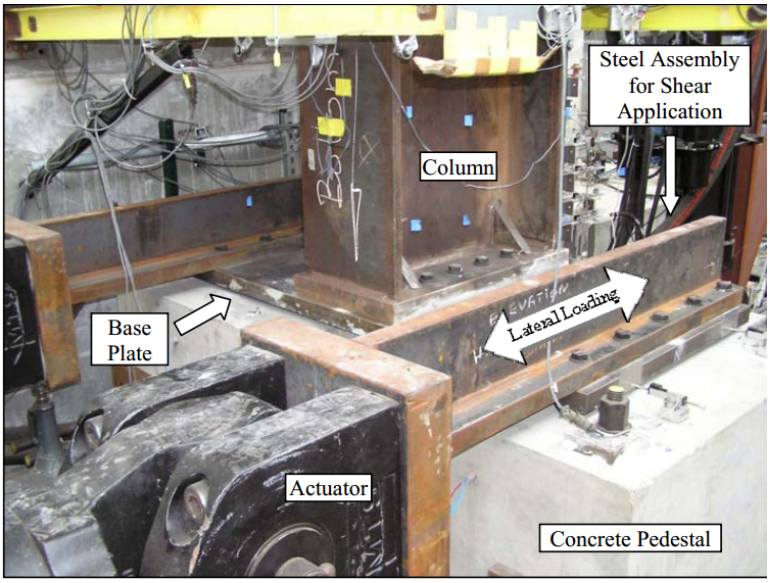

Figure 2.5 Steel shear loading assembly for base plate tests

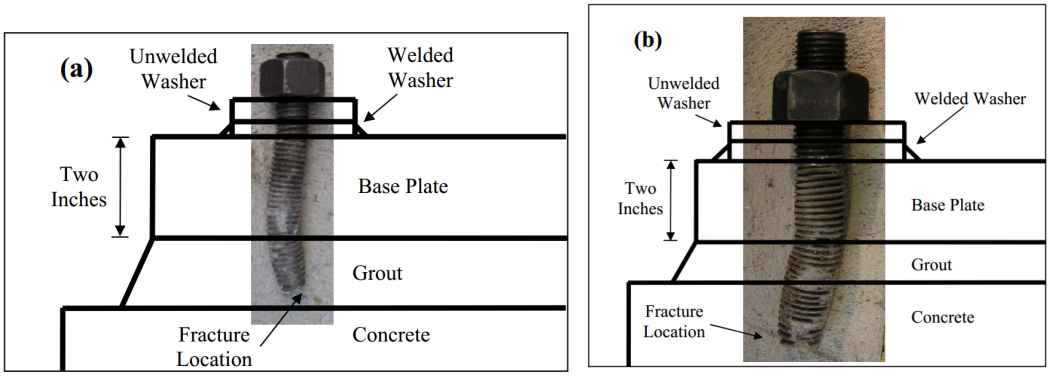

Figure 2.6 To-scale illustration of fractured (a) 19 mm [0.75 in.] diameter anchor rod and (b) 31.8 mm [1.25 in.] rod relative to base plate, grout and concrete

Figure 2.7 Post-test photographs showing (a) grout damage of 19 mm [0.75 in.] diameter anchor Test; (b) concrete damage of 31.8 mm [1.25 in.] diameter anchor and (c) grout damage of 31.8 mm [1.25 in.] diameter anchor

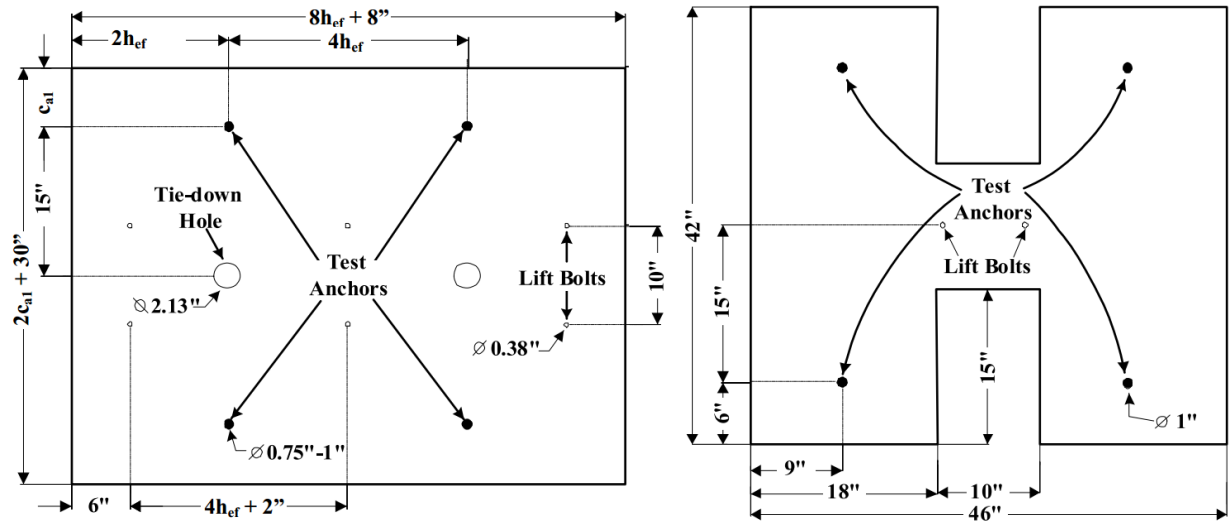

Figure 2.8 Plane view of test specimen containing 4 anchors

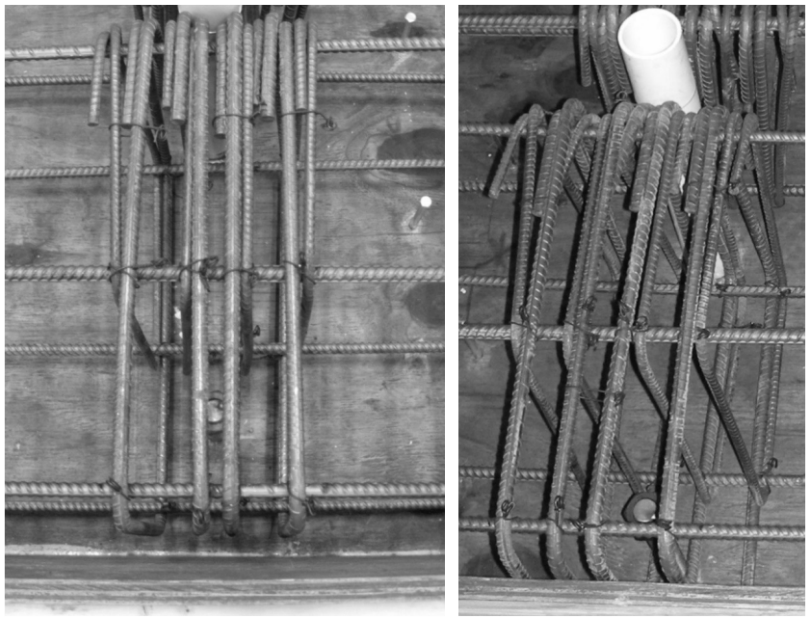

Figure 2.9 Closed loop anchor reinforcement layout

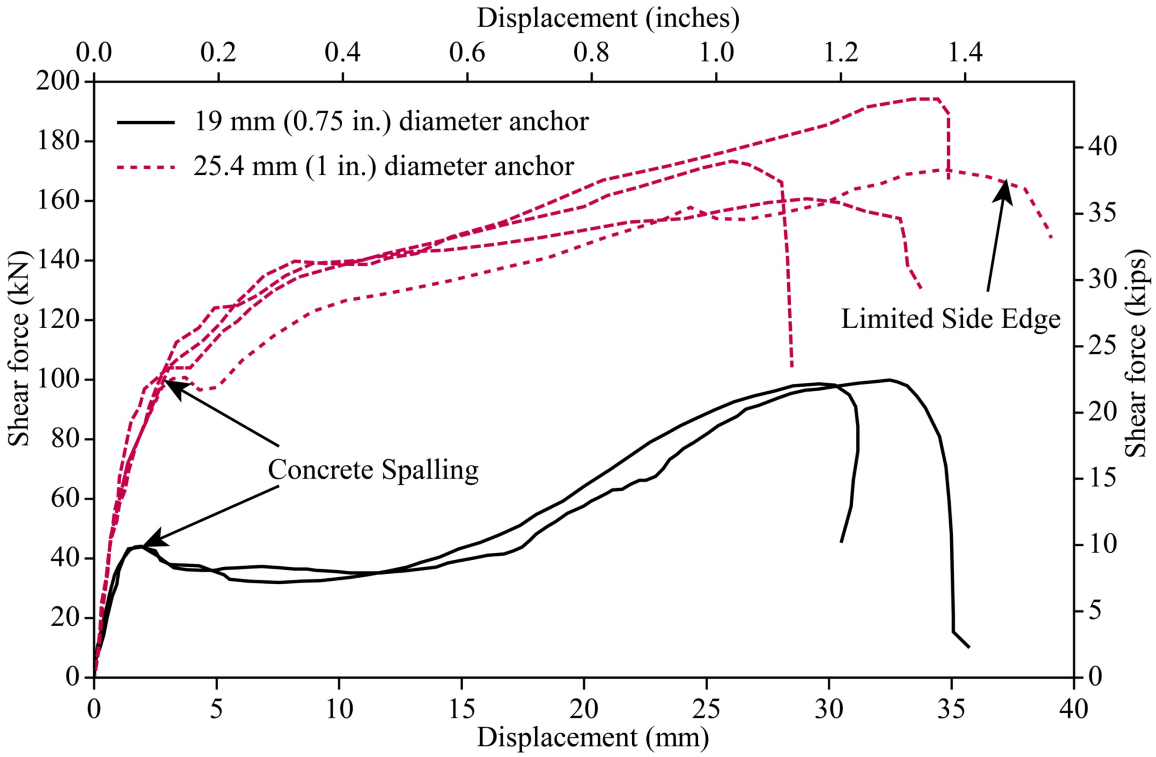

Figure 2.10 Behavior of shear force versus displacement by Petersen (2010)

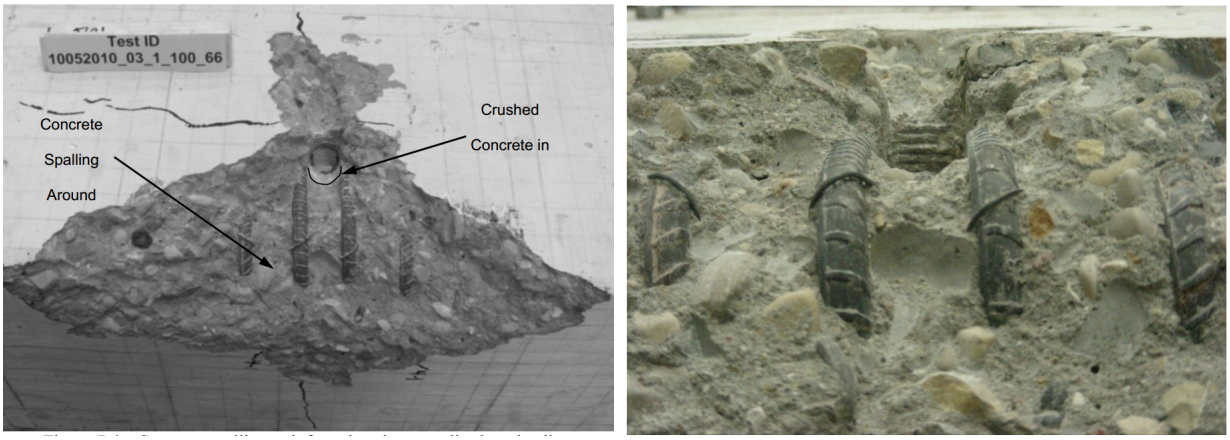

Figure 2.11 Depth of hinge point for reinforced anchors in Petersen (2010)

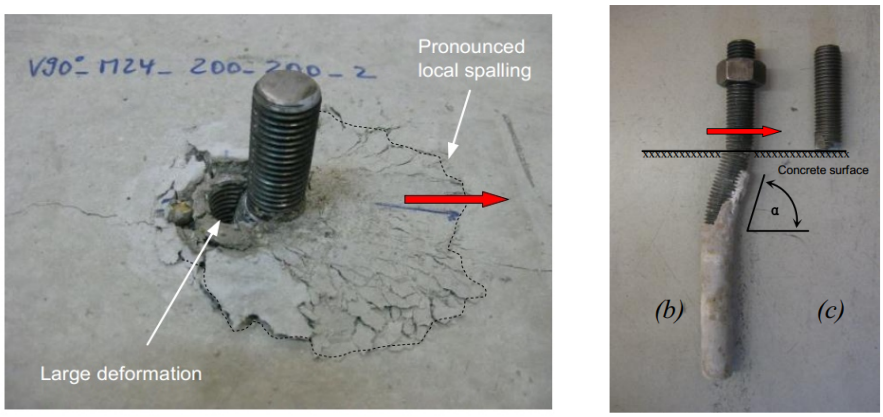

Figure 2.12 Behavior of anchor rod in shear as observed by Grosser (2012)

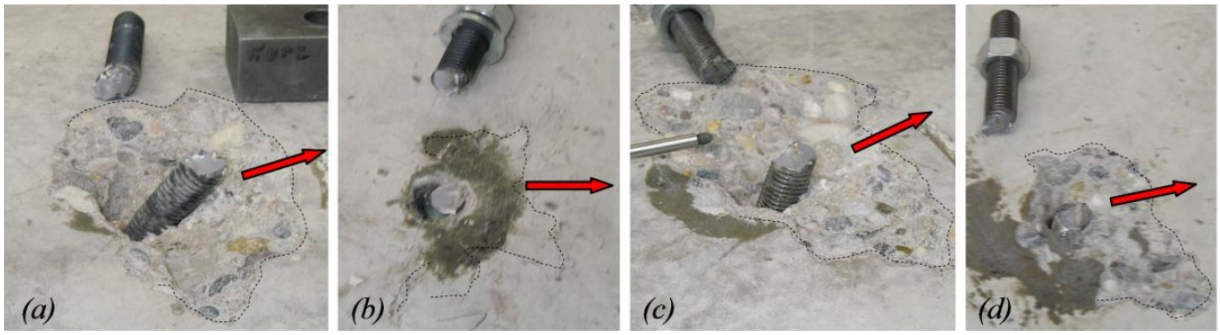

Compressive strength $f_{cc,200}$ = 22.7 MPa (a) M16, h_{ef} = 80 mm, grade 10.9 (b) M16, h_{ef} = 130 mm, grade 10.9 (c) M16, h_{ef} = 80 mm, grade 12.9 (d) M16, h_{ef} = 130 mm, grade 12.9

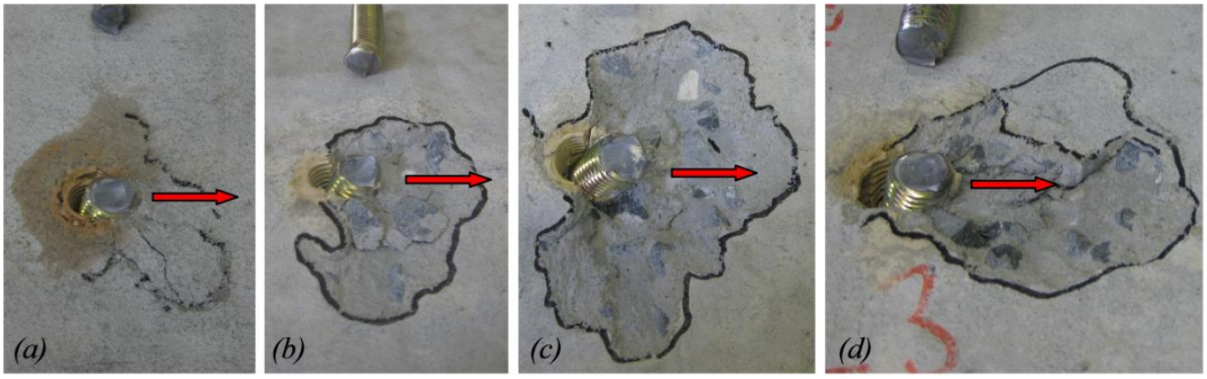

Compressive strength $f_{cc,200}$ = 34.6 MPa (a) 5/8'', h_{ef} = 76.2 mm, grade B7 (b) 5/8'', h_{ef} = 127 mm, grade B7 (c) 7/8'', h_{ef} = 127 mm, grade B7 (d) 7/8'', h_{ef} = 203.2 mm, grade B7

Figure 2.13 Failure patterns of single anchors under shear in concrete by Grosser (2012)

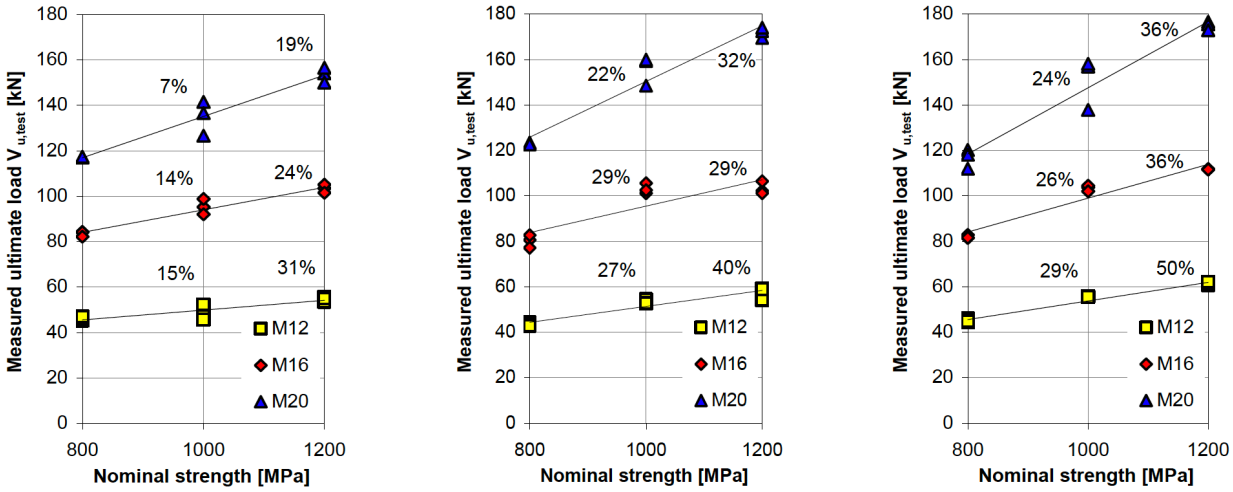

(a) *(b)* *(c)*

Figure 2.14 Measured ultimate loads plotted as a function of the nominal tensile steel strength (a) tests in low strength concrete (b) tests in high strength concrete (c) reference tests in a steel block (Fig. 3.53 in Grosser (2012))

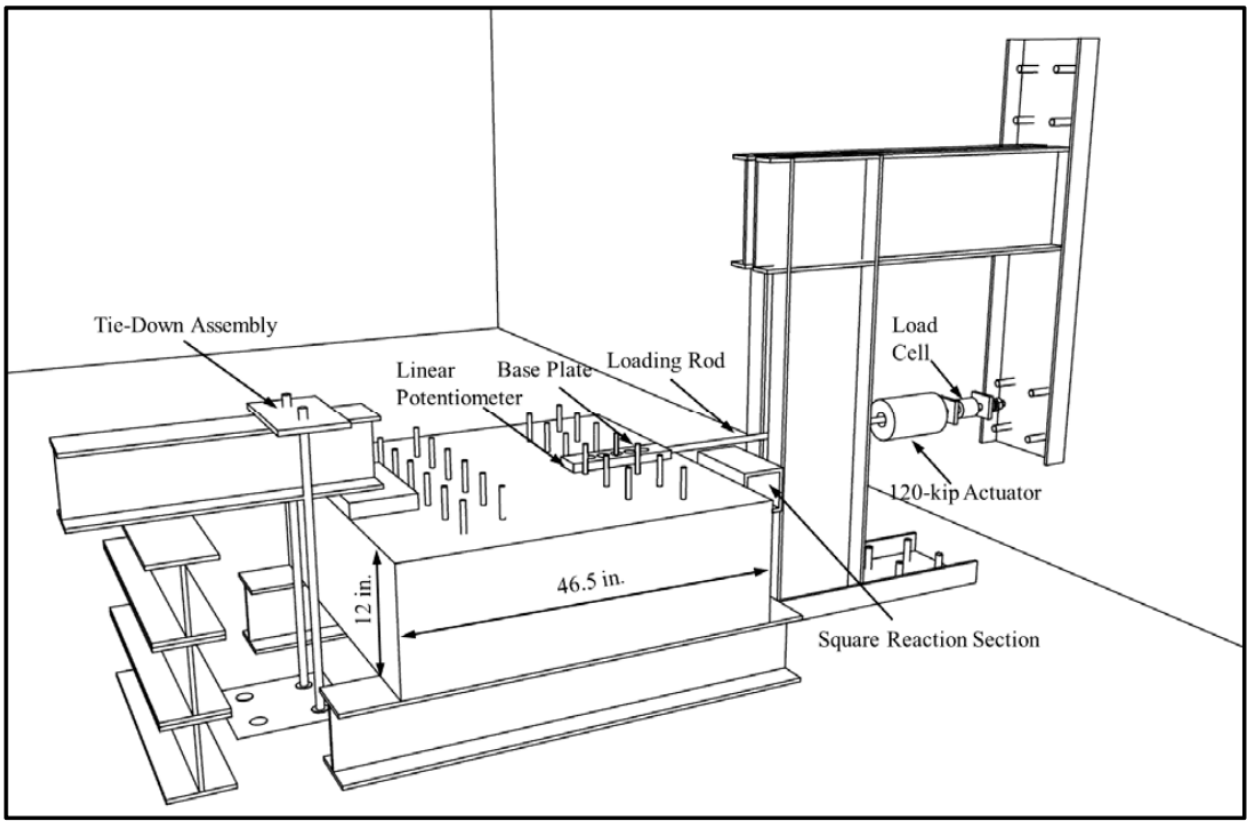

Figure 2.15 Phase 1 test setup by Cook et al. (2013)

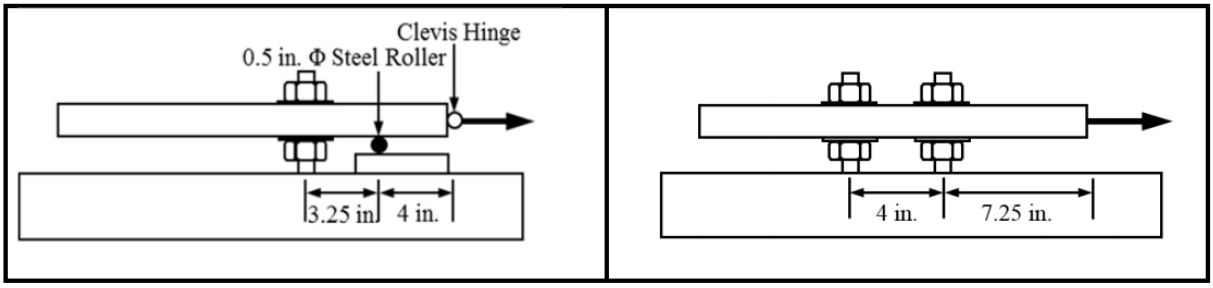

(a) (b)

Figure 2.16 Connection details for (a) single bolt and (b) double-bolt direct shear tests

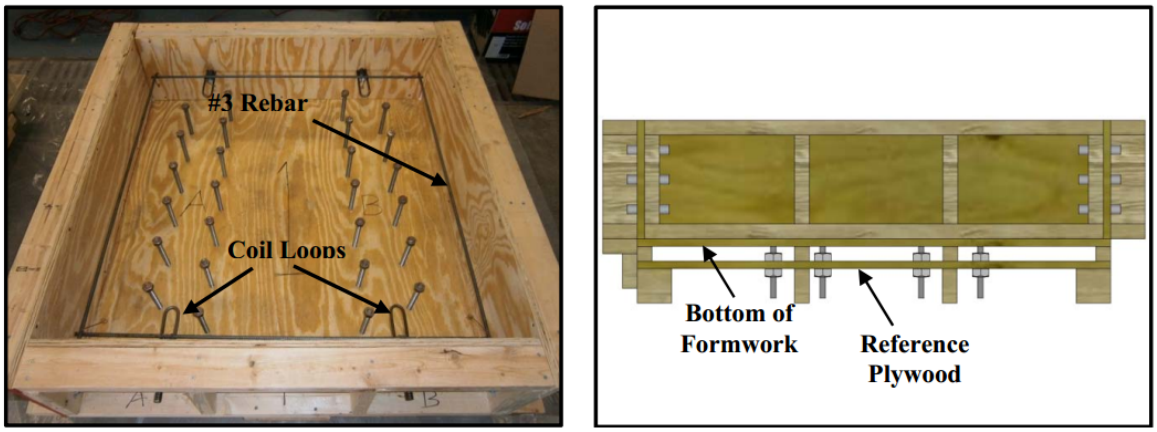

(a) (b)

Figure 2.17 Top view (left) and side view (right) of formwork

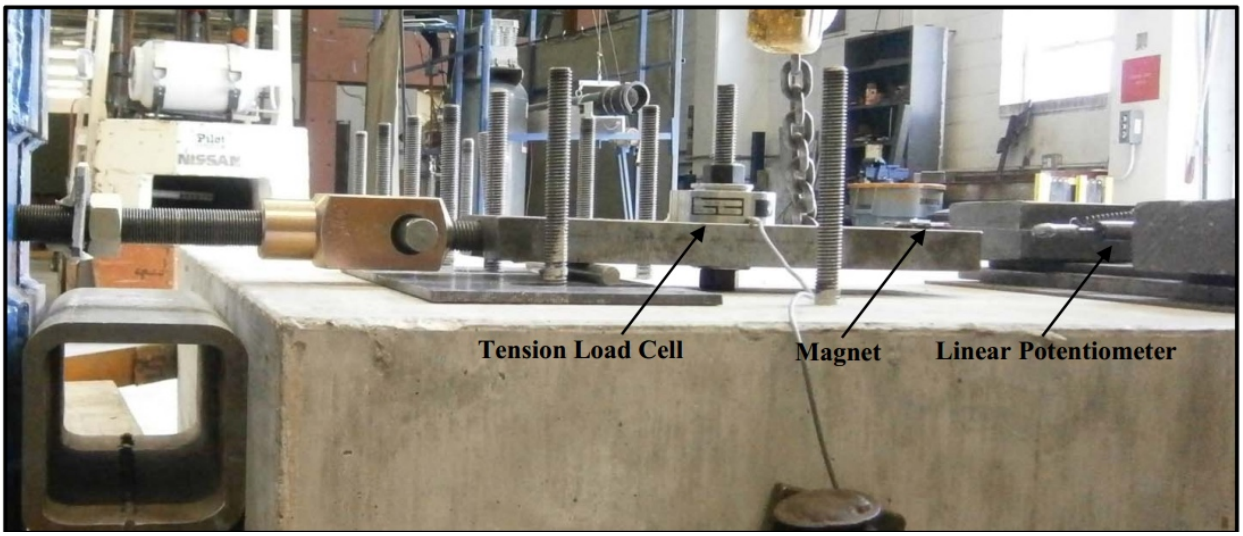

Figure 2.18 Instrumentation in Phase 1 testing by Cook et al. (2013)

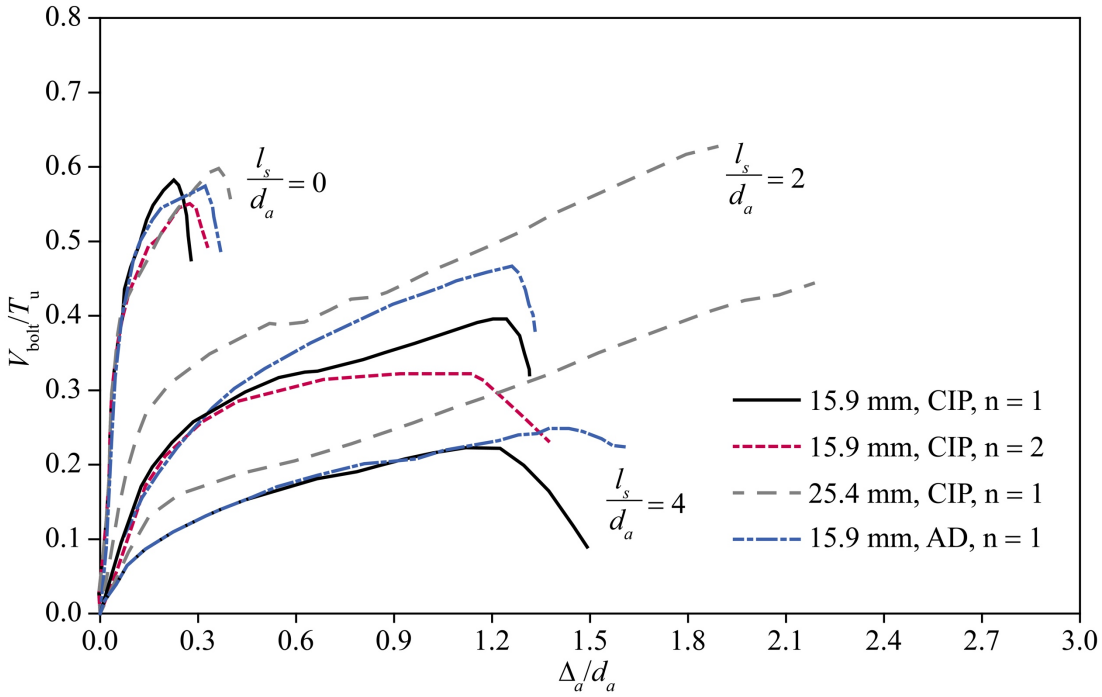

Figure 2.19 Load-displacement behavior of representative Phase 1 tests by Cook et al. (2013)

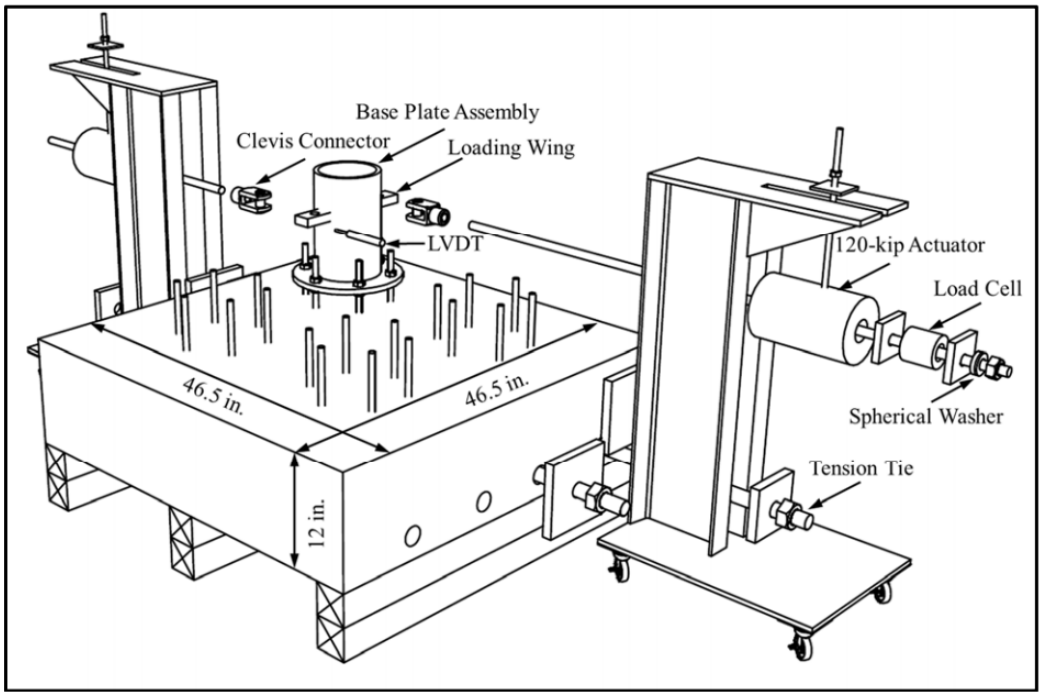

Figure 2.20 Phase 2 test setup by Cook et al. (2013)

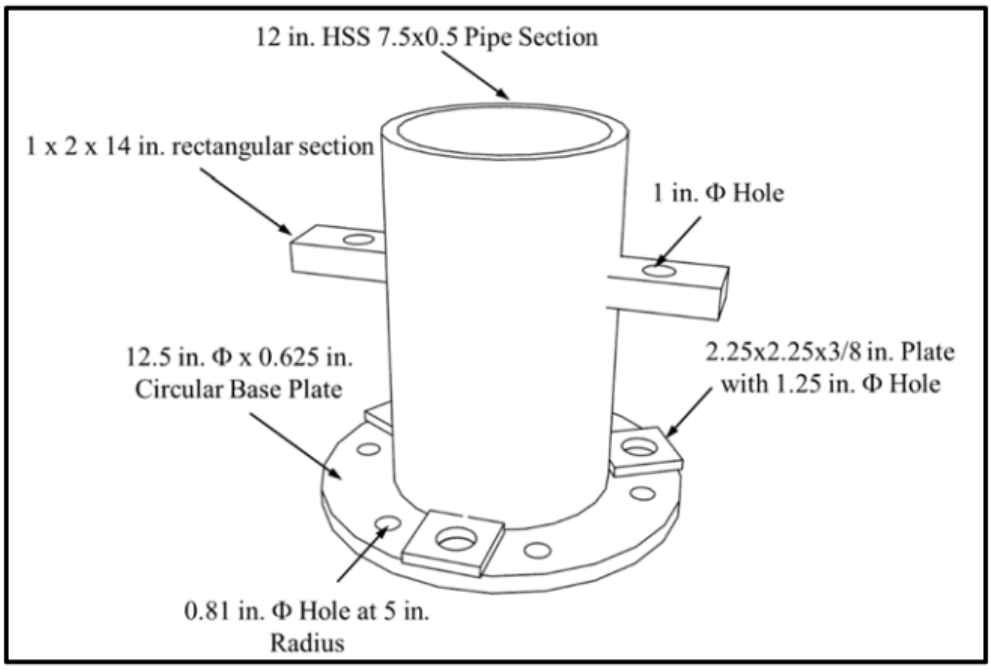

Figure 2.21 Base plate assembly components by Cook et al. (2013)

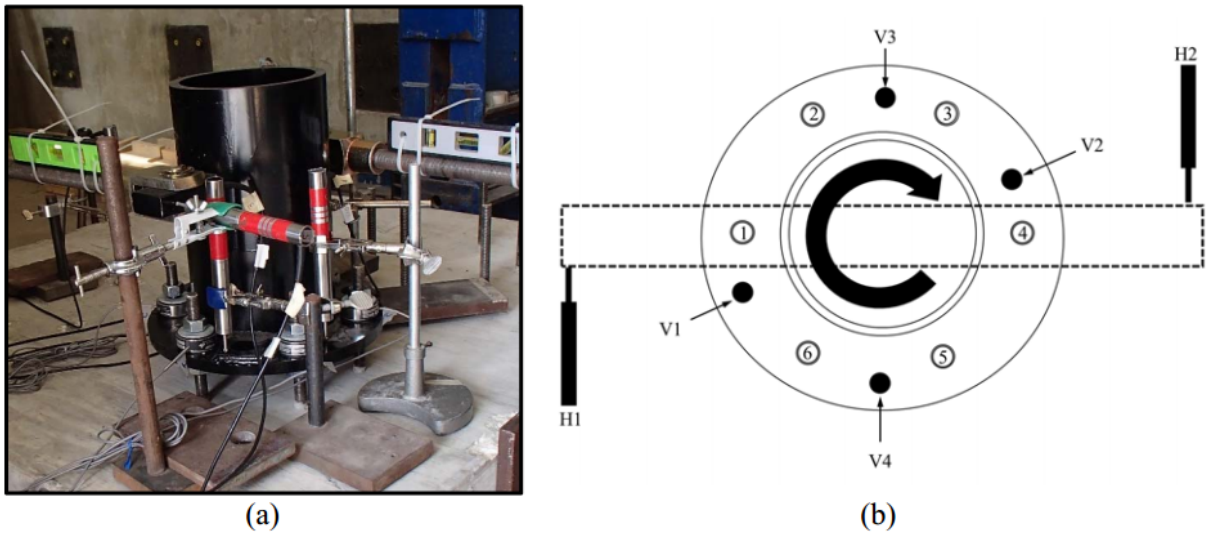

Figure 2.22 (a) Fully instrumented 15.9 mm [5/8 in.] torsion specimen and (b) plan view detail of base plate assembly bolt numbers and instrumentation

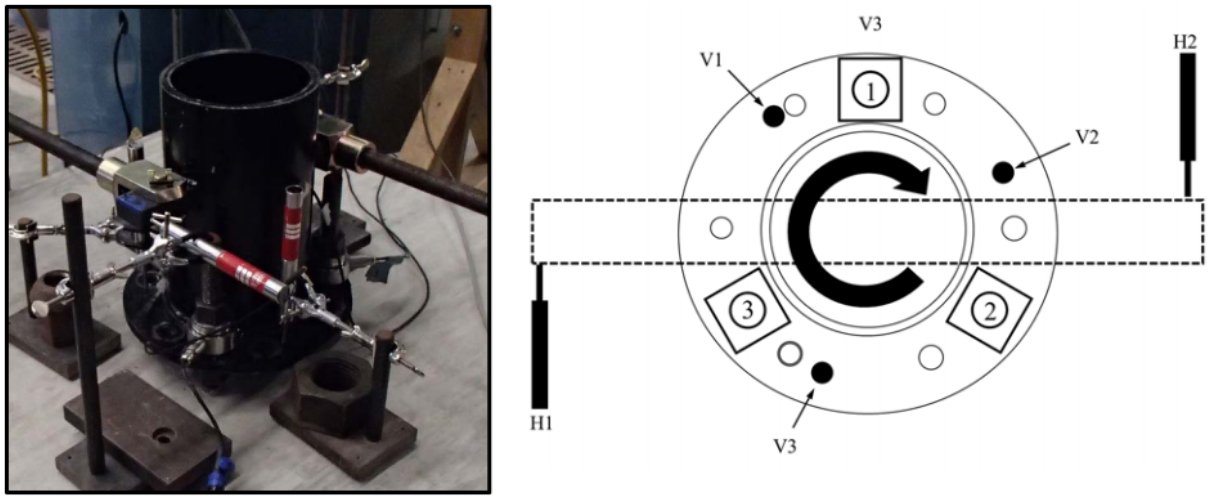

(a) (b)

Figure 2.23 (a) Fully instrumented 25.4 mm [1 in.] torsion specimen and (b) plan view detail of base plate assembly bolt numbers and instrumentation

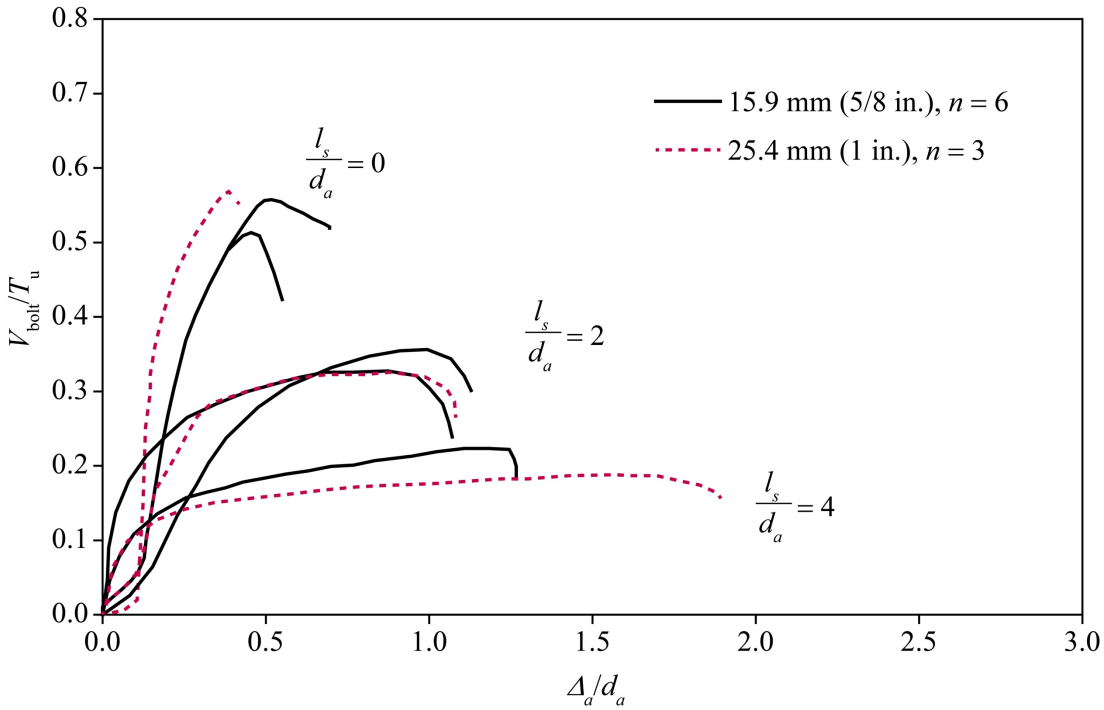

Figure 2.24 Load-displacement behavior of representative ungrouted Phase 2 tests by Cook *et al.* (2013)

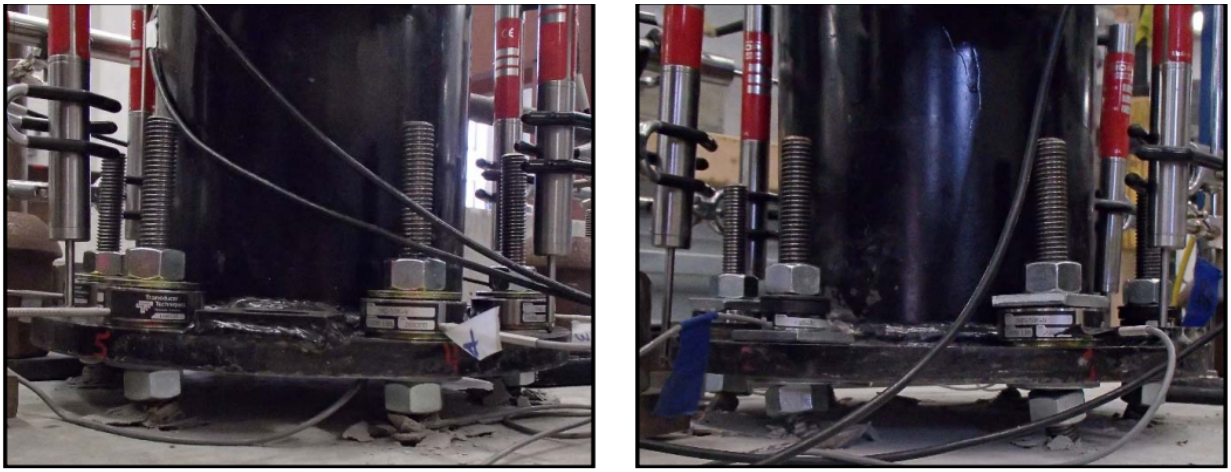

(a) (b)

Figure 2.25 Anchor bolts in failed condition for (a) pretensioned T2-B and (b) non-pretensioned T4 ungrouted 2da base plate tests

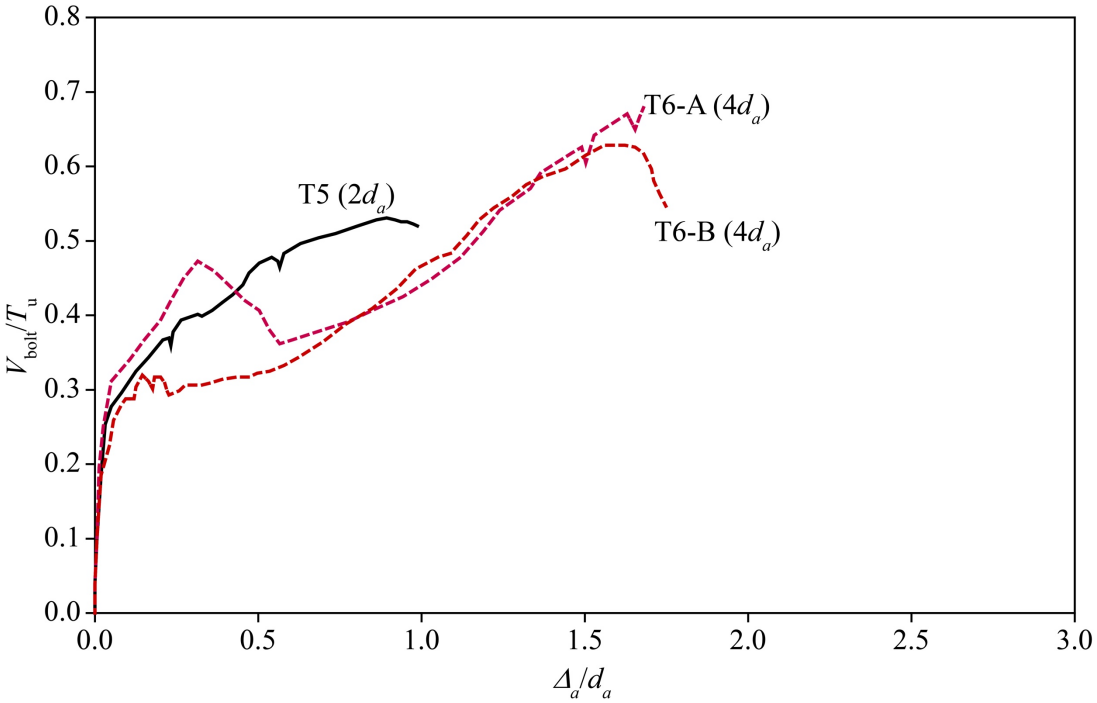

Figure 2.26 Load-displacement behavior of grouted Phase 2 tests by Cook *et al.* (2013)

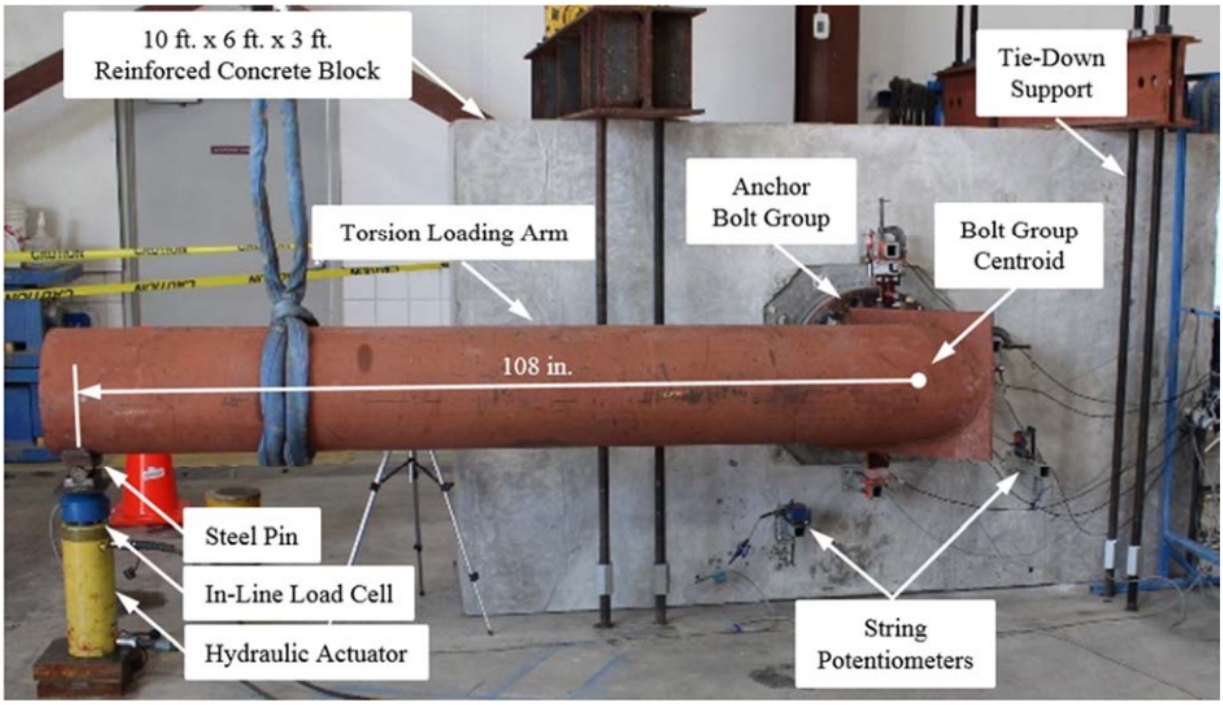

Figure 2.27 Phase 3 test setup by Cook et al. (2013)

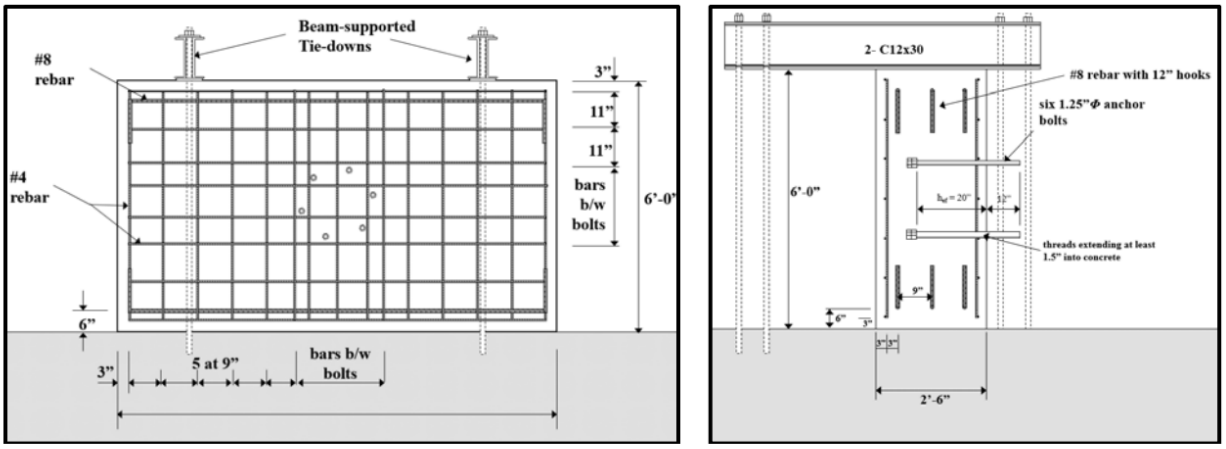

(a) (b)

Figure 2.28 Front (a) and side (b) views of anchor placement details for test specimen blocks

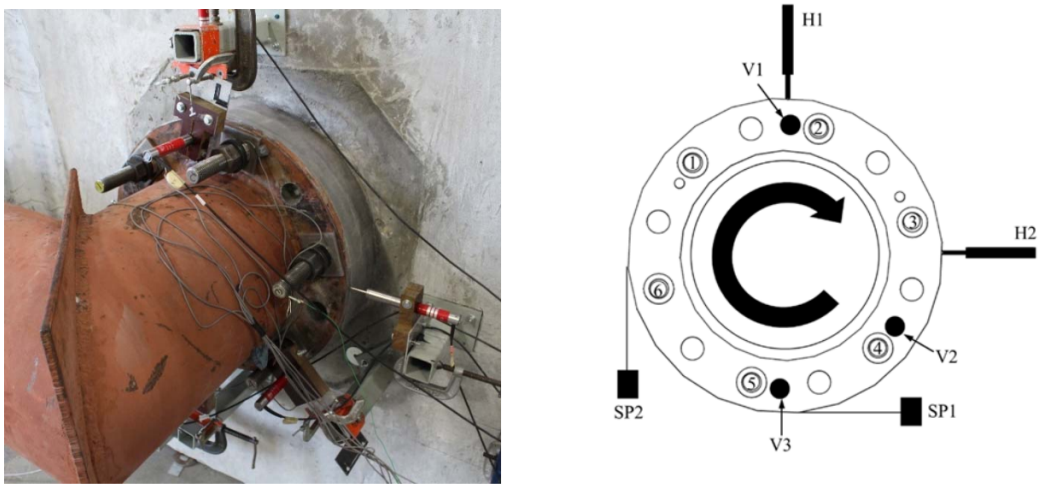

Figure 2.29 (a) Fully instrumented full-scale specimen and (b) plan view detail of base plate assembly bolt numbers and instrumentation

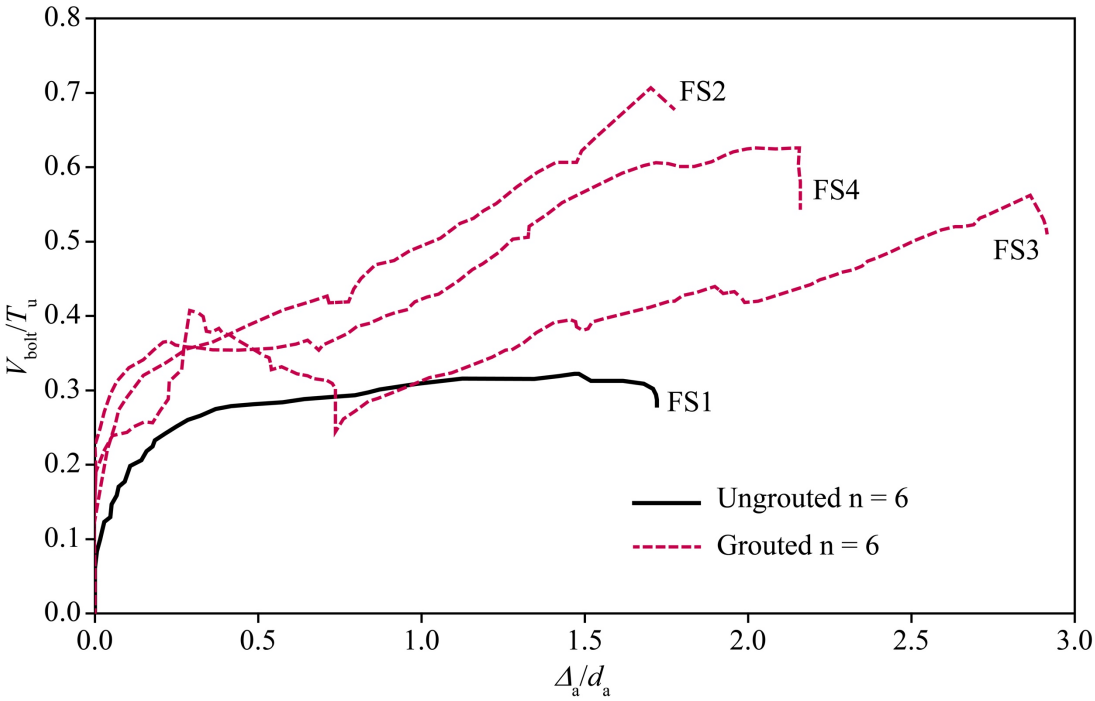

Figure 2.30 Load-displacement behavior of Phase 3 tests by Cook et al. (2013)

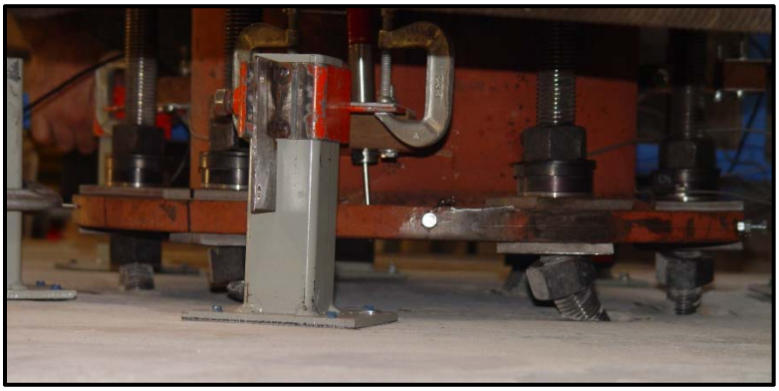

Figure 2.31 FS1 anchor bolts in failed condition

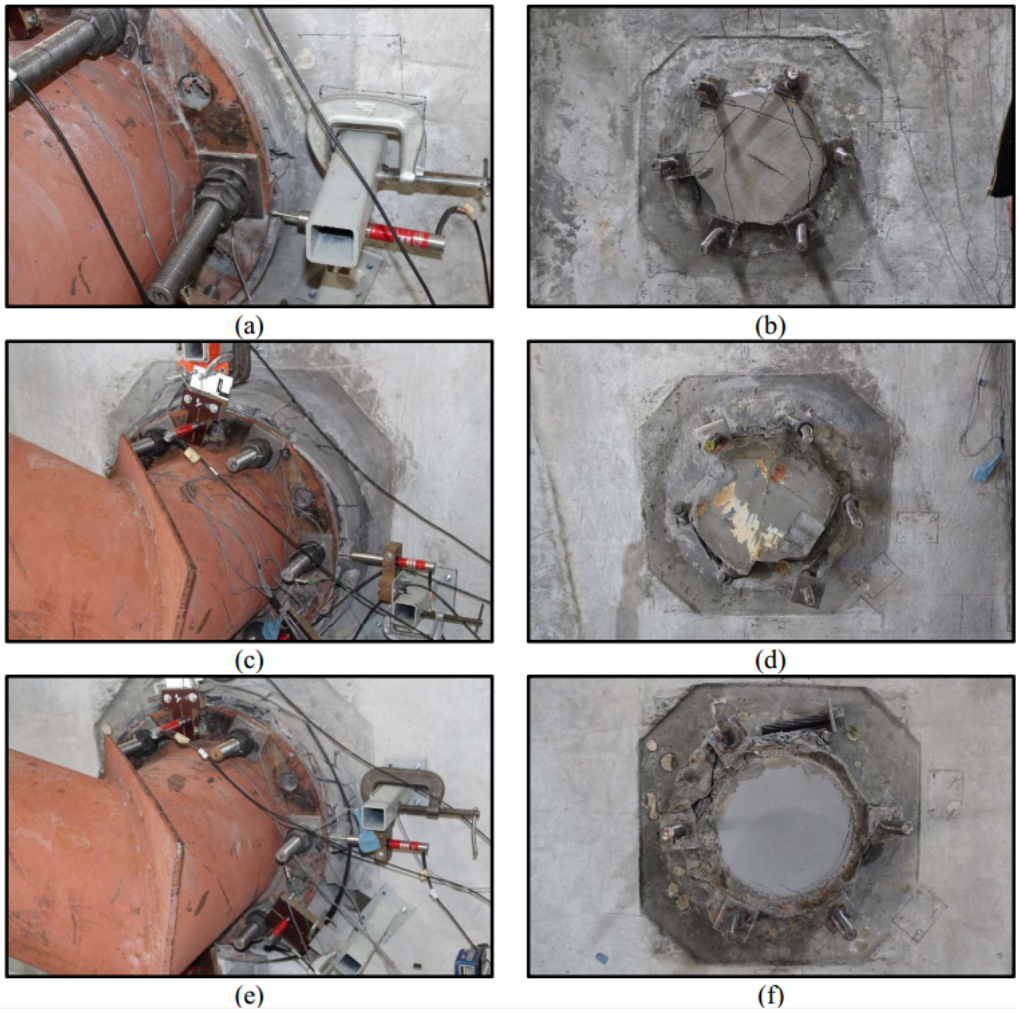

Figure 2.32 (a, c, e) In-test grout cracking and (b, d, f) post-test grout surfaces for FS2, FS3, and FS4

Figure 2.33 Eccentric Shear test setup

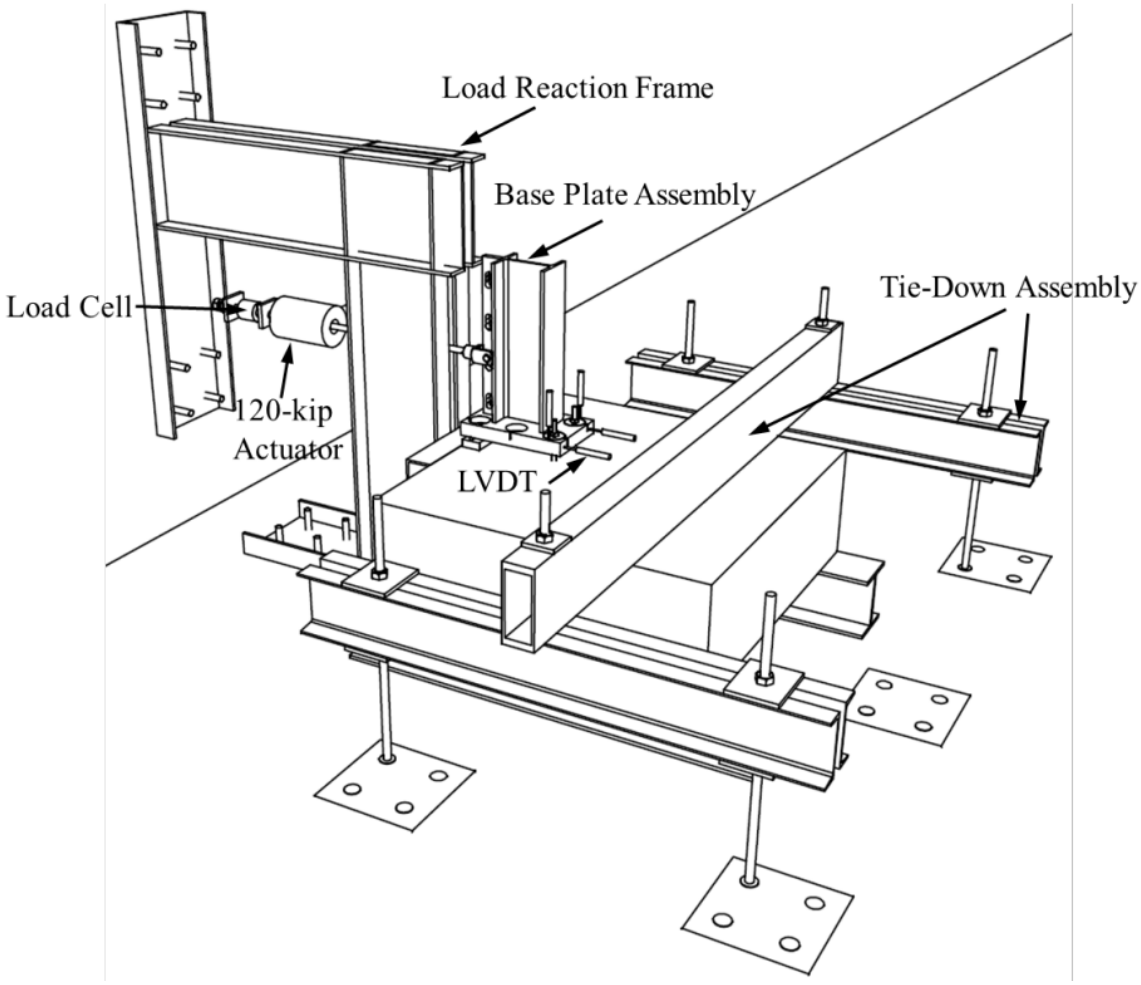

Figure 2.34 Labeled schematic of Eccentric Shear test setup

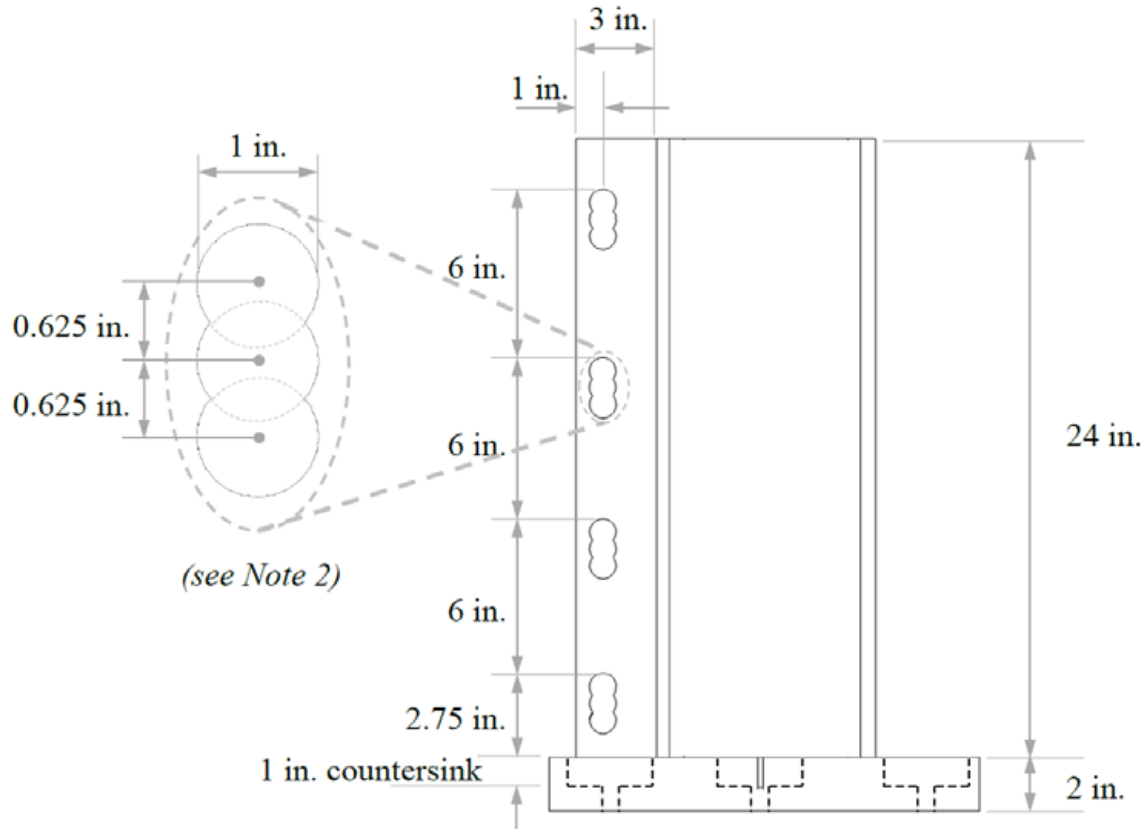

Figure 2.35 Profile view of Eccentric Shear base plate assembly dimensions

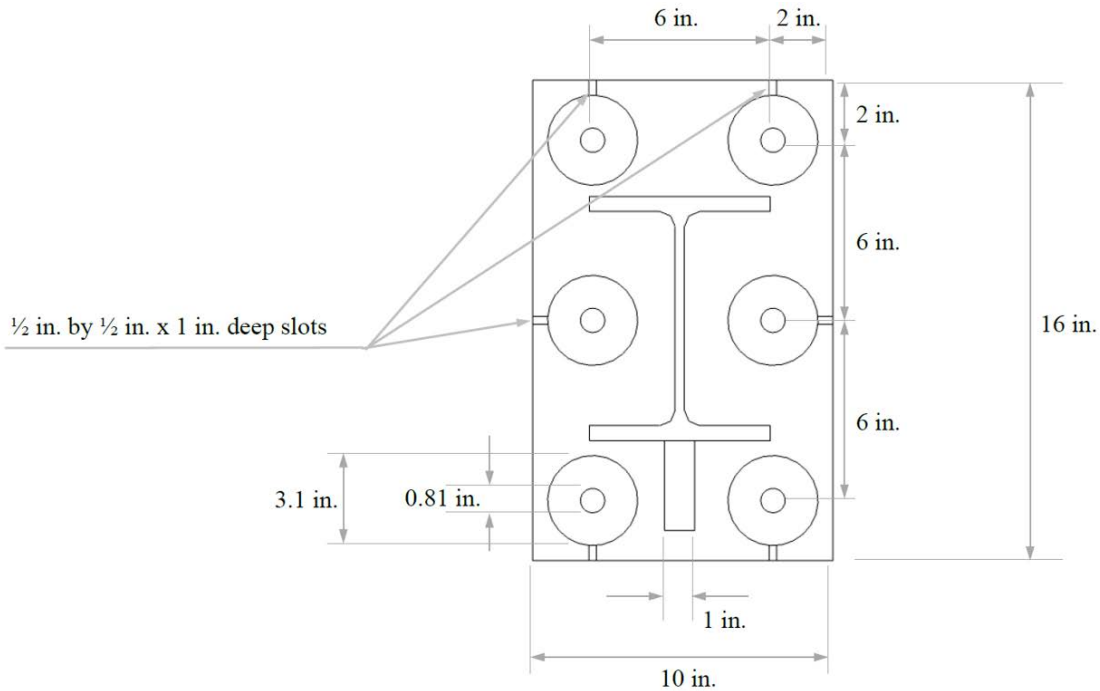

Figure 2.36 Plan view of Eccentric Shear base plate assembly dimensions

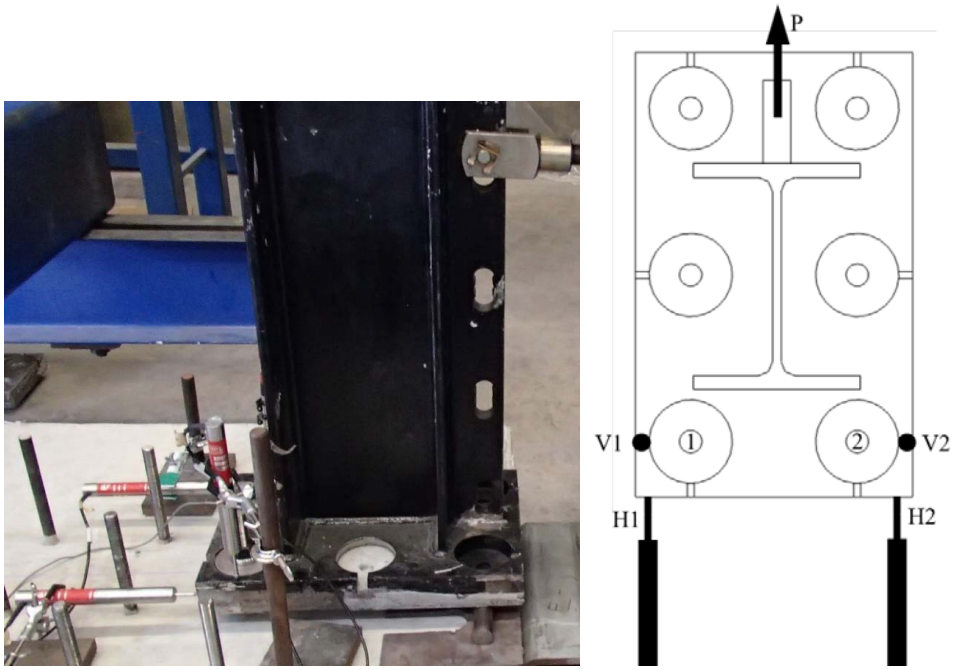

Figure 2.37 Two-bolt tension and shear test. A) Fully instrumented specimen. B) Plan view detail of base plate. (Photo from Mcbride (2019))

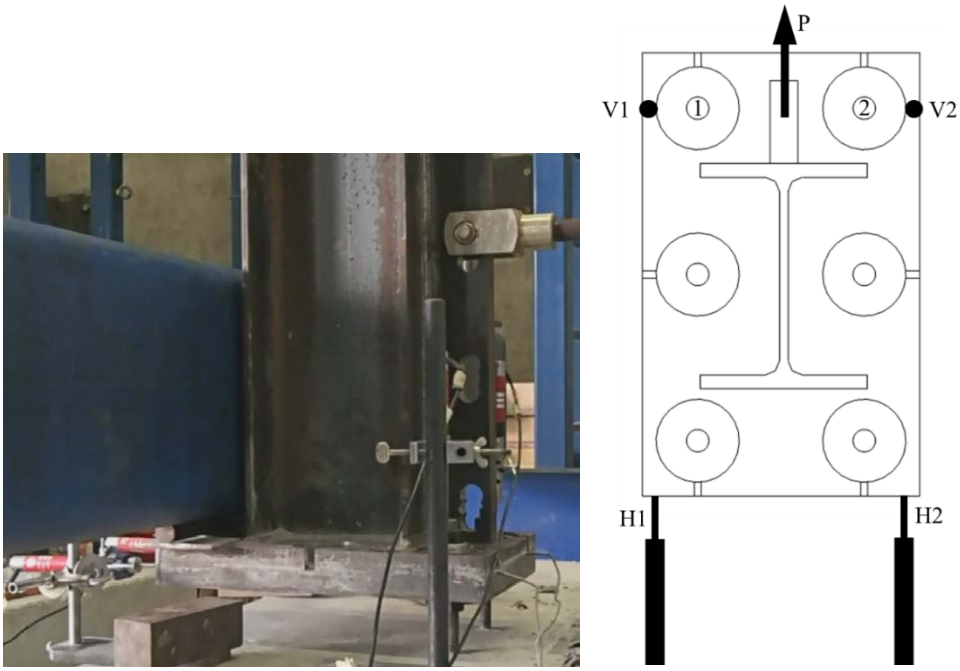

Figure 2.38 Two-bolt compression and shear test. A) Fully instrumented specimen. B) Plan view detail of base plate. (Photo from Mcbride (2019))

Figure 2.39 Eccentric shear test setup by Mcbride et al. (2014).

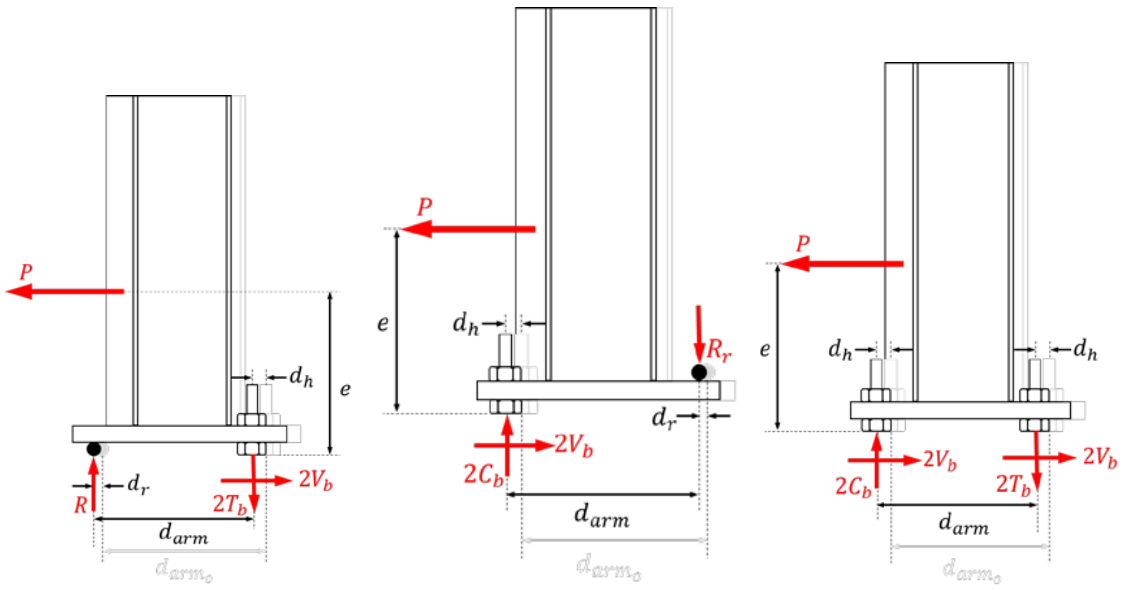

Figure 2.40 Free-body illustrations of Eccentric Shear tests. A) Two-bolt tension and shear. B) two-bolt compression and shear. C) Four-bolt.

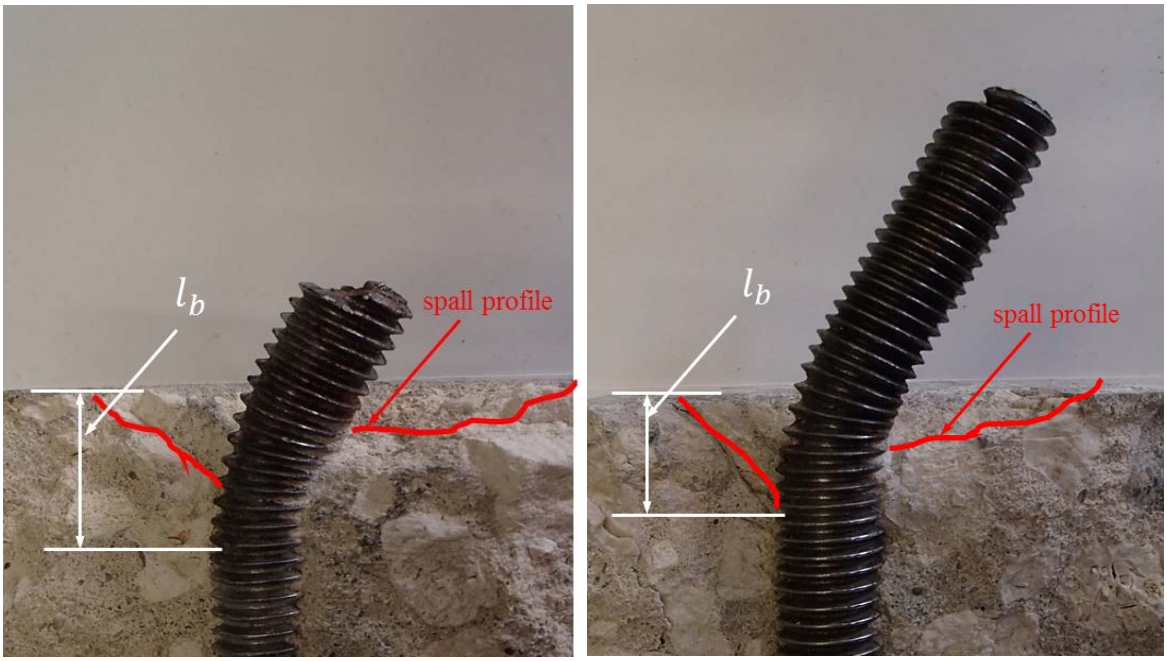

Figure 2.41 Examples of specimens used to measure *lb*. A) DS8-2. B) DS6-5 (Mcbride (2019))

Table 2.1 Test results by Nakashima (1998)

Name	Exposed length (mm [in.])	Ultimate shear load (kN [kips])	Ultimate shear disp. (mm [in.])
B-10-0-S-M	0 [0]	37.9 [8.51]	16.72 [0.658]
B-10-0-S-M	10 [0.394]	35.3 [7.94]	23.94 [0.942]
B-20-0-S-M	20 [0.787]	34.3 [7.71]	30.23 [1.190]
B-40-0-S-M	40 [1.575]	33.4 [7.5]	37.47 [1.475]

Table 2.2 Phase 1 test matrix by Cook *et al.* (2013)

Set	Repeats	d_a (mm [in.])	n	$\frac{l_s}{d_a}$	$\frac{l_{ea}}{d_a}$
DS1	8	15.9 [0.625]	1	0	na
DS2	6	15.9 [0.625]	1	1.2	0
DS3	2	15.9 [0.625]	1	1.6	0.4
DS4	10	15.9 [0.625]	1	2	0.8
DS5	4	15.9 [0.625]	1	3	1.8
DS6	5	15.9 [0.625]	1	4	2.8
DS7	4	15.9 [0.625]	2	0	na
DS8	5	15.9 [0.625]	2	2	0.8
DS9	4	25.4 [1.00]	1	0	na
DS10	2	25.4 [1.00]	1	2	0.75
DS11	2	25.4 [1.00]	1	4	2.75
DS12	4	15.9 [0.625]	1	0	na
DS13	5	15.9 [0.625]	1	2	0.8
DS14	2	15.9 [0.625]	1	4	2.8

n = number of bolts; *na* = not applicable

Table 2.3 Phase 1 test results by Cook *et al*. (2013)

Set	Repeats	$\frac{l_s}{d_a}$	$\frac{l_{ea}}{d_a}$	T_u (kN [kips])	$V_{u,test}$ (kN [kips])	COV	$\frac{V_{u,test}}{T_u}$	δ_u (mm [in.])	$\frac{\delta_u}{d_a}$	l_b (mm [in.])
DS1	8	0	na	93.9 [21.1]	54.7 [12.3]	3%	0.59	4.6 [0.18]	0.29	14.2 [0.56]
DS2	6	1.2	0	93.9 [21.1]	50.3 [11.3]	1%	0.54	14.2 [0.56]	0.89	16.2 [0.64]
DS3	2	1.6	0.4	93.9 [21.1]	43.6 [9.8]	na	0.46	19.6 [0.77]	1.23	16.8 [0.66]
DS4	10	2	0.8	93.9 [21.1]	35.1 [7.9]	6%	0.37	18.3 [0.72]	1.15	18.5 [0.73]
DS5	4	3	1.8	93.9 [21.1]	24.9 [5.6]	6%	0.27	16.3 [0.64]	1.03	13.2 [0.52]
DS6	5	4	2.8	93.9 [21.1]	19.6 [4.4]	10%	0.21	18.8 [0.74]	1.18	11.9 [0.47]
DS7	4	0	na	93.9 [21.1]	50.7 [11.4]	5%	0.54	4.3 [0.17]	0.27	13.7 [0.54]
DS8	5	2	0.8	93.9 [21.1]	30.7 [6.9]	3%	0.33	16.3 [0.64]	1.02	18.3 [0.72]
DS9	4	0	na	248.2 [55.8]	149.0 [33.5]	1%	0.6	7.9 [0.31]	0.31	-
DS10	5	2	0.75	248.2 [55.8]	121.0 [27.2]	19%	0.49	1.64	1.64	
DS11	2	4	2.75	248.2 [55.8]	86.3 [19.4]	*na*	0.35	1.85	1.85	
DS12	4	0	na	93.9 [21.1]	54.3 [12.2]	3%	0.58	4.6 [0.18]	0.29	-
DS13	5	2	0.8	93.9 [21.1]	40.9 [9.2]	5%	0.44	19.0 [0.75]	1.20	-
DS14	2	4	2.8	93.9 [21.1]	22.7 [5.1]	5%	0.24	21.1 [0.83]	1.33	-

na = not applicable

Table 2.4 Calculation of additional exposed length by Cook *et al.* (2013)

Set	$V_{u,test}$ (kN [kips])	T_{usa} (kN [kips])	δ_u (mm [in.])	l_b (mm [in.])
DS1	54.7 [12.3]	16.4 [3.7]	4.6 [0.18]	14.2 [0.56]
DS2	50.3 [11.3]	31.6 [7.1]	14.2 [0.56]	16.2 [0.64]
DS3	43.6 [9.8]	32.9 [7.4]	19.6 [0.77]	16.8 [0.66]
DS4	35.1 [7.9]	33.8 [7.6]	18.3 [0.72]	18.5 [0.73]
DS6	19.6 [4.4]	20.9 [4.7]	18.8 [0.74]	11.9 [0.47]
DS7	50.7 [11.4]	0/21.4 [0/4.8]	4.3 [0.17]	13.7 [0.54]
DS8	30.7 [6.9]	10.2/28.5 [2.3/6.4]	16.3 [0.64]	18.3 [0.72]

Table 2.5 Phase 2 test matrix by Cook *et al.* (2013)

Set[a]	Repeats	d_a (mm [in.])	Hole size (mm [in.])	n	Connecition Type[b]	Top Nut tightness[c]	$\frac{l_s}{d_a}$	$\frac{l_e}{d_a}$
T1	2	16 [0.625]	21 [0.81]	6	FM	FT	0	na
T2	2	16 [0.625]	21 [0.81]	6	U	TOTN	2	0.8
T3	1	16 [0.625]	21 [0.81]	6	U	TOTN	4	2.8
T4	1	16 [0.625]	21 [0.81]	6	U	FT	2	0.8
T5	1	16 [0.625]	21 [0.81]	6	G	TOTN	2	0.8
T6	2	16 [0.625]	21 [0.81]	6	G	TOTN	4	2.8
T7	1	16 [0.625]	21 [0.81]	6	GF	TOTN	4	2.8
T8	1	25 [1.0]	32 [1.25]	3	U	FT	0	na
T9	1	25 [1.0]	32 [1.25]	3	U	TOTN	2	0.75
T10	1	25 [1.0]	32 [1.25]	3	U	TOTN	4	0.75

na = not applicable; [a]T = Torsion,
[b]FM = Flush-Mounted base plate, U = Ungrouted stand-off base plate, G = Grouted stand-off base plate,
[c]FT = Finger-Tightened, TOTN = Turn-of-the-Nut GF = Grouted stand-off base plate with FRP retrofit

Table 2.6 Test results of Phase 2 by Cook *et al.* (2013)

Set	Repeats	$\frac{l_s}{d_a}$	$\frac{l_{ea}}{d_a}$	T_u (kN [kips])	$V_{u,test}$ [kips]	$\frac{V_{u,test}}{T_u}$	δ_u (mm [in.])	$\frac{\delta_u}{d_a}$
T1	2	0	*na*	92.1 [20.7]	49.4 [11.1]	0.54	7.6 [0.3]	0.3
T2	2	2	0.8	92.1 [20.7]	28.9 [6.5]	0.31	14.2 [0.56]	0.56
T3	1	4	2.8	92.1 [20.7]	20.5 [4.6]	0.22	18.5 [0.73]	0.73
T4	1	2	0.8	92.1 [20.7]	32.9 [7.4]	0.36	15.2 [0.6]	0.6
T5	1	2	0.8	92.1 [20.7]	48.5 [10.9]	0.53	14.2 [0.56]	0.56
T6	2	4	2.8	92.1 [20.7]	58.3 [13.1]	0.63	26.2 [1.03]	1.03
T7	1	4	2.8	92.1 [20.7]	65.8 [14.8]	0.71	11.2 [0.44]	0.44
T8	1	0	*na*	248.2 [55.8]	141.0 [31.7]	0.57	9.9 [0.39]	0.39
T9	1	2	0.75	248.2 [55.8]	80.1 [18]	0.32	22.4 [0.88]	0.88
T10	1	4	2.75	248.2 [55.8]	46.7 [10.5]	0.19	39.9 [1.57]	1.57

Table 2.7 Phase 3 test matrix by Cook *et al.* (2013)

Set[a]	Repeats	d_a (mm [in.])	Hole size [in.]	n	Connecition Type	Top Nut tightness	$\frac{l_s}{d_a}$	$\frac{l_{ea}}{d_a}$
FS1	1	31.8 [1.25]	44.4 [1.75]	6	U	TOTN	2.3	1
FS2	1	31.8 [1.25]	44.4 [1.75]	6	G	TOTN	2.3	1
FS3	1	31.8 [1.25]	44.4 [1.75]	6	G	TOTN	4.3	3
FS4	1	31.8 [1.25]	44.4 [1.75]	6	G	TOTN	4.3	3

Table 2.8 Summary of Phase 3 test results by Cook *et al.* (2013)

Set	Repeats	$\frac{l_s}{d_a}$	$\frac{l_{ea}}{d_a}$	T_u (kN (kips])	$V_{u,blot}$ (kN (kips])	$\frac{V_{u,blot}}{T_u}$	δ_u (mm (in.])	$\frac{\delta_u}{d_a}$
FS1	1	2.3	1	375.4 [84.4]	102.5 [27.1]	0.32	48.0 [1.89]	1.52
FS2	1	2.3	1	375.4 [84.4]	262.9 [59.1]	0.70	53.8 [2.12]	1.70
FS3	1	4.3	3	375.4 [84.4]	208.6 [46.9]	0.56	90.7 [3.57]	2.86
FS4	1	4.3	3	375.4 [84.4]	234.9 [52.8]	0.63	64.3 [2.53]	2.02

Table 2.9 Torsion test matrix by Mcbride (2014)

Set	d_a mm [in.]	Hole size mm [in.]	n	Connecition Type[b]	Top Nut tightness[c]	$\frac{l_s}{d_a}$	$\frac{l_e}{d_a}$
T1	16 [0.625]	21 [0.81]	6	FM	FT	0	na
T2	16 [0.625]	21 [0.81]	6	FM	FT	0	na
T3	16 [0.625]	21 [0.81]	6	U	TOTN	2	0.8
T4	16 [0.625]	21 [0.81]	6	U	TOTN	2	0.8
T5	16 [0.625]	21 [0.81]	6	U	TOTN	4	2.8
T6	16 [0.625]	21 [0.81]	6	U	FT	2	0.8
T7	16 [0.625]	21 [0.81]	6	G	TOTN	2	0.8
T8	16 [0.625]	21 [0.81]	6	G	TOTN	4	2.8
T9	16 [0.625]	21 [0.81]	6	G	TOTN	4	2.8
T10	16 [0.625]	21 [0.81]	6	GF	TOTN	4	2.8
T11	25 [1.0]	32 [1.25]	3	U	FT	0	na
T12	25 [1.0]	32 [1.25]	3	U	TOTN	2	0.75
T13	25 [1.0]	32 [1.25]	3	U	TOTN	4	2.75
T14	16 [0.625]	21 [0.81]	6	U	TOTN	1.2	0
T15	16 [0.625]	21 [0.81]	6	U	TOTN	1.7	0.5
T16	16 [0.625]	21 [0.81]	6	U	TOTN	4	2.8
T17	16 [0.625]	21 [0.81]	6	U	TOTN	7.2	6
T18	16 [0.625]	21 [0.81]	6	U	TOTN	2.2	1
T19	16 [0.625]	21 [0.81]	6	U	TOTN	2.2	1
T20	16 [0.625]	21 [0.81]	6	U	TOTN	4.2	3
T21	16 [0.625]	21 [0.81]	6	U	TOTN	7.2	6
T22	16 [0.625]	21 [0.81]	6	U	TOTN	2.2	1
T23	16 [0.625]	21 [0.81]	6	U	TOTN	4.2	3
T24	16 [0.625]	21 [0.81]	6	U	TOTN	2.2	1
T25	16 [0.625]	21 [0.81]	6	G	TOTN	4.2	3
T26	16 [0.625]	21 [0.81]	6	GO	FT	4.2	na
T27	16 [0.625]	21 [0.81]	6	US	FT	3.6	na
T28	16 [0.625]	21 [0.81]	6	M	TOTN	4.2	3

Table 2.10 Summary of torsion test results by Mcbride (2014)

Set	$\frac{l_s}{d_a}$	$\frac{l_{ea}}{d_a}$	T_u (kN [kips])	$V_{u,test}$ (kN [kips])	$\frac{V_{u,test}}{T_u}$	δ_u (mm [in.])	$\frac{\delta_u}{d_a}$
T1	0	na	92.1 [20.7]	51.2 [11.5]	0.56	8.1 [0.32]	0.52
T2	0	na	92.1 [20.7]	47.1 [10.6]	0.51	7.1 [0.28]	0.44
T3	2	0.8	92.1 [20.7]	ERR			
T4	2	0.8	92.1 [20.7]	30.2 [6.8]	0.33	12.4 [0.49]	0.79
T5	2	0.8	92.1 [20.7]	32.9 [7.4]	0.36	15.2 [0.6]	0.96
T6	4	0.8	92.1 [20.7]	ERR			
T7	2	0.8	92.1 [20.7]	492.8 [11]	0.53	14.2 [0.56]	0.9
T8	4	2.8	92.1 [20.7]	DNF			
T9	4	2.8	92.1 [20.7]	59.2 [13.3]	0.64	26.2 [1.03]	1.65
T10	4	2.8	92.1 [20.7]	65.8 [14.8]	0.71	11.2 [0.44]	0.44
T11	0	Na	248.2 [55.8]	141 [31.7]	0.57	9.9 [0.39]	0.39
T12	2	0.75	248.2 [55.8]	80.1 [18]	0.32	22.4 [0.88]	0.88
T13	4	2.75	248.2 [55.8]	46.7 [10.5]	0.19	39.9 [1.57]	1.57
T14	1.2	0	89.0 [20]	49.8 [11.2]	0.56	10.7 [0.42]	0.67
T15	1.7	0.5	89.0 [20]	45.4 [10.2]	0.51	14 [0.55]	0.88
T16	4	2.8	89.0 [20]	14.2 [3.2]	0.16	14.5 [0.57]	0.92
T17	7.2	6	89.0 [20]	7.6 [1.7]	0.09	30.5 [1.2]	1.92
T18	2.2	1	89.0 [20]	32.5 [7.3]	0.36	12.7 [0.5]	0.79
T19	2.2	1	89.0 [20]	26.2 [5.9]	0.29	14.2 [0.56]	0.89
T20	4.2	3	89.0 [20]	13.8 [3.1]	0.15	18.3 [0.72]	1.15
T21	7.2	6	89.0 [20]	7.6 [1.7]	0.09	30.5 [1.2]	1.92
T22	2.2	1	170.4 [38.3]	48 [10.8]	0.28	11.4 [0.45]	0.73
T23	4.2	3	170.4 [38.3]	21.8 [4.9]	0.13	8.3 [0.73]	1.17
T24	2.2	1	97.9 [22]	75.2 [16.9]	0.77	41.7 [1.64]	2.62
T25	4.2	3	89.0 [20]	42.3 [9.5]	0.48	17.8 [0.7]	1.12
T26	4.2	na	89.0 [20]	77 [17.3]	0.86	28.2 [1.11]	1.78
T27	3.6	na	89.0 [20]	47.6 [10.7]	0.54	32.5 [1.28]	2.04
T28	4.2	3	89.0 [20]	40.5 [9.1]	0.45	20.8 [0.82]	1.31

na = not applicable, ERR = error in data acquisition, DNF = did not fail AN = Above Nut, BN = Below Nut, CS = Concrete Surface

Table 2.11 Eccentric shear test matrix by Mcbride (2014)

Set	d_a (mm [in.])	Hole size (mm [in.])	n	Connecit ion Typeb	Top Nut tightnessc	$\frac{l_s}{d_a}$	$\frac{l_e}{d_a}$	Load type	Load ecc.e (mm [in.])
ES1	16 [0.625]	21 [0.81]	2	U	FT	1.2	0	TS	135 [5.3]
ES2	16 [0.625]	21 [0.81]	2	U	FT	2.2	1	TS	150 [5.9]
ES3	16 [0.625]	21 [0.81]	2	U	TOTN	2.2	1	TS	150 [5.9]
ES4	16 [0.625]	21 [0.81]	2	U	TOTN	2.2	1	TS	150 [5.9]
ES5	16 [0.625]	21 [0.81]	2	U	FT	4.2	3	TS	168 [6.6]
ES6	16 [0.625]	21 [0.81]	2	U	TOTN	2.2	1	TS	302 [11.9]
ES7	16 [0.625]	21 [0.81]	2	U	TOTN	2.2	1	TS	455 [17.9]
ES8	16 [0.625]	21 [0.81]	2	U	TOTN	4.2	3	TS	455 [17.9]
ES9	16 [0.625]	21 [0.81]	2	U	FT	2.2	1	TS	577 [22.7]
ES10	16 [0.625]	21 [0.81]	2	U	TOTN	2.2	1	TS	577 [22.7]
ES11	16 [0.625]	21 [0.81]	2	U	FT	4.2	3	TS	607 [23.9]
ES12	16 [0.625]	21 [0.81]	2	U	TOTN	2.2	1	TS	607 [23.9]
ES13	16 [0.625]	21 [0.81]	2	U	FT	2.2	1	CS	135 [5.3]
ES14	16 [0.625]	21 [0.81]	2	U	FT	4.2	3	CS	168 [6.6]
ES15	16 [0.625]	21 [0.81]	2	U	TOTN	4.2	3	CS	305 [12]

ES16	16 [0.625]	21 [0.81]	2	U	TOTN	2.2	1	CS	610 [24]
ES17	16 [0.625]	21 [0.81]	2	U	FT	2.2	1	CS	607 [23.9]
ES18	16 [0.625]	21 [0.81]	2	U	TOTN	4.2	3	CS	610 [24]
ES19	16 [0.625]	21 [0.81]	2	U	FT	4.2	3	CS	607 [23.9]
ES20	16 [0.625]	21 [0.81]	2	U	FT	4.2	3	CS	610 [23.9]
ES21	16 [0.625]	21 [0.81]	4	U	TOTN	4.2	3	TCS	138 [7.2]
ES22	16 [0.625]	21 [0.81]	4	U	TOTN	4.2	3	TCS	607 [23.9]
ES23	16 [0.625]	21 [0.81]	2	G	TOTN	1.2	0	TS	135 [5.3]
ES24	16 [0.625]	21 [0.81]	2	G	TOTN	2.2	1	TS	150 [5.9]
ES25	16 [0.625]	21 [0.81]	2	G	TOTN	4.2	3	TS	183 [7.2]
ES26	16 [0.625]	21 [0.81]	2	G	TOTN	2.2	1	TS	607 [23.9]
ES27	16 [0.625]	21 [0.81]	2	G	TOTN	4.2	3	TS	607 [23.9]
ES28	16 [0.625]	21 [0.81]	2	G	TOTN	2.2	1	CS	150 [5.9]
ES29	16 [0.625]	21 [0.81]	2	G	TOTN	2.2	1	CS	607 [23.9]
ES30	16 [0.625]	21 [0.81]	2	G	TOTN	2.2	1	CS	607 [23.9]
ES31	16 [0.625]	21 [0.81]	4	G	TOTN	4.2	3	TCS	610 [24]
ES32	16 [0.625]	21 [0.81]	4	G	TOTN	4.2	3	TCS	610 [24]

bU = Ungrouted stand-off base plate with leveling nut, G = Grouted stand-off base plate,

cFT = Finger-Tightened, TOTN = Turn-of-the-Nut

eMeasured to the top of the concrete surface

Table 2.12 Summary of eccentric shear ultimate load and displacement results by Mcbride (2014)

Set	$\frac{l_s}{d_a}$	$\frac{l_{ea}}{d_a}$	n	Load type	Eff. Ecc. [in]	T_u [kips]	P_u [kips]	$V_{u,test}$ [kips]	$T_{u,test}$ [kips]	δ_u [in.]	$\frac{\delta_u}{d_a}$
ES1	1.2	0	2	TS	5	20	22.9	11.4	4.8	0.64	1.02
ES2	2.2	1	2	TS	5.3	20	12.6	6.3	2.8	0.58	0.93
ES3	2.2	1	2	TS	5.3	20	16.7	8.3	3.7	0.65	1.05
ES4	2.2	1	2	TS	5.3	20	13.9	7	3.1	0.64	1.02
ES5	4.2	3	2	TS	5.3	20	6.7	3.4	1.5	0.91	1.45
ES6	2.2	1	2	TS	11.3	20	14.5	7.3	6.8	0.79	1.27
ES7	2.2	1	2	TS	17.3	20	16.8	8.4	12.2	0.94	1.5
ES8	4.2	3	2	TS	16.7	20	18.2	9.1	12.7	1.72	2.75
ES9	2.2	1	2	TS	22.1	20	18.8	9.4	17.3	1.01	1.62
ES10	2.2	1	2	TS	22.1	20	18.9	9.4	17.4	0.91	1.46
ES11	4.2	3	2	TS	22.7	20	18.6	9.3	17.6	1.39	2.23
ES12	2.2	1	2	TS	23.3	20	19.6	9.8	19	1.38	2.21
ES13	2.2	1	2	CS	4.7	20	12.1	6.1	-2.4	0.61	0.97
ES14	4.2	3	2	CS	5.3	20	6.3	3.2	-1.4	0.53	0.84
ES15	4.2	3	2	CS	10.7	20	5	2.5	-2.2	0.52	0.82
ES16	4.2	3	2	CS	17.9	20	5.2	2.6	-3.9	0.3	0.48
ES17	2.2	1	2	CS	23.3	20	ERR				
ES18	2.2	1	2	CS	23.3	20	11	5.5	-10.7	0.3	0.48
ES19	4.2	3	2	CS	22.7	20	4.6	2.3	-4.4	0.46	0.74
ES20	4.2	3	2	CS	22.7	20	4.7	2.3	-4.4	0.37	0.6
ES21	4.2	3	4	TCS	5.9	20	11.4	2.9	-2.8	0.52	0.84
ES22	4.2	3	4	TCS	22.7	20	9	2.3	8.5	0.7	1.11
ES23	1.2	0	2	TS	4.3	20	22.5	11.2	4	0.36	0.58
ES24	2.2	1	2	TS	4.3	20	24.2	12.1	4.3	0.15	0.23
ES25	4.2	3	2	TS	4.3	20	31.5	15.7	5.6	1.3	2.08
ES26	2.2	1	2	TS	22.3	20	15.2	7.6	14.1	0.63	1.01
ES27	4.2	3	2	TS	21	20	16.4	8.2	14.3	1.25	1.99

ES28	2.2	1	2	CS	4.3	20	28.4	14.2	-5	0.79	1.26
ES29	2.2	1	2	CS	22.3	20	DNF				
ES30	2.2	1	2	CS	22.3	20	20.8	10.4	-19.2	0.91	1.45
ES31	4.2	3	4	TCS	3	20	40.1	10	2.5	0.86	1.37
ES32	4.2	3	4	TCS	21	20	24.7	6.2	21.6	0.26	0.42

na = not applicable, ERR = error in data acquisition, DNF = did not fail.

Chapter 3 Equations of Shear Capacity of Stand-off Anchors

3.1 Recommendations by ACI 318 (2014)

ACI 318-14 does not directly consider the impact of exposure length of anchor on its shear capacity in stand-off installations. Specifically, Section 17.5.1.2 (b) stipulates the shear capacity of a cast-in headed bolt, hooked bolt anchor, and post-installed anchor,

$$V_{sa} = 0.6A_{se,V}f_{uta}, \tag{3.1}$$

where $A_{se,V}$ is the effective cross-sectional area of an anchor in shear, in.^{2}, and f_{uta} shall not be taken greater than the smaller of $1.9f_{ya}$ and 861.8 MPa [125 ksi]. In addition, when grout pads are present, Section 17.5.1.3 indicates that the shear capacity in Eq. 3.1 shall be reduced by a factor of 0.80.

3.2 Recommendations by AASHTO (2017)

AASHTO (2017) section 6.13.2.7 provisions the nominal shear resistance of a high-strength bolt (ASTM F3125) or an ASTM A307 bolt (Grade A or B) at the strength limit state in joints whose length between extreme fasteners measured parallel to the line of action of the force is less than 965 mm [38.0 in.] shall be taken as:

Where threads are excluded from the shear plane:

$$V_{sa} = 0.56A_sf_{uta}, \tag{3.2}$$

where: A_s = area of the anchor rod corresponding to the nominal diameter;

Where threads are included in the shear plane:

$$V_{sa} = 0.45A_sf_{uta}. \tag{3.3}$$

The nominal shear resistance of a bolt in lap splice tension connections greater than 965 mm [38.0 in.] in length shall be taken as 0.83 times the value given by Eqs. 3.2 or 3.3. If the threads of a bolt are included in the shear plane in the joint, the shear resistance of the bolt in all shear planes of the joint shall be the value for threads included in the shear plane. For ASTM A307 bolts, shear design shall be based on Eq. 3.3. When the grip length of an ASTM A307 bolt exceeds 5.0 diameters, the nominal resistance shall be lowered one percent for each 1/16 in. of grip in excess of 5.0 diameters.

AASHTO (2017) section 6.13.2.12 specifies the nominal shear resistance of ASTM F1554 anchor rod with one shear planes at the strength limit state shall be taken as:

$$V_{sa} = 0.5A_sf_{uta}. \tag{3.4}$$

Eq. 3.4 assumes threads are included in the shear plane since the thread length of anchor rods is not limited by the specification.

AASHTO (2017) does not provide guidance on designing anchor bolt steel strength for ungrouted or grouted stand-off base plates. AASHTO (2013) 5.17.4.3, however, when the clearance between the bottom of the leveling nuts and the top of the concrete foundation exceeds one bolt diameter, bending stresses in the anchor bolts should be considered. Within the commentary, it is stated that bending moments developing in the anchor bolt from shear forces may be determined by modeling a doubly moment-restraining beam with length equal to the distance between the concrete surface and the bottom of the leveling nut. Stresses due to bolt bending are added to the tensile stress

component of the elliptical interaction relationship provided in Eq. 3.5 (or the compressive stresses in a similar compression/shear interaction).

$$\left(\frac{f_v}{f_{uva}}\right)^2 + \left(\frac{f_t}{f_{uta}}\right)^2 \leq 1.0, \tag{3.5}$$

where

f_v = factored shear stress

f_{uta} = ultimate tensile strength of anchor steel

f_{uva} = ultimate shear strength of anchor steel = $0.6f_{uta}$

f_t = factored tensile stress from both axial bolt tension and bolt bending

The commentary states explicitly that bending stresses in individual bolts can be ignored if the stand-off distance between the top of the foundation and bottom of the leveling nut is less than one bolt diameter. For larger standoff distances, the following beam model should be used. The bending moments in the anchor bolt can be determined using a beam model fixed at the top of the concrete foundation and free to displace laterally but not rotate at the bottom of the leveling nut.

When grout pads are present, AASHTO 5.17.3.3 (2013) states grout shall not be considered as a load-carrying element in double-nut connections.

3.3 Recommendations by CEB Design Guidelines (2008)

Unlike the design codes in ACI 318-08 using a constant reduction factor, the CEB guidelines (2008) for anchor design assume that the failure of an exposed anchor in shear is controlled by plastic yielding of the anchor under bending based on Scheer et al. (1987).

Scheer et al. (1987) carried out an analytical investigation based on bending action of anchors bolts with an exposed length (lever arm) of l_{ee}. The bending moment of the bolts having both ends fixed was derived as:

$$M_u^0 = \frac{V_{sa} l_{ee}}{2}, \text{ and} \tag{3.6}$$

$$M_u^0 = 1.7 S f_{ya} \tag{3.7}$$

where, M_u^0 is the ultimate bending moment (or full plastic bending moment) at fixed end of anchor shaft. V_{sa} is the shear strength of anchor shaft. S is the section modulus of the anchor calculated from the net tensile area, and f_{ya} is the measured yield stress of anchor bolts in tension. Hence, the shear capacity was derived as

$$V_{sa} = 2\frac{1.7 S f_{ya}}{l_{ee}}. \tag{3.8}$$

The background of these provisions was well described in Eligehausen *et al*. (2006).

In the CEB guidelines, the shear strength of an anchor with an exposed length (or lever arm) is defined as.

$$V_{sa} = \alpha_M \left(\frac{M_u}{l_{ee}}\right) \tag{3.9}$$

where α_M= 2.0 for cases where the baseplate is not allowed to rotate while α_M= 1.0 for free end rotation. M_u is defined as

$$M_u = M_u^0\left(1 - {}^{T}/_{T_u}\right) \tag{3.10}$$

where: T is the applied tensile force while T_u is the ultimate tension strength of anchor bolt.

The exposed length as a distance from the applied shear force to a fictitious fixed end, as illustrated in Figure 2.2, is defined as

$$l_{ee} = l_{ea} + 0.5d_a \tag{3.11}$$

where, l_{ea} is the distance from the applied shear force to the concrete surface, for anchors having no restraint in the concrete surface, while zero for the case with a limited rotation by a nut.

With the introduction of moment and exposed length into Eq. 3.9, the nominal shear strength of exposed anchor bolt is

$$V_{sa} = \alpha_M \frac{1.7Sf_{ya}}{l_{ee}}\left(1 - {}^{T}/_{T_u}\right) \tag{3.12}$$

Note that the anchor bolts having a grout pad with a compressive strength less than 30 MPa or its thickness larger than 0.5d_a, are treated as exposed anchor bolts and its shear capacity should be derived based on Eq. 3.12. Also, CEB Design guideline (2008) specify that a grout layer thicker than 3 mm [0.12 in.], must be treated as an exposed length (lever arm).

A further explanation of the shear strength of exposed anchor bolts in Eq. (3.9) by Eligehausen *et al*. (2006) showed that it is valid for rotation angles less than ten degrees measured from the non-deformed axis of the anchor to the deformed position. However, the observation from the reinforced anchor tests in current research (Petersen, 2010) indicated that the anchor rotation angle can reach nearly 30 degrees, much beyond the limitation as the Eq. 3.9 requires. In addition, when the exposed length increases, it may introduce tensile stresses to the anchor shaft, thereby leading to a tension-dominant fracture.

In the draft EN 1993-1-8 (Eurocode 3, 2003), Eurocode 3 for column base anchor rod design stipulated the shear strength of anchor based on the experimental and analytical results of column base carried out by Bouwman *et al*. (1989), as documented by Gresnigt *et al*. (2008).

$$V_{sa} = min\left(\alpha_m A_{se,v} f_{uta},\ \alpha_b A_{se,v} f_{uta}\right) \tag{3.13}$$

where, α_m = 0.6 for classes 4.6, and 8.8 grade anchor; α_m= 0.5 for classes 5.8, and 10.9 grade anchor; α_b = 0.44 + 0.0003f_{ya} and f_{ya} is the yield strength of the anchor bolt between 235 MPa [34 ksi] and 640 MPa [93ksi].

Unlike the explicit expression about the effects of exposed length on shear strength of anchor bolt like CEB, the Eurocode 3 model in Eq. 3.13 is developed to account for the effects of bending and tensile force in the bolt due to deflection when the anchor is subjected to shear forces. Such empirical equation, similar to ACI 318-08, provides constant shear strength for anchor bolt with varying exposed length. Obviously, within the range of yield strength of anchor bolt, the α_b varies from 0.25 to 0.37. Introducing α_b into Eq. 3.13 suggested that the shear strength predicted by Eurocode 3 model gives very conservative results, especially when exposed length is relatively short, as compared to ACI 318-08.

3.4 Recommendations being discussed by *fib* TG2.9 (2018)

Recent *fib* meeting changed the formula for calculating shear resistance of bolts with exposed length. The newest formula as follow:

$$V_{sa} = \left(\sqrt{\alpha_{sm}^2 + 1} - \alpha_{sm}\right)V_s \tag{3.14a}$$

where V_s is the characteristic shear resistance for lever arm equal to zero taken from $V_s = 0.5A_s f_{tua}$, in which A_s is cross-sectional area of steel; $\alpha_{sm} = 1.67\frac{l_{ee}}{\alpha_M d_a}$, in which $l_{ee} = 0.5d_a + l_{ea}$, and α_M depends on the degree of restraint of the anchor at the side of the fixture of the application in question and should be determined according to good engineering practice. Single curvature of the bolt ($\alpha_M = 1.0$) should be assumed if the fixture can rotate freely (see Figure 3.1a), $\alpha_M = 1.0$ should be assumed if the conditions for double curvature are not met. Double curvature of the bolt $\alpha_M = 2.0$ may be assumed only if the fixture cannot rotate (see Figure 3.1b) and either. (1) the anchor is welded to, or threaded into the fixture, or (2) is clamped by prestressing the anchor with nuts and washers. If restrain of the anchor is assumed, the fixture and/or the anchored element should be able to take up the restraining moment. Eq. (3.14a) can be rewritten to

$$V_{sa} = \left(\sqrt{\left(1.67\frac{0.5d_a + l_{ea}}{\alpha_M d_a}\right)^2 + 1} - 1.67\frac{0.5d_a + l_{ea}}{\alpha_M d_a}\right)0.5A_s f_{tua} \tag{3.14b}$$

The derivation of Eq. 3.14b proposed by *fib* TG2.9 is briefly explained here.

The direct solution for the characteristic shear steel resistance for an anchor loaded by a shear force with lever arm, V_{Sa}, is based on the interaction equation presented in McBride (2014) (Eq. 3.15a), and the fact that M_{Sd} is directly related to V_{Sa} by Eq. 3.15b:

$$\left(\frac{V_{Sa}}{V_s}\right)^2 + \frac{M_{sa}}{M_s^0} \leq 1.0 \tag{3.15a}$$

$$M_{sa} = \frac{l_{ee}}{\alpha_M d_a} \tag{3.15b}$$

With the definition of $M_{Rk,s}^0$, based on Scheer et al. (1987):

$$M_s^0 = 1.5W_{el}f_{ya} \tag{3.15c}$$

Where $W_{el} = A_s\frac{d_a}{8}$, and $f_{ya} \approx 0.8f_{uta}$.

Eq. (15d) can be rewrite to

$$\left(\frac{V_{Sa}}{V_s}\right)^2 + \left(3.33\frac{l}{\alpha_M d_a}\right)\frac{V_{Sa}}{V_s} = 1.0 \tag{3.15d}$$

The direct solution of Eq. (3.15d) yields solutions such as formula (3.14a). It should be noted that l_{ea} in Equation (3.14b) is the stand-off height or the distance from the bottom of a leveling nut to concrete surface, which is the same as the apparent exposed length (l_{ea}) as defined in Figure 1.1. In addition, $0.5d_a$ accounts for the additional exposed length from crushed concrete, as shown in Figure 3.1. Although tests by Mcbride (2014) supports this additional exposed length; this study focused on the additional exposed length due to concrete crushing (l_{ec} as defined in Figure 1.1).

3.5 Recommendations by Lin *et al.* (2011)

Lin et al. (2011) conducted experimental investigation on the shear capacity of anchor rods with an exposed length using double-shear tests. A formula for calculating the shear resistance of anchors with exposed length has been proposed. For the anchor with short exposed length ($l_{ee} \leq 0.5d_a$), the ultimate shear strength, V_{sa}, may be estimate by

$$V_{sa} = \frac{f_{ya}}{\frac{1}{0.9A_{se,V}} + \frac{l_{ee}}{3.4S}}, \tag{3.16}$$

where f_{ya} is yield strength of anchor steel, S is section modulus of the anchor shaft corresponding to the net tensile area.

For the anchor with an effective exposed length larger than 0.5 times diameter of bolt, anchor shafts may deform significantly under shear loading such that tension contributes to the ultimate shear strength

$$V_{sa} = f_{ya}A_{se,V}sin(\beta) + \frac{f_{ya}cos(\beta)}{\frac{1}{0.9A_{se,V}} + \frac{l_{ee}}{3.4S}}, \tag{3.17a}$$

where S = Section modulus of the anchor shaft corresponding to the net tensile area. So, Eq. 3.17a can be rewritten as

$$V_{sa} = f_{ya}A_{se,V}sin(\beta) + \frac{f_{ya}cos(\beta)}{\frac{1}{0.9A_{se,V}} + \frac{40l_{ee}}{17d_{ae}A_{se,V}}}, \tag{3.17b}$$

Where d_{ae} is the effective anchor diameter, β is the rotation of the exposed anchor with respect to the initial undeformed shape. The rotation angle β at failure is related to the initial end rotations, the exposed length relative to the anchor diameter, and the plastic deformation capability of the anchor steel. The ultimate plastic rotation angle of an exposed anchor may be estimated using the plastic hinge concept for ductile flexural members subjected to tension and bending. Author assumed that the plastic rotation is uniform within the plastic hinge, hence the plastic end rotation can be estimated as the maximum curvature multiplied by the plastic hinge length. the maximum curvature φ at of a section can be estimated using the maximum tensile strain ε_{max} that can be developed in the anchor steel and the anchor diameter d_a,

$$\varphi = tan^{-1}\frac{\varepsilon_{max}}{d_a} \tag{3.18}$$

The rotation angle of the exposed anchor is thus the exposed anchor is thus the summation of the end rotation and the plastic rotation,

$$\beta = \theta + l_p tan^{-1}\frac{\varepsilon_{max}}{d_a}, \tag{3.19}$$

where θ is the initial end rotation allowed by the oversized holes and/or concrete deformation, l_p is the length of plastic hinge and may be taken as d_a, but should be larger than $l_p/2$ for anchor with exposed lengths short than $2d_a$.

Note that l_{ee} in Eqs. 3.17a and 3.17b should be the effective exposed length (l_{ee}) as defined in Figure 1.1. In addition, the first term in the equations accounts for the contribution of tensile capacity when the stand-off height is large such that the anchor shaft may deform significantly in the lateral direction, and the deformed anchor shaft may eventually fail in tensile fracture as

supported by the double shear tests by the authors. For anchors with a small stand-off height, the anchor rotation (β) may be small and the tensile contribution ($f_{ya}A_{se,V}sin(\beta)$) can be negligible.

3.6 Recommendations by Cook *et al.* (2013)

According to the statements by AASHTO, Cook *et al.* (2013) provide a conservative interpretation of the method, as shown in Eqs. 3.20 through 3.27, to calculate the shear force of an individual bolt in annular base plates.

$$\left(\frac{f_{t,1}+f_{t,2}}{F_t}\right)^2+\left(\frac{f_v}{F_v}\right)^2 \le 1 \tag{3.20}$$

$$f_{t,1}=\frac{M_{group}}{S_{group}}+\frac{N_{group}}{n\cdot A_{se}} \tag{3.21}$$

$$S_{group}=\frac{n\cdot r_{group}}{2} \tag{3.22}$$

$$f_{t,2}=\frac{m_2}{Z_{bolt}} \tag{3.23}$$

$$m_2=\frac{V_{bolt}l_{ea}}{2} \tag{3.24}$$

$$V_{bolt}=\frac{V_{group}}{n}+\frac{T_{group}}{r_{group}\cdot n} \tag{3.25}$$

$$V_{sa}=f_{tua}\sqrt{\frac{1}{\frac{l_{ea}^2}{4Z_{bolt}^2}+\frac{1}{0.36A_{se}^2}}}, \tag{3.26a}$$

where $f_{t,1}$ is defined as the individual bolt tensile stress from global equilibrium, conservatively assumed to be oriented perpendicular to the axis of overturning moment, $f_{t,2}$ is individual bolt tensile stress produced by bolt bending over the exposed length, M_{group} is the overturning moment, N_{group} is the axial force, T_{group} is the torsion within a group, S_{group} is the section modulus of bolt positioned for maximum global moment-induced tension, r_{group} is the radius of bolt group.

n is number of bolts in the group; m_2 is bolt-level moment produced by V_{bolt} acting over l_{ea}; Z_{bolt} is plastic section modulus of the bolt $=\frac{d_{ae}^3}{6}$. Therefore, Eq. 26a can also be written to

$$V_{sa}=f_{tua}\sqrt{\frac{1}{\frac{9l_{ea}^2}{d_{ae}^6}+\frac{1}{0.36A_{se,V}^2}}}, \tag{3.26b}$$

where d_{ae} is the effective diameter of anchor bolt.

For grouted base plates, the shear resistance can predict by

$$V_{sa}=0.48A_{se,V}f_{uta} \tag{3.27}$$

The equations for calculating the shear bearing capacity of bolts in various codes and researchers are summarized in Table 3.1.

3.7 Recommendations by McBride (2014)

McBride attempted to determine the lower and upper limits of the bearing capacity of anchors under the combined action of normal force, bending moment and shear force.

For anchor bolt with ungrouted base plate, when the anchor bolt experiencing pure shear, the predictive equations for the upper limit and lower-bound are given by Eq. 3.28 and 3.29 by ignoring the normal force, respectively,

$$\left(\frac{\rho_{NV}V_{sa}/(N_0)}{\sqrt{1-\frac{V_{sa}l_{ee}}{2f_{uta}Z_{bolt}}}}\right)^2+\left(\frac{V_{sa}/(V_0)}{\sqrt{1-\left(\frac{V_{sa}l_{ee}}{2f_{uta}Z_{bolt}}\right)^2}}\right)^2=1, \tag{3.28a}$$

or alternatively,

$$V_{sa}=\sqrt{\frac{1}{\frac{1}{V_0^2}+\left(\frac{l_{ee}}{2f_{uta}Z_{bolt}}\right)^2}}=f_{uta}\sqrt{\frac{1}{\frac{1}{0.36A_{se,V}^2}+\frac{l_{ee}^2}{4Z_{bolt}^2}}}. \tag{3.28b}$$

The equation was from a three-variable interaction equation considering the normal force, bending moment and shear force,

$$\left(\frac{\rho_{NV}V_{sa}}{N_0}\right)^2+\left(\frac{V_{sa}}{V_0}\right)^2+\frac{V_{sa}l_{ee}}{2f_{uta}Z_{bolt}}=1 \tag{3.29}$$

where V_{sa} is applied shear force, V_0 is ultimate shear capacity of circular section, f_{uta} is ultimate normal stress capacity of bolt material, Z_{blot} plastic section modulus of circular section, and ρ_{NV} is the ratio of applied normal to shear force; In case of anchors subjected to shear only, $\rho_{NV}=\frac{l_{ee}}{\delta_h}$.

For anchor bolt with grouted base plate, the shear force may influent by the friction between the grouted pad surface and steel plate, thus the equation of applied shear force is as follows,

$$\left(\frac{\frac{V_{sa}l_{ee}}{\delta_h}}{N_0}\right)^2+\left(\frac{V_{sa}\left(1-\mu\frac{l_{ee}}{\delta_h}\right)}{V_0}\right)^2=1 \tag{3.30a}$$

or alternatively,

$$V_{sa}=f_{uta}A_{se,v}\sqrt{\frac{1}{\left(\frac{l_{ee}}{\delta_h}\right)^2+\left(\frac{1-\mu\frac{l_{ee}}{\delta_h}}{0.6}\right)^2}}, \tag{3.30b}$$

where δ_h is horizontal bolt displacement, N_0 is normal strength capacity of anchor bolt, μ is least coefficient of friction in horizontal force transfer.

3.8 Summary of Design Recommendations

Most equations in Table 3.1 consider the tension(moment)-shear interaction acting on an anchor shaft. The bending moment resulted from the applied shear in most design equations is based on

the apparent exposed length (l_{ea}), which is the distance from the concrete surface to the bottom of leveling nut/base plate as shown in Figure 3.1. An additional length of $0.5d_a$, below concrete surface, is included in the equation by *fib* Task Group TG2.9. This additional length (a_3 (l_{ec}) in Figure 3.1) may be viewed as the crushed concrete depth (l_{ec}) as defined in Chapter 1. The equation by Lin *et al*. (2011) use the effective exposed length (l_{ee}) because the equations were based on double shear tests of threaded rods. In addition, the first term of Eqs. 3.17a and 3.17b accounts for the contribution of tension, resulted from severely deformed anchor shafts, especially for those with a large stand-off height, in which case, anchors subjected to shear may be controlled by tension fracture (Petersen 2010).

The main difference is the exponent used in the interaction equations. Specifically, the exponent in Lin *et al*. (2011) is 1.0 for both tension and shear while the exponent in AASHTO (2013) and Cook *et al*. (2013) is 2.0, as illustrated in Figure 3.2. McBride (2014) used an exponent of 1.0 for shear and 2.0 for tension (moment). The proposed interaction equation by *fib* Task Group TG2.9 is roughly 1.0 for the moment contribution and 2.0 for the shear contribution, indicating that the stand-off anchors are mainly controlled by bending moments, which is similar to the early equation by CEB guidelines (2008).

These equations are summarized in Figure 3.3. Note that the X-axis is the apparent exposed length which is different from that required by the equations by Lin *et al*. (2011). In general, the anchor shear capacity decreases with an increase in the stand-off height or the exposed length. The predictions do not differ much, especially when then apparent exposed length is between 1.5 and $4.0d_a$. The shear capacity of stand-off anchors without a grouting pad can be as low as 20 percent of that stipulated by ACI 318-14. The equations by Lin *et al*. (2011) consider tension-shear-moment interaction when the stand-off height is large, which allows proper prediction of capacity increase for anchors with stand-off heights beyond $4.0d_a$, as shown in the tests of 19-mm [3/4 in.] anchors by Petersen (2010).

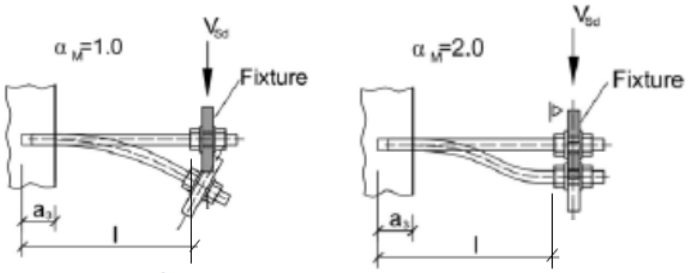

(a) single-curvature bending; (b) double-curvature bending

Figure 3.1 The effect of end constraint on deformed anchors shaft in shear

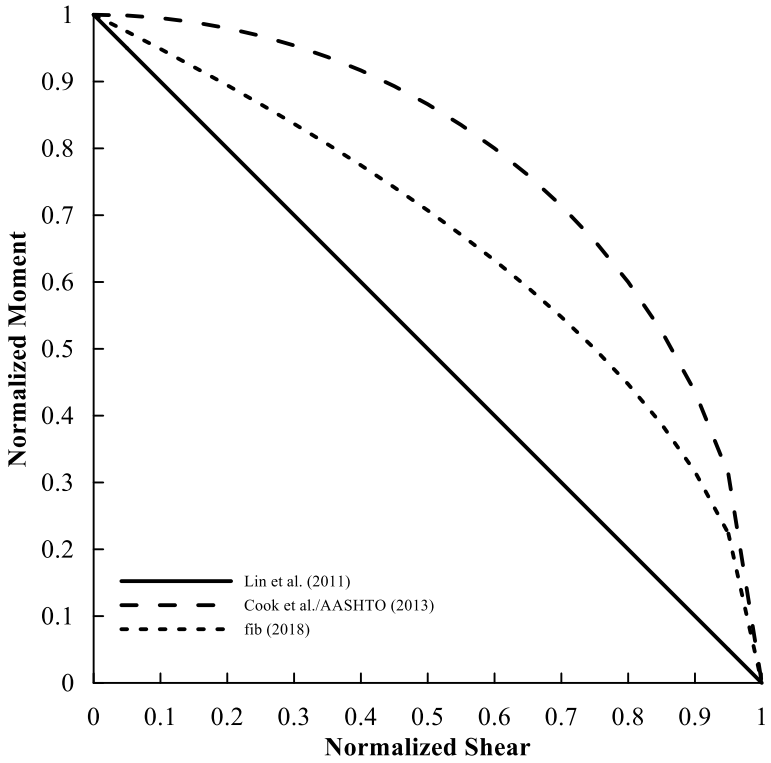

Figure 3.2 Illustration of moment-shear interaction used in design equations

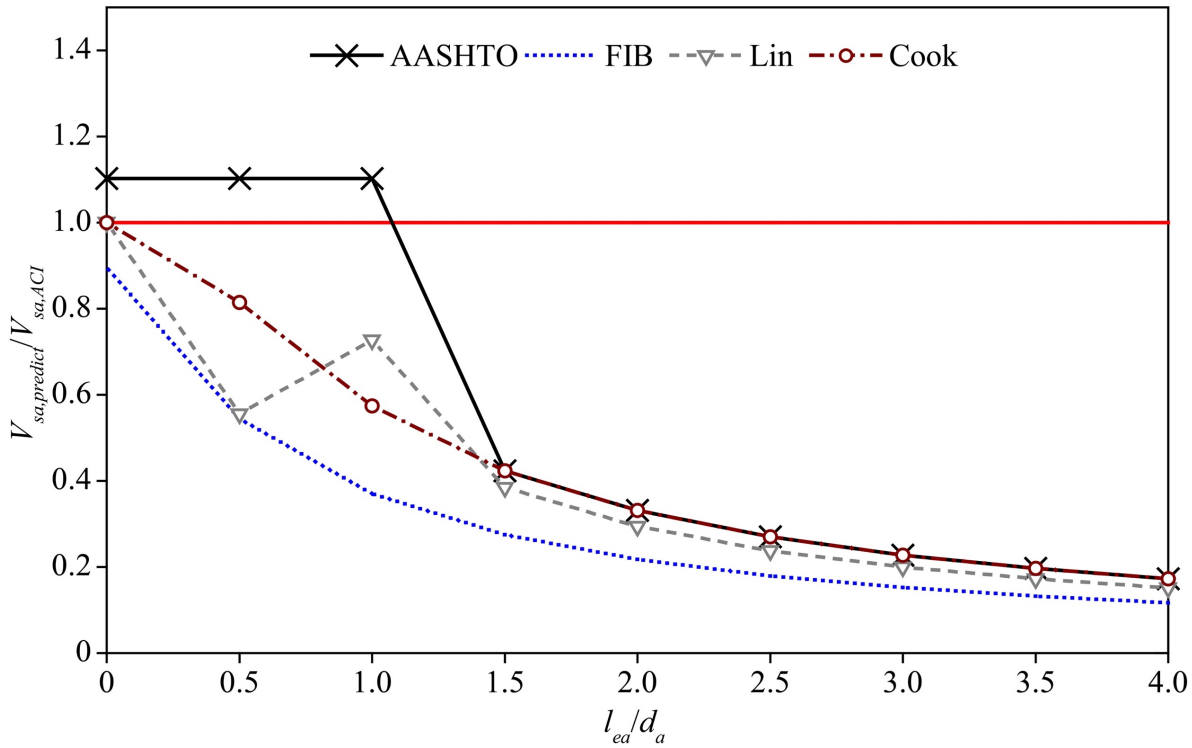

Figure 3.2 Comparison of capacity prediction equations

Table 3.1 Summary of shear strength of stand-off anchor bolts

Equations	Proposer
$V_{sa} = 0.6A_{se,V}f_{tua}$; $V_{sa} = 0.48A_{se,V}f_{tua}$ (with grounted base plate)	ACI
$V_{sa} = 0.6A_{se,V}f_{tua}$ When the clearance between the bottom of the leveling nuts and the top of the concrete foundation exceeds one bolt diameter, bending stresses in the anchor bolts should be considered. (no direct equation provided) $V_{sa} = f_{tua}\sqrt{\frac{1}{\frac{9l_{ea}^2}{d_{ae}^6} + \frac{1}{0.36A_{se,V}^2}}}$	AASHTO (2013)
$V_{sa} = \left(\sqrt{\left(1.67\frac{0.5d_a + l_{ea}}{\alpha_M d_a}\right)^2 + 1} - 1.67\frac{0.5d_a + l_{ea}}{\alpha_M d_a}\right)0.5A_s f_{tua}$	*fib* TG2.9 (2018)
When $l_e \leq 0.5d_a$: $V_{sa} = \frac{f_{ya}}{\frac{1}{0.9A_{se,V}} + \frac{l_{ee}}{3.4S}}$ When $l_e > 0.5d_a$: $V_{sa} = f_{ya}A_{se,V}sin(\beta) + \frac{f_{ya}cos(\beta)}{\frac{1}{0.9A_{se,V}} + \frac{l_{ee}}{3.4S}}$	Lin *et al.* (2011)
For ungrouted base plate with an exposed length: $V_{sa} = f_{tua}\sqrt{\frac{1}{\frac{9l_{ea}^2}{d_{ae}^6} + \frac{1}{0.36A_{se,V}^2}}}$ For ungouted base plate with oversize holes $V_{sa} = f_{tua}\sqrt{\frac{1}{\frac{9l_{ea}^2}{d_{ae}^6} + \frac{1}{0.23A_{se,V}^2}}}$ For grouted base plate: $V_{sa} = 0.48A_{se}f_{uta}$	Cook (2013)

For ungrouted base plate with an exposed length: Upper limit: $$V_{sa} = f_{uta}\sqrt{\frac{1}{\frac{1}{0.36A_{se,V}^2} + \frac{l_{ee}^2}{4Z_{bolt}^2}}}$$ Lower-bound $$\left(\frac{V_{sa}}{V_0}\right)^2 + \frac{V_{sa}l_{ee}}{2f_{uta}Z_{bolt}} = 1$$ For grouted base plate with an exposed length: $$V_{sa} = f_{uta}A_{se,v}\sqrt{\frac{1}{\left(\frac{l_{ee}}{\delta_h}\right)^2 + \left(\frac{1-\mu\frac{l_{ee}}{\delta_h}}{0.6}\right)^2}}$$	McBride (2014)

Chapter 4. Review of Experimental Tests

4.1. Experiment design

A few experimental tests were included in this study in order to provide reference behavior for the calibration of finite element analyses in Chapter 5. These unpublished tests were conducted by Dr. Zhibin Lin using the specimens created by Petersen (2010). A total of 12 single cast-in anchors were available in four concrete blocks, including six under monotonic shear and six under cyclic shear in either load-controlled or displacement-controlled loading. The tests under monotonic shear are included in this chapter while the observed behavior is documented in Appendix I in details. As shown in Figure 4.1, the cast-in anchors consisted of a 19 mm [0.75 in.] diameter ASTM F1554 Grade 55 thread rod and a heavy hex nut at the end. The anchor had a front edge distance of 152 mm [6 in.] and an embedded depth of 152 mm [6 in.]. The side edge distance is 304.8 mm [12 in.] on one side and larger on the other side. According to the shear capacity equations of cast-in anchors in ACI 318-08, steel fracture would control the failure of the anchors at a maximum shear load of 67.7 kN [15.2 kips], which is lower than that corresponding to concrete breakout failure (71.2 kN [16.0 kips]) with the material properties reported below. It was expected that with stand-off heights, the actual shear capacities would be lower than the code stipulated values.

Knowing that the crushed concrete depth (l_{ec}) can be affected by concrete strength (f_c') (Grosser, 2012) and the anchor diameter (d_a) (Gomez *et al*. 2009), this group of tests explored the impact of stand-off height (l_s). Three stand-off heights, 1.5 mm [0.06 in] ($0.08d_a$), 9.5 mm [0.375 in.] ($0.5d_a$), and 19 mm [0.75 in.] ($1.0d_a$), were chosen that were allowed by the geometry of the specimen. anchors with a stand-off height of 1.5 mm [0.06 in] and 9.5 mm [0.375 in.] were tested twice while the anchor with a stand-off height of 19 mm [0.75 in.] was tested one time. Note that 1.5 mm [0.06 in] is about one pitch of the threaded rod, which is basically the minimum distance between the load plate and the concrete surface, which can absolutely eliminate the influence of the concrete surface friction during the hole test without additional tension or special treatment of the concrete surface. In the sixth test, the load plate (shown in Figure 4.1) had zero stand-off height such that the surface friction contributed to its shear capacity. The failure was controlled by concrete breakout at a slightly higher ultimate load.

4.2. Material properties

Ready mixed concrete with a targeted strength of 27.6 MPa [4000 psi] was used. The strength of concrete was derived from three 100×200 mm [4×8 in.] cylinders cured under the same indoor curing condition as the test blocks. The measured compressive strength was 36.5 MPa [5300 psi] at 56 days and 38.6 MPa [5600 psi] at 109 days. The shear tests were conducted roughly three years after the blocks were cast, during which the concrete likely developed higher strengths.

Tensile test was carried out on a coupon made of the ASTM F1554 Grade 55 threaded rod. The measured stress-strain relationship is shown in Figure 4.2. The Young's modulus was estimated as 190.1 GPa [27,571 ksi]. The initial proportional range ends at a stress of 434.4 MPa [63 ksi] and the material does not have an apparent yield plateau; hence the yield strength, 482.7 MPa [70 ksi], was determined at the 0.2% offset strain. The measured ultimate strength was 524 MPa [76 ksi] at a strain near 0.03.

4.3. Test setup and instrumentation

The test setup is illustrated in Figure 4.3 and shown inn Figure 4.4. inserted through a standard 3.2 mm [1/8 in.] oversize hole in the load plate and fixed by a heavy hex nut. In order to eliminate the gap between the hole and the threaded rod, which would create a dead band when the specimen is subjected to cyclic loading, and to prevent the hole wall being permanently damaged by the high-strength threads during testing, a steel sleeve shim (new one for each test, as shown in Figure 4.6b), was inserted between them before each test similar to those used in Lin *et al*. (2011). No additional leveling nut was used under the load plate; hence the stand-off height was the apparent exposed length (l_{ea}).

The shear force was applied by a horizontally mounted MTS Model 244.31, 245-kN [55-kip] actuator with a full stroke of 254 mm [10 in.], which through a specially designed transfer block connected to a reaction frame. Actuator was free to rotate horizontal. In order to make ensure that the actuator could not move downward during test, the swivel head of the hydraulic actuator was braced to eliminate its rotation; hence the test anchors were subjected to double curvature bending, as illustrated in Figure 3.1b. The ball bearing roller between the support and the actuator swivel head caused negligible friction such that the force measured by the actuator load cell was the shear force applied to the test anchors. The thickness of the loading plate was 25.4 mm [1 in.], similar to that by Klingner *et al*. (1982). The reaction was provided by a steel tube with a section of 100×178 mm [4×7 in.], placed in front of the concrete block, and fixed to the strong floor in the lab. The concrete block height was 406.4 mm [16.0 in.], which was determined by 45 degrees stress propagation angle from a 101.6 mm [4 in.] high shear reaction steel beam that ensuring the reaction had no influence on anchor behavior.

4.4. Experimental results

Detailed observations during the tests are documented in Appendix I. The twelve tests were divided into three groups. Group 1 was used to examine the impact of stand-off heights on anchor shear behavior. Four tests were conducted with a stand-off height (l_{ea}) ranging from $0.08d_a$ to $1.0d_a$, where d_a is the anchor diameter (19 mm [3/4 in.]), as shown in Figure 4.5. After the tests, a point chisel was used to remove loose concrete in front of anchor shafts, and the depths of crushed concrete were measured (Figure 4.6a). In this group of tests, the measured crushed concrete depths were 20.6 mm [0.8125 in.], 22.2 mm [0.875 in.], and 23.8 mm [0.9375 in.], for anchors with a stand-off height of $0.08d_a$, $0.50d_a$ and $1.0d_a$, respectively. With an effective exposed length around $2.0d_a$, a 50 percent reduction is expected for the anchor shear capacity.

With a near zero stand-off height, Specimen 08092011-0.08da-MD had a relatively large crushed concrete depth, and the kink as pointed by the arrow in Figure 4.5 indicated that the anchor fracture may have been affected by bending deformation. Note that a load cell to capture the tension in anchor shafts, similar to that used in Cook *et al*. (2013), was not used in this study partly because with bending, measurements from a load cell with a center hole may be affected by such bending deformation (Figure 4.6b). Secondly, the measured shear capacities in this group are higher than those predicted by Lin *et al*. (2011) with the actual effective exposed length, which is defined in Chapter 1 as the stand-off height plus the crushed concrete depth. This indicates that the actual crushed concrete depth as measured in this experimental study may not be l_{ea}, the goal of this study, especially for the numerical study in Chapter 5.

The loading plate was bolted to concrete surface (with the nut snug-tightened) without a stand-off height for Specimen 08092011_0.00da-MD. This resulted in a friction force about 10 kN [2.2 kips] that contributed to the measured shear capacity of this specimen, as shown by the solid lines in Figure 4.5. This in turn indicates that anchors with small stand-off heights (or an effective exposed length less than $0.5d_a$) are not expected to have large reduction in their shear capacities. It is envisioned that the loading plate (or well-constructed grout) may provide additional confinement to concrete such that crushing (and complete loss of lateral support to anchor shaft) may be prevented. Further research with innovative methods for experimental measurements/observation is needed.

To further evaluate the impact of crushed concrete depth to anchor shear capacity, the anchors in Groups 2 and 3 were subjected to three types of cyclic loading (Figures 4.7 and 4.8). The measured load-displacement behavior under monotonic lading is shown in solid lines. The anchor with a stand-off height of $0.08d_a$ (and an effective exposed length of $0.5d_a$) reached at the code-stipulated capacity while the specimen with a stand-off height of $0.50d_a$ (and an effective exposed length of $1.2d_a$) saw a 25 percent capacity reduction. When the cyclic load is controlled by certain peak displacement (three cycles per peak displacement level), the crushed concrete depths did not increase much, hence the ultimate shear capacities were close to those achieved by the anchors under monotonic loading. Within each displacement group, the impact of unrecoverable concrete crushing is shown by the loads achieved in consecutive loading cycles, as shown by dotted lines in Figures 4.7 and 4.8. When the cyclic load is controlled by certain peak loads (CL1-three cycles per peak load level), the crushed concrete depths increased after each loading cycle. This is shown by increased shear displacement required for the anchors to reach at the same shear loads at consecutive loading cycles. Correspondingly, the ultimate shear capacities were lower than those achieved by the anchors under monotonic loading, as shown by the short-dashed lines in Figures 4.7 and 4.8. This observation was further confirmed by the two tests using another load-controlled cyclic loading (CL2-indefinite number of cycles at roughly 75 percent of the measured monotonic loading capacity). The crushed concrete depth further increased (and the total effective exposed length went up to $1.5d_a$). The anchors failed at smaller loads, as shown by the long-dashed lines in Figures 4.7 and 4.8.

Note that only one specimen (08092011_0.5da-CL1) fractured below the concrete surface. This may have been. Due to the fact that when the applied shear forces increased, the inelastic deformation/damage in the anchor shaft accumulated at the same location just below the steel loading plate whereas the crushed concrete depth may have increased such that the location of inelastic deformation at the bottom may have lowered. Considering the fact that with confinement, concrete experiencing large deformation may be able to sustain stresses deep below the concrete surface, the goal of the numerical analyses in Chapter 5 is not the location of steel fracture; instead, it was a suitable “crushed” concrete depth that can be used to predict shear capacity of concrete anchors controlled by steel fracture.

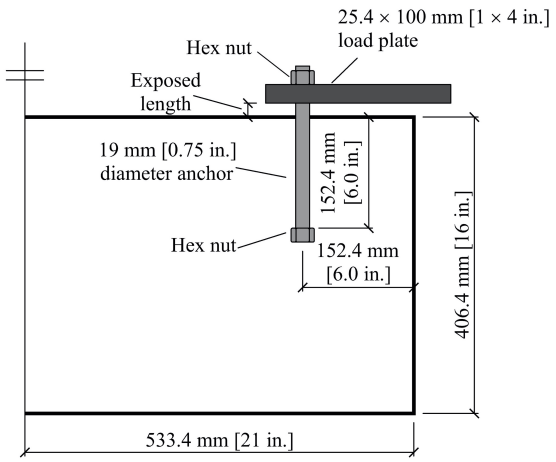

Figure 4.1 Dimension of specimens

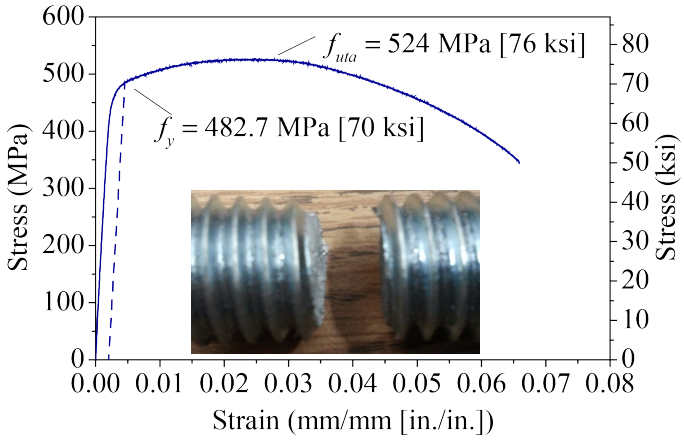

Figure 4.2 Stress–strain behavior of ASTM F1554 Grade 55 threaded rod

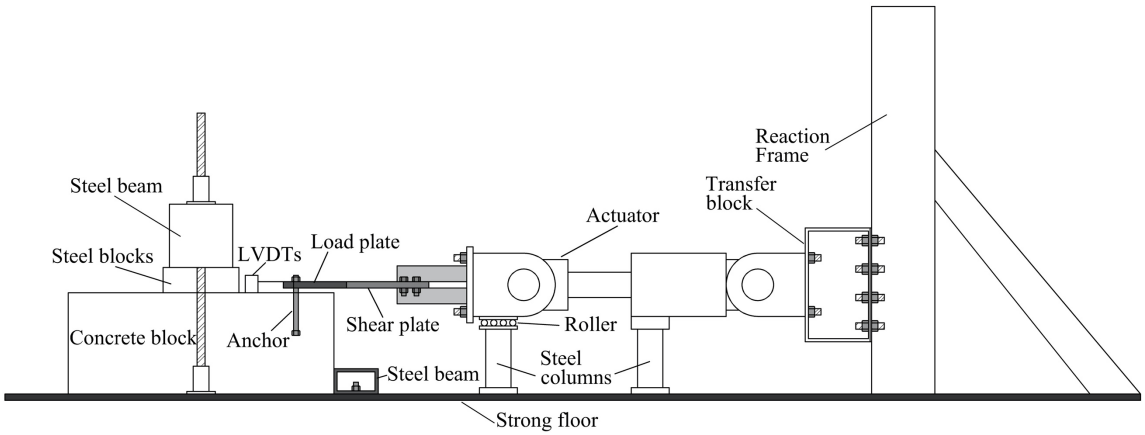

Figure 4.3 Schematic of test setup

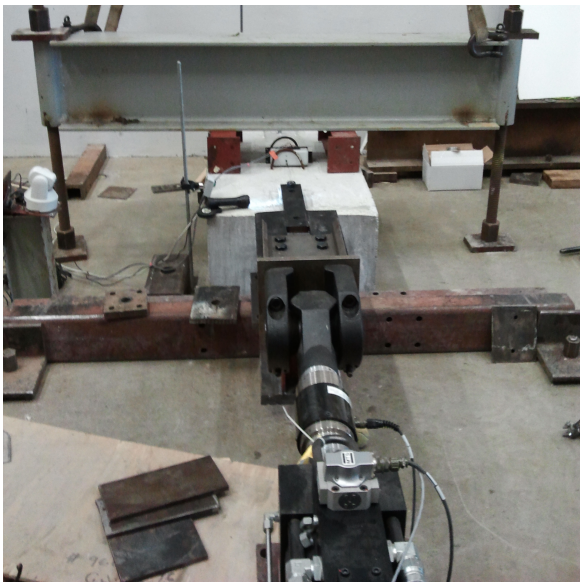

Figure 4.4 Picture of test setup of instrumentation plan

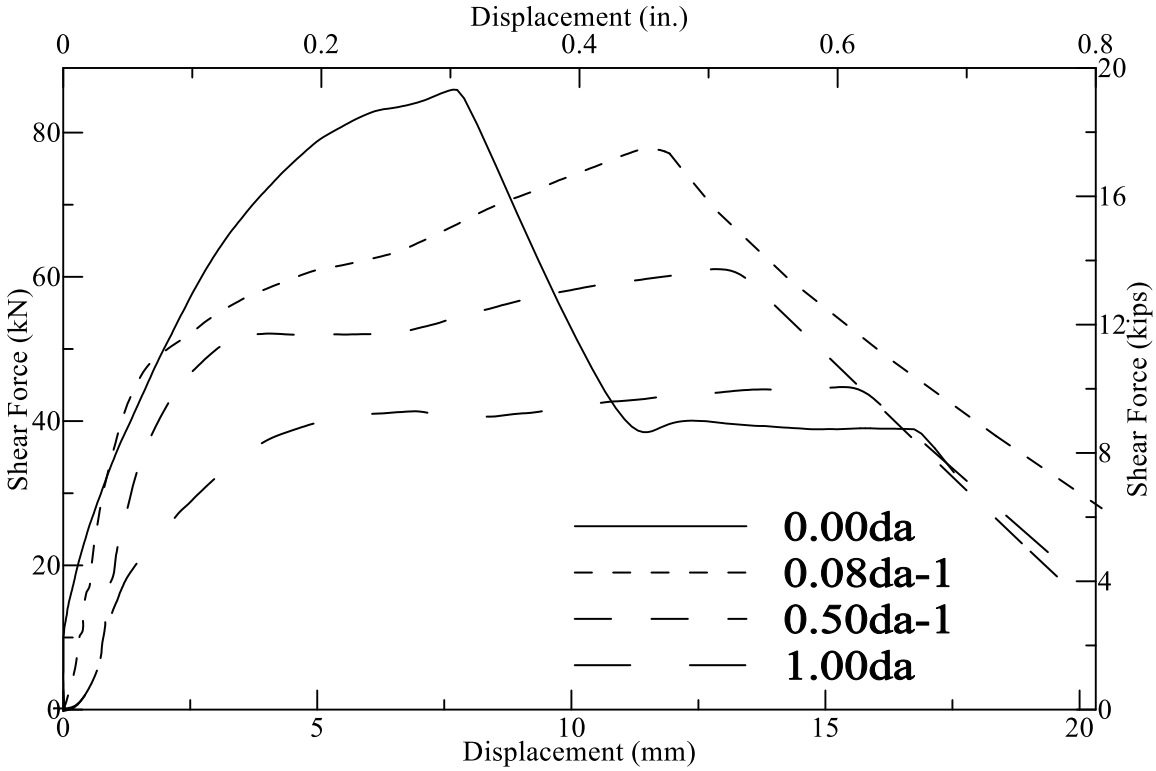

Figure 4.5 Behavior of anchors with different stand-off heights

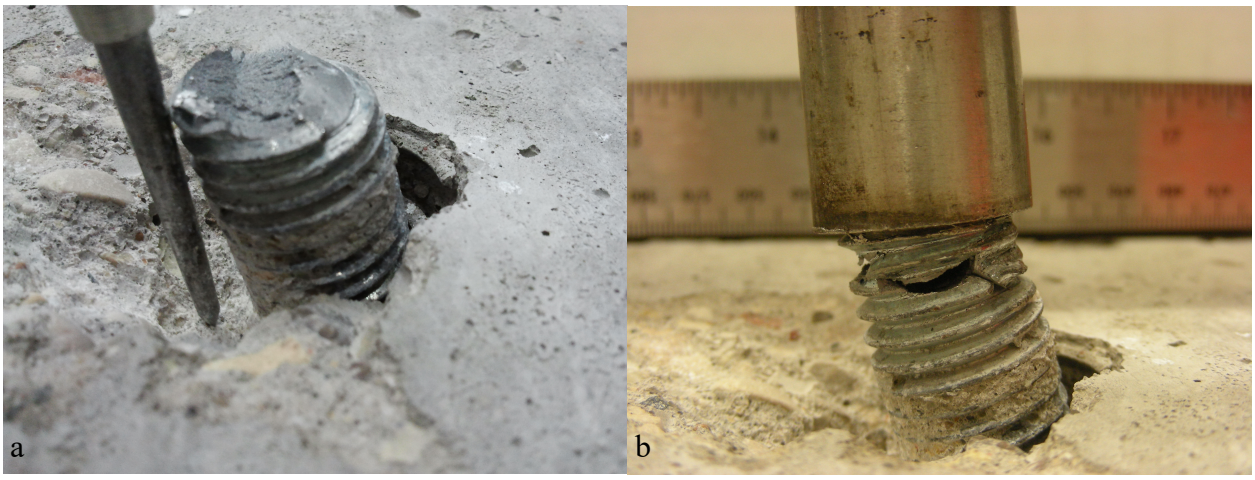

Figure 4.6 Measurement of crushed concrete depth and specimen recovery after tests (Specimen 08092011_0.5da-MD)

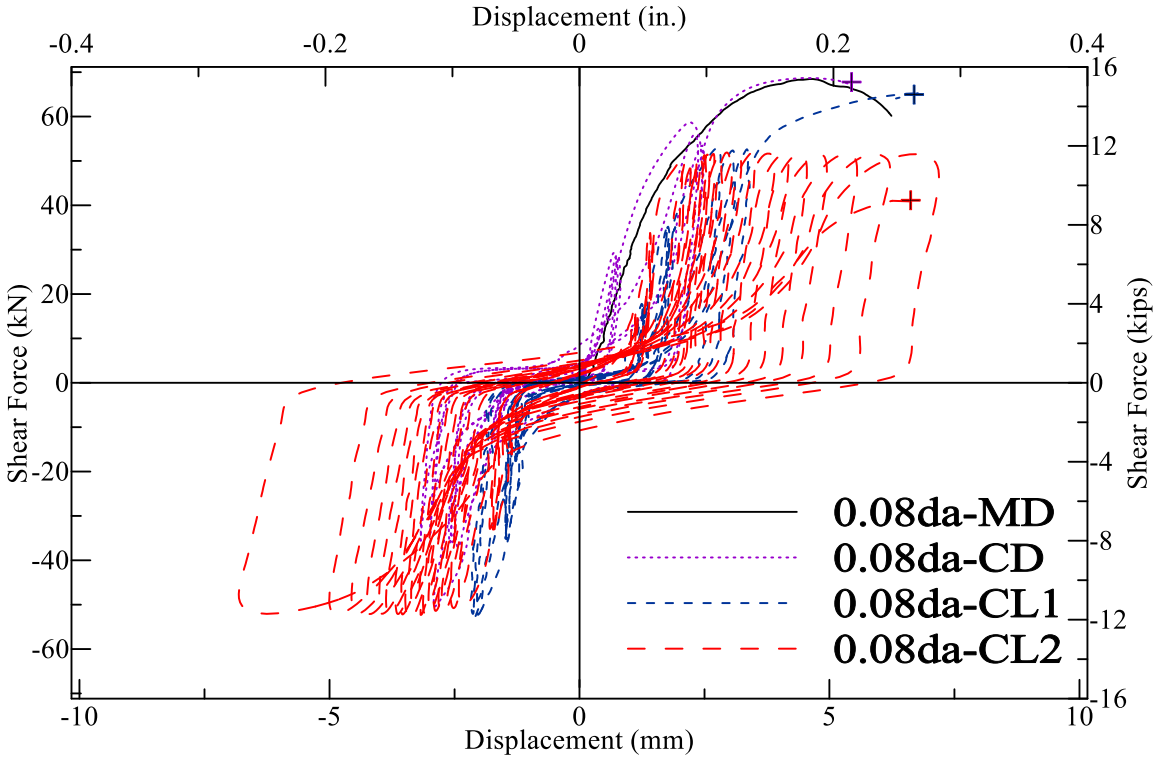

Figure 4.7 Behavior of anchors without stand-off heights under cyclic shear

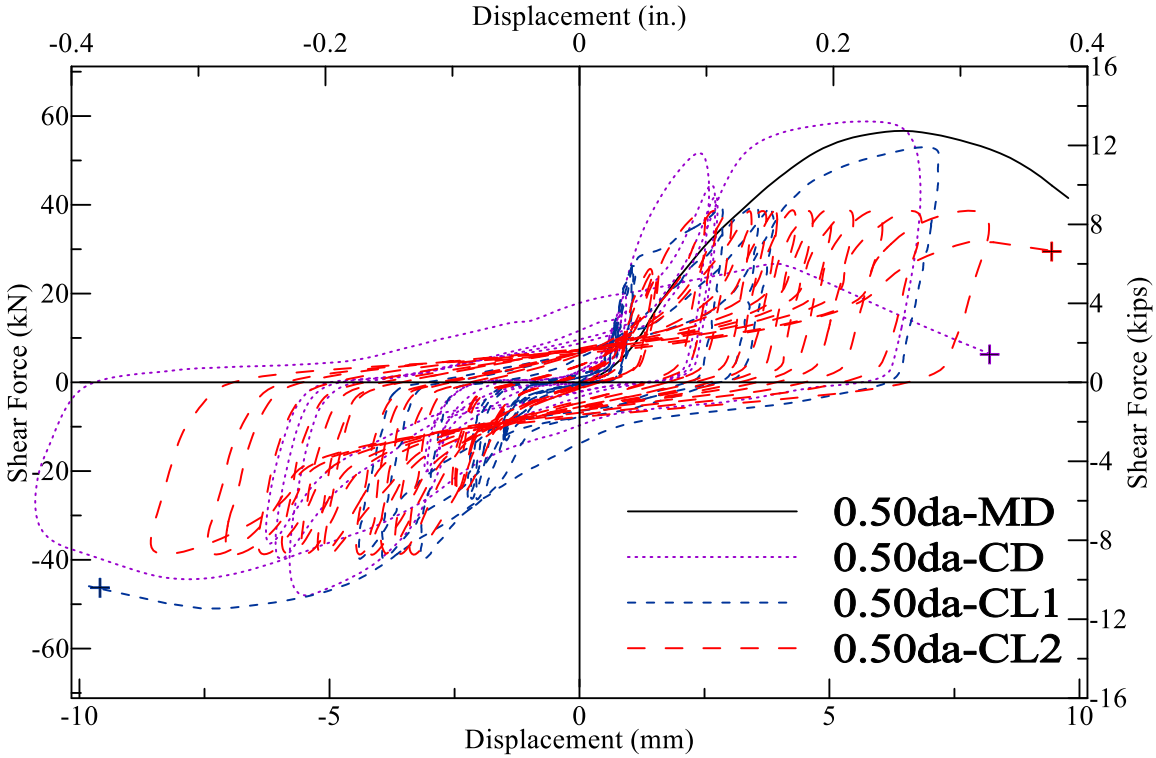

Figure 4.8 Behavior of anchors with stand-off heights under cyclic shear

Chapter 5. Finite Element Analyses

5.1. Introduction

The limited experimental tests in both the literature and Chapter 4 indicate that a crushed concrete depth and thus an effective exposed length, instead of a stand-off height, is critical to the prediction of shear capacity of concrete anchors controlled by shear fracture. The crushed concrete depth can be affected by the concrete material, anchor material and diameter, stand-off height, and loading. A series of finite element (FE) analyses were conducted to explore these factors. Knowing that modeling concrete damage due to cyclic loading can be extremely challenging, the impact of cyclic loading was not considered in this study.

5.2. FE simulation of Experimental Tests

FE models were first created for the shear tests, documented in Chapter 4, on cast-in-place single anchor with a diameter of 19 mm [0.75 in.], embedded depth of 6 in. ($8d_a$). Based on symmetry, only half of specimen was simulated. The modeled concrete block, as shown in Figure 5.1, is 305 mm [12 in.] wide, 686 mm [27 in.] long, and by 406 mm [16 in.] deep. The front edge distance of the anchor specimens is 152.4 mm [6 in.].

The 19 mm [0.75 in.] diameter anchors consist of F1554 Grade 55 threaded rod and a heavy hex nut tack welded to the embedded end. The F1554 Grade 55 threaded rod has a yield strength of 482.7 MPa [70 ksi] at the 0.2% offset strain and an ultimate strength of 524.0 MPa [76 ksi]. While the measured stress-strain relationship is shown in Figure 5.2, a trilinear model, shown in dashed lines in the figure, was used in the analyses. The elastic range of behavior was defined by the apparent proportional limit at a stress of a stress of 434.4 MPa [63 ksi], while the post-yield range was defined by a straight line from the proportional limit to the peak stress, beyond which, the stress was assumed constant.

The measured compressive strength of concrete for majority blocks was about 34.5 MPa [5000 psi]. However, the compressive strength of the front concrete should be obviously higher than that of measured due to the size effect. Therefore, the cube compressive strength, 43 MPa [6250 psi] was used in the analyses with a conversion formula of $f_{cc} = \frac{f_c'}{0.8}$. TNO DIANA® offers many constitutive models for plasticity-based analyses of concrete. The model proposed by Thorenfeldt et al. (1987) was used and the compressive stress-strain (f-α) behavior is defined by:

$$f = -f_p \frac{\alpha}{\alpha_p} \left(\frac{b}{b - \left(1 - \left(\frac{\alpha}{\alpha_p}\right)^{bk}\right)} \right), \tag{5.1}$$

where $b = 0.8 + \frac{f_{cc}}{17}$, $k = \begin{cases} 1.0 & if\ \alpha_p < \alpha < 0 \\ 0.67 + \frac{f_{cc}}{62} & if\ \alpha \le \alpha_p \end{cases}$, and f_{cc} is the cube compressive strength f_p is the peak compressive stress of concrete, α_p is the corresponding strain,

A scaling parameter l can be used to capture the post-peak behavior, and α in Eq. 5.1 is then replaced by $\alpha_p + \left(\alpha - \alpha_p\right)\frac{h}{l}$. h is the crack bandwidth of an element and is calculated as the cube root of the volume of the element. Thus, a lateral confinement model proposed by Selby and

Vecchio (1983) can be well combined with the compressed constitutive model in the finite element software TNO DIANA (2014). The smeared crack model in TNO DIANA software is selected for simulating the concrete cracking behavior, which assumed that the concrete element cracks once the principle tensile stress of that element reaches the tensile strength. After that, a constant tensile softening model is selected, which means the tensile stress of the cracks concrete is equal to tensile strength. This assumption slightly overestimates the behavior of concrete after cracking, but it can well cope with the large strain of concrete in those finite element models. In addition, for the study of the shear capacity of anchors with sufficient front edge distance, the influence of tensile stress of concrete after cracking on the behavior of anchor can be limited. The concept of coaxial rotation is also used in this model, which means the stress of the concrete element is determined by the principal strain directions based on the uniaxial stress–strain behavior.

The characteristic parameters of the material models were based on available reported values. Unreported parameters, such as the elastic modulus and tensile strength of concrete, were calculated in accordance with the recommendations in ACI 318 (2014). Additional details on the material models and the calibration of their parameters are shown in Appendix II.

Four-node, three-side isoparametric solid tetrahedron elements (Type TE12L) in TNO DIANA® were used for modeling the concrete block, steel anchor, loading plate, and the nuts, as shown in Figure 5.1a. In the model, the diameter of the rod was set as its effective diameter of 16.6 mm [0.652 in.], resulting in a proper net shear area of 215.4 mm^2 [0.334 $in.^2$]. Interface elements (Types Q24IF) were used for modelling the contact behavior between anchor and concrete such that under shear loading the back of anchor rod can separate from the concrete while the front of anchor rod can press the concrete (Figure 5.1c). Additional interface elements (Type T18IF) were used to model the interaction between the anchor and loading plate, and between the nut and loading plate, respectively. The thickness of the interface elements between the anchor and the concrete or the loading plate is half of nominal anchor diameter (19 mm [3/4 in.]) minus the effective diameter of the rod, that is 1.247 mm [0.049 in.]. The thickness of the interface elements between the top nut and loading plate is assumed as 1.27 mm [0.05 in.].

All interface elements, including those between concrete and bolt, bolt and loading plate, and loading plates and nuts are assumed to carry compressive only, that is zero tension and shear strengths. Moreover, the compressive stiffness is assumed to be the minimum of the materials on both sides of the interface and be linear elastic during the entire analyses. It is deemed acceptable that the tensile strength between concrete and bolt is zero, but the shear strength on the interface, due to mechanical bite force and chemical bonding, is usually hard to ignore. Fortunately, the vertical force mainly passed by the nut at the bottom of anchor to the concrete. when the bolt with a certain exposure length begins to bear larger bending moment, the concrete around it has already cracked or separated, and the bond between the bolt and the concrete inn this case can also be considered irrelevant. Therefore, the shear stiffness of the interface can be equal to 0. This assumption reduced the computational complexity of the analyses with material nonlinearity and improve the convergence.

A vertical (Z-axis) constraint was applied to the bottom of the block. The horizontal constraints in X-axis, which represents the steel tube reaction beam in Figure 4.3, was imposed to the concrete 102 mm [4 in.] from the bottom. Additional vertical displacement restraint in Z-axis was applied to the top of the block within 114.3 mm [4.5 in.] on the back side to resist the overturning moment created by the applied shear on the loading plate at the top and the reaction by the tube beam at the bottom (Figure 5.1b). The shear force was applied to the anchor through a target displacement in

the X-direction one the end of the loading plate, which was restrained at all other degrees of freedom.

Element size must be reduced near the anchor to create proper geometry transition from the round anchor to the rectangular concrete block (Figure 5.1a). This was accomplished automatically by the program with some mesh size control measures. On the other hand, the element size within the 152-mm [6-in.] embedment, along the Z-axis, was chosen as 6.4 mm [0.25 in.] (Figure 5.1c). Parametric studies were conducted later in Section 5.3 to determine an optimized element size in the height direction before the crushed concrete depth was calculated.

Figures 5.4 through 5.6 show the results of FE analyses for the experimental tests. In general, the FE models were able to capture the behavior of the three specimens with stand-off heights summarized in Figure 4.5. It should be noted that in order to capture the anchor fracture (Figure 5.4b), the post peak stress-strain curve in Figure 5.2 was revised to have a random negative slope, and it was specified that when the strain is 0.4, the stress drops to 6.9 MPa [1.0 ksi]. The designated excessive ultimate strain here is to prevent the premature shear failure at the condition of the sudden decrease of the stiffness of the anchor bolt due to an integral point exceeds the peak strain and the relative stress decreased suddenly when the average strain of the failure section is far less than the peak strain at non-convergence stage. This created convergence problems in most of FE analysis in this study; therefore, ideal plasticity (shown in dashed lines in Figure 5.2) was assumed in all other FE analyses in this report. Meanwhile, by ignoring post peak behavior of anchor materials, neither the anchor fracture nor the peak shear force was captured by the FE analyses, as shown in Figures. 5.5b and 5.6b. The load-displacement curves from the FE analyses were terminated at a displacement equal to the measured peak displacements and the corresponding simulated shear forces were used as the anchor capacities.

The principle strains in concrete at the peak loads are shown in Figures 5.4c through 5.6c. Note that the colored strain contours do not have the same color scale and the strain contours are limited by the element sizes in the height direction (24 element layers were used in this group of analyses, resulting in an element height of 6.4 mm [0.25 in.]). In fact, when the compressive strain of concrete in the finite element models exceeds a certain value, it will lose its bearing capacity completely and cannot continue to support the anchor bolt. In the results of finite element analysis, with the increase of the depth from the concrete surface, the compressive strain decreases gradually. This reduction is obviously related to the stand-off heights and the material properties of concrete and steel. Therefore, a certain compressive strain of concrete was used as threshold value to determine the l_{ec} measurement endpoint, as explain later inn Section 5.3.3.

The principle tensile strains in the anchors at the peak loads are shown in Figures 5.4d through 5.6d. The largest tensile strains in the anchor shaft occur just below the loading plate, which was assumed linear elastic during the analyses. This indicates that the fracture will most likely occur just below the loading plate. Below the concrete surface, two local maximum tensile strains can be seen, especially for the anchors with a stand-off height of $0.50d_a$ and $1.00d_a$. The maximum tensile strain location of the anchor at the peak load were also tried to determine the crushed concrete depth and the results are compared with that by the above method in figure 5.9. For the specimens with a small stand-off height (e.g. $0.08d_a$), its result is 0, which is because the stress is mainly concentrated on the shear failure surface due to the shear failure of anchor bolt, while for the specimen with a relatively stand-off height (e.g. $0.5d_a$, $0.8d_a$), its results is larger than that of determined by concrete stain. Considering the fact that the shear forces were applied through monotonically increased displacements on the loading plate, one may deduct that 1) crushing of

concrete progressed downwards during the loading; and 2) with confinement, concrete experiencing large compressive strains may be able to sustain compressive loading and provide certain (though unknown) lateral support to the anchor shaft. This reasoning indicates that the crushed concrete depth may not be determined as the location of the maximum tensile strain in anchor elements.

5.3. Parametric Study of Anchors with Stand-off Heights in Shear

The behavior and shear capacity of concrete anchors are related to both their stand-off heights (assumed no properly placed grout) and the crushed concrete depths during loading. The term "stand-off height" is thus not able to properly represent the condition around such anchors. Hence, we use a term "exposed length" in this study. In addition, the concept of "effective exposed length" (l_{ee}) is defined in Chapter 1, which includes the stand-off height (l_{ea}) and the crushed concrete depth (l_{ec}). A parametric study was conducted to investigate the key factors for the crushed concrete depth: the concrete/steel materials, anchor diameters, and stand-off heights (assuming no leveling nuts). The parametric study is based on the specimens used in the experimental tests described in Chapter 4, especially the geometry of the FE models. In addition, the following trial analyses were performed before the parametric study.

5.3.1 Model calibration of concrete under confinement

The concrete below surface is subjected to confinement when being pressed laterally by an anchor in shear; hence, being able to reasonably model the behavior of concrete under confinement is critical to the FE analyses. We have examined all concrete models available to TNO DIANA® and selected the models summarized in Table 5.1. The model parameters were calibrated using experimental tests of concrete under both active and passive confinement in the literature. The details of the model calibration are documented in Appendix II.

5.3.2 Mesh sensitivity study

Mesh sensitivity studies were conducted to determine optimized mesh sizes, especially in the direction of anchor embedment. The results analysis using a vertical element size of 6.4 mm [0.25 in.] are compared with the experimental tests in Figure 5.7. Knowing the limitation of the FE analyses shown in the comparison, two addition mesh sizes (1.3 mm [0.05 in.] and 3.2 mm [1/8 in.]) were studied and the results are compared with each other in Figure 5.8. The mesh sensitivity analyses indicate that a vertical mesh size of 6.35 mm [1/4 in.] is suitable for the parametric study. This mesh size leads to manageable computing resource required by the FE parametric study with reasonable analysis results as shown by the calculated crushed concrete depths in Figure 5.9.

5.3.3 Method of determining crushed concrete depth

Stand-off anchors are assumed to be subjected to double curvature bending as illustrated in Figure 3.1b; hence it is natural to use the location of the maximum principal tensile strain of the anchor to determine the crushed concrete depths. A target tensile strain of 0.07 was used in the results shown in Figure 5.10. The peak strain (0.03) measured from the material test in Figure 5.3 was not used because it was from a full-size threaded rod test instead of a standard coupon test. The minimum elongation stipulated by ASTM F1554 (2015) was used as the target strain. The calculated l_{ec} is plotted against the concrete strength in Figure 5.10a and also plotted against the ratios of the stand-off heights to the anchor diameters in Figure 5.10b.

It is difficult to summarize the observed influence of the key parameters from Figure 5.9. In addition, one must recognize the following factors in determining crushed concrete depths:

1) anchor fracture is unlikely to occur below concrete surface; hence the crushed concrete depth does not correspond to the potential fracture location;

2) anchor fracture is likely occur below the steel base plate, and the inclusion of crushed concrete depth would lead to a reasonably estimated bending stress at the location;

3) the location of the maximum tensile strain may vary during loading as revealed in Section 5.2; and

4) it is difficult to select a target steel strain for the mostly used anchors because anchor materials may very vastly, as shown by the three threaded rods used in Lin *et al*. (2013).

Therefore, we assumed that concrete is crushed below the concrete surface when the lateral compressive strain of concrete (in X-direction, as adopted by the models in this study) reached a value of 0.1 mm/mm. Correspondingly, the crushed concrete depth is the distance from the concrete surface to the location, where the strain in the X-direction reaches at this specified strain. The crushed concrete depth is not from the location, where the lateral concrete deformation is negligible as shown in Figures 5.4c through 5.6c because significantly deformed concrete can still carry pressure from the anchor shafts when it is confined, thus providing lateral support to the anchor shaft. Such lateral support is ignored in all the capacity equations listed in Chapter 3. Selecting a specific strain in compression is in line with the common practice in the design of concrete structures, where a maximum useable strain of 0.003 mm/mm is adopted for commonly used concrete with a range of compressive strengths (ACI 318, 2014).

The calculated l_{ec} based on this rather randomly selected target strain in concrete is plotted against the concrete strength in Figure 5.11a and also plotted against the ratios of the stand-off heights to the anchor diameters in Figure 5.11b. The crushed concrete depth increases with an increase in anchor diameters and decreases with an increase in stand-off heights and concrete strength.

5.4. Results of Parametric Study

Figures 5.12-5.15 described the influences of ratio of stand-off height to diameter of anchor, bolt diameter, concrete strength and steel ultimate strength on crushed concrete depth respectively. All the parameter values of specimens in the figures are the same as the test except for the specially specified parameter changes. Different from the fixed value of $0.5d_a$ specified by *fib* (2018), crushed concrete depths are rather different under various parameter combinations. In most cases, the crushed concrete depth is greater than or even far greater than 0.5da, which may lead the anchors failed before reaching design capacity.

As shown in Figure 5.12, within the parameter investigate range, the crushed concrete depth reaches the maximum value when the stand-off height is $0.5d_a$. This is because when the stand-off height is relatively small (less than $0.5d_a$), large shear strains accumulated in the anchor bolt before obvious bending deformation appeared, and the anchor prefer to shear failure, which results relatively small damage to the concrete surface even the anchor bolt reaches its maximum shear capacity. With the increase of stand-off height, the failure mode of the anchor turns into bending failure, and its shear capacity decrease with the increase of effective exposed length, which means that the lateral compressive stress in concrete was decreased under peak load, which eventually

lead to the reduction of crushed concrete depth. As the stand-off height continues to increase, from the downward trend of each curve in the figure, it can be inferred that the crushed concrete depth may decrease to zero. This is because that too long stand-off height will significantly reduce the shear capacity of the anchor as predicted by Lin *et al*. (2011), which makes the lateral strain of the concrete near the concrete surface may smaller than crushed strain when the bolt failed. In addition, the change of concrete strength has limited influence on the tendency of the influence of the ratio of stand-off height to anchor diameter on the crushed concrete depth, especially when the anchor diameter is 19 mm [0.75 in.] and 25 mm [1.0 in.].

With various concrete strengths, as shown in the Figure 5.13, when the stand-off height is greater than 0.5da, the crushed concrete depth shows a significant increase with the increase of anchor diameter, and the increase trend slightly decreases with the increase of stand-off height. This may be possible due to the fact that the lateral displacement of the anchor bolt is proportional to its diameter with the same strains conditions, but the size effect of the anchor bolt deduced from the equation by Lin *et al*. (2011) leads to the slight decrease of the ratio of the lateral deformation to diameter with the increase of the diameter.

As shown in Figure 5.14, with the increase of concrete strength, the crushed concrete depth is significantly reduced, and the reduction trend is relieved by the gradual increase of concrete strength. When the stand-off height is more than $0.5d_a$, the downward trend is similar, while the downward trend is more obvious when the exposed length is $0.08d_a$. This is because when the concrete strength is relatively low, a certain crushed concrete depth can be generated under lower load level, which will lead to a large amount of bending deformation of anchor under the peak load, and eventually lead to the occurrence of crushed concrete depth.

As shown in Figure 5.15, increasing the steel ultimate strength can increase the crushed concrete depth in proportion when the stand-off height is more than $0.5d_a$. higher steel strength leads the bolt failed in bending rather than shear easier when the stand-off height is $0.08d_a$. When the steel ultimate strength is 855 MPa [124 ksi] and concrete strength is less than 50MPa, the crushed concrete depth of the anchor with stand-off height of $0.08d_a$ is higher than that of $0.5d_a$. This because it is not only failed in bending, but also has a higher peak load.

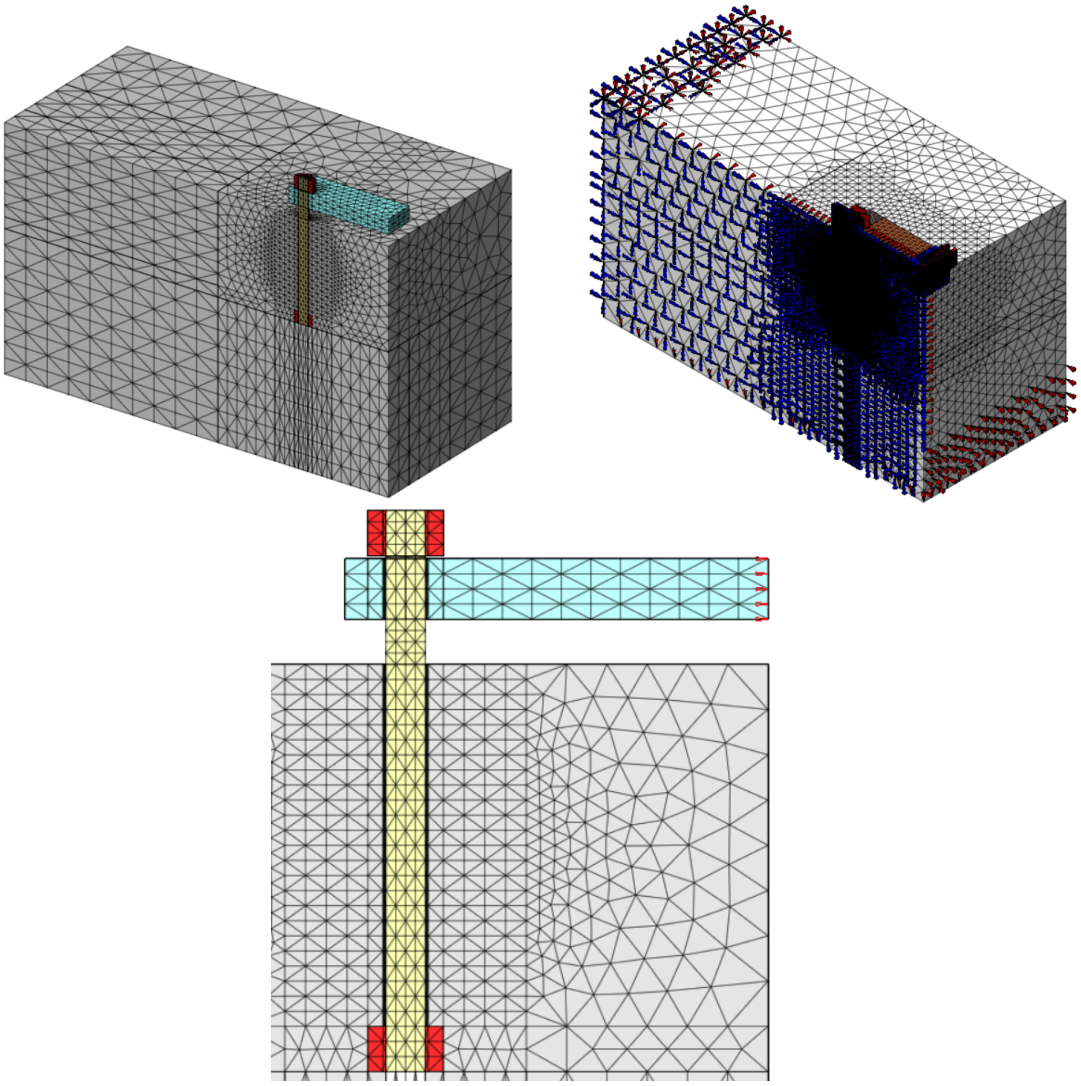

Figure 5.1 Model of cast-in-place anchors with stand-off heights

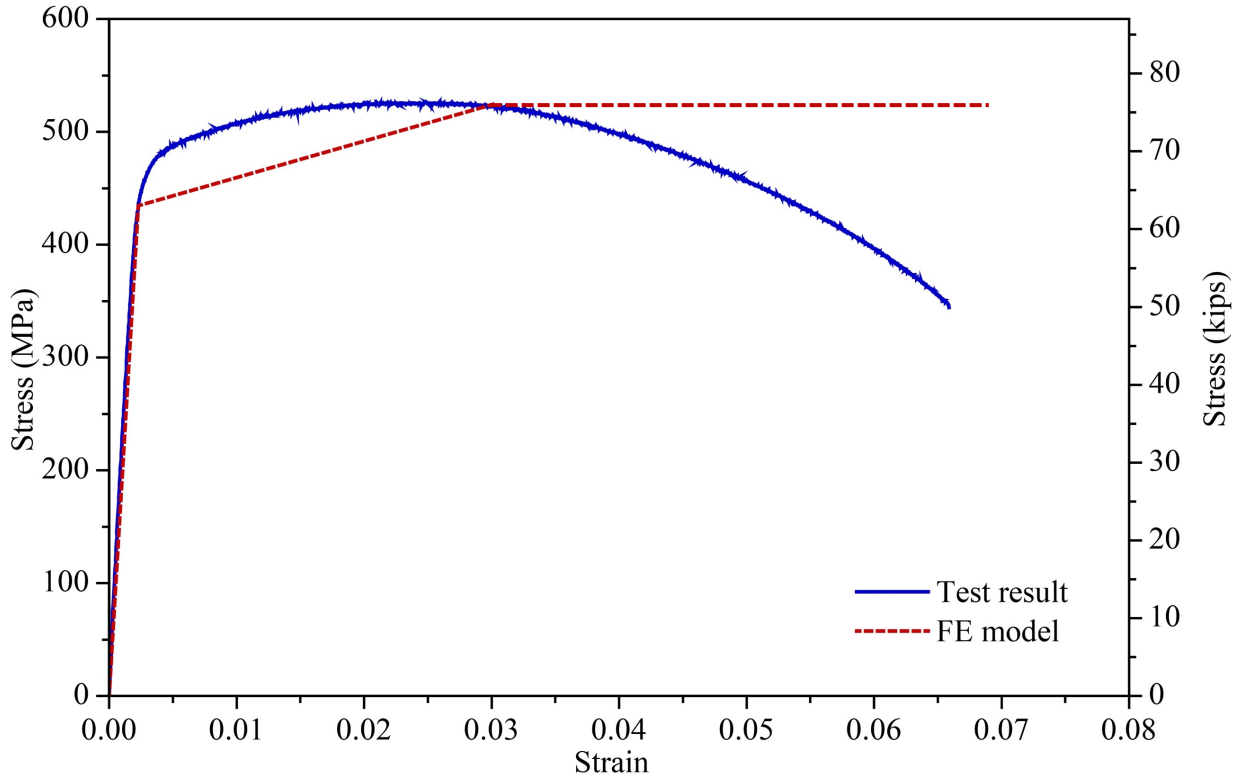

Figure 5.2 Material model of steel anchors

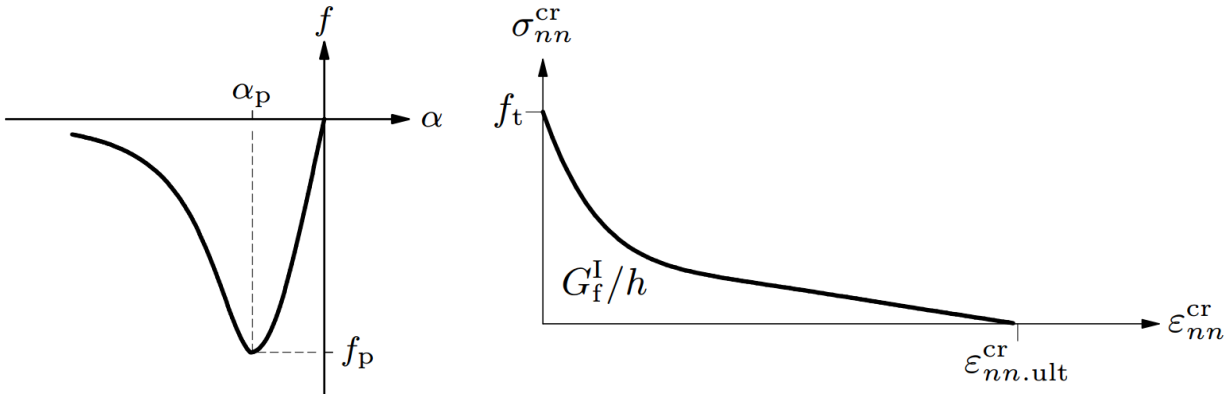

Figure 5.3 Material models of concrete; a) for concrete in compression by Thorenfeldt *et al.* (1987); b) for concrete in tension by Hordijk et al. (1991)

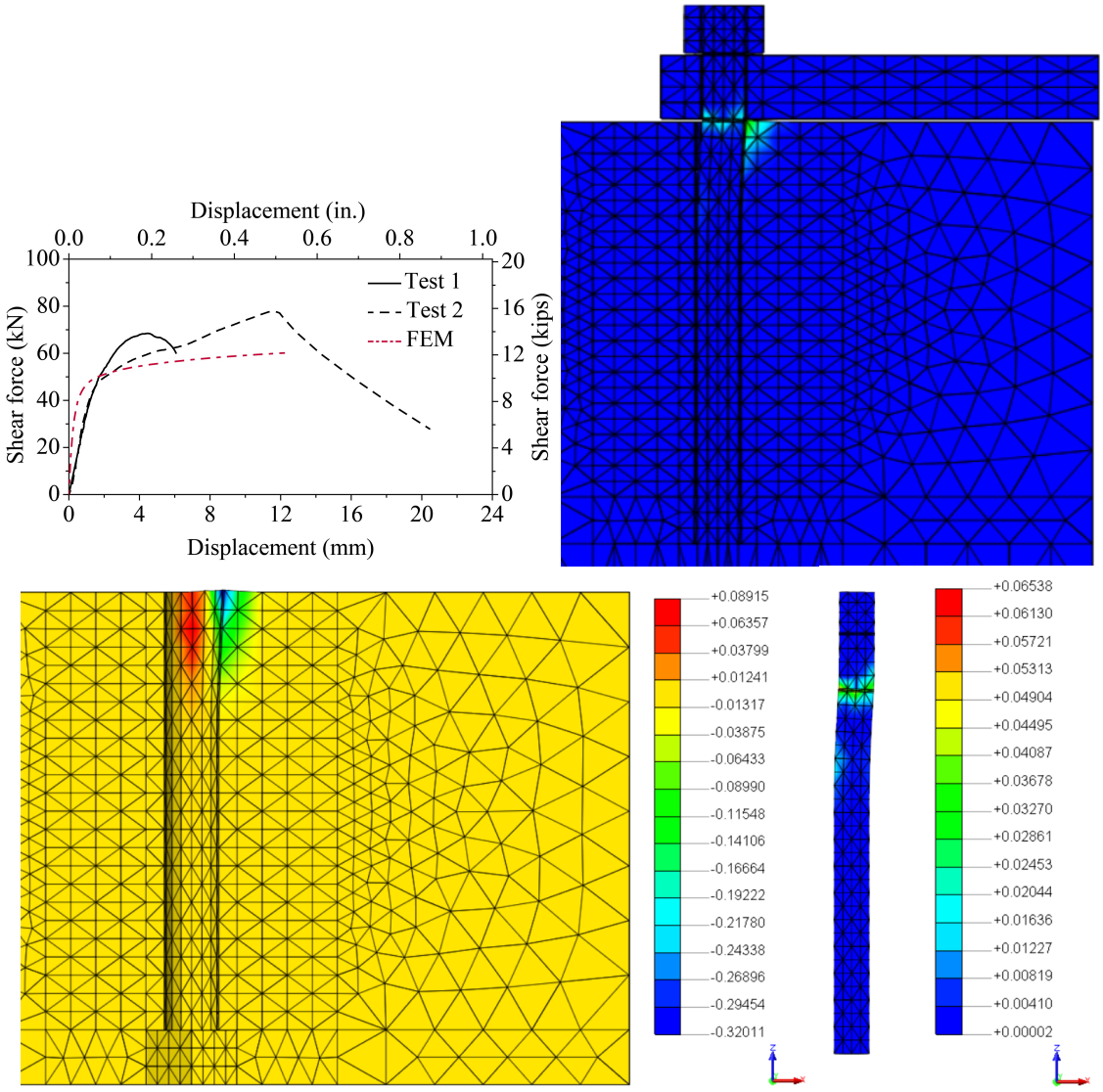

Figure 5.4 Simulated behavior of Specimen 08092011_0.08da-MD; a) load-displacement curve; b) failure mode; c) the X-direction strain of concrete; and d) the 1st principal strain of anchor.

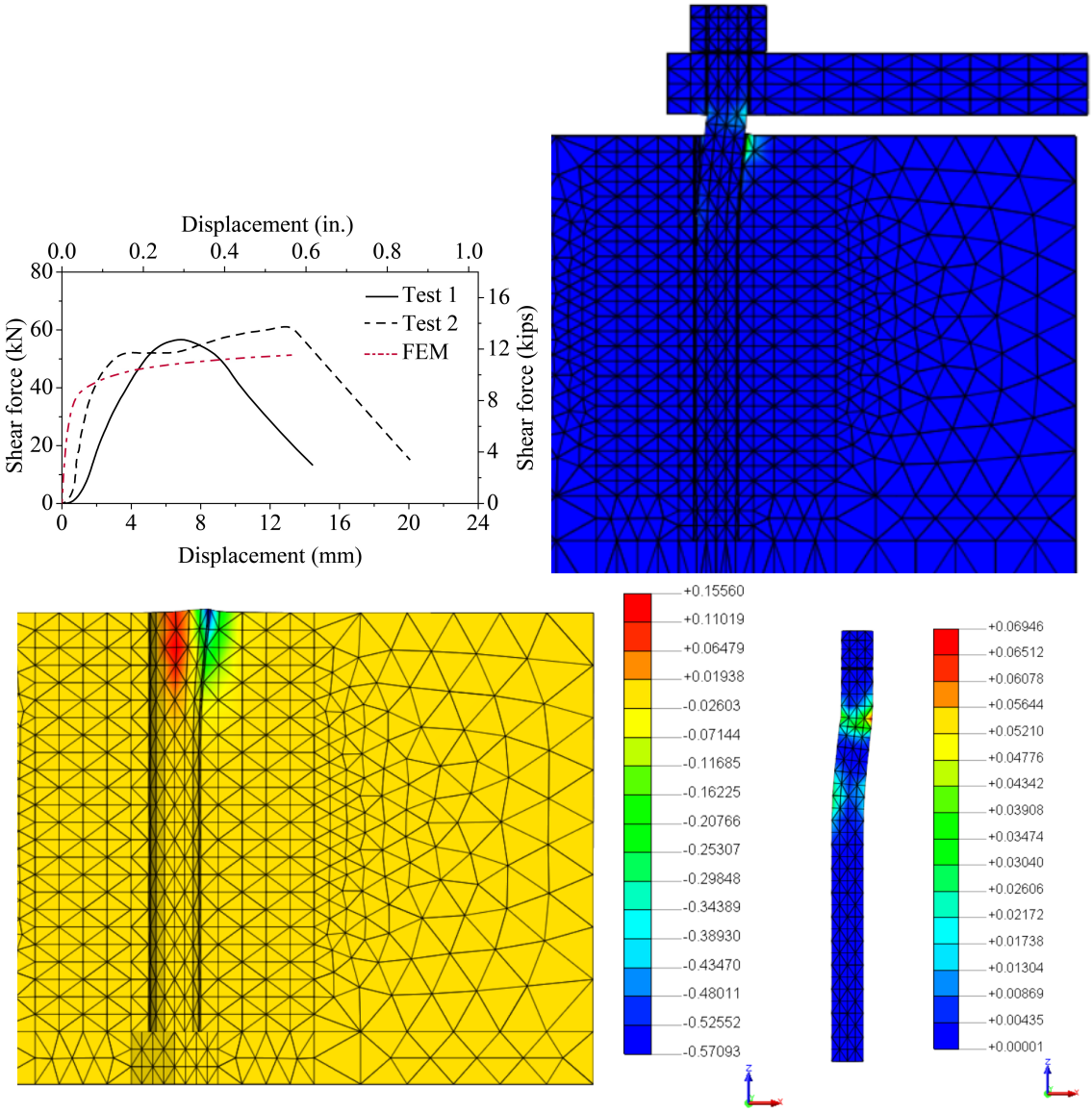

Figure 5.5 Simulated behavior of Specimen 08092011_0.50da-MD; a) load-displacement curve; b) failure mode; c) the X-direction strain of concrete; and d) the 1st principal strain of anchor.

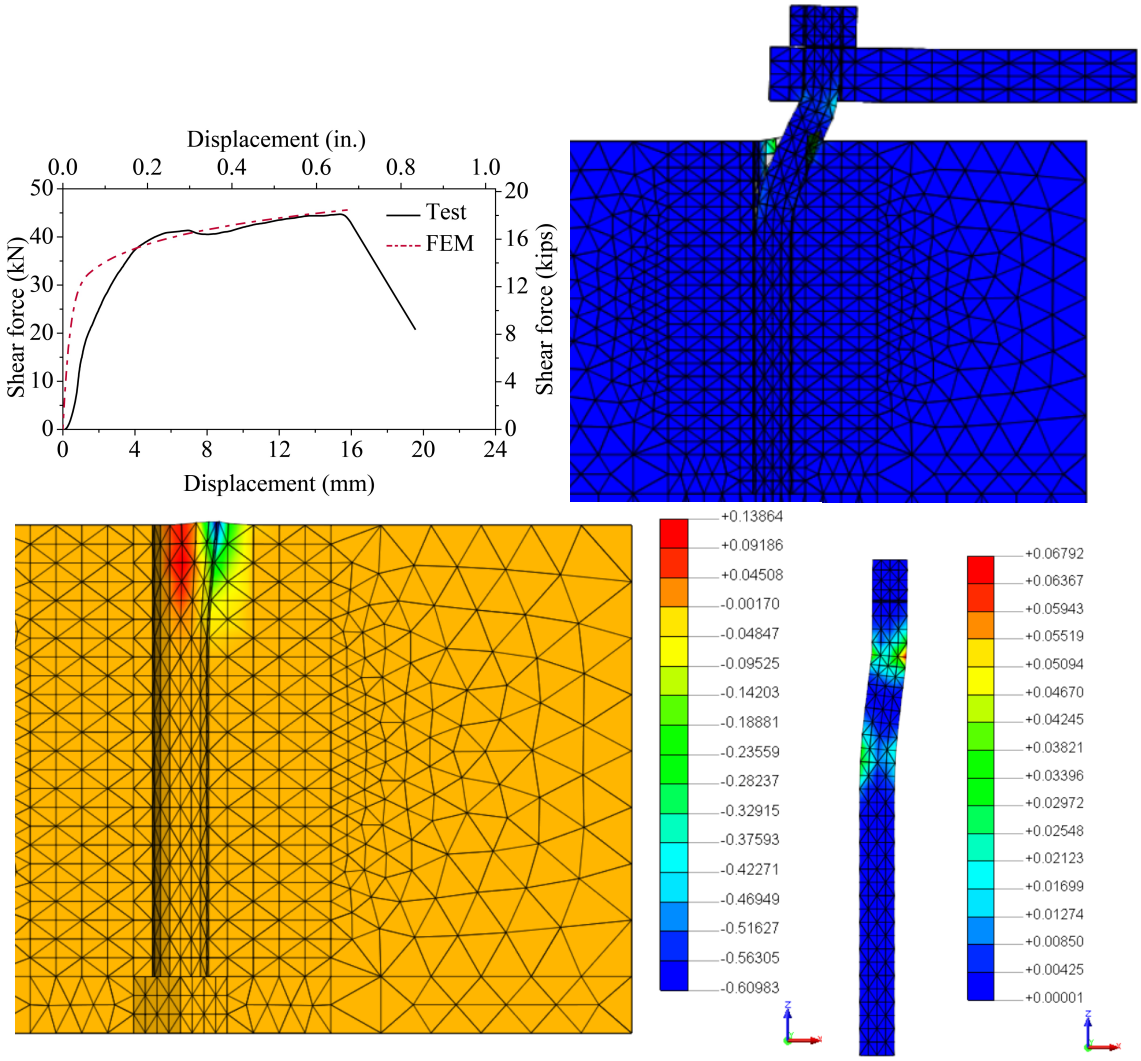

Figure 5.6 Simulated behavior of Specimen 08092011_1.00da-MD; a) load-displacement curve; b) failure mode; c) the X-direction strain of concrete; and d) the 1st principal strain of anchor.

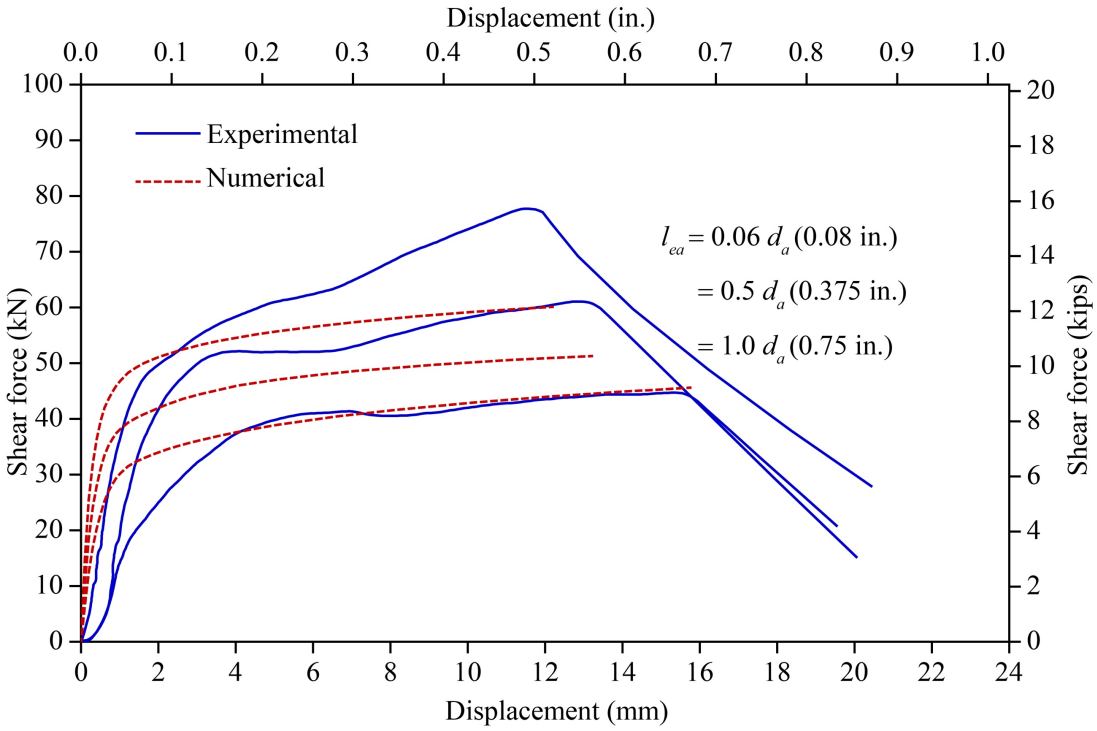

Figure 5.7 Comparison of FE analysis results with experiments

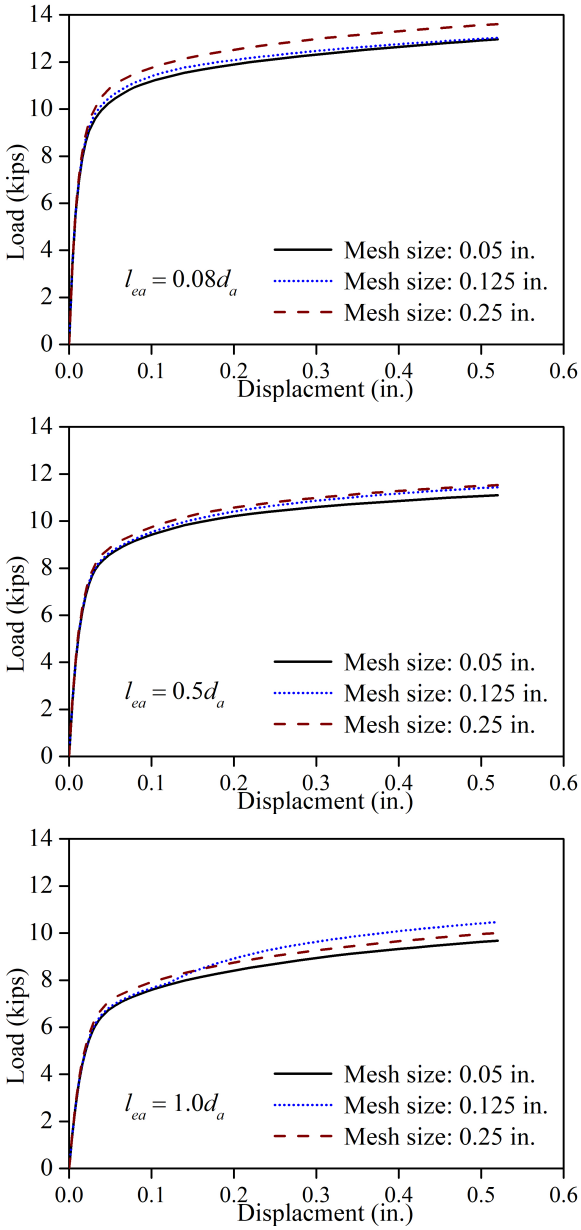

Figure 5.8 Mesh sensitivity analyses to determine suitable vertical mesh size

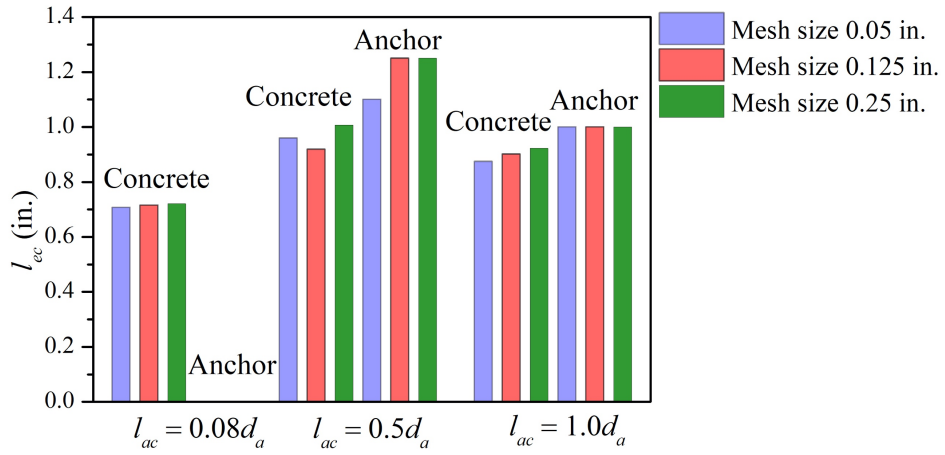

Figure 5.9 Influence of vertical mesh size on the calculated crushed concrete depth

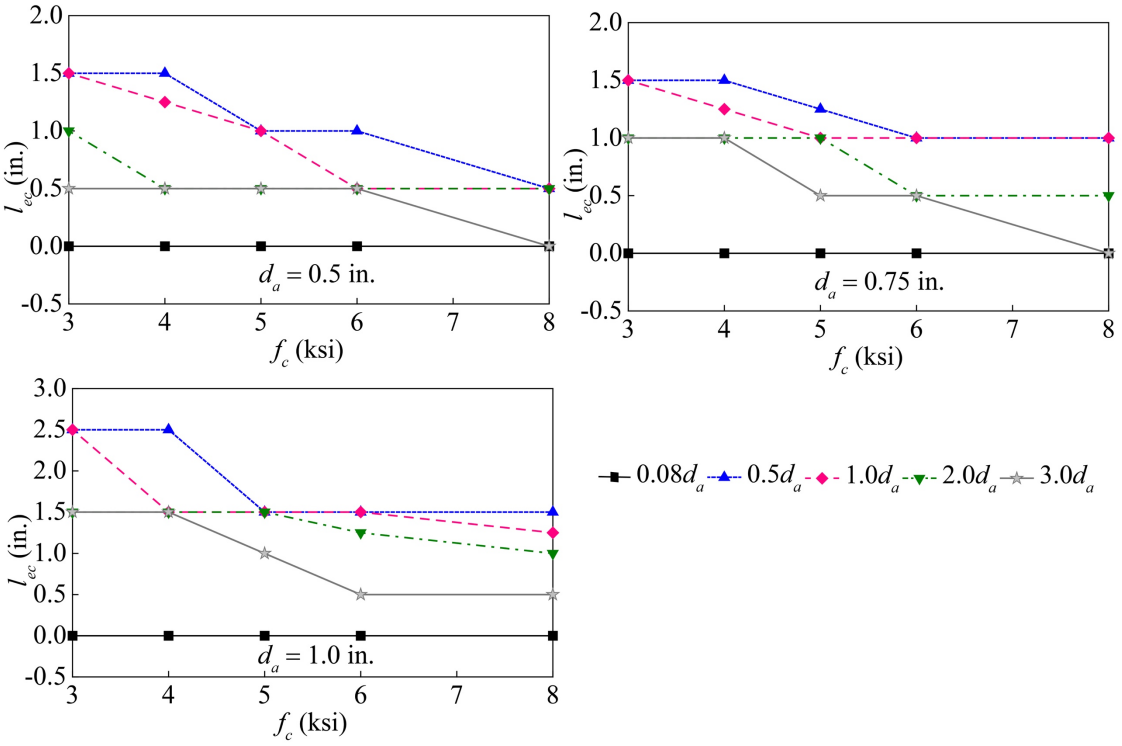

(a)

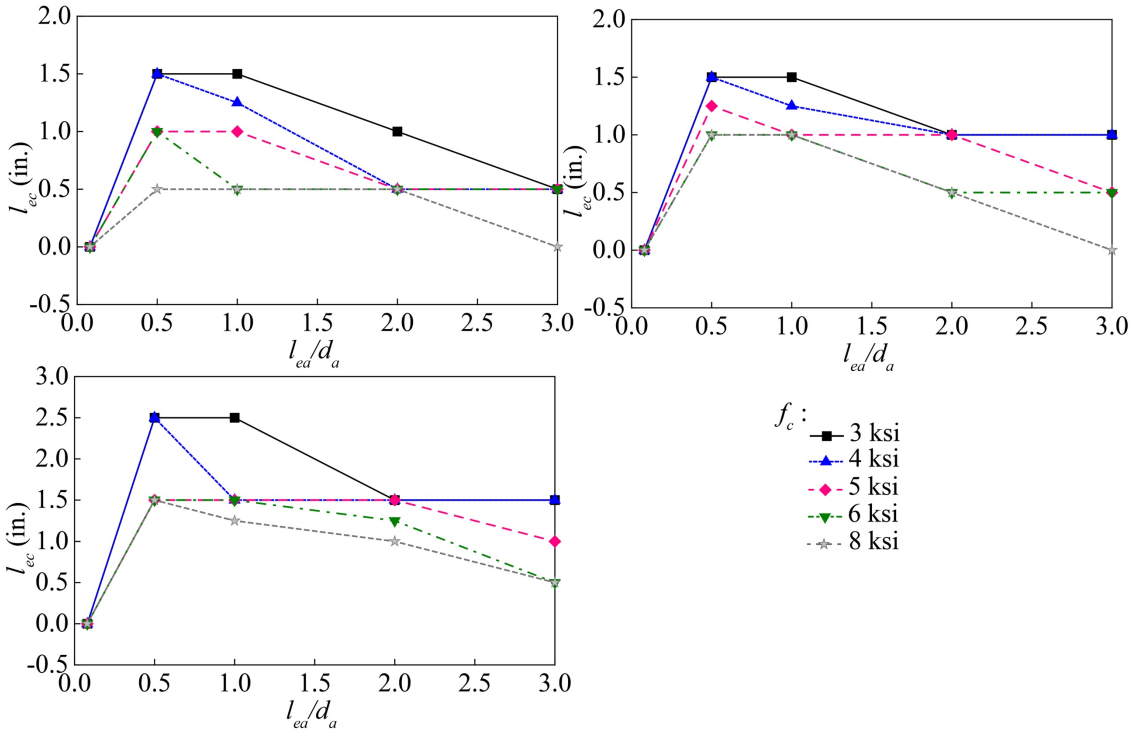

(b)

Figure 5.10 Crushed concrete depths determined by a target steel strain

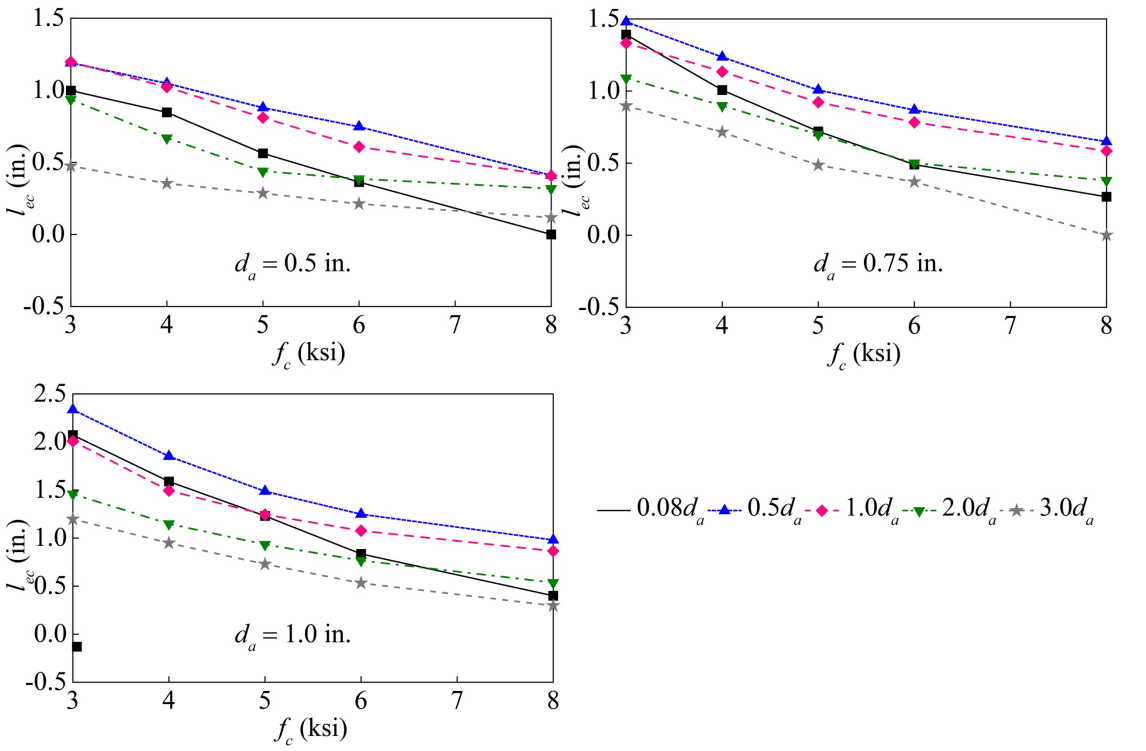

(a)

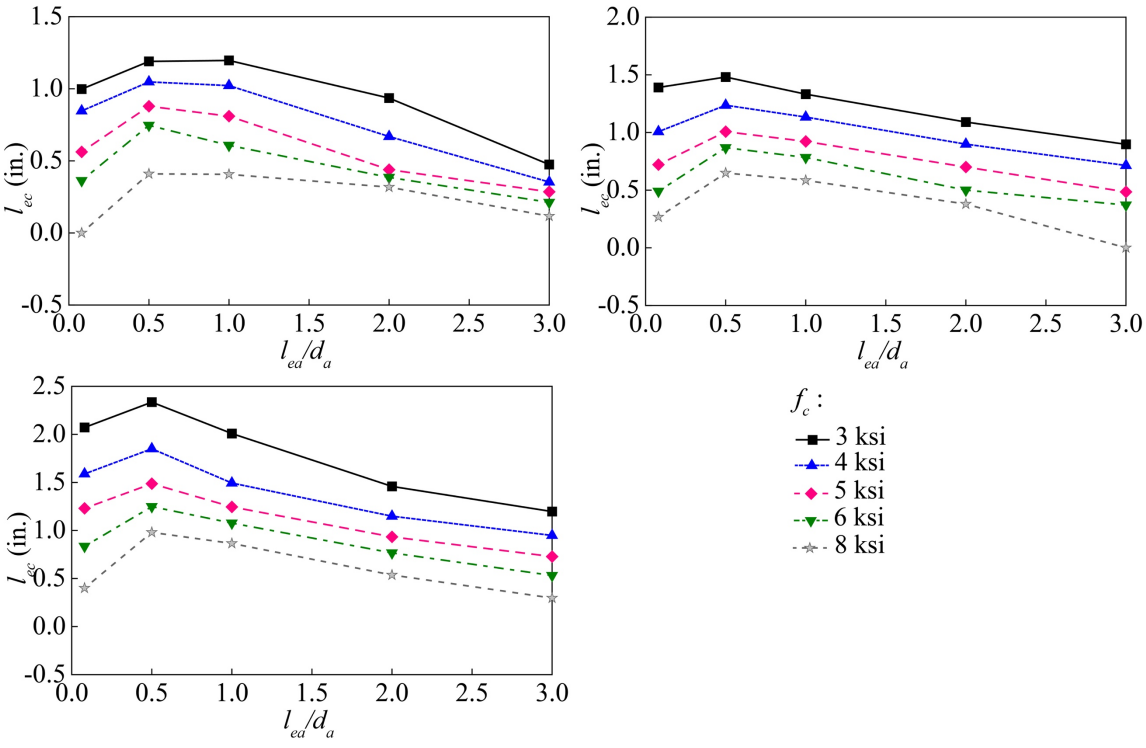

(b)

Figure 5.11 Crushed concrete depths determined by a target concrete strain

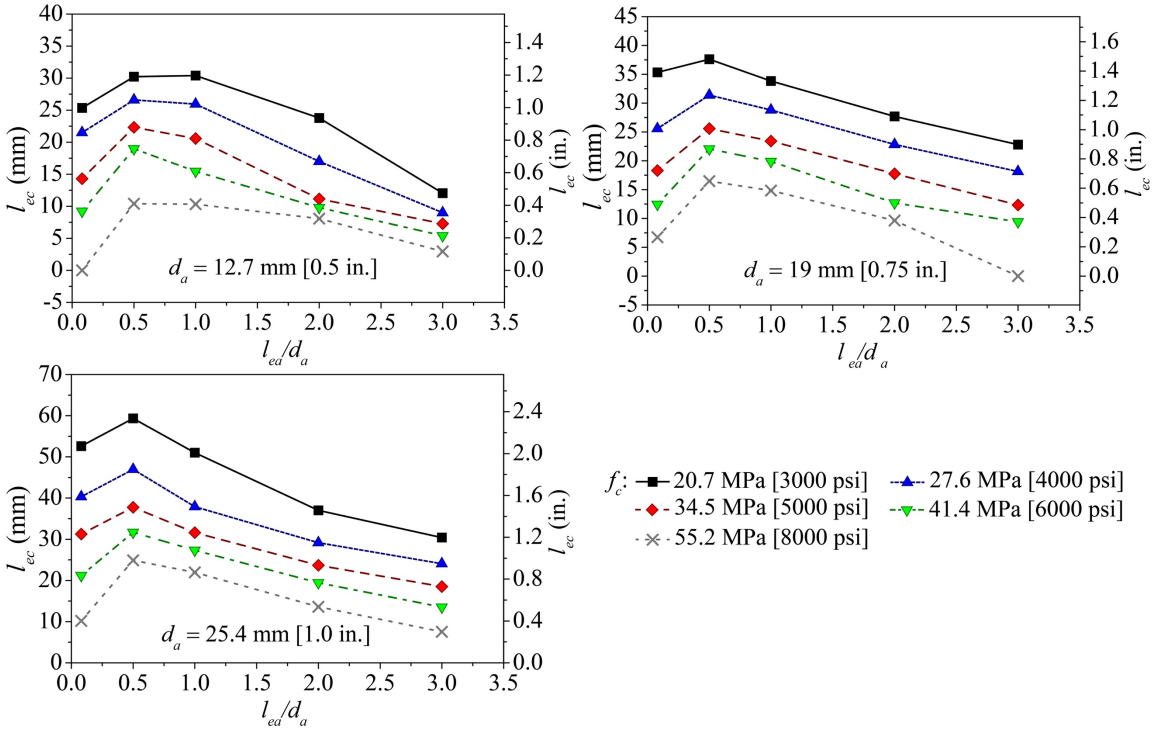

Figure 5.12 Influence of stand-off height on crushed concrete depth

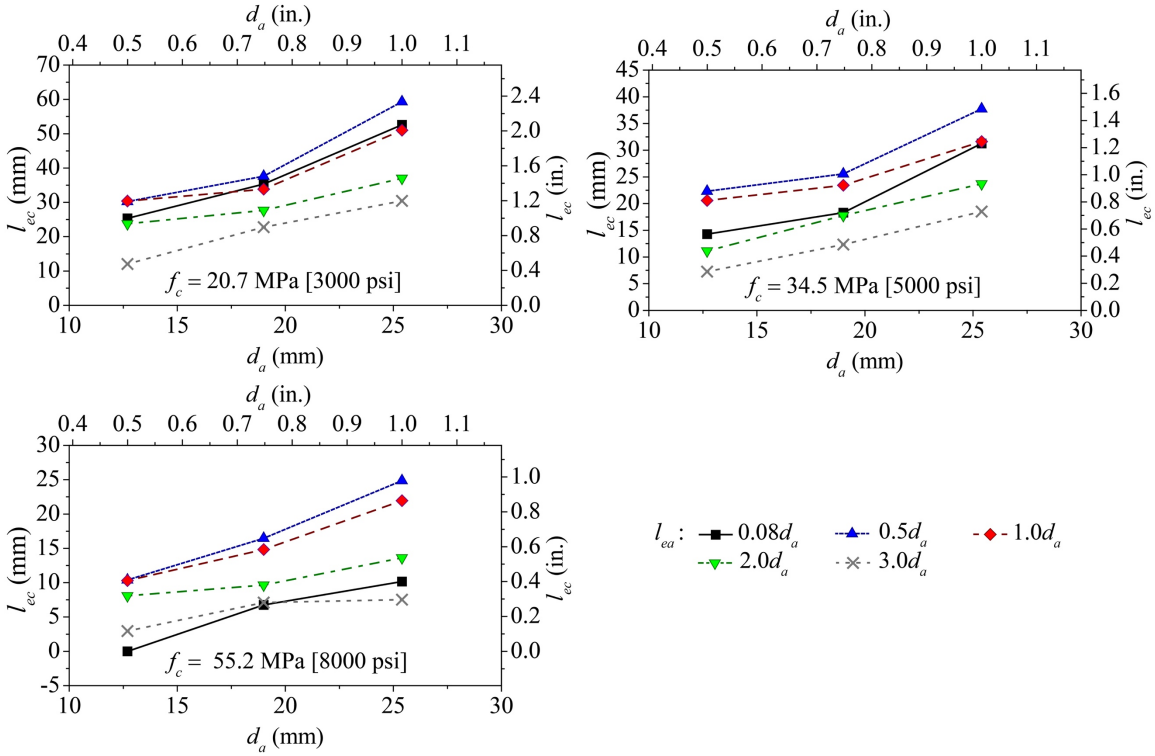

Figure 5.13 Influence of stand-off height on crushed concrete depth

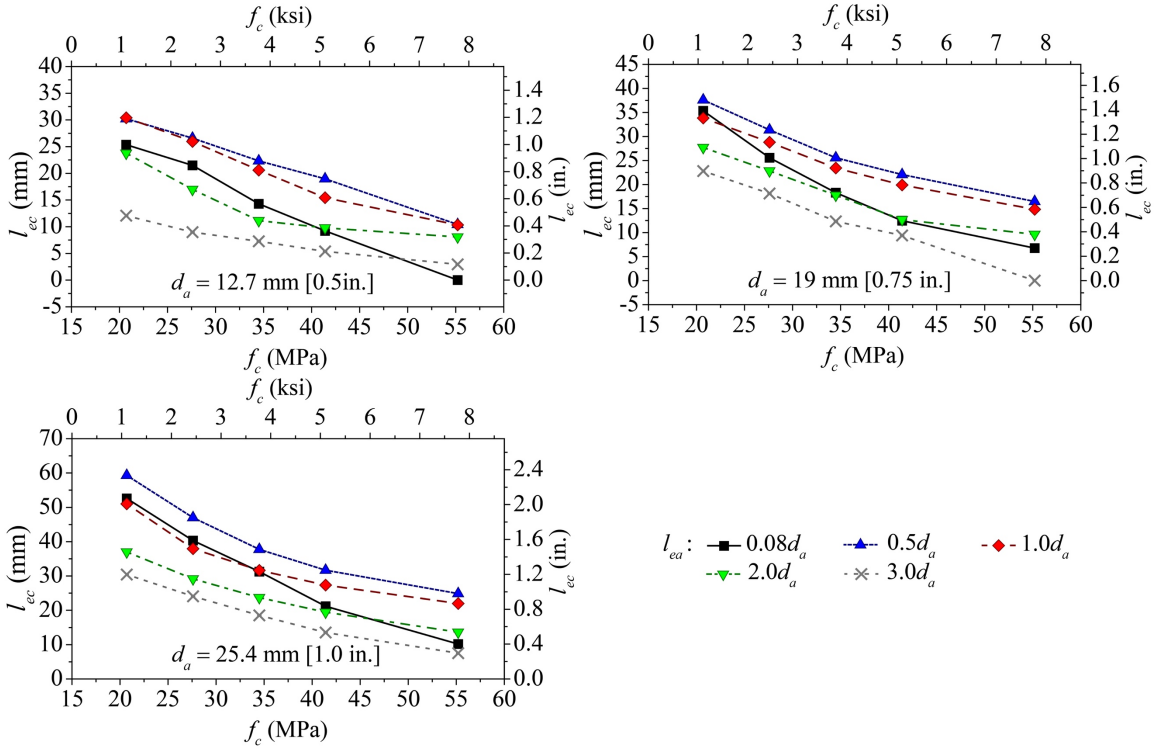

Figure 5.14 Influence of stand-off height on crushed concrete depth

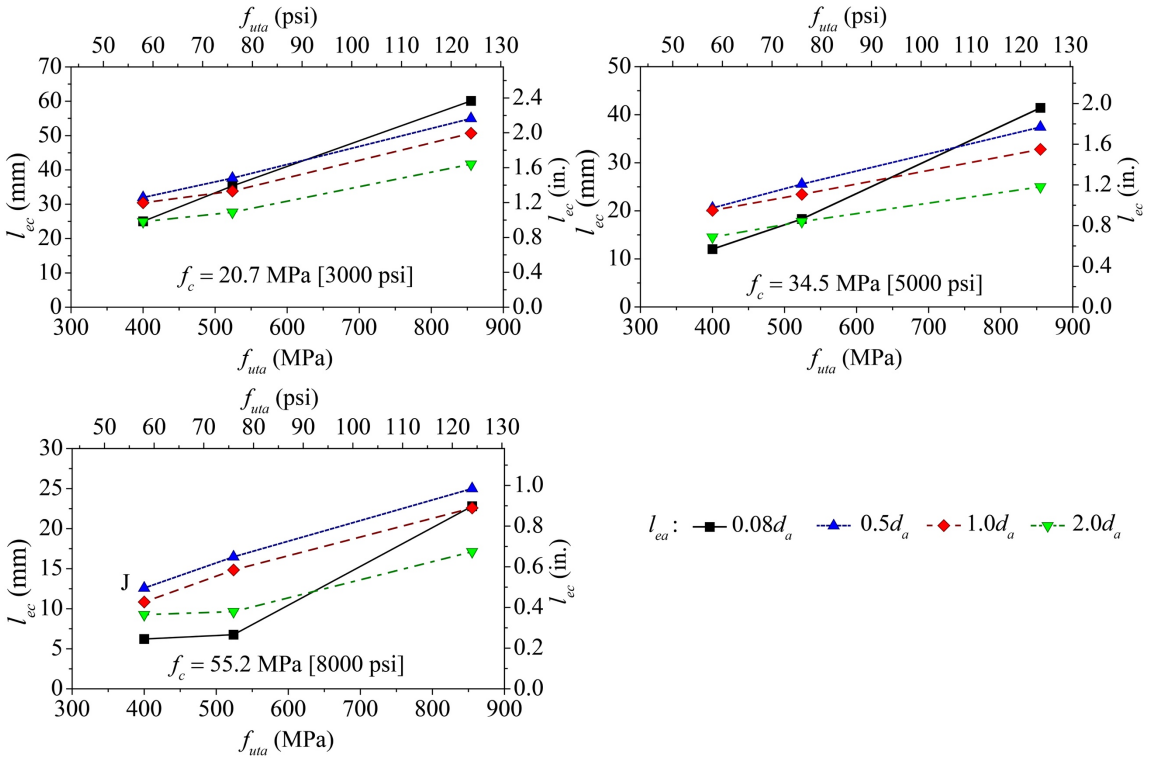

Figure 5.15 Influence of stand-off height on crushed concrete depth

Table 5.1 Base model parameters for the parametric study

Linear material properties
Young's modulus of concrete: 36845 MPa
Poisson's ratio: 0.2
Total strain based crack model
Crack orientation: Rotating
Tensile behavior
Concrete tensile Model: Hordijk
Tensile strength: 4.33 MPa
Tensile fracture energy: 18.5 N/m
Reduction model: Vecchio and Collins 1993
Poisson's ratio reduction: Damage based
Compressive behavior
Concrete compressive Model: Thorenfeldt
Compressive strength: 60.6 MPa
Length scale parameter of Thorenfeldt curve: Default
Confinement model: Selby and Vecchio (1983)

Chapter 6. Recommendations on Effective Exposed Lengths

6.1 Introduction

Concrete in front of anchors in shear, especially those with a stand-off height. The resulted bending moment in anchor shafts may significantly lower the shear capacity of anchors controlled by steel fracture. The estimation of the bending moment from the applied shear requires a moment arm as illustrated in Figure 3.1. Most of the design recommendations directly use the stand-off heights while an additional length of $0.5d_a$, below concrete surface, is included in the equation by *fib* Task Group TG2.9. Both the experimental tests in Chapter 4 and the numerical analyses in Chapter 5 indicate that the depth of $0.5d_a$ cannot represent the crushed concrete depths. A series of FE analyses have been conducted to investigate critical factors for the crushed concrete depths. Empirical equations are derived for engineers to estimate this parameter.

6.2 Results of FE analyses and Experimental tests

It is recommended that an effective exposed length (l_{ee}) is used in design equations for anchors in shear, which includes the apparent exposed length (l_{ea}) and the crushed concrete depth (l_{ec}). The apparent exposed length is closely related to the stand-off height when grout is not provided between the base plate and concrete or when the grout is susceptible to damage during loading. The crushed concrete depth is determined as follows.

6.2.1 FE analysis results

The crushed concrete depths were calculated using finite element analyses as the distance from the concrete surface to the location, where the compressive strain in concrete is equal to 0.1 mm/mm [0.1 in./in.]. A total of 101 FE analyses were conducted, considering the following factors:

1. Concrete compressive strengths: 20.5 MPa [3000 psi] through 55.2 MPa [8000 psi];
2. Steel strength: 400 MPa [58 ksi], 524 MPa [76 ksi], 855 MPa [124 ksi] representing ASTM F1554 Grade 36, Grade 55, and Grade 105 threaded rods, respectively;
3. Anchor diameters: 13 mm [0.5 in.], 19 mm [0.75 in.], and 25 mm [1.0 in.];
4. Stand-off heights: $0.08d_a$, $0.5d_a$, $1.0d_a$, $2.0d_a$, and $3.0d_a$.

The results of these FE analyses are listed in Table III.1.

6.2.2 Test results

Crushed concrete depths were measured in a total of 16 tests, including five reported by McBride (2019) and eleven reported in Chapter 4. The crushed concrete depths by McBride (2019) were determined by visually locating the depth, below which anchor shafts had no apparent permanent deformation. The crushed concrete depths in the tests in Chapter 4 were measured after the loose concrete next to the anchor shafts was removed after the shear tests. Monotonic loading was used in five out of the eleven reported tests while a variety of cyclic loading was used in the rest. Note that cyclic loading in general would cause extra crushing in concrete. The following factors were covered in these experimental tests:

1. Concrete compressive strengths: 34.5 MPa [5000 psi] and 38.6 MPa [5600 psi];
2. Steel strength: 524 MPa [76 ksi] and 644 MPa [93.4 ksi];
3. Anchor diameters: 16 mm [0.625 in.] and 19 mm [0.75 in.];
4. Stand-off heights: $0.08d_a$ through $2.8d_a$.

The results of the limited tests are listed in Table III.2.

The parametric study in Chapter 5 indicates that the crushed concrete depth (l_{ec}) reduces with an increase in concrete compressive strengths and stand-off heights, which should consider the anchor diameter because of the size of level nuts used in stand-off base connections. In addition, the crushed concrete depth increases with an increase in anchor diameters and their ultimate strength. The data from both the FE analyses and the limited experimental tests are used to verify a design model below.

6.3 Effective exposed lengths

6.3.1 Recommendation based on best fit of FE analyses

An empirical equation of the ratio of crush depth to anchor diameter for stand-off anchors ($\frac{l_{ea}}{d_a} \geq 0.5$) is proposed as follows,

$$\frac{l_{ec}}{d_a} = 0.0374\left(\frac{f_{uta}}{f_c'} + 9.732\right)\left(\frac{l_{ea}}{d_a} - 6.388\right)\left(\frac{d_a}{1} - 0.631\left(\frac{d_a}{1}\right)^2 - 0.72\right) - 0.47, \quad (6.1)$$

where $\frac{l_{ec}}{d_a}$ is the crushed concrete depth normalized by the anchor diameter, $\frac{l_{ea}}{d_a}$ the apparent exposed length normalized by the anchor diameter, and the impact of anchor diameter is normalized by 25 mm [1 in.] in Eq. 6.1.

As shown in Figure 6.1, Eq. 6.1 can well predict the ratio of crush depth to anchor diameter compared with FE analyses, while the predictions are slightly higher than test results. This would lead to a conservative prediction of anchor shear capacity in Section 6.4.

6.3.2 Recommendation based on robust fit of FE analyses

A second empirical equation was derived based on a simple load balance in a stand-off anchor, as illustrated in Figure 6.2: the applied shear is taken as $0.6f_{uta}A_{se,V}$, where the effective cross-sectional area of anchor in shear ($A_{se,V}$) may be roughly estimated by a fraction (75%) of $\frac{1}{4}\pi {d_a}^2$. The balance force provided by concrete is $kf_c'd_ah$ based on an assumption that the compressive stress in concrete is linearly varying within *h* deep in concrete. The equation of equilibrium leads to an estimation of crushed concrete depth,

$$\frac{l_{ec}}{d_a} = \frac{1}{2}\frac{h}{d_a} \approx \frac{f_{uta}}{kf_c'}0.18. \quad (6.2)$$

Note that kf_c' represents maximum usable strength of concrete in compression. The number *k* is 8 in the case of estimating the pullout strengths of headed anchors, where concrete above the anchor head is well confined be the surrounding concrete (Petersen *et al*. 2018). In the case where a gap exists in between the base plate and concrete, such confinement can be small near the free concrete surface; hence *k* may be small. The factor *k* may be large in cases where flush-mounted or grouted standoff base plates are used due to 3D confinement. Knowing that coefficient, ψ_s, would decrease with an increase in the standoff height, a general term is assumed for the factor and all the constants in Eq. 6.2,

$$\psi_s = \frac{0.18}{k} = \frac{a}{b + c\left(\frac{l_{ea}}{d_a}\right)^d}. \quad (6.3)$$

The four parameters in Eq. 6.3 were determined through a robust regression analysis of the FE analysis results in Table III.1. The regression analysis was done with the curve fitting tool in Matlab® with a nonlinear least square method with the trust region algorithm. The FE analysis data has a few outliers as shown in Figure 6.3, especially for ASTM F1554 Grade 105 anchors embedded in low strength concrete, hence, the least absolute residuals (LAR) method was used to minimize the impact of the outliers. The robust regression analysis indicates

$$\psi_s = \frac{0.35}{4+0.5\left(\frac{l_{ea}}{d_a}\right)^2}, \tag{6.4}$$

and the crushed concrete depth can be estimated as

$$\frac{l_{ec}}{d_a} = \frac{f_{uta}}{f_c}\psi_s. \tag{6.5}$$

Eq. 6.5 with a standoff factor in Eq. 6.4 is compared with the calculated crushed concrete depths in Figure 6.3 along with those measured in a total of 16 tests. The predicted crushed concrete depth is close to $0.5d_a$ for low to medium strength anchors in medium to high strength concrete with a relatively large stand-off height. This seems agree with general observations made from the tests available in the literature. However, Equation 6.5 may provide a reasonable estimation for a variety of situations.

Note that the parameters in Equation 6.5 were obtained from regression analyses of FE analyses, which randomly selected a maximum usable strain of 0.1 mm/mm [0.1 in./in.]. Considering the purpose of the FE parametric study was to explore the impact of critical factors rather than accurately predicting the experimentally obtained results, Equation 6.5 seems to consistently overestimate the crushed concrete depths. Hence, it is recommended to reduce the crushed concrete depths from Equation 6.5 by a factor of 0.6 before the resulting effective exposed lengths are used to calculate the shear capacity of standoff anchors.

6.4 Comparison with measured shear capacity of stand-off anchors

A database was assembled for the measured shear capacities of stand-off anchors, as shown in Appendix III. Table III.3 shows the configuration of the tests from three references in the literature in addition to the tests documented in Chapter 4. The database has a total of 81 tests, among which four tests from Nakashima (1998), nine tests from Petersen (2010), 56 tests from Cook et al. (2013), and eleven tests from Chapter 4. The details of the tests from the literature are documented in Chapter 2. The following factors were covered in these experimental tests, as listed in Table III.3:

1. Concrete compressive strengths: 24.1 MPa [3500 psi] and 45.5 MPa [6600 psi];
2. Steel strength: 483 MPa [70 ksi] to 896 MPa [130 ksi];
3. Anchor diameters: 12 mm [0.47 in.] to 25 mm [1.0 in.];
4. Stand-off heights: $0.06d_a$ through $3.5d_a$.

The measured shear capacities of exposed anchors are compared with those predicted by the capacity equations in the literature documented in Chapter 3 in Fig. 6.4. The capacity ratios are listed in Table III.4 with the results of simple statistical analysis at the end of the table.

6.4.1 Comparison with equations in the literature

The capacity reduction factor (0.8) recommended by ACI 318 document design is not sufficient as more than half of the tests showed a lower capacity, with the lowest ratio of 0.365, as shown in Fig. 6.4a and Table III.4. The design equation currently recommended by a *fib* TG2.9 is the conservative with only two tests showing lower shear capacity, as shown in Fig. 6.4b. These two tests are from this study with Type 2 cyclic loading as documented in Chapter 4. The repeated loading, shown in Figs. I.4 and I.8, may have caused low-cycle fatigue in anchor shafts, leading to low shear capacities, further reduced from the combined shear and bending. With these two tests removed from the statistical analysis in Table III.4, the measured shear capacities from all reported tests are higher than the predicted capacities. Meanwhile, the recommended design equation ignores the contribution of tension, especially when the anchor fractures at a large displacement in shear and the observed fracture clearly indicates tensile fracture. As a result, the prediction for seven tests is less than half of the measured capacity, with the largest test-to-prediction ratio of 8.0. Specifically, the tests collected from Petersen (2010) which were for anchors with specially designed anchor reinforcement, did not have any stand-off heights; however, concrete covers (with a thickness of 38 mm [1.5 in.]) spalled during the tests leading to significant exposed lengths. Despite an underestimated exposed length of $0.5d_a$ used, the equation by *fib* TG2.9 (Eq. 3.14b) is able to predict the shear capacities by ignoring the tensile contribution.

The equation recommended by Lin et al. (2011), Eq. 17a, requires an effective exposed length; hence the prediction shown in Fig. 6.4c used the actual exposed lengths (Column (14) in Table III.4). Again, the predicted shear capacities are conservative compared with measured capacities with only five tests underpredicted. The conservativeness is mainly from the use of yield strength of anchor steel (f_{yta}) in estimating the ultimate capacity of anchors controlled by steel fracture though this seemed necessary for the authors' double shear tests of anchor rods.

The equation recommended by Cook et al. (2013), Eq. 26b, better predicts the capacity of anchors conducted by the authors. Note that the further modification by McBride (2014) is not included in the equation, such that the second-order tensile effects, specific to the test setup used by the authors. The test-to-prediction ratios for 39 tests are slightly below 1.0 and 12 tests above 2.0. Eq. 26b also predicts well the tests documented in Chapter 4 except the two with Type 2 cyclic loading. Similar to the equation by *fib* TG2.9, tension contribution is ignored; hence the prediction can be overconservative for the tests showing tensile fracture, both by Nakashima (1998) and Petersen (2010).

6.4.2 Comparison with an empirical equation

The equation by Lin et al. (2011) is modified to better explain the existing tests of exposed anchors,

$$V_{sa} = f_{uta}A_{se,V}sin\beta + \frac{f_{uta}A_{se,V}}{1.11+2.74\frac{l_{ee}}{d_a}}, \tag{6.6}$$

where f_{uta} is the specified ultimate tensile strength, $A_{se,V}$ is the net shear area of anchors (knowing that threads rods are often used in stand-off connections, threads should be included in the fracture face), $\beta = d_a tan^{-1}\frac{\varepsilon_{max}}{d_a}$ is the plastic end rotation of exposed anchors, in which ε_{max} is the minimum elongation, obtained either through tensile tests of threaded rods or from material specifications, $\frac{l_{ee}}{d_a} = 0.6\frac{f_{uta}}{f_c}\psi_s + \frac{l_{ea}}{d_a}$ is the effective exposed length, in which $\psi_s = \frac{0.35}{4+0.5\left(\frac{l_{ea}}{d_a}\right)^2}$ is the stand-off coefficient, and l_{ea} is the apparent exposed length, measured from the bottom of

leveling nuts to the concrete surface. The equivalent exposed length, l_{ee}, should be larger than $0.5d_a$.

For an anchor made of a 25-mm [1 in.] ASTM F1554 Grade 36 threaded rod (f_{uta}=400 MPa [58 ksi]) embedded in 34.5-MPa [5000-psi] concrete, assuming minimum stand-off height (the multi-anchor connection prohibits the base plate from bearing on concrete), ψ_s is calculated as 0.0875, the crushed concrete depth is $0.61d_a$, the effective exposed length is $0.61d_a$. From the ASTM standard, the minimum elongation for the material is about 20%, leading to a plastic end rotation of 0.19 rad [11 degrees] at failure. The predicted shear capacity by Eq. 6.6 is $0.58f_{uta}A_{se,V}$. The shear capacity further reduces with an increase in the stand-off height.

If the anchor is made of a 25-mm [1 in.] ASTM F1554 Grade 105 threaded rod (f_{uta}=862 MPa [125 ksi]) embedded in 34.5-MPa [5000-psi] concrete, assuming minimum stand-off height (the multi-anchor connection prohibits the base plate from bearing on concrete), ψ_s is calculated as 0.0875, the crushed concrete depth is $1.31d_a$, the effective exposed length is $1.31d_a$. From the ASTM standard, the minimum elongation for the material is about 15%, leading to a plastic end rotation of 0.148 rad [8.5 degrees] at failure. The predicted shear capacity by Eq. 6.6 is $0.36f_{uta}A_{se,V}$. The shear capacity further reduces with an increase in the stand-off height.

Eq. 6.6 is obtained from Eq. 17a by assuming

1) the use of ultimate tensile strength (f_{uta}) instead of yield strength (f_{yta}) is justified by the limited shear tests of exposed anchors in the literature though the use of yield strength seemed reasonable in double shear tests of anchor rods. This change may be justified by the conservativeness built into Eq. 17a compared with other models, as shown in Fig. 3.2

2) the section modulus of threaded rods, which was calculated as a round section with an area of $A_{se,V}$, is replaced by $A_{se,V}(0.86d_a)$, where d_a is the nominal diameter of anchors made of threaded rods. The 0.86 factor is the average ratio of the diameter of the equivalent round section to the nominal anchor diameter.

3) the modification for the combined shear and bending ($cos\beta$) is ignored because the end rotation from oversized holes in the connecting plate is excluded from the estimation of maximum end rotation of exposed anchors (β).

The shear capacities predicted by Eq. 6.6 are compared with the test results in Fig. 6.5. The average capacity ratio is 1.34 with a standard deviation of 0.318, all improved compared with other equations as shown in Table III.4. The equation can explain the tests by Cook et al. (2013) except that one test in DS6 group is overestimated, which may have been due to the second-order tension as discussed by McBride (2014). In addition, tests in DS9 group are underestimated because the base plates were flush mounted, which is outside the scope of this study. The tests were included because the test setup used in the study prevented the base plate from compressing the concrete. It should be noted that the both the steel plate beneath the roller near the test anchors and the steel tube on the front face (acting as reaction to the applied shear) in the direct shear tests by Cook et al. (2013) (Fig. 2.18) may have confined concrete leading to a lower crushed concrete depth and higher anchor shear capacities. Eq. 6.6 can also explain well the tests documented in Chapter 4 except the two tests using Type 2 cyclic loading. The over-prediction is about 5% when these two tests are excluded.

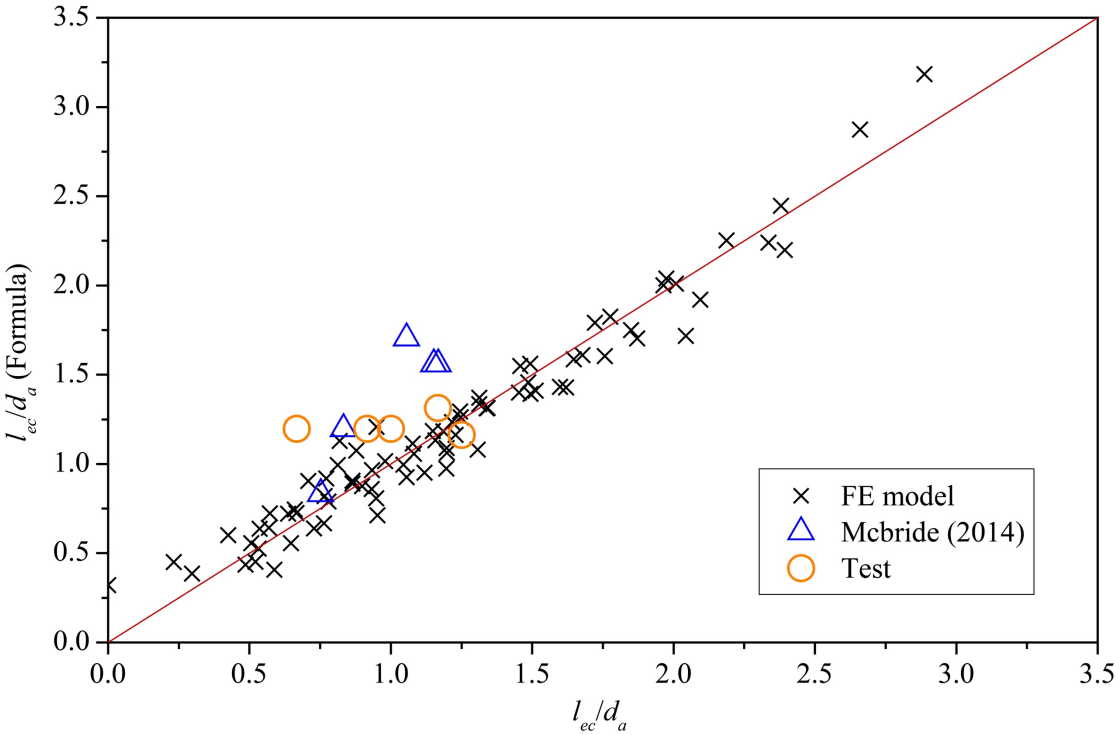

Figure 6.1. Comparison of Equation 6.1 with FE analysis results and test results

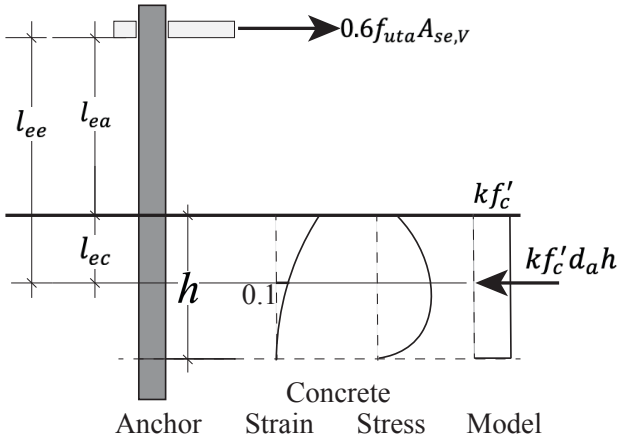

Figure 6.2. Illustration of load balance in stand-off anchors

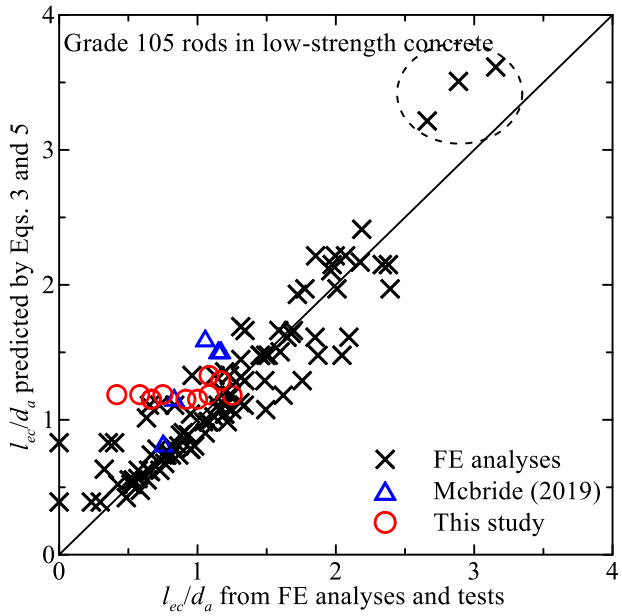

Figure 6.3. Comparison of Equation 6.5 with FE analysis results and test results

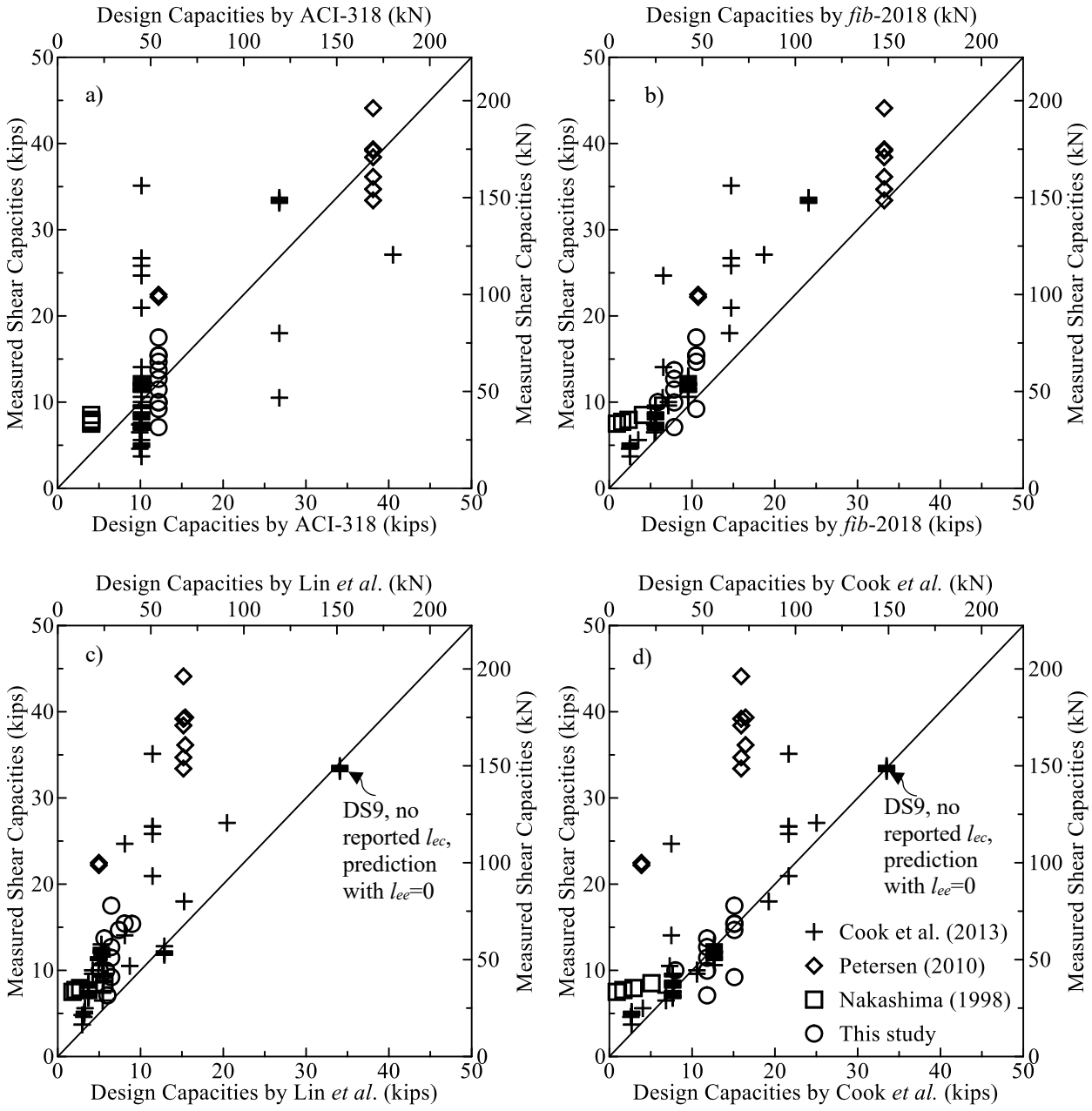

Figure 6.4. Comparison of predicted shear capacities by Equations in Chapter 3 with tests

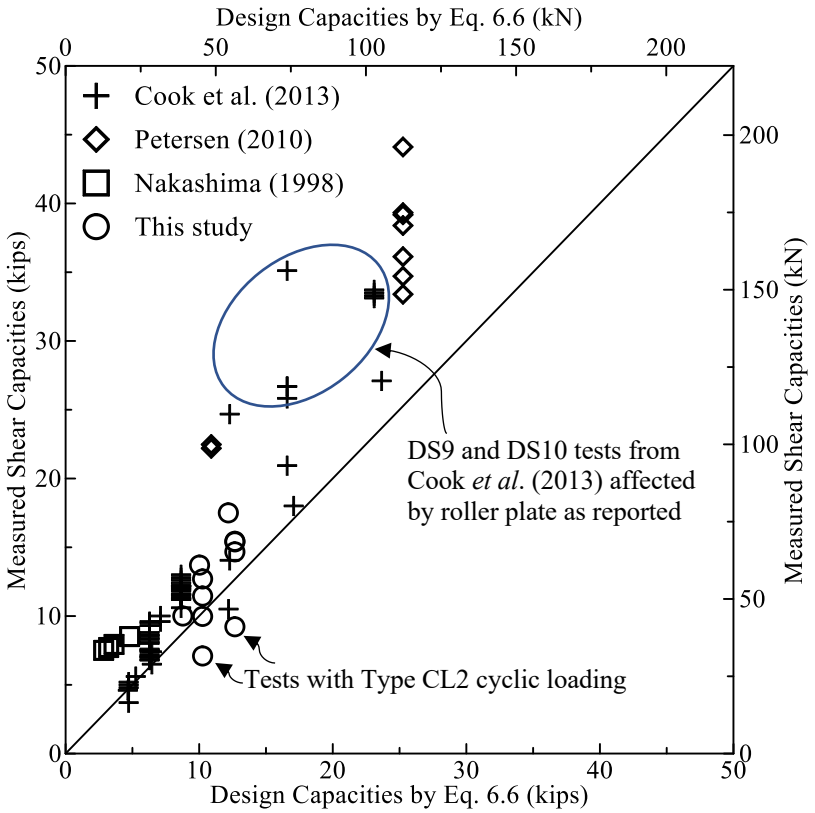

Figure 6.5. Comparison of predicted shear capacities by Eq. 6.6 with tests

Chapter 7. Summary and Conclusions

7.1 Summary of study

Anchor bolts embedded in concrete are commonly used in construction. Anchor connections at column bases are often stand-off connections because the connected based plate is elevated from the concrete surfaces, and leveling nuts are used to adjust the position of attached steel components. In this case (column footing connections without grouting), a portion of anchor bolts may be exposed. Such anchor bolts in shear are subjected to combined bending, shear and tension. The shear capacity of exposed anchors is critically related to the total exposed length because the bending moment applied to anchor shaft is directly related to the applied shear by the exposed length. Equations have been proposed in the literature to calculate shear capacities of stand-off anchors, mostly based on the stand-off height.

Concrete can be crushed in front of an anchor shaft in shear, especially in ungrouted stand-off connection. The crushed concrete causes an increase in the total length of the anchor shaft, laterally unsupported, from which the applied shear leads to a bending moment at both ends of the exposed anchor shaft. This crushed concrete depth in front of anchors in shear is the focus of this study.

A group of shear tests of anchors made of ASTM F1554 Grade 55 threaded rods were presented simulating the behavior of exposed anchors in shear. These tests were conducted by Dr. Zhibin Lin using the specimens by created by Petersen (2010). A total of 12 single cast-in anchors were available in four concrete blocks, including six under monotonic shear and six under cyclic shear in either load-controlled or displacement-controlled loading. Knowing that the crushed concrete depth (l_{ec}) can be affected by concrete strength (f_c') (Grosser, 2012) and the anchor diameter (d_a) (Gomez *et al*. 2009), this group of tests explored the impact of stand-off height (l_s). Three stand-off heights, $0.08d_a$, $0.5d_a$ and $1.0d_a$, were chosen that were allowed by the geometry of the specimens. No leveling nut was used beneath the loading plate. Four types of loading were used: 1) monotonic loading in displacement control; 2) cyclic loading in displacement control with three cycles per displacement level; 3) cyclic loading in force control with three cycles per peak load level; and 4) cyclic loading in force control with indefinite number of cycles at roughly 75 percent of the measured monotonic loading capacity. In addition to the applied shear and the corresponding lateral displacement, the depths of crushed concrete were measured after the it was removed.

Finite element analyses using TNO DIANA® were conducted to explore key parameters, including the concrete and anchor materials, the anchor diameters, and the stand-off heights. FE models were first created for the shear tests documented in this report, on cast-in-place single anchor. Based on symmetry, only half of specimen was simulated. The characteristic parameters of the material models were based on available reported values. Unreported parameters, such as the elastic modulus and tensile strength of concrete, were calculated in accordance with the recommendations in ACI 318 (2014). Four-node, three-side isoparametric solid tetrahedron elements were used for modeling the concrete block, steel anchor, loading plate, and the nut at the embedded end. All interface elements, including those between concrete and bolt, bolt and loading plate, and loading plates and nuts were assumed to carry compressive only, that is zero tension and shear strengths. Moreover, the compressive stiffness is assumed to be the minimum of the materials on both sides of the interface and be linear elastic during the entire analyses. Element size must be reduced near the anchor to create proper geometry transition from the round anchor to the rectangular concrete block, which was accomplished automatically by the program with mesh size control measures. In general, the FE models were able to capture the behavior of the specimens with three stand-off

heights subjected to monotonic loading. Knowing that modeling concrete damage due to cyclic loading can be extremely challenging, the impact of cyclic loading was not considered in this study.

A parametric study with a total of 101 FE analyses was then conducted to investigate the key factors for the crushed concrete depth: the concrete/steel materials, anchor diameters, and stand-off heights (assuming no leveling nuts). The parametric study is based on the model for the specimens used in the experimental tests, especially the geometry of the FE models. In addition, a concrete model considering concrete behavior under 3D confinement was selected and the model parameters were calibrated using experimental tests of concrete under both active and passive confinement in the literature. Furthermore, mesh sensitivity studies were conducted to determine optimized mesh sizes, especially in the direction of anchor embedment. The mesh sensitivity analyses indicate that a vertical mesh size of 6.35 mm [1/4 in.] was suitable for the parametric study. Finally, we assumed that concrete is crushed below the concrete surface when the lateral compressive strain of concrete (in X-direction, as adopted by the models in this study) reached at a value of 0.1 mm/mm [0.1 in./in.].

7.2 Conclusions

The experimental tests indicated that the exposed length in general reduces with an increase in the stand-off heights. In addition, the tests indicated that the crushed concrete depths did not increase much under displacement-controlled cyclic loading, hence the ultimate shear capacities were close to those achieved by the anchors under monotonic loading. When the cyclic load is controlled by peak loads (Type 1 cyclic loading), the crushed concrete depths increased after each loading cycle. Correspondingly, the ultimate shear capacities were lower than those achieved by the anchors under monotonic loading. This observation was confirmed by the two tests using Type 2 load-controlled cyclic loading, leading to further reduced shear capacities. It should be noted that low-cycle fatigue may have also contributed to the lower shear capacities.

The parametric study using 101 FE analyses indicated that different from the fixed value of $0.5d_a$ specified in the literature, crushed concrete depths are rather different under various parameter combinations. Within the parameter of the investigated range, the crushed concrete depth reaches the maximum value when the stand-off height is $0.5d_a$. With the increase of stand-off height, the failure mode of the anchor turns into bending failure, and its shear capacity decrease with the increase of effective exposed length, which means that the lateral compressive stress in concrete was decreased under peak load, which eventually lead to the reduction of crushed concrete depth. In addition, when the stand-off height is greater than $0.5d_a$, the crushed concrete depth shows a significant increase with an increase in anchor diameters and steel ultimate strengths. Furthermore, with an increase in concrete strengths, the crushed concrete depth is significantly reduced.

Equations were proposed for the estimation of total exposed length based on the experimental and the FE analysis results. The proposed equation fits well the total exposed lengths determined from the FE analyses; however, the predicted total exposed lengths are higher than the measured values thought the number of measured crushed concrete depths is very limited. A reduction factor of 0.6 was applied to the proposed equation for practical uses. With the equivalent exposed length, which includes the apparent exposed length measured from the bottom of leveling nuts (or base plate if no leveling nut is used) and the crushed concrete depth, design equations were proposed for the shear capacity of stand-off/exposed anchors. The equation is modified from that proposed by Lin *et al*. (2011), and considers combined shear, bending and tension applied to an anchor shaft from

applied shear forces. The equations are verified by 90 tests, including 79 tests collected from three sources in the literature and 11 tests reported in this study. The proposed equation fits well the available tests.

7.3 Suggested future studies

The recommendation of this report is based on limited experimental tests. Addition tests are needed to explore the applicability of the conclusion of this study, especially outside the range of the investigated parameters such as large-diameter anchors. Furthermore, concrete crushing can be limited when grout is used in stand-off connections; hence further finite element analyses should be conducted for stand-off anchors in grouted connections. Finally, the behavior of exposed anchors under seismic loading should be studied with great details.

References

1. American Concrete Institute (2014). Building Code Requirements for Structural Concrete. ACI 318-14. Farmington Hills, MI.
2. AASHTO (2013). LRFD Bridge Design Specifications. AASHTO, Washington, D.C.
3. Adihardjo, R., and Soltis, L. (1979). Combined Shear and Tension on Grouted Base Details. *AISC Engineering Journal*, Vol. 16, No. 1, pp. 23–26.
4. American Institute of Steel Construction (2010). Steel Construction Manual, 14th ed., Chicago, Ill.
5. Asia-Pacific Economic Cooperation. (2002). Earthquake Disaster Management of Energy Supply System of APEC Member Economies, Energy Commission, Ministry of Economic Affairs, Chinese Taipei.
6. Bouwman, L. P.; Gresnigt, A. M.; Romeijn, A. (1989). Research into the Connection of Steel Base Plates to Concrete Foundations. Stevin Report 25.6.89-05/c6.
7. Candappa, D. C., J. G. Sanjayan, and S. Setunge. (2001). Complete triaxial stress-strain curves of high-strength concrete. Journal of Materials in Civil Engineering. Vol.13 No. 3: pp. 209–215.
8. Chesson, E., Faustino, N., and Munse, W. (1965). High-Strength Bolts Subjected to Tension and Shear. ASCE Journal of the Structural Division, Vol. 91, No. ST 5, pp. 155–180
9. Cook, R. A., and Klingner, R. E. Ductile Multiple-Anchor Steel-to Concrete Connections. ASCE Journal of Structural Engineering, Vol. 118, No. 6, 1992, pp. 1645–1665.
10. Cook, R., Prevatt D., and Mcbride, K. (2013). Steel shear strength of anchors with stand-off base plates. Report No. BDK75 977-49, Department of Civil and Coastal Engineering, College of Engineering, University of Florida, Gainesville, FL, USA.
11. Cornelissen, H. A. W., Hordijk, D. A., and Reinhardt, H. W., "Experimental determination of crack softening characteristics of normalweight and lightweight concrete," *Heron,* Vol. 31, No. 2, 1986, pp. 45-56.
12. Eligehausen, R., Mallée, R., & Silva, J. (2006). Anchorage in concrete construction (Vol. 10). John Wiley & Sons.
13. Fisher, J. and Kloiber, L. (2006). Design Guide 1: Base plate and anchor rod design. *Steel Design Guide Series*.
14. Fichtner, S. (2011). Untersuchungen zum Tragverhalten von Gruppenbefestigungen unter Berücksichtigung der Ankerplattendicke und einer Mörtelschicht, Dissertation Universität Stuttgart. (in German)
15. Foley, C. (2004). "Structural analysis of sign bridge structures and luminaire supports." Rep. No. 04-03, Wisconsin DOT, Madison, WI.
16. Hordijk, D. A., "Local Approach to Fatigue of Concrete," PhD thesis, Delft University of Technology, The Netherlands, 1991.
17. Gomez, I., Kanvinde, A., and Deierlein, G. (2011). Experimental Investigation of Shear Transfer in Exposed Column Base Connections. *AISC Engineering Journal*, Vol. 48, No. 4, pp. 245–264.
18. Grauvilardell, J., Lee, D., Hajjar, J., and Dexter, R. (2005). "Synthesis of design, testing and analysis research on steel column base plate connections in high-seismic zones." Structural Engineering Report No. ST-04-02, University of Minnesota, Minneapolis, MN
19. Gresnigt, N., Romeijn, A., Wald, F., and Steenhuis, M. (2008). Column Bases in Shear and Normal Force. HERON, Vol. 53, No. 1, pp. 87–108.

20. Grosser, P. (2012). Load-Bearing Behavior of Anchorages Subjected to Shear and Torsion Loading in Uncracked Concrete. PhD dissertation. University of Stuttgart, Stuttgart, Germany,
21. Hoehler, M. (2006). "Behavior and testing of fastenings to concrete for use in seismic applications." PhD thesis, University of Stuttgart, Stuttgart, Germany.
22. Kestner J. T., Harries K. A., Pessiki S. P., Sause R., Ricles J.M., "Rehabilitation of reinforced concrete columns using fiber reinforced polymer composite jackets," ATLSS Report 97-07. Lehigh University, 1997.
23. Klingner, R., Mendonca, J., and Malik J. (1982). "Effect of reinforcing details on the shear resistance of anchor bolts under reversed cyclic loading." *ACI Structural Journal*, Vol. 79, No. 1, pp. 471-479.
24. Lifeline Earthquake Engineering (ASCE) (1997). "Northridge earthquake: lifeline performance and post-earthquake response. a report to U.S. department of commerce; technology administration." National Institute of Standards and Technology; Building and Fire Research Laboratory. Gaithersburg, MD 20899.
25. Lin, Z., Petersen, D., Zhao, J., and Tian, Y. (2011) "Simulation and Design of Exposed Anchor Bolts in Shear." *International Journal of Theoretical and Applied Multiscale Mechanics*, Vol. 2, No. 2, pp. 111–129
26. Lin, Z., Zhao, J. and Petersen, D., (2013). Failure analysis of anchors in shear under simulated seismic loads. *Engineering Failure Analysis*, Vol. *31*, pp.59-67.
27. Liu, C. (2014). Evaluation of Anchor Bolts with Excessive Standoff in Cantilever Sign and Signal Structures. *Practice Periodical on Structural Design and Construction*, Vol. 19, No. 2. p.04014002.
28. Mcbride, K. (2014). Mcbride, K., (2014). Steel strength of anchor bolts in stand-off base plate connections. PhD Dissertation, University of Florida, Gainesville, FL.
29. Mcbride, K. (2019) Personal communication.
30. Nakashima, S. (1998). "Mechanical Characteristics of Exposed Portions of Anchor Bolts in Steel Column Bases Under Combined Tension and Shear." *Journal of Constructional Steel Research*, Vol. 46, No. 1, pp. 262-263.
31. Pallarés, L. and Hajjar, J. (2009). "Headed steel stud anchors in composite structures, Part I: Shear." *Journal of Constructional Steel Research*. Vol. 66, pp. 198-212.
32. Petersen, D. (2010). Seismic behavior and design of cast-in-place anchors in plain and reinforced concrete. MS thesis, University of Wisconsin, Milwaukee, WI.
33. Petersen, D., Lin, Z., and Zhao, J. (2018) Design of Anchor Reinforcement for Seismic Tension Loads, *Engineering Structures*, Vol 164, pp. 109-118.
34. Scheer, J., Peil, U. and Nölle, P. (1987). Schrauben mit planmäßiger Biegebeanspruchung (Screws under planned bending). Report No. 6079. Technische Universitat Braunschweig, Germany.
35. Thorenfeldt, E.; Tomaszewicz, A.; and Jensen, J. J., "Mechanical Properties of High-Strength Concrete and Applications in Design," Conference on Utilization of High-Strength Concrete, Stavanger, Norway, 1987, pp. 149-159.

Appendix I: Observed behavior of single stand-off anchors in shear

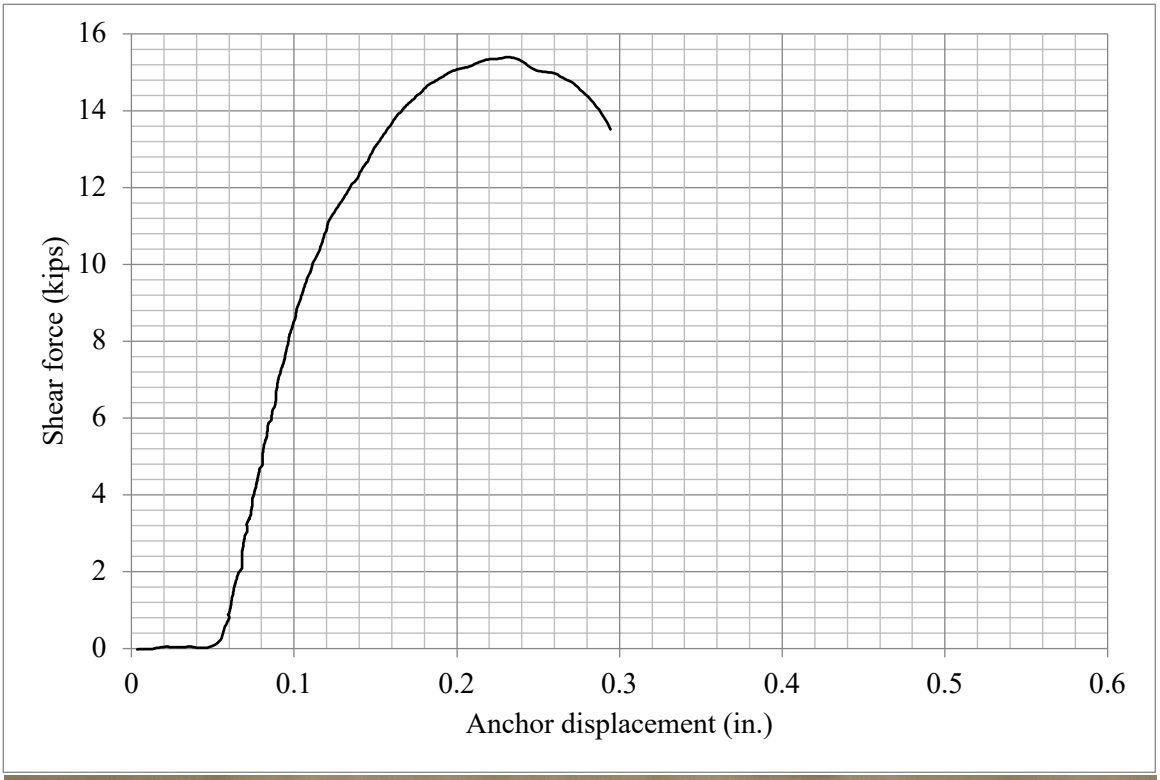

Figure I.1 Behavior of Specimen 08052011_0.08da-MD

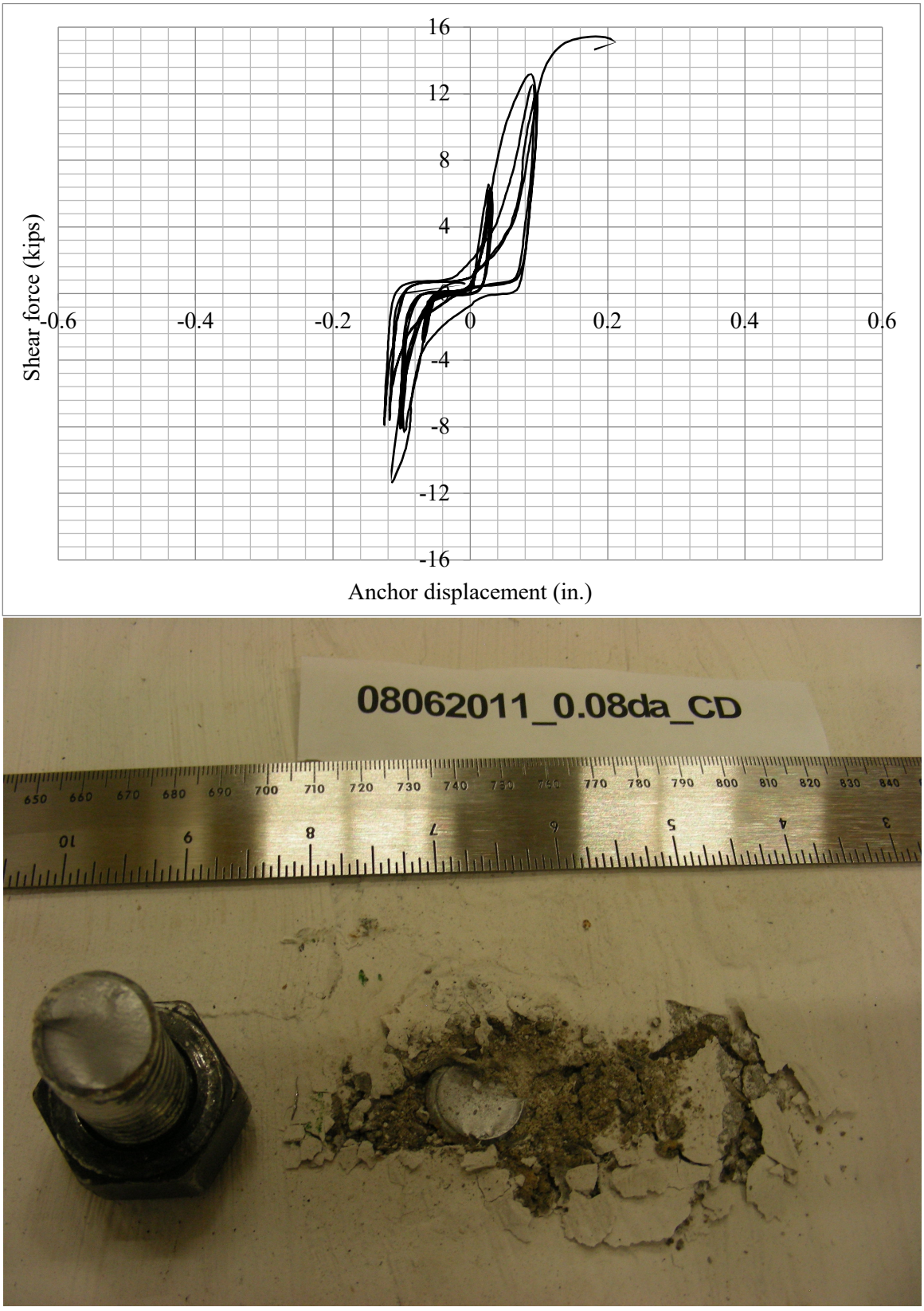

Figure I.2 Behavior of Specimen 08062011_0.08da-CD

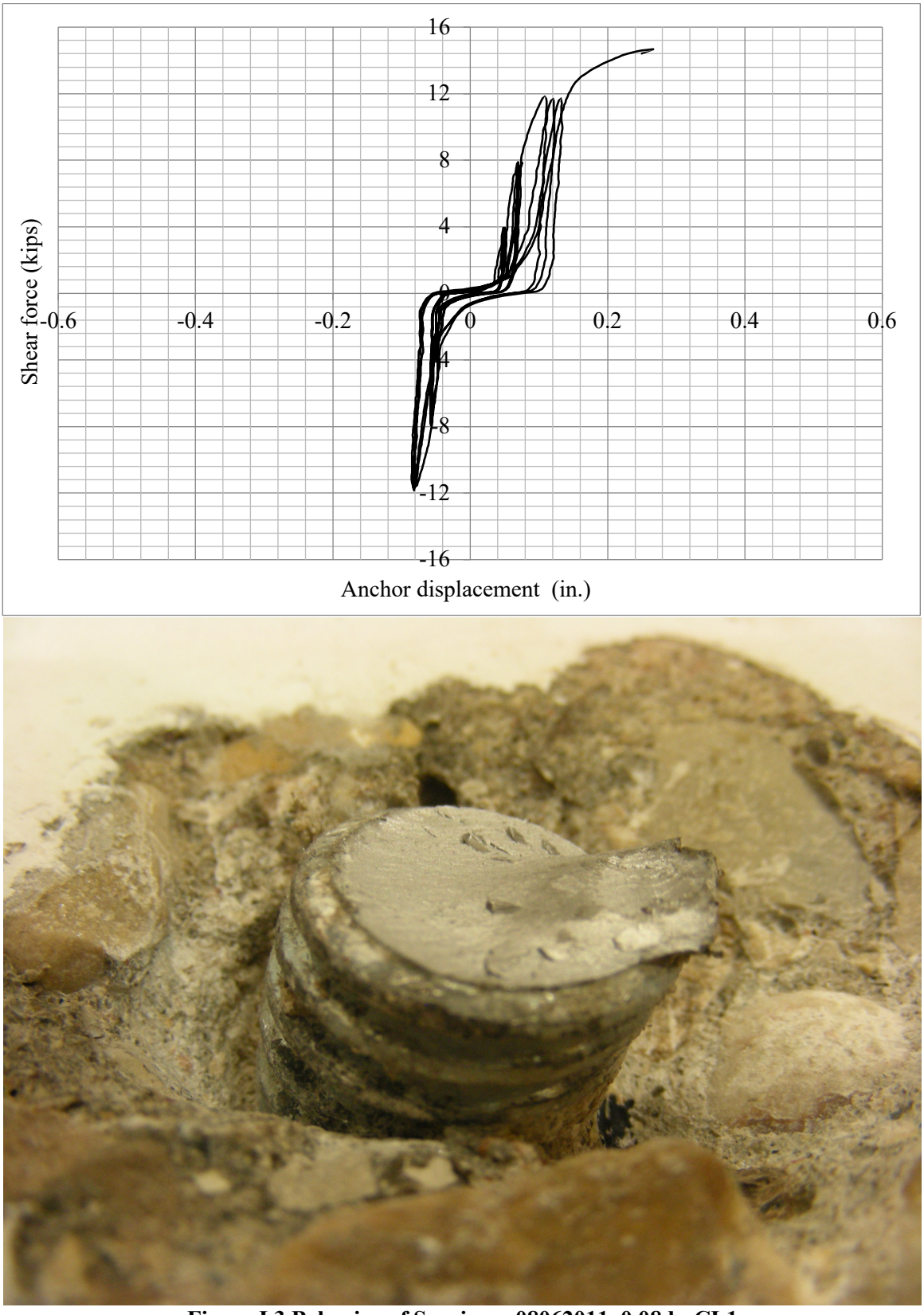

Figure I.3 Behavior of Specimen 08062011_0.08da-CL1

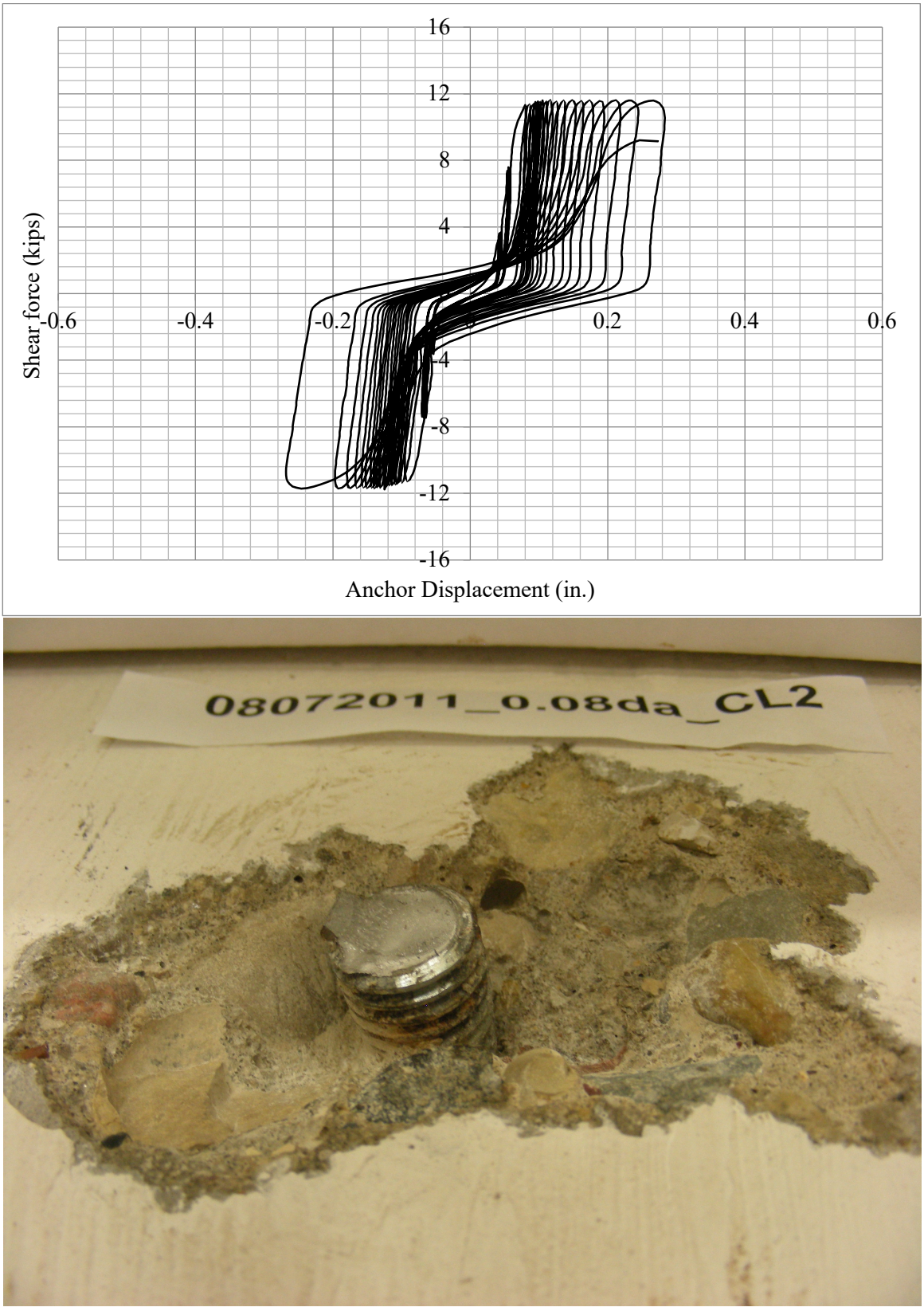

Figure I.4 Behavior of Specimen 08072011_0.08da-CL2

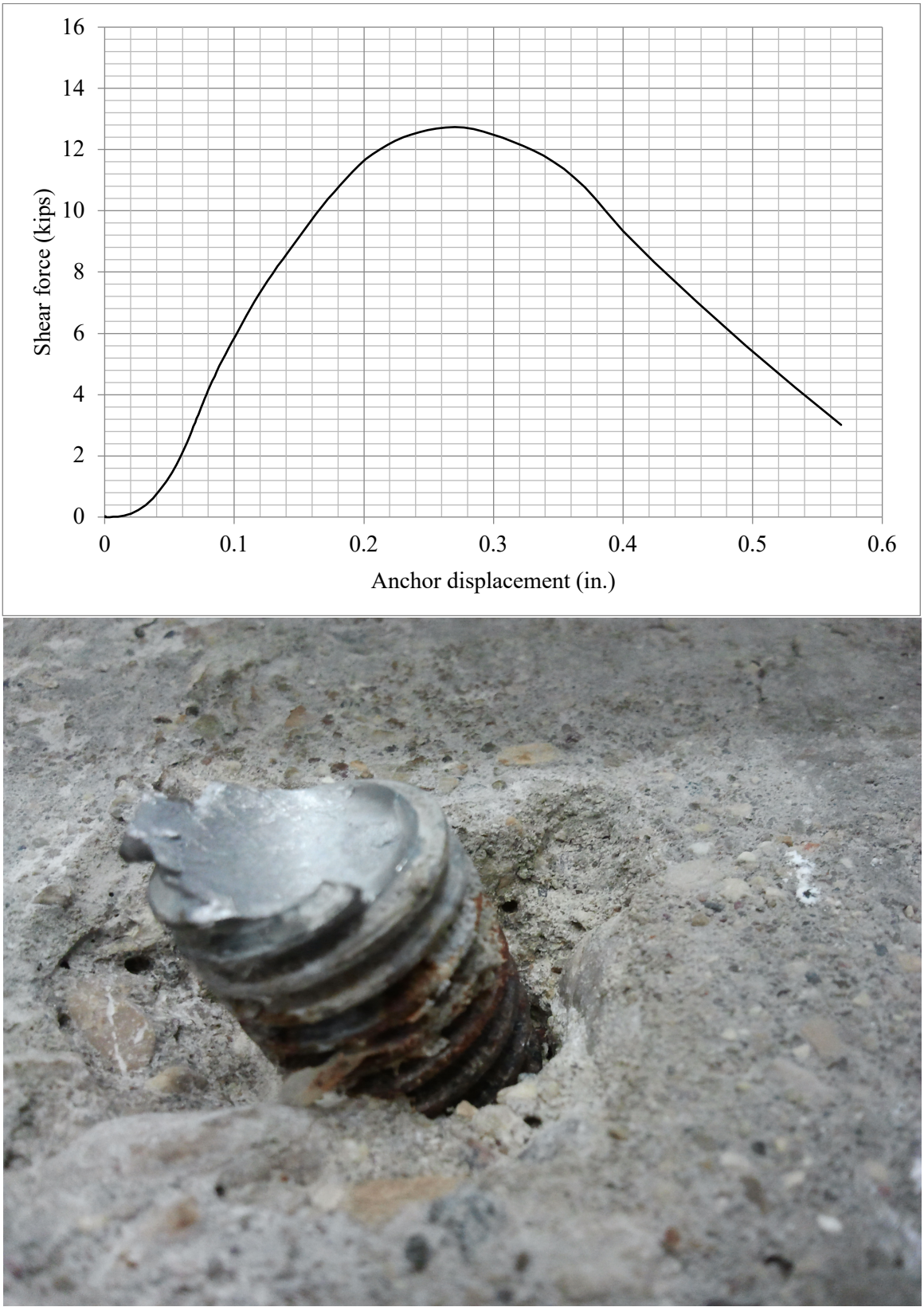

Figure I.5 Behavior of Specimen 08072011_0.50da-MD

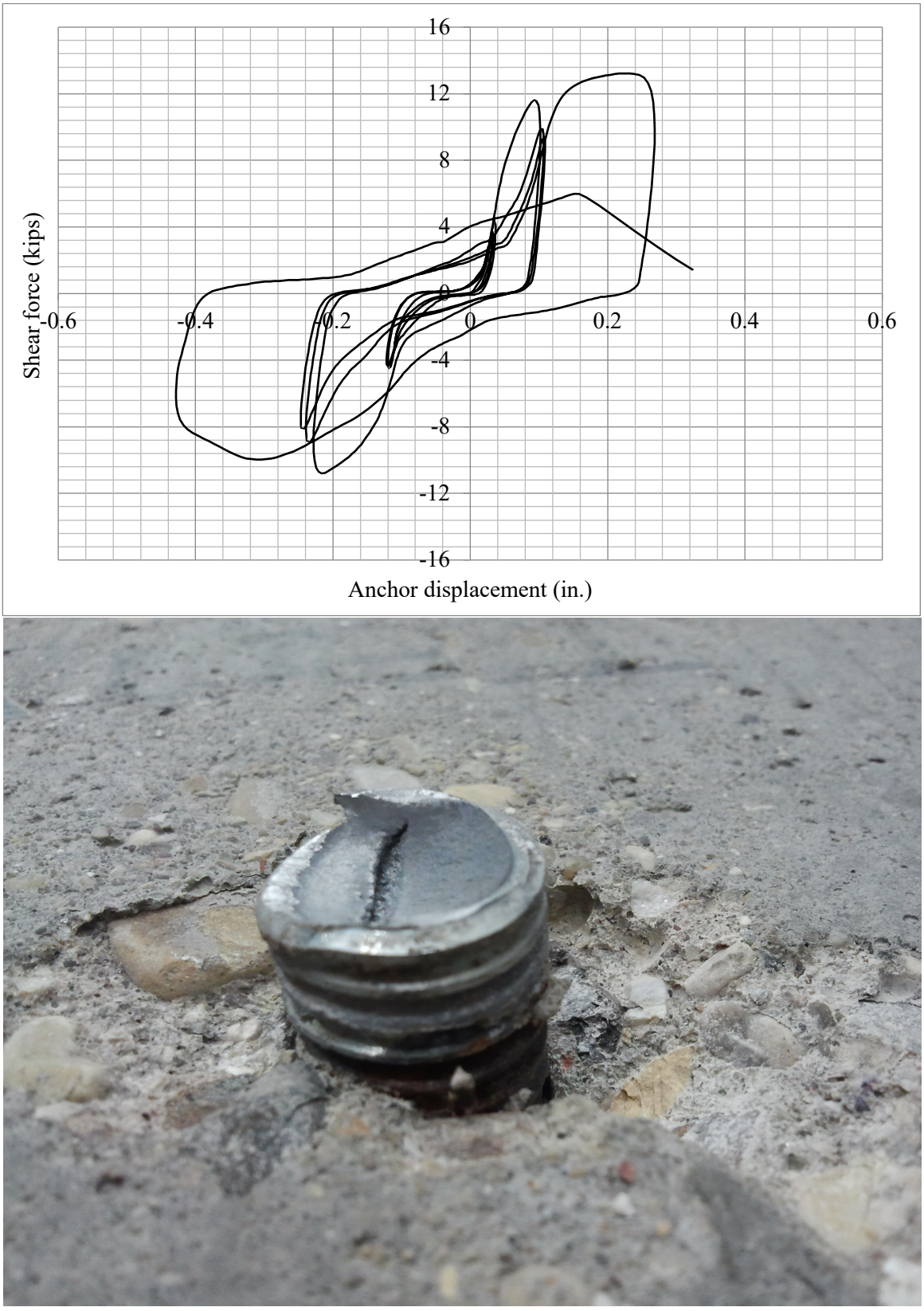

Figure I.6 Behavior of Specimen 08092011_0.50da-CD

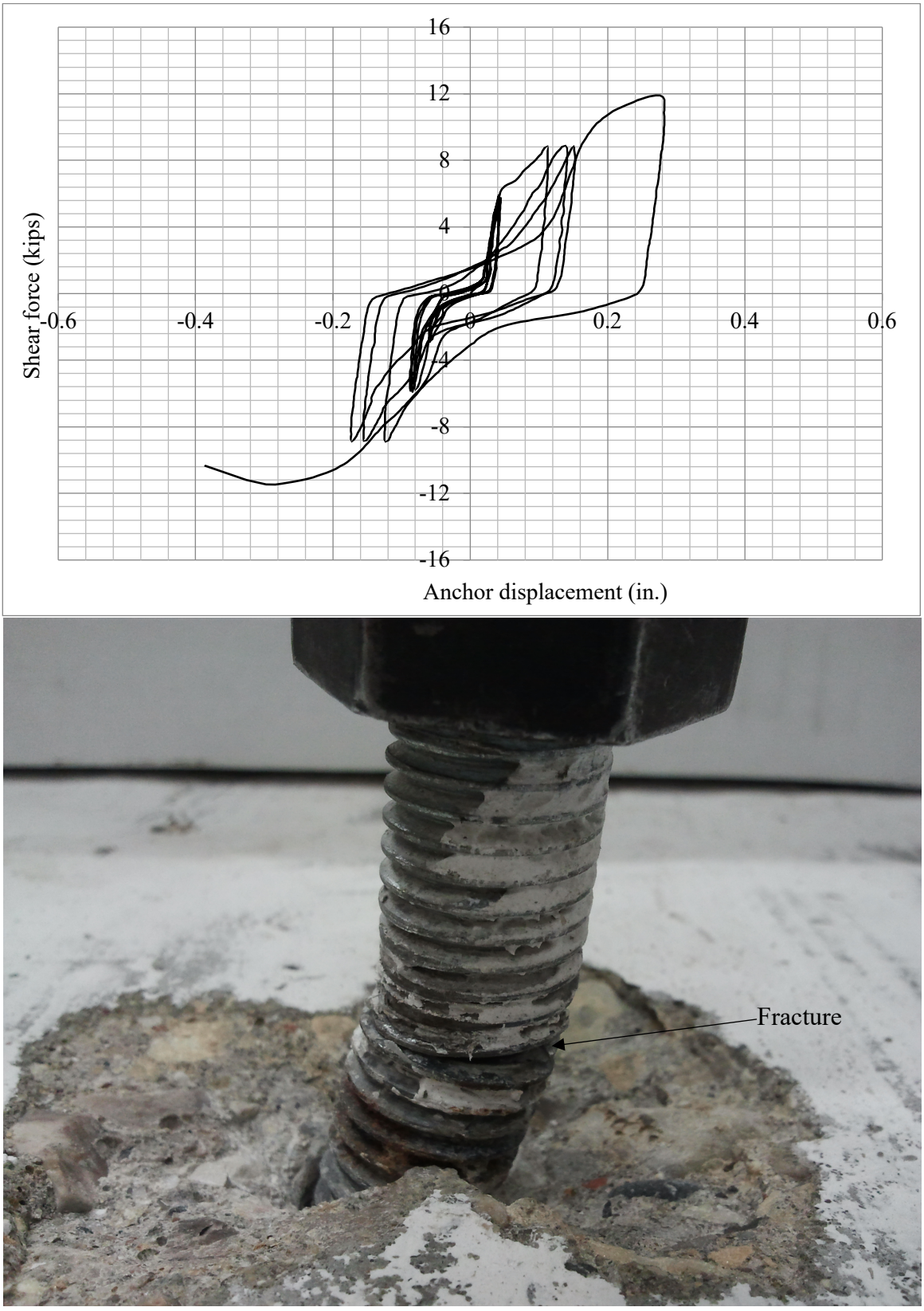

Figure I.7 Behavior of Specimen 08092011_0.50da-CL1

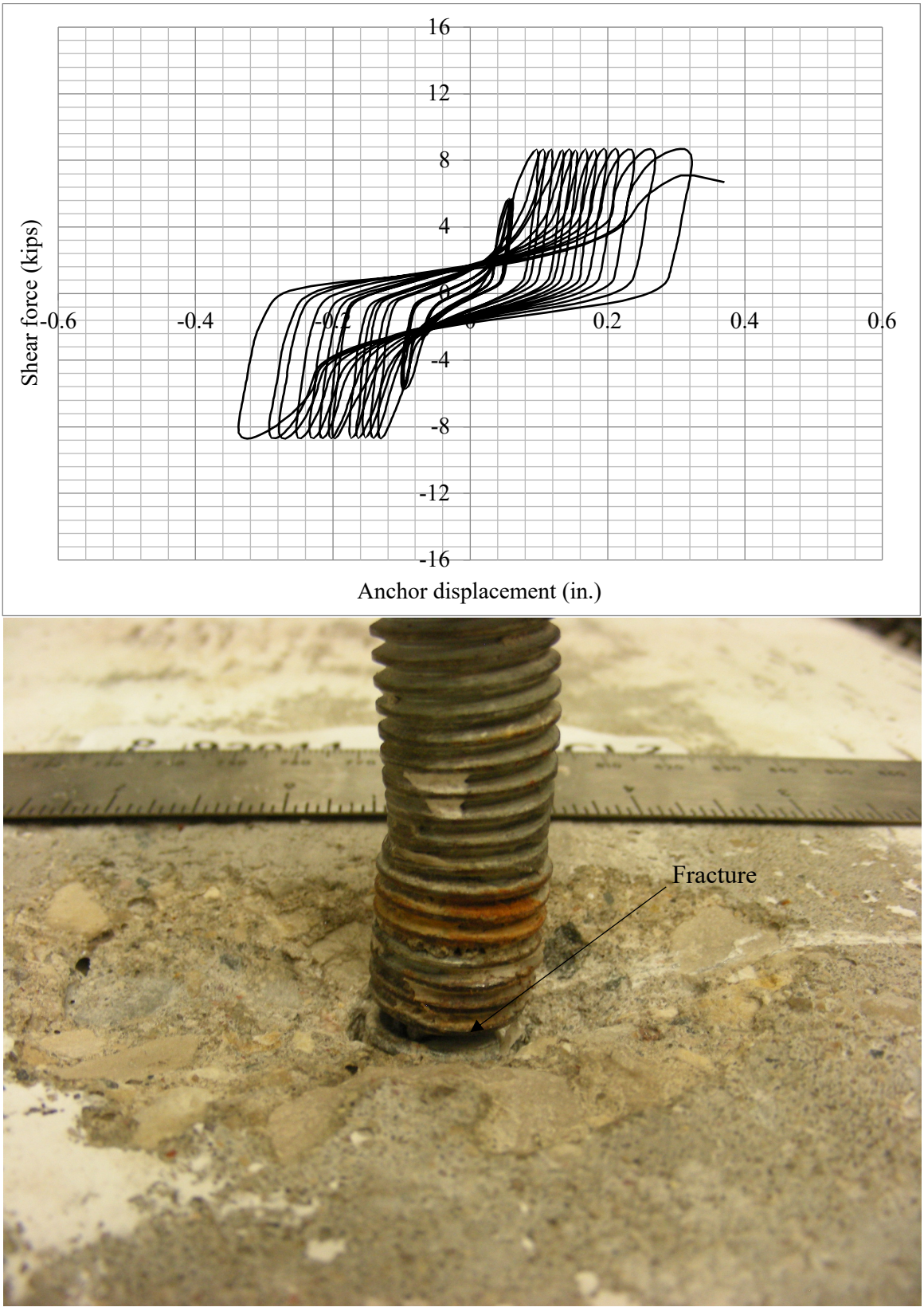

Figure I.8 Behavior of Specimen 08092011_0.50da-CL2

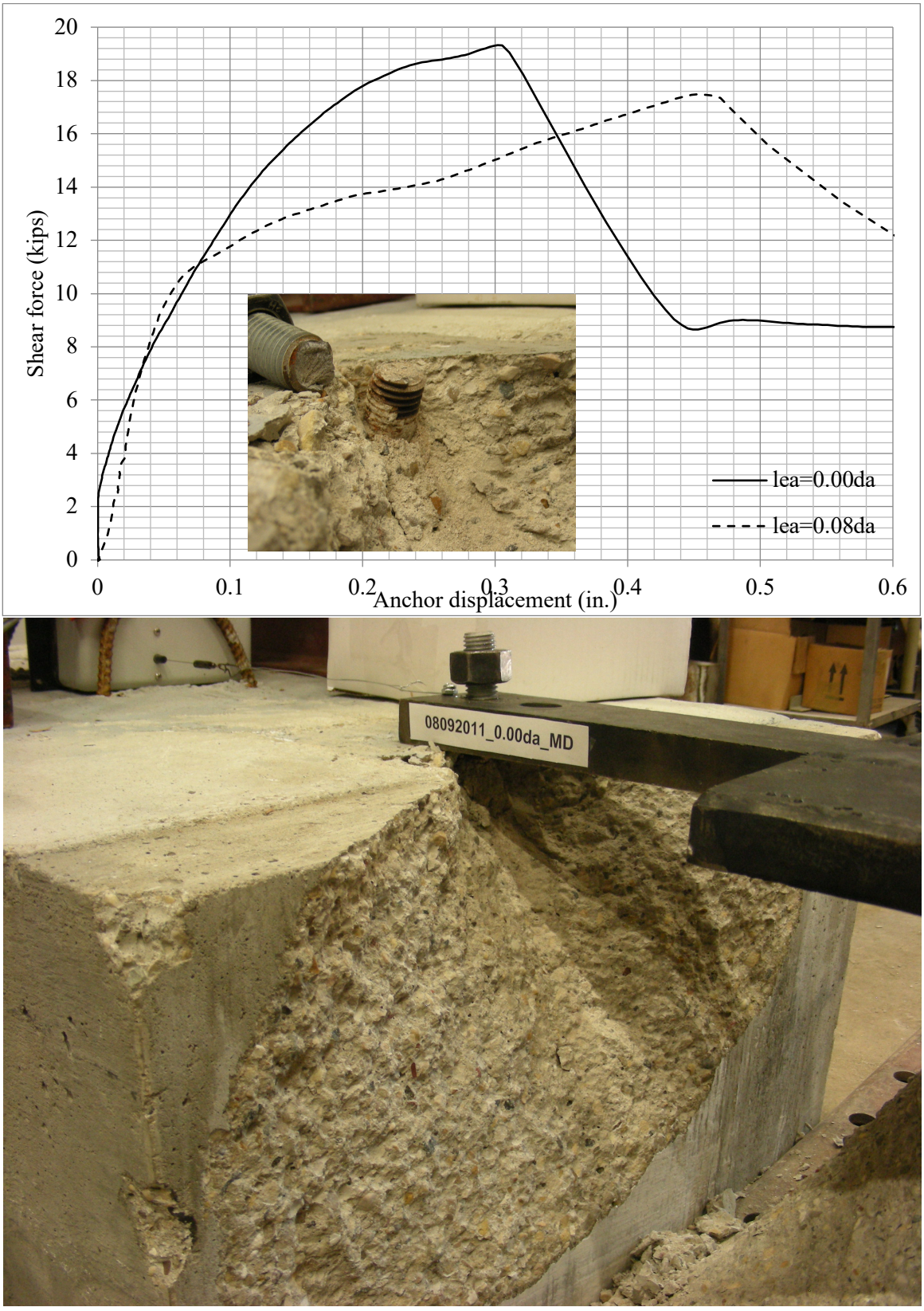

Figure I.9 Behavior of Specimen 08092011_0.00da-MD

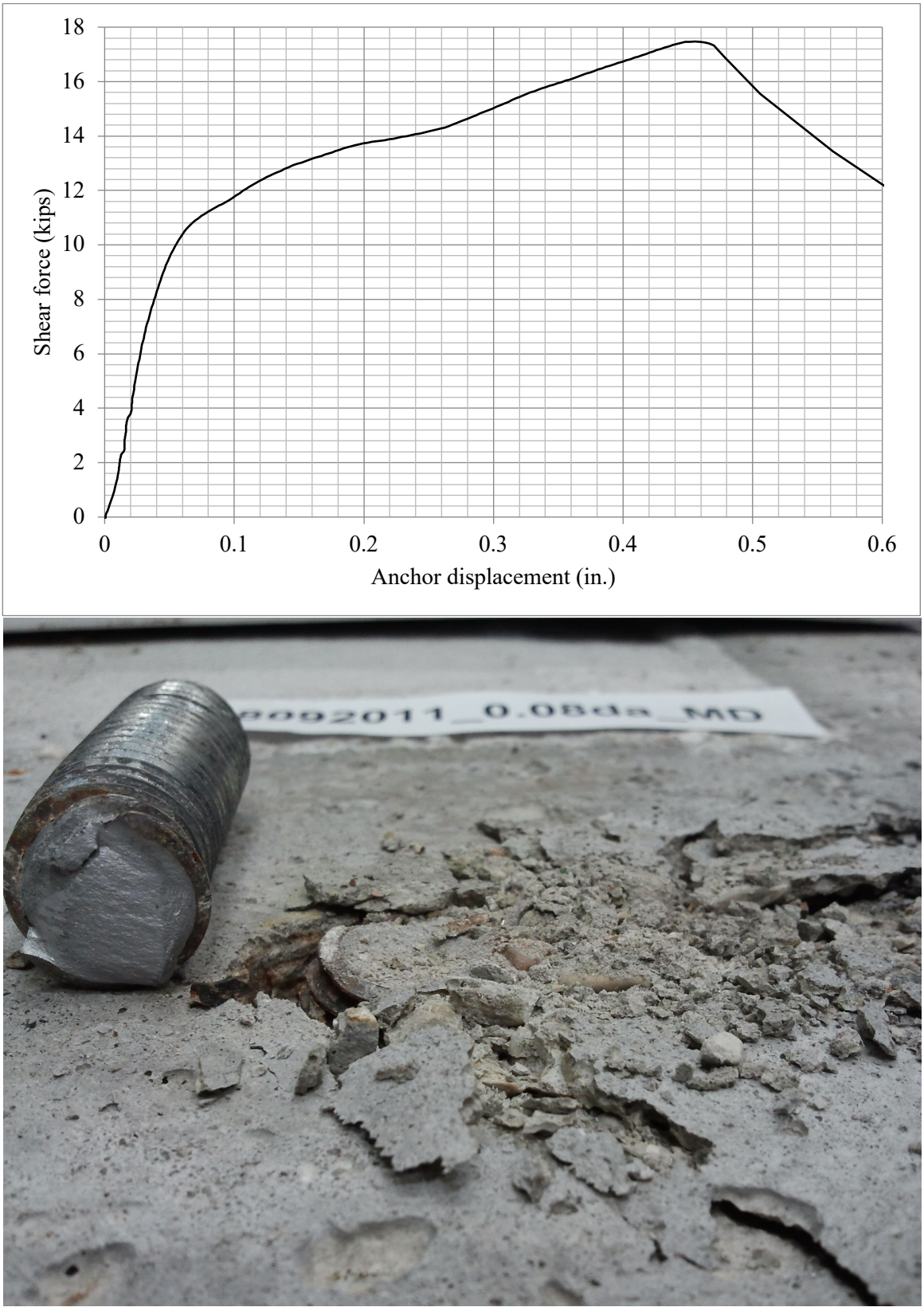

Figure I.10 Behavior of Specimen 08092011_0.08da-MD

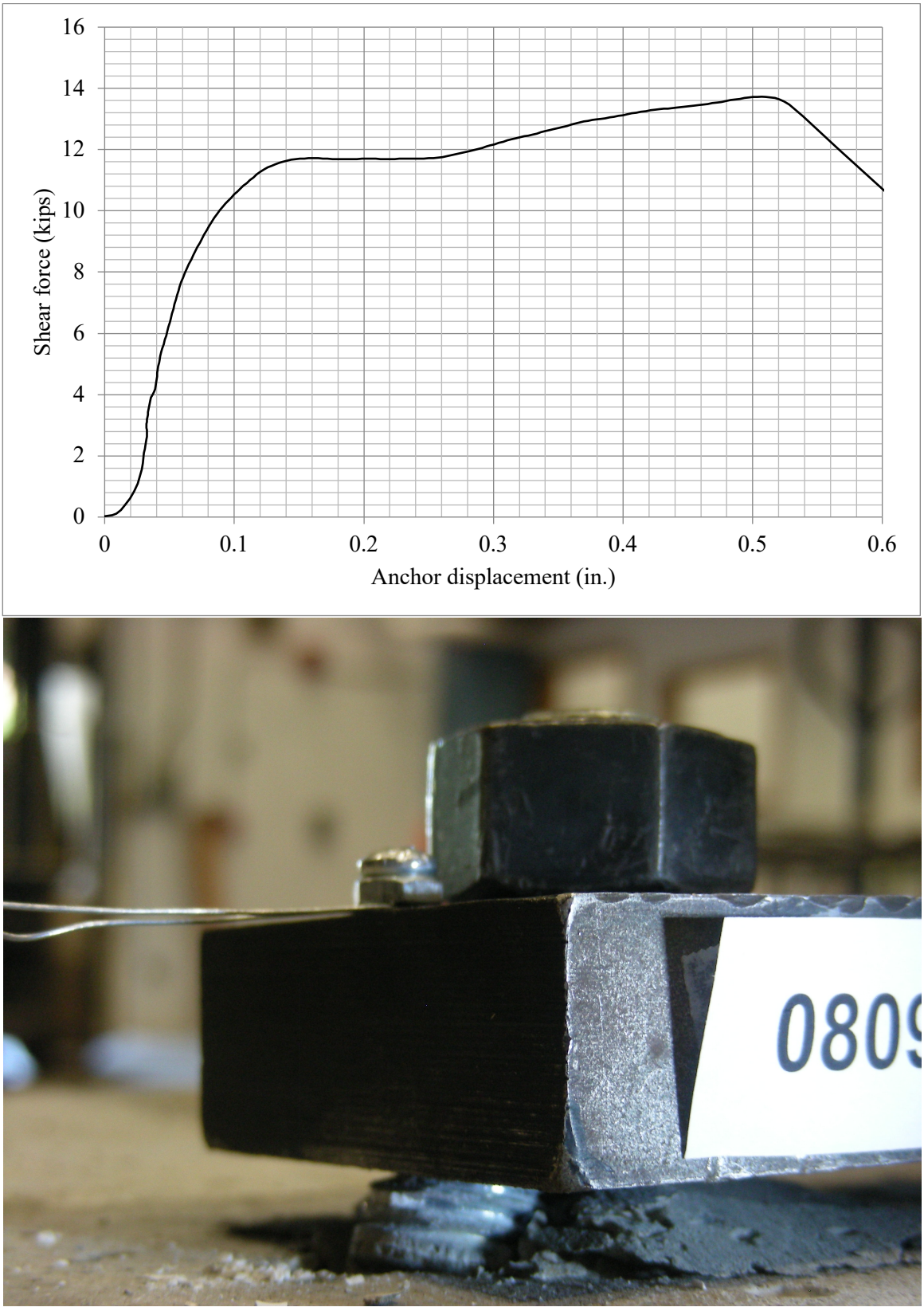

Figure I.11 Behavior of Specimen 08092011_0.50da-MD

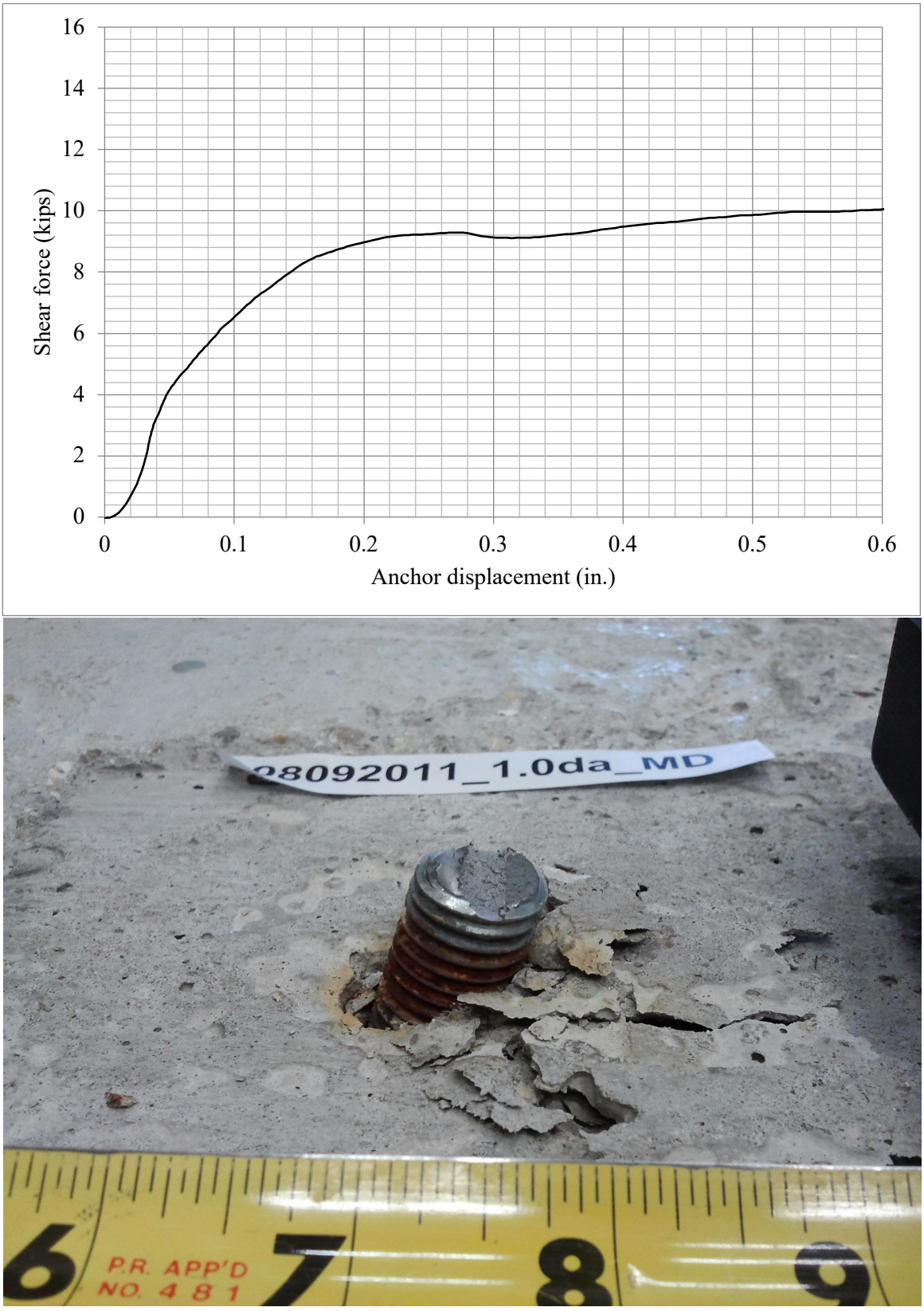

Figure I.12 Behavior of Specimen 08092011_1.00da-MD

Appendix II: Calibration of triaxial stress-strain behavior of concrete

1. Calibration of the stress-strain behavior of concrete with active confinement

For obtaining axial-stress–axial-strain and axial-stress–lateral-strain behavior of concrete, a series of 100 mm × 200 mm cylindrical specimens had been tested under confining pressure of 0 MPa, 4MPa, 8MPa and 12MPa, respectively by Candappa et al. (2000). The specimens with uniaxial strength of 60.6 MPa were chosen here for calibrating the constitutive model of confined concrete in finite element soft. As illustrated in Figure 1, two types of concrete are meshing compared. Type A is radial mesh generation, in which the six-node isoperimetric solid wedge elements (TP18L) were used in the center part and the eight-node isoperimetric solid brick elements were used in the rest. Meanwhile, only the eight-node isoperimetric solid brick elements were used in Type B, then ensured the minimum angle of elements is great than 10 degrees. The vertical displacement (Z-axis) of the bottom face of the model was constrained and the center point of the bottom was fixed. After the given lateral pressure was applied, the vertical displacement-control load was applied on the top of the specimen.

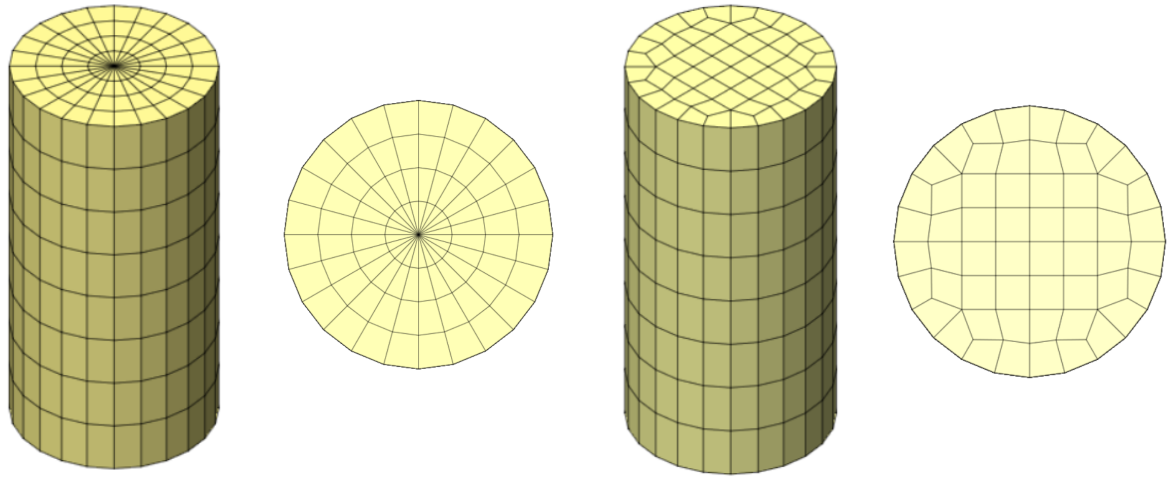

a) elevation of type A b) Plainview of type A c) elevation of type B d) Plainview of type B

Figure II.1 Meshing of cylinder specimen

Specific parameter settings in the model were tabulated in Table 1. Specifically, according to ACI 318-14, the Young's modulus of concrete was calculated by Equation II.1, while the tensile strength of concrete can estimate by Equation II.2.

$$E_c = 57000\sqrt{f_c'}\ (\text{psi}) \qquad \text{(II.1)}$$

$$f_{ct} = 6.7\sqrt{f_c'}\ (\text{psi}) \qquad \text{(II.2)}$$

As shown in Figure II.2, Cornelissen et al. (1986) and Hordijk (1991) proposed an expression for the softening behavior of concrete which also results in a crack stress equal to zero at a crack strain $\varepsilon_{nn.ult}^{\text{cr}}$, the function is defined by:

$$\frac{\sigma_{nn}^{\mathrm{cr}}(\varepsilon_{nn}^{cr})}{f_{ct}} = \begin{cases} \left(1+\left(3\frac{\varepsilon_{nn}^{cr}}{\varepsilon_{nn.ult}^{\mathrm{cr}}}\right)^3\right) exp\left(-6.93\frac{\varepsilon_{nn}^{cr}}{\varepsilon_{nn.ult}^{\mathrm{cr}}}\right) \\ -\frac{28\varepsilon_{nn}^{cr}}{\varepsilon_{nn.ult}^{\mathrm{cr}}}\exp(-6.93) \quad if\ 0 < \varepsilon_{nn}^{cr} < \varepsilon_{nn.ult}^{\mathrm{cr}} \\ 0 \qquad\qquad\qquad\qquad if\ \varepsilon_{nn.ult}^{\mathrm{cr}} < \varepsilon_{nn}^{cr} < \infty \end{cases} \tag{II.3}$$

The ultimate crack strain in the model is auto reads by

$$\varepsilon_{nn.ult}^{\mathrm{cr}} = 5.136\frac{G_f^I}{h_{ele}f_{ct}} \tag{II.4}$$

Where h_{ele} is the equivalent length of the element. In the study of this paper, $\varepsilon_{nn.ult}^{\mathrm{cr}}$ was assumed as 0.0015.

As shown in Figure II.3, the compression curve proposed by Thorenfeldt et al. (1987) was used in this paper, and the function is:

$$f = -f_p\frac{\alpha}{\alpha_p}\left(\frac{n}{n-\left(1-\left(\frac{\alpha}{\alpha_p}\right)^{nk}\right)}\right) \tag{5}$$

With $n = 0.8+\frac{f_{cc}}{17}$; $k = \begin{cases} 1 & if\ \alpha_p < \alpha < 0 \\ 0.67+\frac{f_{cc}}{62} & if\ \alpha \le \alpha_p \end{cases}$

Where f_{cc} is the cube compressive strength.

A scaling parameter ***l*** is set to control the post-peak curve of the Thorenfeldt curve. For the post-peak curve, α in Equation (5) is replaced by $\alpha_p + \left(\alpha-\alpha_p\right)\cdot\frac{h_{ele}}{l}$, so that the post-peak horizontal axis scales with $\frac{h_{ele}}{l}$. Where $\boldsymbol{h_{ele}}$ is the crack bandwidth. In special cases, it may be useful to specify the crack bandwidth explicitly via the input data item. Diana assumes a default for the crack bandwidth h_{ele}. For linear two-dimensional elements, this is $h_{ele} = \sqrt{2A}$, for higher order two-dimensional elements $h_{ele} = \sqrt{A}$ with A is the total area of the element. For solid elements the default $h_{ele} = \sqrt[3]{V}$ with V is the volume of the element.

Figure II.4 compares the stress-strain behavior between the experimental and numerical results. In the FE models with lateral stress of 0 MPa, 4 MPa, 8 MPa and 12 MPa, ***l*** was assigned to $\boldsymbol{h_{ele}}$, 30 $\boldsymbol{h_{ele}}$, 200 $\boldsymbol{h_{ele}}$, and 1000 $\boldsymbol{h_{ele}}$, respectively. As mentioned above, with the increase of ***l***, the stress decreases more smoothly after peak value. Therefore, definition ***l*** is key to the calculation of axial compression behavior under lateral pressure. According to the author's trial calculation, when L is greater than 1000, the post-peak behavior cannot be significantly affected by increasing ***l***. as shown in Figure 3, the numerical model can well predict that the compressive strength of concrete increases with the increase of lateral pressure, but the predicted peak strain is significantly smaller than the experimental value. Specifically, when the lateral compressive stress of the cylinder increases to 4 MPa, 8 MPa and 12 MPa, the experimental compressive strength of concrete is 78.5 MPa, 97.7 MPa and 115.3 MPa with corresponding strain of 0.00462, 0.00987 and 0.01471, respectively, while the predicted value is 79.9 MPa, 97.7 MPa and 114.0 MPa with corresponding strain of 0.0026, 0.003 and 0.0034, respectively. Unlike the gentle drop of the stress after peak stress in the experimental results, the stress of the predicted curves will decrease sharply before a

placid decrease. On the other hand, this model completely ignores the variation of Poisson's ratio with axial stress as the experimental results reported by Candappa et al. (2000)

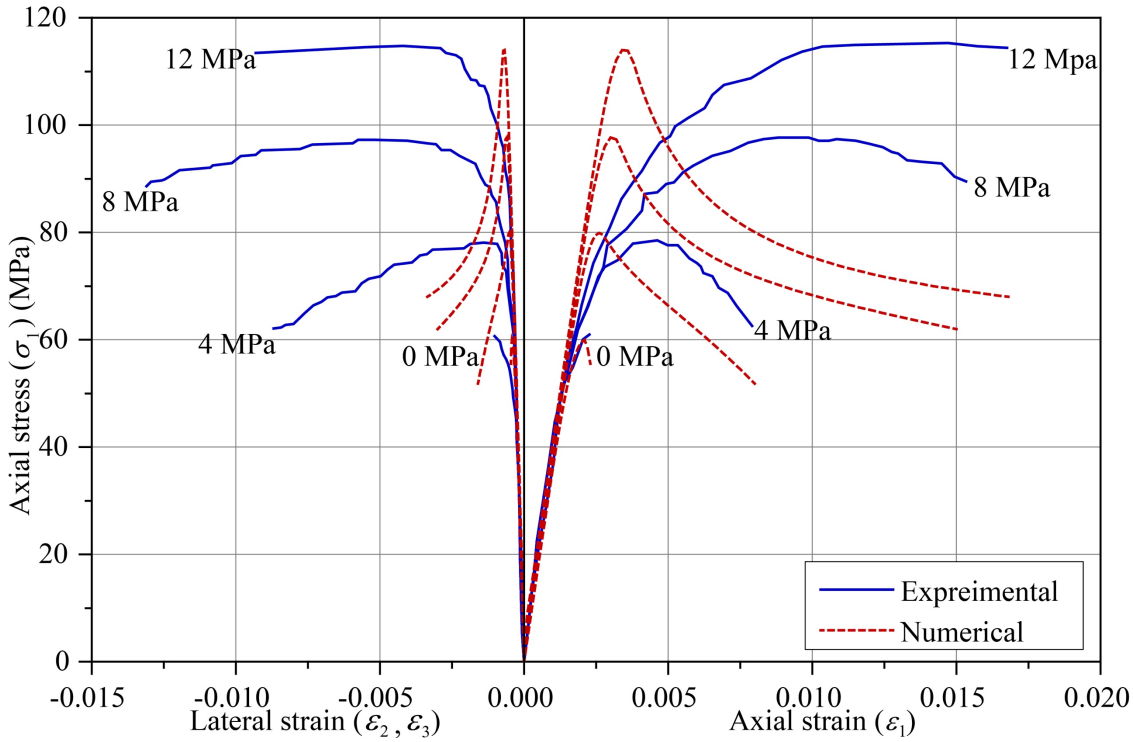

Figure II.2 Comparison of triaxial stress-strain behavior

2. Calibration of the stress-strain behavior of concrete with FRP confinement

Kestner et al. (1997) conducted a series of axial stress-strain behavior tests on cylindrical columns with or without FRP jackets. the dimension of the specimens is 152×610 mm [6×24 in.]. The compressive concrete strength, derived by the tested results of the cylindrical column with FRP jacket, is 26.2 MPa [3800 psi]. the cylinders have an average modulus of elasticity of 21.9 GPa [3170ksi]. The tensile strength can calculate by Equation (2), which is 2.85 MPa in FE model. Three types of fiber reinforced polymer (FRP), 0°/45° GFRP 0° GFRP and 0° CFRP, were tested, and the main material properties are listed in Table 2.

Table II.1 Material properties

Property	0°/45° GFRP	0° GFRP	0° CFRP
Strength	330 N/(mm·ply) 1884 lbs/(in·ply)	383 N/(mm·ply) 1884 lbs/(in·ply)	580 N/(mm·ply) 3312 lbs/(in·ply)
Secant modulus	19.1 kN/(mm·ply) 109 Kips/(in·ply)	21.6 kN/(mm·ply) 123 Kips/(in·ply)	38.1 kN/(mm·ply) 218 Kips/(in·ply)
Strain at rupture	0.024	0.019	0.015

As shown in the Figure 4, the concrete is utilized a similar meshing technique as above. 3D Truss element (L2TRU) is used for modeling the behavior of FRP and perfectly bonded to concrete by merge nodes. The area of the truss elements in the middle part is assumed to be the height of a concrete element multiplied by the thickness of FRP which is assumed to be 1 mm in this study, the area of the truss elements at both ends is assigned as the section area of FRP within the height

range of half of the concrete element. The FRP are assumed to be isotropic and modelled using linear elastic properties.

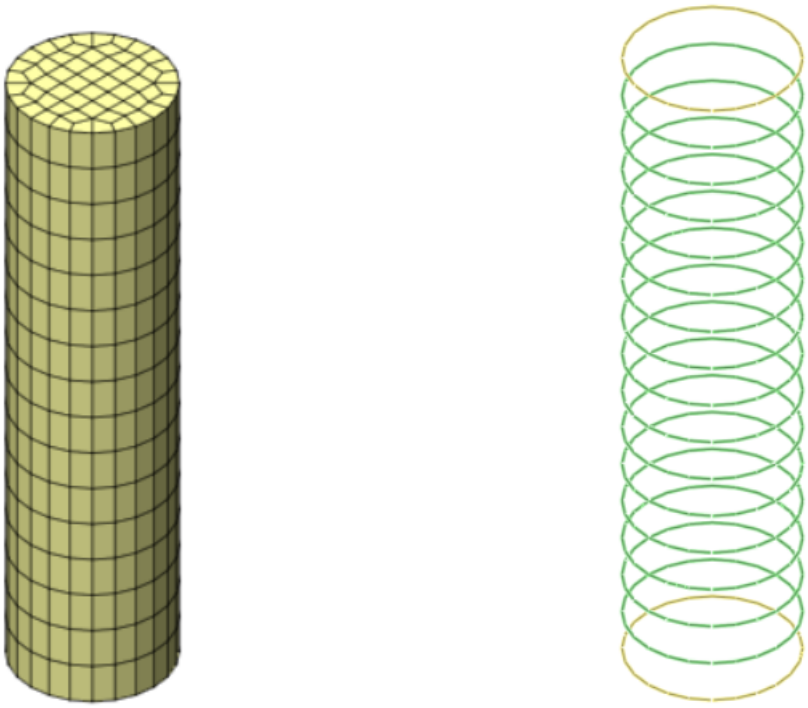

(a) meshing of concrete (b) meshing of FRP

Figure II.3 illustration of the meshing of cylinder column with FRP

Comparison of axial stress-strain relationships of the concrete column confined by various FRP are illustrated in Figure II.6. In those models, the scaling parameter $\boldsymbol{l}$ is assigned to $30\boldsymbol{h}_{ele}$. In general, the models do not predict the axial compressive stress-strain behavior of concrete confined by FRP satisfactorily. With the increase of the elastic modulus of FRP, the peak strength of columns increases slightly. However, as shown in Figure, a significant increase of peak strength of concrete column is obtained by magnifying 10 times of the modulus of elasticity of FRP. Therefore, two possible reasons why the FE models cannot reasonably predict the peak strength of concrete columns with FRP confinement are as follow: on the one hand, the prediction results on cylindrical concrete simple shows that the predicted peak strain is obviously small than that of experiment, and the stress decreases sharply after the peak stress. Due to the memorability of the constitutive of concrete, the compressive stress of concrete will not be higher than the former calculated peak strength after the strain lager than the former calculated peak strain. However, the confined stress by FRP increases with the increase of axial strain, which may lead the influence of the additional lateral confined by FRP on concrete cannot be considered in the FE model after the axial strain of concrete lager than calculated peak strain. On the other hand, the Poisson's ratio of concrete increases with the increase of the axial strain of concrete is not reflected in the model, which will lead to an over underestimating of the lateral dilation of concrete when it is subjected to larger axial loads. This will eventually lead to an underestimation of FRP's constraints.

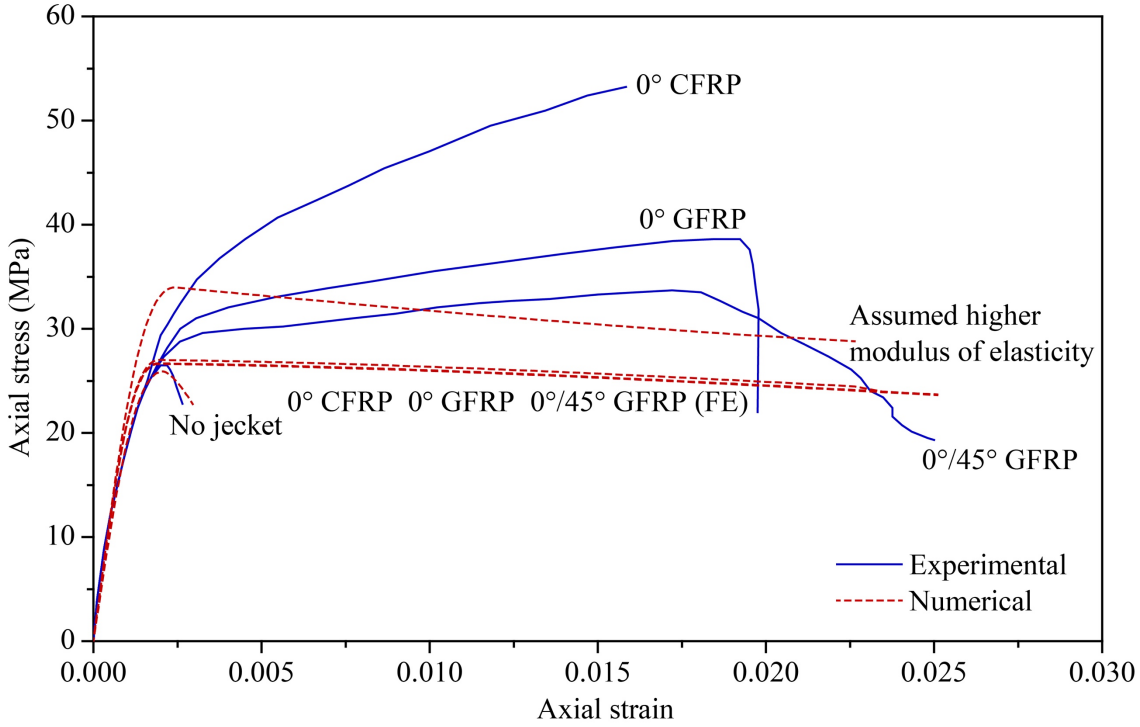

Figure II.4 Comparison of experimental and numerical axial stress-strain behavior of concrete columns confined by FRP

Appendix III: Database of Shear Tests of Stand-off Anchors

Table III.1 FE analyses of crushed conncrete depths in standoff annchors in shear

FE Analysis Number	Anchor Dia. d_a (in.)	Concrete Strength f_c' (psi)	Apparent Exposed Length l_{ea} (in.)	l_{ea}/d_a	Ultimate Strength f_{uta} (ksi)	Calculated Concrete Crush Depth l_{ec} (in.)	l_{ec}/d_a	Predicated Crush Depth by Equation 6.1	Predicated Crush Depth by Equation 6.5
1	0.50	3000	0.040	0.08	76	0.998	1.996	-	2.215
2	0.50	4000	0.040	0.08	76	0.847	1.693	-	1.661
3	0.50	5000	0.040	0.08	76	0.563	1.126	-	1.329
4	0.50	6000	0.040	0.08	76	0.363	0.726	-	1.107
5	0.50	8000	0.040	0.08	76	0.000	0.000	-	0.831
6	0.50	3000	0.250	0.50	76	1.190	2.380	2.447	2.149
7	0.50	4000	0.250	0.50	76	1.047	2.095	1.920	1.612
8	0.50	5000	0.250	0.50	76	0.879	1.757	1.604	1.290
9	0.50	6000	0.250	0.50	76	0.747	1.494	1.393	1.075
10	0.50	8000	0.250	0.50	76	0.410	0.819	1.130	0.806
11	0.50	3000	0.500	1.00	76	1.197	2.393	2.199	1.970
12	0.50	4000	0.500	1.00	76	1.022	2.044	1.717	1.478
13	0.50	5000	0.500	1.00	76	0.810	1.620	1.428	1.182
14	0.50	6000	0.500	1.00	76	0.608	1.216	1.235	0.985
15	0.50	8000	0.500	1.00	76	0.406	0.812	0.994	0.739
16	0.50	3000	1.000	2.00	76	0.936	1.871	1.704	1.478
17	0.50	4000	1.000	2.00	76	0.669	1.338	1.311	1.108
18	0.50	5000	1.000	2.00	76	0.439	0.877	1.076	0.887
19	0.50	6000	1.000	2.00	76	0.386	0.771	0.919	0.739
20	0.50	8000	1.000	2.00	76	0.318	0.636	0.722	0.554
21	0.50	3000	1.500	3.00	76	0.475	0.949	1.208	1.043
22	0.50	4000	1.500	3.00	76	0.354	0.708	0.905	0.782
23	0.50	5000	1.500	3.00	76	0.286	0.572	0.723	0.626
24	0.50	6000	1.500	3.00	76	0.212	0.425	0.602	0.522
25	0.50	8000	1.500	3.00	76	0.116	0.233	0.451	0.391
26	0.75	3000	0.060	0.08	76	1.391	1.854	-	2.215
27	0.75	4000	0.060	0.08	76	1.007	1.343	-	1.661
28	0.75	5000	0.060	0.08	76	0.720	0.960	-	1.329
29	0.75	6000	0.060	0.08	76	0.490	0.654	-	1.107
30	0.75	8000	0.060	0.08	76	0.266	0.355	-	0.831
31	0.75	3000	0.375	0.50	76	1.480	1.974	2.039	2.149
32	0.75	4000	0.375	0.50	76	1.236	1.647	1.586	1.612

FE Analysis Number	Anchor Dia. d_a (in.)	Concrete Strength f_c' (psi)	Apparent Exposed Length l_{ea} (in.)	l_{ea}/d_a	Ultimate Strength f_{uta} (ksi)	Calculated Concrete Crush Depth l_{ec} (in.)	l_{ec}/d_a	Predicated Crush Depth by Equation 6.1	Predicated Crush Depth by Equation 6.5
33	0.75	5000	0.375	0.50	76	1.007	1.342	1.314	1.290
34	0.75	6000	0.375	0.50	76	0.868	1.158	1.133	1.075
35	0.75	8000	0.375	0.50	76	0.649	0.865	0.906	0.806
36	0.75	3000	0.750	1.00	76	1.332	1.776	1.826	1.970
37	0.75	4000	0.750	1.00	76	1.134	1.512	1.411	1.478
38	0.75	5000	0.750	1.00	76	0.922	1.229	1.163	1.182
39	0.75	6000	0.750	1.00	76	0.783	1.044	0.997	0.985
40	0.75	8000	0.750	1.00	76	0.584	0.779	0.789	0.739
41	0.75	3000	1.500	2.00	76	1.090	1.454	1.400	1.478
42	0.75	4000	1.500	2.00	76	0.899	1.198	1.062	1.108
43	0.75	5000	1.500	2.00	76	0.699	0.932	0.860	0.887
44	0.75	6000	1.500	2.00	76	0.500	0.666	0.724	0.739
45	0.75	8000	1.500	2.00	76	0.380	0.506	0.556	0.554
46	0.75	3000	2.250	3.00	76	0.897	1.196	0.974	1.043
47	0.75	4000	2.250	3.00	76	0.714	0.952	0.713	0.782
48	0.75	5000	2.250	3.00	76	0.485	0.647	0.557	0.626
49	0.75	6000	2.250	3.00	76	0.390	0.521	0.452	0.522
50	0.75	8000	2.250	3.00	76	0.000	0.000	0.322	0.391
51	1.00	3000	0.080	0.08	76	2.071	2.071	-	2.215
52	1.00	4000	0.080	0.08	76	1.588	1.588	-	1.661
53	1.00	5000	0.080	0.08	76	1.231	1.231	-	1.329
54	1.00	6000	0.080	0.08	76	0.835	0.835	-	1.107
55	1.00	8000	0.080	0.08	76	0.401	0.401	-	0.831
56	1.00	3000	0.500	0.50	76	2.336	2.336	2.240	2.149
57	1.00	4000	0.500	0.50	76	1.850	1.850	1.751	1.612
58	1.00	5000	0.500	0.50	76	1.486	1.486	1.457	1.290
59	1.00	6000	0.500	0.50	76	1.248	1.248	1.261	1.075
60	1.00	8000	0.500	0.50	76	0.979	0.979	1.017	0.806
61	1.00	3000	1.000	1.00	76	2.008	2.008	2.010	1.970
62	1.00	4000	1.000	1.00	76	1.493	1.493	1.562	1.478
63	1.00	5000	1.000	1.00	76	1.245	1.245	1.293	1.182
64	1.00	6000	1.000	1.00	76	1.077	1.077	1.114	0.985
65	1.00	8000	1.000	1.00	76	0.865	0.865	0.890	0.739
66	1.00	3000	2.000	2.00	76	1.458	1.458	1.550	1.478
67	1.00	4000	2.000	2.00	76	1.149	1.149	1.185	1.108
68	1.00	5000	2.000	2.00	76	0.933	0.933	0.966	0.887

FE Analysis Number	Anchor Dia. d_a (in.)	Concrete Strength f_c' (psi)	Apparent Exposed Length l_{ea} (in.)	l_{ea}/d_a	Ultimate Strength f_{uta} (ksi)	Calculated Concrete Crush Depth l_{ec} (in.)	l_{ec}/d_a	Predicated Crush Depth by Equation 6.1	Predicated Crush Depth by Equation 6.5
69	1.00	6000	2.000	2.00	76	0.766	0.766	0.820	0.739
70	1.00	8000	2.000	2.00	76	0.536	0.536	0.638	0.554
71	1.00	3000	3.000	3.00	76	1.197	1.197	1.090	1.043
72	1.00	4000	3.000	3.00	76	0.948	0.948	0.808	0.782
73	1.00	5000	3.000	3.00	76	0.729	0.729	0.639	0.626
74	1.00	6000	3.000	3.00	76	0.532	0.532	0.526	0.522
75	1.00	8000	3.000	3.00	76	0.296	0.296	0.385	0.391
76	0.75	5000	0.060	0.08	58	0.474	0.632	-	1.014
77	0.75	5000	0.060	0.08	124	1.632	2.175	-	2.168
78	0.75	5000	0.375	0.50	58	0.812	1.082	1.056	0.984
79	0.75	5000	0.375	0.50	124	1.473	1.964	2.001	2.104
80	0.75	5000	0.750	1.00	58	0.792	1.056	0.927	0.902
81	0.75	5000	0.750	1.00	124	1.291	1.722	1.791	1.929
82	0.75	5000	1.500	2.00	58	0.573	0.763	0.668	0.677
83	0.75	5000	1.500	2.00	124	0.984	1.312	1.371	1.447
84	0.75	5000	2.250	3.00	58	0.440	0.587	0.408	0.478
85	0.75	5000	2.250	3.00	124	0.840	1.119	0.952	1.021
86	0.75	3000	0.060	0.08	58	0.985	1.313	-	1.690
87	0.75	3000	0.060	0.08	124	2.367	3.156	-	3.614
88	0.75	3000	0.375	0.50	58	1.259	1.678	1.610	1.640
89	0.75	3000	0.375	0.50	124	2.165	2.887	3.184	3.507
90	0.75	3000	0.750	1.00	58	1.198	1.598	1.433	1.504
91	0.75	3000	0.750	1.00	124	1.995	2.660	2.874	3.215
92	0.75	3000	1.500	2.00	58	0.981	1.308	1.080	1.128
93	0.75	3000	1.500	2.00	124	1.641	2.188	2.253	2.411
94	0.75	8000	0.060	0.08	58	0.245	0.327	-	0.634
95	0.75	8000	0.060	0.08	124	0.897	1.197	-	1.355
96	0.75	8000	0.375	0.50	58	0.495	0.661	0.745	0.615
97	0.75	8000	0.375	0.50	124	0.984	1.313	1.335	1.315
98	0.75	8000	0.750	1.00	58	0.427	0.569	0.642	0.564
99	0.75	8000	0.750	1.00	124	0.889	1.186	1.182	1.206
100	0.75	8000	1.500	2.00	58	0.364	0.486	0.436	0.423
101	0.75	8000	1.500	2.00	124	0.674	0.899	0.876	0.904

Table III.2 Tests of crushed conncrete depths in standoff annchors in shear

Specimen Name	Anchor Dia. d_a (in.)	Concrete Strength f_c' (psi)	Apparent Exposed Length l_{ea} (in.)	l_{ea}/d_a	Ultimate Strength f_{uta} (ksi)	Measured Concrete Crush Depth l_{ec} (in.)	l_{ec}/d_a	Predicated Crush Depth by Equation 6.1	Predicated Crush Depth by Equation 6.5
DS3	0.625	4990	0.250	0.40	93.36	0.660	1.056	1.705	1.605
DS4	0.625	4990	0.500	0.80	93.36	0.730	1.168	1.560	1.516
DS5	0.625	4990	1.125	1.80	93.36	0.520	0.832	1.197	1.165
DS6	0.625	4990	1.750	2.80	93.36	0.470	0.752	0.833	0.827
DS8	0.625	4990	0.500	0.80	93.36	0.720	1.152	1.560	1.516
20110811_0.08da-MD	0.75	5000	0.060	0.08	76.00	0.813	1.083	1.441	1.329
20110811_0.5da-MD	0.75	5000	0.375	0.50	76.00	0.875	1.167	1.314	1.290
20110811_1.0da-MD	0.75	5000	0.750	1.00	76.00	0.938	1.250	1.163	1.182
20110805_.08da-MD	0.75	5600	0.060	0.08	76.00	0.313	0.417	1.316	1.187
20110806_.08da-CD	0.75	5600	0.060	0.08	76.00	0.438	0.583	1.316	1.187
20110806_.08da-CL1	0.75	5600	0.060	0.08	76.00	0.563	0.750	1.316	1.187
20110807_.08da-CL2	0.75	5600	0.060	0.08	76.00	0.813	1.083	1.316	1.187
20110807_0.5da-MD	0.75	5600	0.375	0.50	76.00	0.500	0.667	1.197	1.152
20110809_0.5da-CD	0.75	5600	0.375	0.50	76.00	0.750	1.000	1.197	1.152
20110809_0.5da-CL1	0.75	5600	0.375	0.50	76.00	0.500	0.667	1.197	1.152
20110809_0.5da-CL2	0.75	5600	0.375	0.50	76.00	0.688	0.917	1.197	1.152

Note: Specimens DSx from Ref. 10 were from McBride (2019). One specimen from each test series was saw cut to allow observation of anchor shaft deformation, from which a crushed depth was determined as illustrated in Figure 2.41 (l_b).

Table III.3 Tests of standoff annchors in shear

Ref.	Specimen Name	Grout Use	Anchor Dia. d_a (in.)	Embed. depth h_{ef} (in.)	Concrete Strength f_c (psi)	Anchor Strength f_{uta} (ksi)	Stand-off Height l_s (in.)	Exposed Length l_{ea} (in.)	l_{ea}/d_a	Crush Depth l_{ec} (in.)	l_{ec}/d_a	Effective Exp. length l_{ee} (in.)	l_{ee}/d_a	Shear Capacity $V_{u,test}$ (kips)	Ultimate Disp. $\delta_{u,test}$ (in.)
(1)	(2)	(3)	(4)	(5)	(6)	(7)	(8)	(9)	(10)	(11)	(12)	(13)	(14)	(15)	(16)
[10]-1	DS2	no	0.63	5.38	4990	93.36	0.75	0.00	0.00	0.640	1.02	0.640	1.02	11.50	0.48
[10]-1	DS2	no	0.63	5.38	4990	93.36	0.75	0.00	0.00	0.640	1.02	0.640	1.02	11.20	0.42
[10]-1	DS2	no	0.63	5.38	4990	93.36	0.75	0.00	0.00	0.640	1.02	0.640	1.02	11.30	0.59
[10]-1	DS2	no	0.63	5.38	4990	93.36	0.75	0.00	0.00	0.640	1.02	0.640	1.02	11.30	0.59
[10]-1	DS2	no	0.63	5.38	4990	93.36	0.75	0.00	0.00	0.640	1.02	0.640	1.02	11.20	0.66
[10]-1	DS2	no	0.63	5.38	4990	93.36	0.75	0.00	0.00	0.640	1.02	0.640	1.02	11.50	0.65
[10]-1	DS3	no	0.63	5.38	4990	93.36	1.00	0.25	0.40	0.660	1.06	0.910	1.46	10.00	0.79
[10]-1	DS3	no	0.63	5.38	4990	93.36	1.00	0.25	0.40	0.660	1.06	0.910	1.46	9.60	0.76
[10]-1	DS4	no	0.63	5.38	4990	93.36	1.25	0.50	0.80	0.730	1.17	1.230	1.97	7.50	0.65
[10]-1	DS4	no	0.63	5.38	4990	93.36	1.25	0.50	0.80	0.730	1.17	1.230	1.97	8.60	0.85
[10]-1	DS4	no	0.63	5.38	4990	93.36	1.25	0.50	0.80	0.730	1.17	1.230	1.97	8.30	0.78
[10]-1	DS4	no	0.63	5.38	4990	93.36	1.25	0.50	0.80	0.730	1.17	1.230	1.97	8.00	0.73
[10]-1	DS4	no	0.63	5.38	4990	93.36	1.25	0.50	0.80	0.730	1.17	1.230	1.97	7.00	0.61
[10]-1	DS4	no	0.63	5.38	4990	93.36	1.25	0.50	0.80	0.730	1.17	1.230	1.97	8.40	0.80
[10]-1	DS4	no	0.63	5.38	4990	93.36	1.25	0.50	0.80	0.730	1.17	1.230	1.97	8.10	0.80
[10]-1	DS4	no	0.63	5.38	4990	93.36	1.25	0.50	0.80	0.730	1.17	1.230	1.97	7.60	0.71
[10]-1	DS4	no	0.63	5.38	4990	93.36	1.25	0.50	0.80	0.730	1.17	1.230	1.97	7.50	0.66
[10]-1	DS4	no	0.63	5.38	4990	93.36	1.25	0.50	0.80	0.730	1.17	1.230	1.97	7.40	0.63
[10]-1	DS5	no	0.63	5.38	4990	93.36	1.88	1.13	1.80	0.520	0.83	1.645	2.63	5.60	0.64
[10]-1	DS6	no	0.63	5.38	4990	93.36	2.50	1.75	2.80	0.470	0.75	2.220	3.55	3.70	0.76
[10]-1	DS6	no	0.63	5.38	4990	93.36	2.50	1.75	2.80	0.470	0.75	2.220	3.55	4.80	0.85
[10]-1	DS8	no	0.63	5.38	4990	93.36	1.25	0.50	0.80	0.720	1.15	1.220	1.95	7.20	0.57
[10]-1	DS8	no	0.63	5.38	4990	93.36	1.25	0.50	0.80	0.720	1.15	1.220	1.95	7.00	0.53
[10]-1	DS8	no	0.63	5.38	4990	93.36	1.25	0.50	0.80	0.720	1.15	1.220	1.95	7.10	0.73
[10]-1	DS8	no	0.63	5.38	4990	93.36	1.25	0.50	0.80	0.720	1.15	1.220	1.95	6.80	0.51
[10]-1	DS8	no	0.63	5.38	4990	93.36	1.25	0.50	0.80	0.720	1.15	1.220	1.95	6.80	0.76
[10]-1	DS10	no	1.0	7.0	4990	92.08	2.0	0.75	0.75	0	0	0.75	0.75	35.12	1.88
[10]-1	DS10	no	1.0	7.0	4990	92.08	2.0	0.75	0.75	0	0	0.75	0.75	26.69	1.58
[10]-1	DS10	no	1.0	7.0	4990	92.08	2.0	0.75	0.75	0	0	0.75	0.75	26.69	1.58
[10]-1	DS10	no	1.0	7.0	4990	92.08	2.0	0.75	0.75	0	0	0.75	0.75	25.82	1.68
[10]-1	DS10	no	1.0	7.0	4990	92.08	2.0	0.75	0.75	0	0	0.75	0.75	20.94	1.53

Ref.	Specimen Name	Grout Use	Anchor Dia. d_a (in.)	Embed. depth h_{ef} (in.)	Concrete Strength f_c' (psi)	Anchor Strength f_{uta} (ksi)	Stand-off Height l_s (in.)	Exposed Length l_{ea} (in.)	l_{ea}/d_a	Crush Depth l_{ec} (in.)	l_{ec}/d_a	Effective Exp. length l_{ee} (in.)	l_{ee}/d_a	Shear Capacity $V_{u,test}$ (kips)	Ultimate Disp. $\delta_{u,test}$ (in.)
(1)	(2)	(3)	(4)	(5)	(6)	(7)	(8)	(9)	(10)	(11)	(12)	(13)	(14)	(15)	(16)
[10]-1	DS11	no	1.0	7.0	4990	92.08	4.0	2.75	2.75	0	0	2.75	2.75	24.68	2.21
[10]-1	DS11	no	1.0	7.0	4990	92.08	4.0	2.75	2.75	0	0	2.75	2.75	14.05	1.54
[10]-1	DS13	no	0.63	5.38	4990	93.36	1.25	0.50	0.80	0.000	0.00	0.500	0.80	9.60	0.79
[10]-1	DS13	no	0.63	5.38	4990	93.36	1.25	0.50	0.80	0.000	0.00	0.500	0.80	9.50	0.75
[10]-1	DS13	no	0.63	5.38	4990	93.36	1.25	0.50	0.80	0.000	0.00	0.500	0.80	9.30	0.72
[10]-1	DS13	no	0.63	5.38	4990	93.36	1.25	0.50	0.80	0.000	0.00	0.500	0.80	8.80	0.78
[10]-1	DS13	no	0.63	5.38	4990	93.36	1.25	0.50	0.80	0.000	0.00	0.500	0.80	8.60	0.77
[10]-1	DS14	no	0.63	5.38	4990	93.36	2.50	1.75	2.80	0.000	0.00	1.750	2.80	5.20	0.89
[10]-1	DS14	no	0.63	5.38	4990	93.36	2.50	1.75	2.80	0.000	0.00	1.750	2.80	5.00	0.79
[10]-1	T2	no	0.63	5.38	6360	91.59	1.25	0.50	0.80	0.000	0.00	0.500	0.80	6.50	0.56
[10]-1	T3	no	0.63	5.38	6360	91.59	2.50	1.75	2.80	0.000	0.00	1.750	2.80	4.60	0.73
[10]-1	T4	no	0.63	5.38	6360	91.59	1.25	0.50	0.80	0.000	0.00	0.500	0.80	7.40	0.60
[10]-1	T9	no	1.00	7.00	6360	92.08	2.00	0.75	0.75	0.000	0.00	0.750	0.75	18.00	0.88
[10]-1	T10	no	1.00	7.00	6360	92.08	4.00	2.75	2.75	0.000	0.00	2.750	2.75	10.50	1.57
[10]-1	FS1	no	1.25	20.00	6590	87.1	2.88	1.25	1.00	0.000	0.00	1.250	1.00	27.10	1.89
[10]-1	DS1	no	0.63	5.38	4990	93.36	0.00	0.00	0.00	0.560	0.90	0.560	0.90	12.00	0.23
[10]-1	DS1	no	0.63	5.38	4990	93.36	0.00	0.00	0.00	0.560	0.90	0.560	0.90	13.00	0.20
[10]-1	DS1	no	0.63	5.38	4990	93.36	0.00	0.00	0.00	0.560	0.90	0.560	0.90	12.40	0.20
[10]-1	DS1	no	0.63	5.38	4990	93.36	0.00	0.00	0.00	0.560	0.90	0.560	0.90	12.20	0.16
[10]-1	DS1	no	0.63	5.38	4990	93.36	0.00	0.00	0.00	0.560	0.90	0.560	0.90	12.60	0.16
[10]-1	DS1	no	0.63	5.38	4990	93.36	0.00	0.00	0.00	0.560	0.90	0.560	0.90	12.10	0.18
[10]-1	DS1	no	0.63	5.38	4990	93.36	0.00	0.00	0.00	0.560	0.90	0.560	0.90	12.20	0.14
[10]-1	DS1	no	0.63	5.38	4990	93.36	0.00	0.00	0.00	0.560	0.90	0.560	0.90	12.20	0.18
[10]-1	DS7	no	0.63	5.38	4990	93.36	0.00	0.00	0.00	0.540	0.86	0.540	0.86	11.90	0.16
[10]-1	DS7	no	0.63	5.38	4990	93.36	0.00	0.00	0.00	0.540	0.86	0.540	0.86	11.60	0.19
[10]-1	DS7	no	0.63	5.38	4990	93.36	0.00	0.00	0.00	0.540	0.86	0.540	0.86	11.60	0.18
[10]-1	DS7	no	0.63	5.38	4990	93.36	0.00	0.00	0.00	0.540	0.86	0.540	0.86	10.60	0.15
[10]-1	DS9	no	1.00	5.38	4990	93.36	0.00	0.00	0.00	0.000	0.00	0.000	0.00	33.51	0.28
[10]-1	DS9	no	1.00	5.38	4990	93.36	0.00	0.00	0.00	0.000	0.00	0.000	0.00	33.11	0.27
[10]-1	DS9	no	1.00	5.38	4990	93.36	0.00	0.00	0.00	0.000	0.00	0.000	0.00	33.71	0.34
[10]-1	DS9	no	1.00	5.38	4990	93.36	0.00	0.00	0.00	0.000	0.00	0.000	0.00	33.30	0.37
[10]-1	DS12	no	0.63	5.38	4990	93.36	0.00	0.00	0.00	0.000	0.00	0.000	0.00	12.80	0.16
[10]-1	DS12	no	0.63	5.38	4990	93.36	0.00	0.00	0.00	0.000	0.00	0.000	0.00	12.20	0.18
[10]-1	DS12	no	0.63	5.38	4990	93.36	0.00	0.00	0.00	0.000	0.00	0.000	0.00	12.00	0.21

Ref.	Specimen Name	Grout Use	Anchor Dia. d_a (in.)	Embed. depth h_{ef} (in.)	Concrete Strength f_c' (psi)	Anchor Strength f_{uta} (ksi)	Stand-off Height l_s (in.)	Exposed Length l_{ea} (in.)	l_{ea}/d_a	Crush Depth l_{ec} (in.)	l_{ec}/d_a	Effective Exp. length l_{ee} (in.)	l_{ee}/d_a	Shear Capacity $V_{u,test}$ (kips)	Ultimate Disp. $\delta_{u,test}$ (in.)
(1)	(2)	(3)	(4)	(5)	(6)	(7)	(8)	(9)	(10)	(11)	(12)	(13)	(14)	(15)	(16)
[10]-1	DS12	no	0.63	5.38	4990	93.36	0.00	0.00	0.00	0.000	0.00	0.000	0.00	11.80	0.20
[32]	9132010	no	0.75	6.00	3520	76.00	0.04	0.04	0.05	1.750	2.33	1.790	2.39	22.19	1.20
[32]	9132010_2	no	0.75	6.00	3520	76.00	0.04	0.04	0.05	1.750	2.33	1.790	2.39	22.47	1.29
[32]	9282010	no	1.00	6.00	3800	130.00	0.04	0.04	0.04	1.750	1.75	1.790	1.79	39.18	1.03
[32]	9292010	no	1.00	6.00	3800	130.00	0.04	0.04	0.04	1.750	1.75	1.790	1.79	44.11	1.34
[32]	10062010	no	1.00	6.00	3800	130.00	0.04	0.04	0.04	1.750	1.75	1.790	1.79	38.40	1.37
[32]	10062010_2	no	1.00	6.00	3800	130.00	0.04	0.04	0.04	1.750	1.75	1.790	1.79	34.71	1.25
[32]	10072010	no	1.00	6.00	3800	130.00	0.04	0.04	0.04	1.750	1.75	1.790	1.79	33.40	1.40
[32]	10292010 SG	no	1.00	6.00	3800	130.00	0.04	0.04	0.04	1.688	1.69	1.728	1.73	36.13	1.16
[32]	11192010 SG	no	1.00	6.00	3800	130.00	0.04	0.04	0.04	1.688	1.69	1.728	1.73	39.33	1.39
[30]	B-10-0-S-M	no	0.47	9.45	4550	70.00	0.00	0.00	0.00	0.000	0.00	0.000	0.00	8.51	0.66
[30]	B-10-0-S-M	no	0.47	9.45	4550	70.00	0.39	0.39	0.83	0.000	0.00	0.394	0.83	7.94	0.94
[30]	B-20-0-S-M	no	0.47	9.45	4550	70.00	0.79	0.79	1.67	0.000	0.00	0.787	1.67	7.71	1.19
[30]	B-40-0-S-M	no	0.47	9.45	4550	70.00	1.57	1.57	3.33	0.000	0.00	1.575	3.33	7.50	1.48
-	20110811_0.08da-MD	no	0.75	6.00	5000	76.00	0.06	0.06	0.08	0.813	1.08	0.873	1.16	17.50	0.46
-	20110811_0.5da-MD	no	0.75	6.00	5000	76.00	0.38	0.38	0.50	0.875	1.17	1.250	1.67	13.70	0.50
-	20110811_1.0da-MD	no	0.75	6.00	5000	76.00	0.75	0.75	1.00	0.938	1.25	1.688	2.25	10.00	0.60
-	20110805_.08da-MD	no	0.75	6.00	5600	76.00	0.06	0.06	0.08	0.313	0.42	0.373	0.50	15.40	0.23
-	20110806_.08da-CD	no	0.75	6.00	5600	76.00	0.06	0.06	0.08	0.438	0.58	0.498	0.66	15.43	0.18
-	20110806_.08da-CL1	no	0.75	6.00	5600	76.00	0.06	0.06	0.08	0.563	0.75	0.623	0.83	14.67	0.27
-	20110807_.08da-CL2	no	0.75	6.00	5600	76.00	0.06	0.06	0.08	0.813	1.08	0.873	1.16	9.22	0.25
-	20110807_0.5da-MD	no	0.75	6.00	5600	76.00	0.38	0.38	0.50	0.500	0.67	0.875	1.17	12.70	0.27
-	20110809_0.5da-CD	no	0.75	6.00	5600	76.00	0.38	0.38	0.50	0.750	1.00	1.125	1.50	9.97	0.30
-	20110809_0.5da-CL1	no	0.75	6.00	5600	76.00	0.38	0.38	0.50	0.500	0.67	0.875	1.17	11.46	0.28
-	20110809_0.5da-CL2	no	0.75	6.00	5600	76.00	0.38	0.38	0.50	0.688	0.92	1.063	1.42	7.10	0.31

Note: The measured crushed concrete depths for specimens from Ref. 10 were obtained from Mcbride (2019). One specimen from each test series was saw cut to allow observation of anchor shaft deformation, from which a crushed depth was determined as illustrated in Figure 2.41 (l_b).

The specimens from Ref. 32 did not have a stand-off height, the listed values are from the description of the teste, in which a 1mm gap was kept between the loading plate and concrete surface. The crushed concrete depths were recorded during the tests.

Table III.4 Comparison of test results with design equations

Specimen Name	l_{ee}/d_a	Shear Capacity $V_{u,test}$	ACI 318 $V_{u,ACI}$ (kips)	$V_{u,test}/V_{u,ACI}$	AASHTO $V_{u,AASHTO}$ (kips)	$V_{u,test}/V_{u,AASHTO}$	*fib-2018* $V_{u,FIB}$ (kips)	$V_{u,test}/V_{u,FIB}$	*Lin et al.* $V_{u,Lin}$ (kips)	$V_{u,test}/V_{u,Lin}$	*Cook et al.* $V_{u,Cook}$ (kips)	$V_{u,test}/V_{u,Cook}$	*Pred.* l_{ee}/d_a (Eq. 6.5)	$V_{u,pred}$ (Eq. 6.6)	$V_{u,test}/V_{u,pred}$
(2)	(14)	(15)	(17)	(18)	(19)	(20)	(21)	(22)	(23)	(24)	(25)	(26)	(27)	(28)	(29)
DS2	1.02	11.50	10.13	1.135	14.31	0.803	9.54	1.205	4.95	2.322	12.66	0.908	0.98	8.65	1.330
DS2	1.02	11.20	10.13	1.106	14.31	0.782	9.54	1.174	4.95	2.261	12.66	0.885	0.98	8.65	1.295
DS2	1.02	11.30	10.13	1.116	14.31	0.789	9.54	1.184	4.95	2.282	12.66	0.893	0.98	8.65	1.307
DS2	1.02	11.30	10.13	1.116	14.31	0.789	9.54	1.184	4.95	2.282	12.66	0.893	0.98	8.65	1.307
DS2	1.02	11.20	10.13	1.106	14.31	0.782	9.54	1.174	4.95	2.261	12.66	0.885	0.98	8.65	1.295
DS2	1.02	11.50	10.13	1.135	14.31	0.803	9.54	1.205	4.95	2.322	12.66	0.908	0.98	8.65	1.330
DS3	1.46	10.00	10.13	0.987	14.31	0.699	7.15	1.398	4.23	2.366	10.57	0.946	1.51	7.11	1.407
DS3	1.46	9.60	10.13	0.948	14.31	0.671	7.15	1.342	4.23	2.272	10.57	0.908	1.51	7.11	1.350
DS4	1.97	7.50	10.13	0.741	14.31	0.524	5.59	1.341	3.71	2.023	7.65	0.980	2.01	6.28	1.193
DS4	1.97	8.60	10.13	0.849	14.31	0.601	5.59	1.538	3.71	2.320	7.65	1.124	2.01	6.28	1.369
DS4	1.97	8.30	10.13	0.820	14.31	0.580	5.59	1.484	3.71	2.239	7.65	1.085	2.01	6.28	1.321
DS4	1.97	8.00	10.13	0.790	14.31	0.559	5.59	1.431	3.71	2.158	7.65	1.045	2.01	6.28	1.273
DS4	1.97	7.00	10.13	0.691	14.31	0.489	5.59	1.252	3.71	1.888	7.65	0.915	2.01	6.28	1.114
DS4	1.97	8.40	10.13	0.829	14.31	0.587	5.59	1.502	3.71	2.266	7.65	1.098	2.01	6.28	1.337
DS4	1.97	8.10	10.13	0.800	14.31	0.566	5.59	1.449	3.71	2.185	7.65	1.058	2.01	6.28	1.289
DS4	1.97	7.60	10.13	0.750	14.31	0.531	5.59	1.359	3.71	2.050	7.65	0.993	2.01	6.28	1.209
DS4	1.97	7.50	10.13	0.741	14.31	0.524	5.59	1.341	3.71	2.023	7.65	0.980	2.01	6.28	1.193
DS4	1.97	7.40	10.13	0.731	14.31	0.517	5.59	1.323	3.71	1.996	7.65	0.967	2.01	6.28	1.178
DS5	2.63	5.60	10.13	0.553	14.31	0.391	3.51	1.598	3.29	1.700	4.05	1.384	3.17	5.25	1.067
DS6	3.55	3.70	10.13	0.365	14.31	0.258	2.52	1.469	2.95	1.253	2.68	1.379	4.35	4.72	0.785
DS6	3.55	4.80	10.13	0.474	14.31	0.335	2.52	1.906	2.95	1.626	2.68	1.789	4.35	4.72	1.018
DS8	1.95	7.20	10.13	0.711	14.31	0.503	5.59	1.288	3.72	1.936	7.65	0.941	2.01	6.28	1.146
DS8	1.95	7.00	10.13	0.691	14.31	0.489	5.59	1.252	3.72	1.882	7.65	0.915	2.01	6.28	1.114
DS8	1.95	7.10	10.13	0.701	14.31	0.496	5.59	1.270	3.72	1.909	7.65	0.928	2.01	6.28	1.130
DS8	1.95	6.80	10.13	0.671	14.31	0.475	5.59	1.216	3.72	1.828	7.65	0.889	2.01	6.28	1.082
DS8	1.95	6.80	10.13	0.671	14.31	0.475	5.59	1.216	3.72	1.828	7.65	0.889	2.01	6.28	1.082
DS10	0.75	35.12	26.78	1.311	36.14	1.049	14.53	2.418	15.27	2.300	21.36	1.644	2.11	16.58	2.119
DS10	0.75	26.69	26.78	0.996	36.14	0.797	14.53	1.837	15.27	1.748	21.36	1.250	2.11	16.58	1.610
DS10	0.75	26.69	26.78	0.996	36.14	0.797	14.53	1.837	15.27	1.748	21.36	1.250	2.11	16.58	1.610
DS10	0.75	25.82	26.78	0.964	36.14	0.771	14.53	1.777	15.27	1.691	21.36	1.209	2.11	16.58	1.558
DS10	0.75	20.94	26.78	0.782	36.14	0.625	14.53	1.442	15.27	1.371	21.36	0.980	2.11	16.58	1.263
DS11	2.75	24.68	26.78	0.921	36.14	0.737	6.45	3.826	8.70	2.838	7.38	3.345	4.90	12.28	2.010
DS11	2.75	14.05	26.78	0.525	36.14	0.420	6.45	2.178	8.70	1.616	7.38	1.904	4.90	12.28	1.144

Specimen Name	l_{ee}/d_a	Shear Capacity $V_{u,test}$	ACI 318 $V_{u,ACI}$ (kips)	$V_{u,test}/V_{u,ACI}$	AASHTO $V_{u,AASHTO}$ (kips)	$V_{u,test}/V_{u,AASHTO}$	*fib-2018* $V_{u,fib}$ (kips)	$V_{u,test}/V_{u,fib}$	*Lin et al.* $V_{u,Lin}$ (kips)	$V_{u,test}/V_{u,Lin}$	*Cook et al.* $V_{u,Cook}$ (kips)	$V_{u,test}/V_{u,Cook}$	*Pred.* l_{ee}/d_a (Eq. 6.5)	$V_{u,pred}$ (Eq. 6.6)	$V_{u,test}/V_{u,pred}$
(2)	(14)	(15)	(17)	(18)	(19)	(20)	(21)	(22)	(23)	(24)	(25)	(26)	(27)	(28)	(29)
DS13	0.80	9.60	10.13	0.948	14.31	0.671	5.59	1.717	5.54	1.734	7.65	1.254	2.01	6.28	1.528
DS13	0.80	9.50	10.13	0.938	14.31	0.664	5.59	1.699	5.54	1.716	7.65	1.241	2.01	6.28	1.512
DS13	0.80	9.30	10.13	0.918	14.31	0.650	5.59	1.663	5.54	1.680	7.65	1.215	2.01	6.28	1.480
DS13	0.80	8.80	10.13	0.869	14.31	0.615	5.59	1.574	5.54	1.590	7.65	1.150	2.01	6.28	1.400
DS13	0.80	8.60	10.13	0.849	14.31	0.601	5.59	1.538	5.54	1.554	7.65	1.124	2.01	6.28	1.369
DS14	2.80	5.20	10.13	0.513	14.31	0.363	2.52	2.065	3.22	1.616	2.68	1.938	4.35	4.72	1.103
DS14	2.80	5.00	10.13	0.494	14.31	0.349	2.52	1.985	3.22	1.554	2.68	1.864	4.35	4.72	1.060
T2	0.80	6.50	9.94	0.654	14.04	0.463	5.49	1.185	5.43	1.197	6.84	0.951	1.80	6.46	1.006
T3	2.80	4.60	9.94	0.463	14.04	0.328	2.47	1.862	3.16	1.457	2.60	1.770	4.23	4.67	0.986
T4	0.80	7.40	9.94	0.745	14.04	0.527	5.49	1.349	5.43	1.363	6.84	1.082	1.80	6.46	1.145
T9	0.75	18.00	26.78	0.672	36.14	0.498	14.53	1.239	15.27	1.179	19.27	0.934	1.91	17.07	1.054
T10	2.75	10.50	26.78	0.392	36.14	0.291	6.45	1.628	8.70	1.207	7.28	1.442	4.79	12.20	0.861
FS1	1.00	27.10	40.51	0.669	53.42	0.507	18.72	1.448	20.44	1.326	25.03	1.083	2.37	23.67	1.145
DS1	0.90	12.00	10.13	1.185	14.31	0.838	9.54	1.258	5.26	2.281	12.66	0.948	0.98	8.65	1.388
DS1	0.90	13.00	10.13	1.284	14.31	0.908	9.54	1.363	5.26	2.471	12.66	1.027	0.98	8.65	1.504
DS1	0.90	12.40	10.13	1.224	14.31	0.866	9.54	1.300	5.26	2.357	12.66	0.979	0.98	8.65	1.434
DS1	0.90	12.20	10.13	1.205	14.31	0.852	9.54	1.279	5.26	2.319	12.66	0.964	0.98	8.65	1.411
DS1	0.90	12.60	10.13	1.244	14.31	0.880	9.54	1.321	5.26	2.395	12.66	0.995	0.98	8.65	1.457
DS1	0.90	12.10	10.13	1.195	14.31	0.845	9.54	1.268	5.26	2.300	12.66	0.956	0.98	8.65	1.400
DS1	0.90	12.20	10.13	1.205	14.31	0.852	9.54	1.279	5.26	2.319	12.66	0.964	0.98	8.65	1.411
DS1	0.90	12.20	10.13	1.205	14.31	0.852	9.54	1.279	5.26	2.319	12.66	0.964	0.98	8.65	1.411
DS7	0.86	11.90	10.13	1.175	14.31	0.831	9.54	1.247	5.35	2.225	12.66	0.940	0.98	8.65	1.376
DS7	0.86	11.60	10.13	1.145	14.31	0.810	9.54	1.216	5.35	2.169	12.66	0.916	0.98	8.65	1.342
DS7	0.86	11.60	10.13	1.145	14.31	0.810	9.54	1.216	5.35	2.169	12.66	0.916	0.98	8.65	1.342
DS7	0.86	10.60	10.13	1.047	14.31	0.741	9.54	1.111	5.35	1.982	12.66	0.837	0.98	8.65	1.226
DS9	0.00	33.51	26.78	1.251	36.14	1.001	24.09	1.391	34.08	0.983	33.48	1.001	0.97	23.10	1.451
DS9	0.00	33.11	26.78	1.236	36.14	0.989	24.09	1.375	34.08	0.971	33.48	0.989	0.97	23.10	1.433
DS9	0.00	33.71	26.78	1.259	36.14	1.007	24.09	1.399	34.08	0.989	33.48	1.007	0.97	23.10	1.459
DS9	0.00	33.30	26.78	1.243	36.14	0.995	24.09	1.382	34.08	0.977	33.48	0.995	0.97	23.10	1.442
DS12	0.00	12.80	10.13	1.264	14.31	0.894	9.54	1.342	12.87	0.995	12.66	1.011	0.98	8.65	1.481
DS12	0.00	12.20	10.13	1.205	14.31	0.852	9.54	1.279	12.87	0.948	12.66	0.964	0.98	8.65	1.411
DS12	0.00	12.00	10.13	1.185	14.31	0.838	9.54	1.258	12.87	0.932	12.66	0.948	0.98	8.65	1.388
DS12	0.00	11.80	10.13	1.165	14.31	0.824	9.54	1.237	12.87	0.917	12.66	0.932	0.98	8.65	1.365

Specimen Name	l_{ee}/d_a	Shear Capacity $V_{u,test}$	ACI 318 $V_{u,ACI}$ (kips)	$V_{u,test}/V_{u,ACI}$	AASHTO $V_{u,AASHTO}$ (kips)	$V_{u,test}/V_{u,AASHTO}$	*fib-2018* $V_{u,fib}$ (kips)	$V_{u,test}/V_{u,fib}$	*Lin et al.* $V_{u,Lin}$ (kips)	$V_{u,test}/V_{u,Lin}$	*Cook et al.* $V_{u,Cook}$ (kips)	$V_{u,test}/V_{u,Cook}$	*Pred.* l_{ee}/d_a (Eq. 6.5)	$V_{u,pred}$ (Eq. 6.6)	$V_{u,test}/V_{u,pred}$
(2)	(14)	(15)	(17)	(18)	(19)	(20)	(21)	(22)	(23)	(24)	(25)	(26)	(27)	(28)	(29)
9132010	2.39	22.19	12.18	1.821	16.78	1.322	10.74	2.067	4.97	4.468	3.88	5.716	1.21	10.90	2.037
9132010_2	2.39	22.47	12.18	1.844	16.78	1.339	10.74	2.093	4.97	4.524	3.88	5.788	1.21	10.90	2.062
9282010	1.79	39.18	38.11	1.028	51.42	0.762	33.24	1.179	15.18	2.581	15.94	2.458	1.87	25.26	1.551
9292010	1.79	44.11	38.11	1.158	51.42	0.858	33.24	1.327	15.18	2.905	15.94	2.768	1.87	25.26	1.746
10062010	1.79	38.40	38.11	1.008	51.42	0.747	33.24	1.155	15.18	2.529	15.94	2.409	1.87	25.26	1.520
10062010_2	1.79	34.71	38.11	0.911	51.42	0.675	33.24	1.044	15.18	2.286	15.94	2.178	1.87	25.26	1.374
10072010	1.79	33.40	38.11	0.877	51.42	0.650	33.24	1.005	15.18	2.200	15.94	2.096	1.87	25.26	1.322
10292010 SG	1.73	36.13	38.11	0.948	51.42	0.703	33.24	1.087	15.41	2.345	16.46	2.195	1.87	25.26	1.430
11192010 SG	1.73	39.33	38.11	1.032	51.42	0.765	33.24	1.183	15.41	2.552	16.46	2.390	1.87	25.26	1.557
B-10-0-S-M	0.00	8.51	4.07	2.093	6.13	1.388	4.09	2.082	5.64	1.509	5.08	1.675	0.81	4.79	1.778
B-10-0-S-M	0.83	7.94	4.07	1.953	6.13	1.295	2.35	3.377	2.70	2.941	2.93	2.711	1.81	3.63	2.187
B-20-0-S-M	1.67	7.71	4.07	1.896	6.13	1.257	1.58	4.871	2.14	3.603	1.69	4.562	2.74	3.22	2.394
B-40-0-S-M	3.33	7.50	4.07	1.845	6.13	1.223	0.94	8.012	1.77	4.235	0.88	8.500	4.62	2.85	2.629
20110811_.08da-MD	1.16	17.50	12.18	1.436	16.78	1.043	10.52	1.663	6.47	2.706	15.10	1.159	0.91	12.19	1.436
20110811_0.5da-MD	1.67	13.70	12.18	1.124	16.78	0.816	7.85	1.745	5.64	2.431	11.82	1.159	1.50	10.03	1.366
20110811_1.0da-MD	2.25	10.00	12.18	0.821	16.78	0.596	5.88	1.701	5.07	1.974	7.98	1.253	2.16	8.77	1.140
20110805_.08da-MD	0.50	15.40	12.18	1.264	16.78	0.918	10.52	1.464	8.99	1.713	15.10	1.020	0.83	12.67	1.215
20110806_.08da-CD	0.66	15.43	12.18	1.266	16.78	0.920	10.52	1.466	8.07	1.913	15.10	1.022	0.83	12.67	1.217
20110806_.08da-CL1	0.83	14.67	12.18	1.204	16.78	0.874	10.52	1.394	7.39	1.985	15.10	0.971	0.83	12.67	1.157
20110807_.08da-CL2	1.16	9.22	12.18	0.756	16.78	0.549	10.52	0.876	6.47	1.425	15.10	0.610	0.83	12.67	0.727
20110807_0.5da-MD	1.17	12.70	12.18	1.042	16.78	0.757	7.85	1.617	6.46	1.966	11.82	1.075	1.42	10.25	1.239
20110809_0.5da-CD	1.50	9.97	12.18	0.818	16.78	0.594	7.85	1.270	5.86	1.701	11.82	0.844	1.42	10.25	0.973
20110809_0.5da-CL1	1.17	11.46	12.18	0.941	16.78	0.683	7.85	1.459	6.46	1.774	11.82	0.970	1.42	10.25	1.118
20110809_0.5da-CL2	1.42	7.10	12.18	0.583	16.78	0.423	7.85	0.904	5.99	1.185	11.82	0.601	1.42	10.25	0.693
Average ratio				1.004		0.714		1.547		2.052		1.450			1.361
Min. ratio				0.365		0.258		0.876		0.917		0.601			0.693
Max. ratio				2.093		1.388		8.012		4.524		8.500			2.629
Standard deviation				0.357		0.244		0.895		0.687		1.226			0.323
Statistical analysis excluding the tests controlled by low-cycle fatigue (loading type CL2)															
Average ratio				1.013		0.720		1.564		2.071		1.472			1.376
Min. ratio				0.365		0.258		1.005		0.917		0.837			0.785
Max. ratio				2.093		1.388		8.012		4.524		8.500			2.629
Standard deviation				0.357		0.244		0.900		0.685		1.234			0.311